UNIVERSITY OF LIVERPOOL

Mechanical Properties of Metal Matrix Syntactic Foam

Thesis submitted in accordance with the requirements of the University of Liverpool for the degree of Doctor in Philosophy

by

Yue Zhang

January 2020

ABSTRACT

Over the last few decades, metal matrix syntactic foams (MMSF) have received a large amount of interest in both academia and industry, due to lightweight, high specific stiffness, strength and energy absorption capability. Their unique properties and multi-functionality allow them to be used in many different applications throughout different industrial sectors.

This thesis investigated the compressive, energy absorption and energy dissipation properties of Al matrix syntactic foams. Ceramic microspheres (CM) with three different particle size ranges (75-150 μm, 125-250 μm and 250-500 μm) and the Al 6082 alloy were used to fabricate MMSFs. The Al/CM syntactic foams with different CMs and varying Al/CM ratios were fabricated by the pressure infiltration casting method.

The compressive and energy absorption properties of all the types of syntactic foams were measured by static compression tests. The compressive strength of the syntactic foams was mainly determined by strength of both the Al matrix and the CM particles. The strength of the syntactic foams increased slightly with the volume percentage of CM particles. The densification strain of all the syntactic foams was dependent upon the porosity arising from the CM particles. The energy absorption of the syntactic foam was determined by both plateau strength and densification strain. The energy absorption of bimodal syntactic foams mixing large and small CM particles was nearly twice of the monomodal syntactic foams. Among the three types of the monomodal syntactic foams, the large CM particle reinforced syntactic foam absorbed the highest amount of energy under the Charpy impact.

The energy dissipation properties of the Al/CM syntactic foams were assessed by intermittent compression tests. Hysteresis loops, which represent an energy dissipation, were present in the stress-strain curves of all the syntactic foams samples. The specific damping capacity of all syntactic foams was not affected by the CM particle size but was dependent upon the volume percentage of the CM particles in the syntactic foam. The dissipated energy was proportional to the square of the applied stress in the cyclic loading.

One-stage repetitive cyclic compression tests were conducted on the monomodal syntactic foams and the syntactic foams toughened with Al particles. The specific damping capacity the syntactic foams evidentially decreased after 20 cycles. The hysteretic energy dissipation in repetitive cyclic compression of syntactic foams was sensitive to the CM particle size and the volume percentages of the CM particles.

Two-stage repetitive cyclic compression tests were conducted on one monomodal syntactic foam. The cyclic loading history was found to have influence on the hysteretic energy dissipation. When the stress level was below the maximum stress experienced in the previous cycles, the specific dissipated energy and specific damping capacity were much lower than those measured at the same stress in the previous cycles. The hysteretic energy dissipation was caused by microcrack formation and propagation in the CM particles. The accumulation of crack development led to CM particle fracture, which resulted in a small permanent plastic deformation.

The energy dissipation behaviour of syntactic foams with different sizes and volume percentages of the CM particles under impulsive loading was assessed. Both the particle size and volume percentage of the CM particles had an influence on the energy

dissipation capacity of the Al/CM syntactic foams under free oscillation. As in cyclic compression, the damping of the syntactic foams in free oscillation was also caused by microcrack initiation and propagation in the CM particles.

DECLARATION

I hereby certify that the content of this project work entitled “Mechanical Properties of Metal Matrix Syntactic Foam”, submitted for the degree of Doctor in Philosophy in the Faculty of Science and Engineering at the University of Liverpool, is a record of an original work done by me under the supervision of Prof. Yuyuan Zhao and Dr. Robert Birch of the School of Engineering, University of Liverpool, and this project work has not been used as the basis for the award of any other degree/diploma.

Yue Zhang

September 2019

ACKNOWLEDGMENTS

This thesis could not have been finished without the help and support of many people who are gratefully acknowledged here.

Primarily, I would like to say thanks to my supervisor, Prof. Yuyuan Zhao for guiding me well throughout the research work from topic selection to identifying important results. His immense knowledge, motivation and patience motivated and encouraged me during the research. Conducting academic study regarding such a difficult topic could not have been as simple as he made this for me. He is my mentor and a better advisor for my doctorate study beyond the imagination.

I must express my gratitude to my secondary supervisor, Dr. Robert Birch, for his knowledge and technical support in operating the shock tube apparatus. Without his support, the shock tube experiment would never succeed.

Apart from my supervisors, I won't forget to express my gratitude to the rest of the people in the school: Dr. Liping Zhang, Mr. Dave Atkinson, Mr. Jiji Mathew and Mr. Tony Topping, for giving encouragements and sharing insightful suggestions. They all have played a major role in helping with fabricating, cleaning, grinding and polishing of samples and training and building experimental facilities.

I will always remember my fellow lab mates and roommates too, in particular, Kaikan, Jan, Edgar, Zhining, Pengcheng, Xianke, Dong, Chen, Zejun, Hua, Yanlong, Bhavik, Yue, Simong and Haonan, for the fun-time we spent together.

In the end, I am grateful to my parents, Yuanqing Zhang and Fan Lu, my girlfriend, Kun Zhao, and my family, who prayed for my success. I consider myself nothing without them. They gave me a lot of moral support, encouragement and motivation to accomplish my personal goals. My parents have always supported me financially so that I only need to pay attention to the studies and achieve my objective without any obstacle on the way.

TABLE OF CONTENTS

LIST OF PUBLICATIONS

Zhang, Y., & Zhao, Y. (2019). Hysteretic energy dissipation in aluminium matrix syntactic foam under intermittent cyclic compression. Materialia, 6, 100286. doi:10.1016/j.mtla.2019.100286.

LIST OF FIGURES

LIST OF TABLES

LIST OF SYMBOLS

A_i	Initial amplitude	
A_{i+n}	Number of amplitude	
D (3,2)	Surface weighted mean diameter	μm
E	Elastic modulus of the syntactic foam	MPa
E^*	Young's modulus of the foam	MPa
E_a	Charpy impact energy	J
E_s	Young's modulus of the cell wall material	MPa
g	Gravitational acceleration	m/s^2
I^+	Positive impulse	
I^-	Negative impulse	
m_p	Pendulum hammer mass	kg
t	Wall thickness of microsphere	μm
t_0	Shockwave front arrives at the time	
t^+	Duration of first part of the Friedlander curve	
t^-	Duration of second part of the Friedlander curve	
P_p	Porosity	

P^+	Positive pressure	
P^-	Negative pressure	
Q^{-1}	Quality factor	
R	Radius of microsphere	μm
R_p	Pendulum hammer arm	m
$Volt_{out}$	Output voltage	V
$Volt_m$	Measured voltage	V
W_D	Specific dissipated energy	kJ/m^3
W_E	Specific elastic energy	kJ/m^3

Greek symbols

α	Starting angle	°
β	follow-through swing angle	°
γ	Fraction of solid contained in the cell edges	
δ	Logarithmic decrement	
ε	Strain	
ε_f	Strain amplitude	
η	Loss factor	

π	Pi	
ρ_{eff}	Density of effective density of microspheres	kg/m^3
ρ_f	Density of foam/syntactic foam	kg/m^3
ρ_{m}	Density of matrix	kg/m^3
ρ_{me}	Measured density	kg/m^3
ρ_{sm}	Density of solid part of microsphere	kg/m^3
ρ_s	Density of the cell wall material	kg/m^3
ρ_{th}	Theoretical density	kg/m^3
σ	Stress	MPa
σ_{pl}	Plateau stress of the foam	MPa
σ_{ys}	Yield stress of the cell wall material	MPa
$\sigma_{unloading}$	Unloading stress	MPa
$\sigma_{reloading}$	Reloading stress	MPa
ϕ	Diameter	
φ	Loss angle	
ψ	Specific damping capacity	

Abbreviations

BV	Bridge excitation voltage	
CFMMC	Continuous fibre reinforced metal matrix composite	
CM	Ceramic microsphere	
GF	Gauge factor	
MFMMC	Monofilament reinforced metal matrix composite	
MMC	Metal matrix composite	
MMSF	Metal matrix syntactic foam	
SDC	Specific damping capacity	
SDE	Specific dissipated energy	kJ/m^3
SFMMC	Whisker or short fibre reinforced metal matrix composite	
PMMC	Particle reinforced metal matrix composite	
PMSF	Polymer matrix syntactic foam	

Chapter 1 INTRODUCTION

1.1 Background and motivation of the research

Global warming has been a major topic of concern in recent years. It is believed to be mainly contributed by fuel emissions from automobiles and other transportations. Reduction in vehicles fuel consumptions and emissions has been widely agreed as a priority for the environment. Lighter vehicles have advantages of reducing energy consumption, irrespective of advancement in vehicle power technologies. Hence, the development of lightweight composite materials is essential for the automotive, aerospace and marine sectors. Syntactic foam, which is a relatively new type of lightweight composite material, has attracted more attention recently. It has a potential to replace components made by monolithic materials in automobiles and other modes of transportation.

Syntactic foam was first introduced in the 1960s, initially is defined as a material consisting of hollow sphere fillers in a resin matrix (John & Nair 2010). 'Syntactic' is derived from the Greek word 'syntaktikos', meaning 'to arrange together'. The term 'foam' is used because of the cellular nature of the material. Polymer matrix syntactic foam has been studied quite extensively and has found many applications ranging from tea cups to thermal insulation of space shuttle (Gupta et al. 2013a; John & Nair 2010; Kar 2016; Klempner & Frisch 1991). Metallic syntactic foam has recently attracted a lot of attention in the academic field, as well as in industry due to its excellent mechanical properties.

Metal matrix syntactic foam (MMSF) normally consists of a lightweight alloy (Al, Mg or Ti) and low density ceramic hollow microspheres (SiO, Al_2O_3, etc). In existing studies (Gupta et al. 2012; Luong et al. 2016; Orbulov & Dobránszky 2008; Orbulov et al. 2008; Tao et al. 2008; Zhang & Zhao 2007), it is commonly fabricated by a pressure infiltration casting method, where a molten metal or its alloy infiltrates packed ceramic particles. The MMSFs fabricated by infiltration casting have the characteristics of high volume fraction and uniform distribution of hollow microspheres. MMSFs can also be fabricated by a powder metallurgy methods, especially for syntactic foams containing low volume fractions of hollow particles (Mondal et al. 2012; Vogiatzis et al. 2015; Xue & Zhao 2011).

MMSFs are essentially a class of metal matrix composites with hollow microspheres as the reinforcement. The properties of the MMSFs are significantly dependent upon the shape, size, distribution and volume fraction of the hollow microspheres and the microstructure and mechanical properties of the metal matrix, so the MMSFs can be customized by tailoring these parameters. Compared with polymer matrix syntactic foam, metal matrix syntactic foam has better properties in many cases, such as higher strength, better thermal stability and higher melting point, which make them suitable for high strength and high temperature applications (Gupta & Rohatgi 2014).

MMSFs are also considered as a class of foam material because of the porosity embedded in the low density ceramic hollow microspheres. It overcomes several limitations of conventional metal foams. Filing metals with hollow microspheres can lead to lightweight syntactic foams with higher strength than other types of metal foams (Gibson & Ashby 1999; Kiser et al. 1999). The lightweight makes MMSFs potentially applicable in furniture, bumpers, engine casings and engine blocks. The

high specific compressive strength, thermal stability, high damping capacity and energy absorption capabilities of MMSFs make them suitable for energy absorbers, sound absorbers and submarine applications (Balch et al. 2005; Rohatgi et al. 2011).

Compared to the vast amount of literature available on the compressive properties, study on the damping capacity and energy dissipation of MMSFs is very limited. Only a few studies investigated damping properties of MMSFs using multifunctional internal friction apparatus and dynamic mechanical analyser (DMA) (Cox et al. 2014; Katona et al. 2017; Luong et al. 2013; Wu et al. 2006). In these studies, the dynamic tests were conducted at low stress, low strain conditions in the elastic region. The investigations were generally confined to the effects of particle size, temperature and test conditions on the damping capacity of a number of MMSFs. The mechanism of energy dissipation in dynamic damping in syntactic foams, especially under high stress conditions, has rarely been investigated. In addition, the existing studies on dynamic compressive properties of the MMSFs were focused on crushing properties and energy absorption. The behaviour and energy dissipation of MMSFs under shockwave impact have not been studied in detail.

1.2 Aim and objectives of the study

The main aim of this study is to investigate the energy dissipation and damping properties of MMSFs manufactured by infiltration casting under cyclic and free oscillation stress conditions.

The objectives of the study are:

- To fabricate three different types of Al/CM syntactic foams, with different microstructures and varying Al/CM volume ratios.
- To investigate the compressive and energy absorption properties of the syntactic foams under static and impact loading conditions.
- To investigate the energy dissipation properties of the syntactic foams under intermittent and repetitive cyclic compression.
- To investigate the response and energy dissipation properties of the syntactic foams under shockwave impact.
- To understand energy dissipation and damping mechanisms of syntactic foams.

1.3 Outline of the thesis

Chapter 2 of the thesis reviews the literature relevant to the present work, including the manufacturing processes, mechanical properties and applications of cellular solids, metal matrix composites, polymer matrix syntactic foams and metal matrix syntactic foams. The literature on damping measurements, types of damping in metal matrix composites and behaviours of materials under shockwaves is also reviewed.

Chapter 3 presents the details of the experimental apparatus and processes used in this work, including the properties of ceramic microspheres and Al 6082 alloy; the fabricating process of different types of Al/CM syntactic foams; the procedures for density measurement, microstructural observation, quasi-static compressive test, Charpy impact test, shock tube test and calculation of the damping capacity.

Chapter 4 presents the results obtained from the microstructural observation, density measurement, static compression, impact, intermittent cyclic compression, repetitive cyclic compression and shock tube experiments. The Al/CM syntactic foams with different CM particle sizes and volume percentages were tested to analyse and discuss the effects of CM particle parameters (particle size and volume percentage) on compressive strength, energy absorption and energy dissipation. The damping mechanism of Al/CM syntactic foams is also described in detail.

Chapter 5 summarises important results and findings in this study. Recommendations for future work are also presented.

Chapter 2 LITERATURE REVIEW

2.1 Introduction

Syntactic foam, which is synthesised by filling a matrix with hollow spheres (usually microsphere) or non-hollow spheres (e.g., perlite), is a unique class of composite material (Gupta et al. 2013a). Figure 2-1 shows a 3D solid model representation of a syntactic foam containing hollow spheres. The reinforcing spheres are usually ceramic particles or metal spheres, and the matrix materials are usually either a polymer or a lightweight metal. In general, syntactic foam has better mechanical properties than the foam comprising gas porosity in the matrix material and is much lighter than solid particle reinforced composite materials (Gupta et al. 2013a).

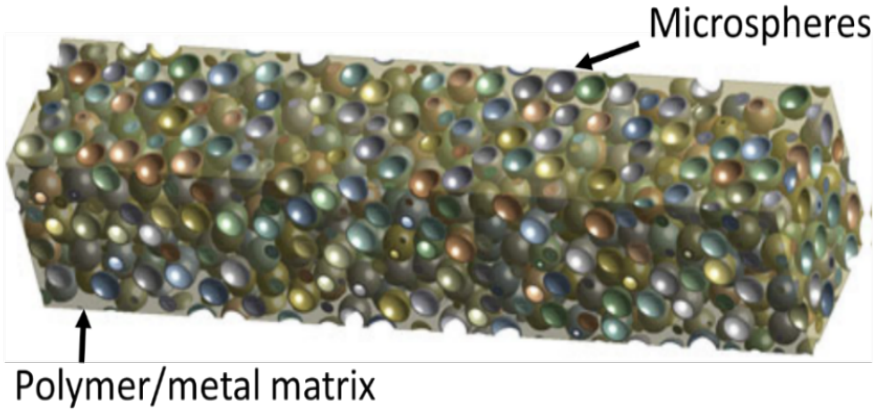

Figure 2-1 3D solid model representation of syntactic foams containing hollow spheres (Gupta et al. 2014).

Syntactic foams are classified as polymer matrix syntactic foams (PMSFs) and metal matrix syntactic foams (MMSFs) depending upon the matrix materials. PMSFs are normally fabricated by the stirring casting process, which can also be used to fabricate MMSFs. Although PMSFs and MMSFs have a similar microstructure, their

mechanical properties are very different. PMSFs have advantages of low density, good flexibility to design and low cost, whereas MMSFs have higher strength, better energy absorption and higher temperature capability.

MMSFs virtually combine the characteristics of cellular solid materials and metal matrix composites (MMCs). The fabrication processes, mechanical properties and applications of cellular solid materials (e.g., closed-cell metal foam) and MMCs are highly relevant. Both cellular metals and MMSFs can be fabricated by powder metallurgy processes. Although metal foams and MMSFs have different morphologies and mechanical properties, MMSFs can also be viewed as porous materials because of the embedded hollow microspheres. Some mechanical behaviours of MMSFs are also similar to those of metal foams. Both MMSFs and MMCs are composite materials. Most fabrication processes used for MMCs are also applicable to MMSFs. Due to different reinforcements, MMSFs have slightly different microstructures and mechanical properties from MMCs. MMSFs have an opportunity to replace metal foam or MMCs in some applications due to lightweight and better energy absorption.

In this chapter, the fabrication processes, mechanical properties and applications of closed-cell metal foams, MMCs, PMSFs and MMSFs are reviewed. As this study mainly focuses on energy dissipation of MMSFs under cyclic loading and shockwave impact, the methods of damping measurement, type of damping in MMCs and the behaviour of materials under shockwave are also reviewed.

2.2 Closed-cell metal foams

2.2.1 Introduction

Closed-cell metal foam is a type of cellular metallic material that has been brought into attention for many years. Presently, it is widely used in engineering applications due to the virtue of unique properties (Gibson & Ashby 1999; Lefebvre et al. 2008). Figure 2-2 shows a typical structure of a closed-cell metal foam. This section reviews the manufacturing processes, mechanical properties and applications of closed-cell metal foams, which may have some common characteristics with MMSFs.

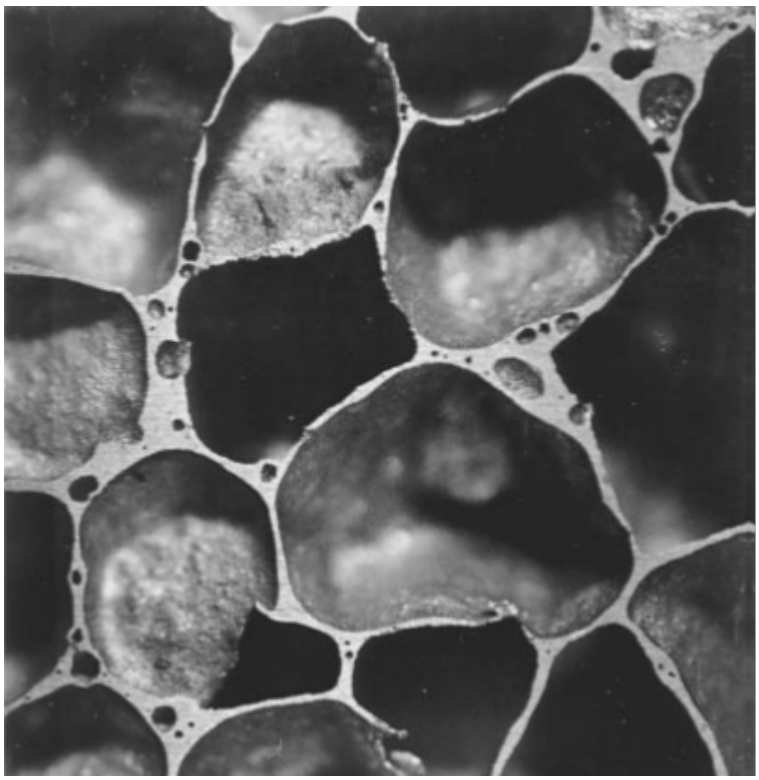

Figure 2-2 Typical structure of closed-cell metal foam (Simone & Gibson 1998).

2.2.2 Fabrication processes

Closed-cell aluminium foams are the most common metal foam products in the current commercial market. A large number of manufacturing processes are available for making aluminium foams. In this section, four major fabricating processes used in the commercial closed-cell Al foam industry are reviewed. These manufacturing processes are based on two manufacturing routes, either the melt route or the powder metallurgy route. The melt and powder metallurgy routes for closed-cell metal foams often are referred to as direct and indirect foaming methods, respectively.

ALPORAS aluminium foam produced by Shinko Wire (Amagasaki, Japan) is one of the popular closed-cell metal foams. The manufacturing process was designed by Akiyama et al. (1987). Figure 2-3 shows the fundamental manufacturing process for ALPORAS foam. In this process, a thickening agent (1.5 wt% calcium) is mixed into the molten aluminium in order to increase its viscosity for stabilising the bubbles. Subsequently, a blowing agent (1.6 wt% TiH_2) is used in the thickened aluminium, and then this molten aluminium is foamed and expanded to a big block inside a closed mould. Finally, this foam block is cooled and machined into plates of desired thicknesses.

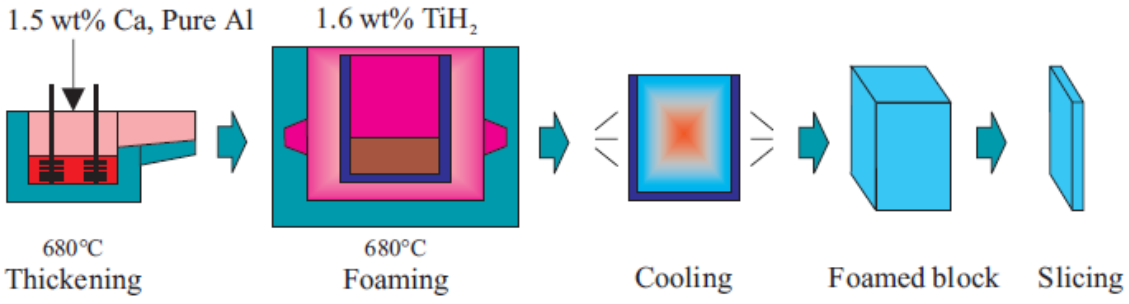

Figure 2-3 Schematic diagram of manufacturing process of ALPORAS (Mahadev et al. 2018).

Another popular process of direct foaming an aluminium alloy is used by Cymat (Mississauga, ON, Canada) (see Figure 2-4). In this process, ceramic particles (10%~20% SiC or Al_2O_3) are mixed into the molten aluminium to raise its viscosity for stabilising the liquid cell walls. Subsequently, air is injected into this thickened molten aluminium by using specially designed rotating impellers or vibrating nozzles. The resultant viscous mixture of bubbles and molten aluminium floats to the surface of the melt and then this aluminium foam is pulled off and allowed to cool and solidify (Jin et al. 1990).

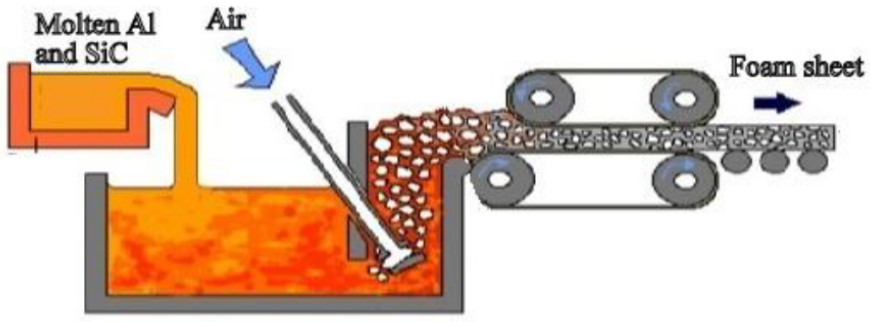

Figure 2-4 Schematic diagram of manufacturing process of aluminium foam by melt gas injection (Mahadev et al. 2018).

Recently, Aluinvent (Miskolc, Hungary) invented a new manufacturing process for aluminium foam, using ultrasound oscillations to induce earlier detachment of bubbles during their growing stage. This process has an advantage in reducing the pore size and improving the pore size distribution of gas-injected foams by treating the melt during bubble formation (Babcsán et al. 2015).

ALM (Saarbrücken, Germany) uses a powder metallurgy method to produce aluminium foam sandwiches. Figure 2-5 shows the general procedure of this process. In this method, a mixture of the aluminium powder and a blowing agent (typically 0.5 to 1.0 wt% of TiH_2) is firstly prepared, and then the powder blend is compacted to a

solid semi-finished product by uniaxial pressing or powder extrusion. Subsequently, this semi-finished product is sintered at a certain temperature where the aluminium starts melting and the gas of the blowing agent nucleates. During this sintering process, the gas diffuses to the nucleated pores, letting them grow into big bubbles and expanding the foam. When the foam development is fulfilled, the foamed metal structure is conserved and solidified by temperature reduction (Allen et al. 1963; Baumeister 1990).

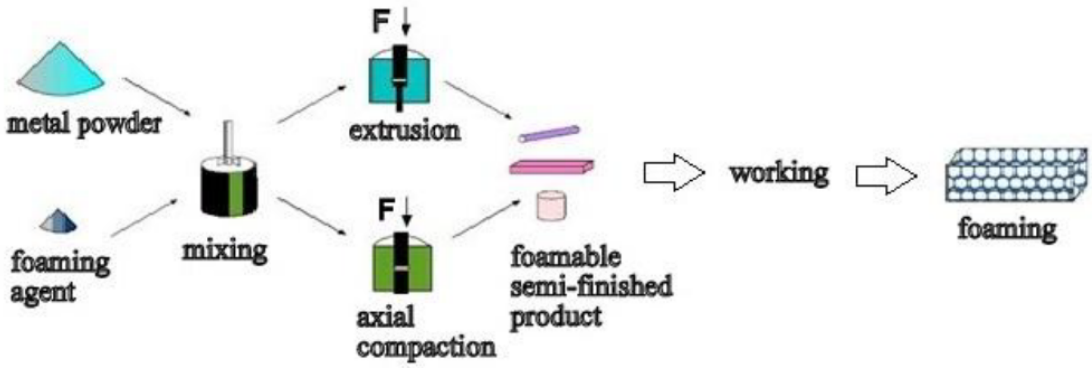

Figure 2-5. Schematic diagram of manufacturing process of foam from powder compacts (Mahadev et al. 2018).

2.2.3 Mechanical properties

The applications of closed-cell metal foams are strongly linked to their mechanical properties. The compressive behaviour of closed-cell metal foams is one of the major mechanical properties that is primarily considered. The compressive stress-strain curve of closed-cell metal foam is similar to other foam materials. Figure 2-6 shows the three typical compressive stress-strain curves of foam materials (Gibson 2000). Although these three compressive behaviours are slightly different, they mainly consist of three stages. The first stage is the linear elastic region. The second stage is the plateau or plastic region where pores are collapsed and the cell walls are buckled

and failed. The final stage is the densification region where cells are completely crushed. The starting point of densification is usually treated as the intersection between the tangents of the curves in the crushing and densification regions (Nieh et al. 2000).

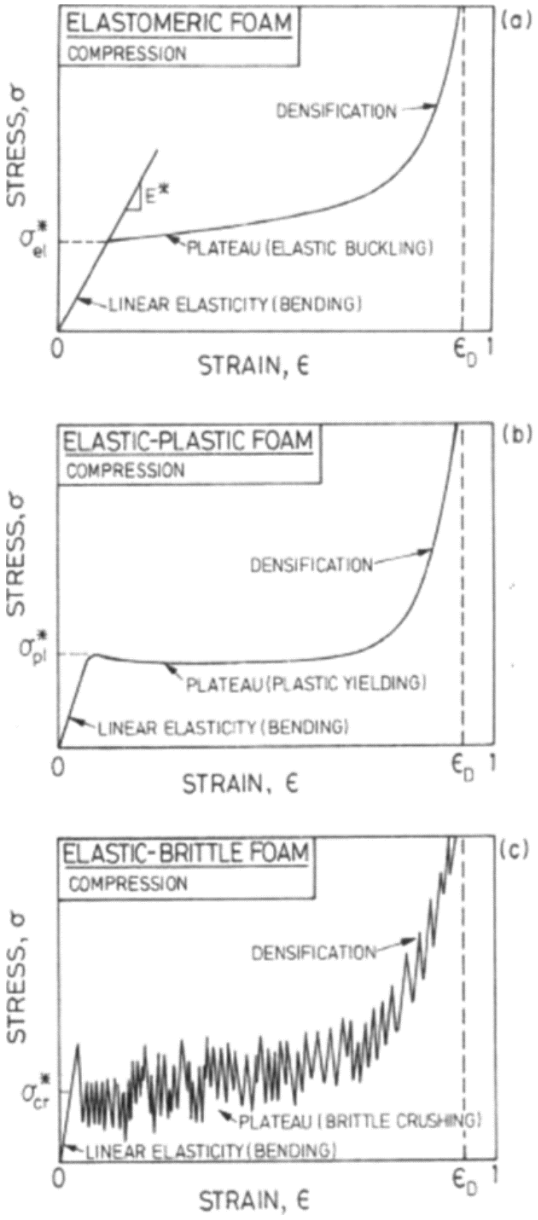

Figure 2-6 Schematic compressive stress-strain curves for foams, showing the three regimes of linear elastic, collapse and densification: (a) an elastomeric foam; (b) an elastic-plastic foam; (c)an elastic-brittle foam (Gibson 2000).

The compressive properties of closed-cell metal foams have been extensively studied. The compressive properties of the closed-cell metal foams are fundamentally evaluated in accordance with the weight i.e., density, even though other parameters such as cell size, structure and distribution also have some influences (Deqing et al. 2005). Gibson and Ashby (1999) proposed a theoretical model for describing the mechanical response of closed-cell foams. They viewed the closed-cell metal foam as a regular hexagonal cellular structure and developed the general equations for evaluating the plateau stress and Young's modulus during compression loading:

$$\frac{\sigma_{pl}}{\sigma_{ys}} = 0.3\left(\phi\frac{\rho_f}{\rho_s}\right)^{\frac{3}{2}} + 0.4(1-\gamma)\left(\frac{\rho_f}{\rho_s}\right) \quad (2\text{-}1)$$

$$\frac{E^*}{E_s} = \phi^2\left(\frac{\rho_f}{\rho_s}\right)^{\frac{3}{2}} + (1-\gamma)\left(\frac{\rho_f}{\rho_s}\right) \quad (2\text{-}2)$$

where σ_{pl} is the plateau stress of the foam, σ_{ys} is the yield stress of the cell wall material, γ is the fraction of solid contained in the cell edges, ρ_f is the density of foam, ρ_s is the density of the cell wall material, $E^*$is the Young's modulus of the foam and E_s is the Young's modulus of the cell wall material.

Papadopoulos et al. (2004) and Idris et al. (2009) calculated the theoretical plateau stress and Young's modulus of closed-cell Al foams by using Gibson's equations and compared with their experimental results. The experimental results were in good agreement with the results based on the theories of Gibson.

However, closed-cell metal foams have a different compressive behaviour under dynamic compression. Dannemann and Lankford (2000) studied the compressive behaviour of ALPORAS Al foam under high strain rates. They found that the compressive behaviour of closed-cell metal foams is also sensitive to the strain rate. Strain rate strengthening occurs in closed-cell Al foam, especially in the higher density Al foam. This strain rate effect may be related to fluid (air) flow through ruptured cell walls, and it appears to be controlled by cell shape, cell size and distribution, cell wall aspect ratio and uniformity of wall section profile. This behaviour is also observed in other studies (Deshpande & Fleck 2000; Mukai et al. 1999).

Yu et al. (2006) studied the tensile property of closed-cell Al-Si foam with different relative densities. The deformation behaviour of the foam subjected to uniaxial tension was different from compression, where the plateau stress regime was not found in tension. The tensile strength and elastic modulus increased with increasing the relative density of foam, approximately agreeing with the Gibson-Ashby model.

The static compressive and tensile behaviours of three different commercially available closed-cell Al foams were studied by Sugimura et al. (1997). The mechanical properties, as well as the deformation and fracture mechanisms of these Al foams, were found to be governed by the imperfections, including curves and wiggles in the cell walls and nodal inclusions. Controlling these defects upon processing could significantly improve the performance of the Al foams.

The metal foams have good and efficient energy absorption capacity during deformation due to the extensive plateau regime. Figure 2-7 compares the typical energy absorption of foam and full dense solid material. Obviously, the foam absorbs

much more energy at a given peak stress level than the dense solid. Sahu (2013) studied the energy absorption of closed-cell Al foam and concluded that the level of energy absorption is proportional to the densification strain and plateau stress. For very light Al foams, Mondal et al. (2009) reported that the densification strain is almost invariant to the relative density, but the plateau stress depends highly upon the relative density.

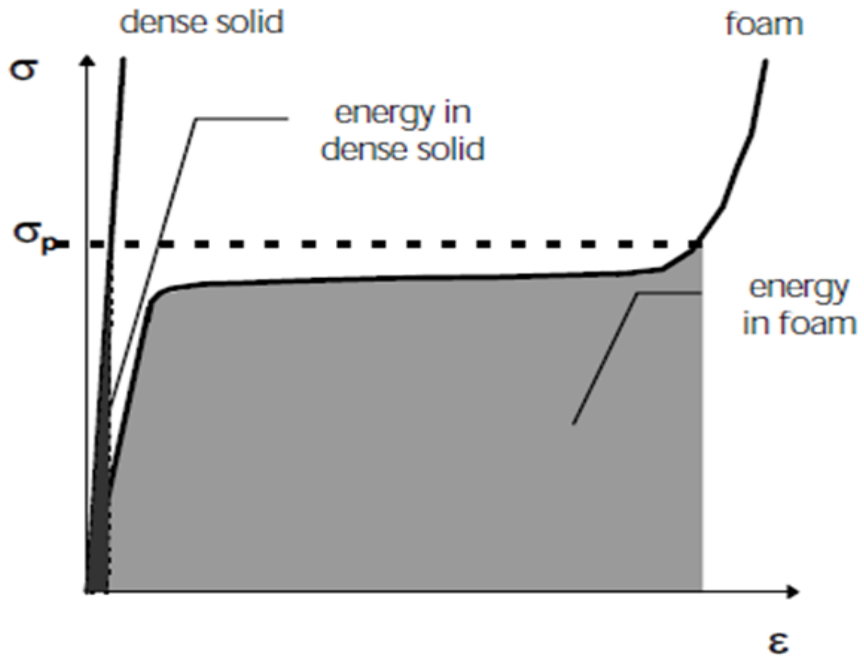

Figure 2-7 Typical energy absorption of a foam and full dense solid (Yu & Banhart 1998).

2.2.4 Applications

Closed-cell metal foams are presently used in a wide range of applications, including the automotive, machinery, building and aeronautics industries. These applications are all based on the characteristics that metal foams have high stiffness in conjunction with a very low specific weight (García-Moreno 2016).

Figure 2-8 shows examples of applications of closed-cell metal foams. Ferrari 360 and 430 Spider use Al foam to fill in the door sill to reinforce the frame and to increase stiffness, as well as to improve the performance in the case of a side crash in high premium cars. Al foam sandwich (AFS) parts have seen applied in a high-speed milling machine of Niles-Simmons (Chemnitz, Germany), making the construction 28% lighter than the cast part with the same stiffness, and improving vibration damping. Metallic foams have also been used as crash elements for a guardrail in the Masan-Chanwon Bridge in Korea. The aeronautics industry is considering metallic foams for protection of planes against bird strikes. Bird strike can seriously damage the aircraft of all forward-facing components, such as the engine fan blades and inlet, the windshield, window frame, radome and forward fuselage skin as well as the leading edges of the wings and empennage (Heimbs 2011). Reglero et al. (2011) studied the use of aluminium foams as filler materials in aeronautical leading edges. Bird-strike impact tests demonstrated improvement in mechanical behaviour of the filled structure compared to the original hollow structure. The composite structure, 13% lighter than the original one, showed four times better in global deformation and an improvement of doubled transmitted load.

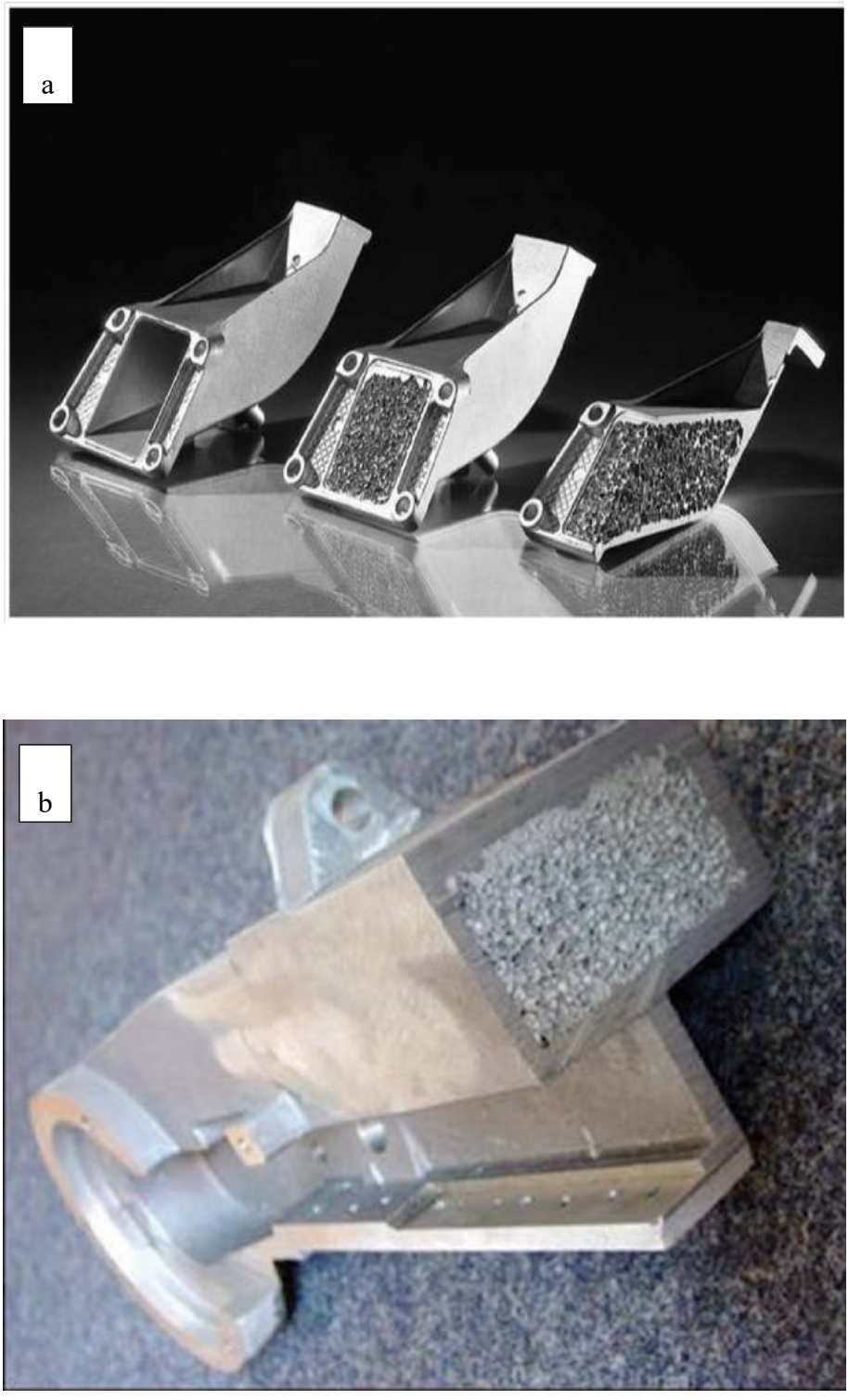

Figure 2-8 (a) Stiffener and crash absorber in cars and (b) high-speed milling machine with aluminium foam sandwich component.

2.3 Metal matrix composites

2.3.1 Introduction

Metal matrix composites (MMCs) are a class of composite materials which combine metallic behaviours (ductility and toughness) with ceramic properties (high strength and high modulus). They are becoming attractive candidate materials for aerospace, automotive and numerous other applications because of the greater strength in shear and compression and higher service temperature capabilities (Ibrahim et al. 1991). Aluminium and magnesium alloys are the most common matrices used to make MMCs because of the low density with reasonably high thermal conductivity (Ibrahim et al. 1991). MMCs can also be based on titanium and copper alloys, but the fabrication process is much more difficult than those for the Al and Mg alloy based composites (Seshan et al. 2013). The reinforcement materials of MMCs are usually carbides (e.g., SiC, B_4C), nitrides (e.g., Si_3N_4, AlN) and oxides (e.g., Al_2O_3, SiO_2) (Ibrahim et al. 1991). This section reviews the fabrication processes, microstructure, mechanical properties and applications of MMCs.

2.3.2 Types of MMCs

The reinforcement materials are in various forms, such as continuous fibres, chopped fibres, whiskers, platelets and particulates. Depending on the form of the reinforcement, MMCs can be classified into three types, including continuous fibre or monofilament reinforced MMC (CFMMC or MFMMC), whisker or short fibre reinforced MMC (SFMMC), and particle reinforced MMC (PMMC). Figure 2-9 schematically shows typical types of MMCs (Clyne & Withers 1995; Guniputi et al. 2013; Nturanabo et al. 2019; Surappa 2003).

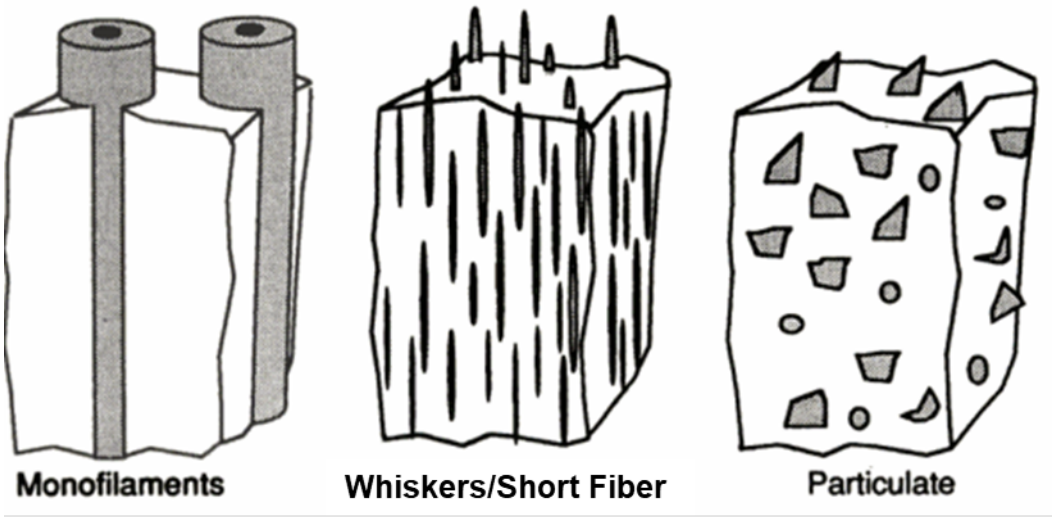

Figure 2-9 Schematic depiction of metal matrix composites, classified according to the form of reinforcement. (Clyne & Withers 1995).

In continuous fibre or monofilament reinforced MMCs, the reinforcement is either relatively fine or coarser fibres or monofilaments. The former, which is made by alumina, SiC or carbon with a diameter less than 20 μm, is usually either parallel or pre-woven prior to infiltration to form a composite. MMCs with fibre volume percentages up to 40% can be fabricated by the infiltration technique. Monofilaments are fibres with a diameter of 100 to 150 μm consisting of either SiC or boron with a

core of carbon fibre or tungsten wire. Monofilament reinforced MMCs are produced by diffusion bonding techniques. Both CFMMC and MFMMC are directional, of which the strength is low in the direction perpendicular to the fibre orientation.

In whisker or short fibre reinforced MMCs, the discontinuous short fibres, which have an aspect ratio greater than 5, are commonly made of alumina and SiC. The length of fibres is usually less than 100 times of diameter. SFMMCs can be produced by infiltration casting techniques. Compared with SFMMCs and PMMCs, the whisker reinforced MMCs have superior mechanical properties. However, usage of whiskers as reinforcements is restricted due to the perceived health hazards. The material properties of SFMMCs are between those of CFMMCs and PMMCs.

In particle reinforced MMCs, the ceramic reinforcements are equiaxed with an aspect ratio less than about 5. The ceramic reinforcements are commonly Al_2O_3 or SiC or TiB_2. Either solid state or liquid state processes can be used to fabricate PMMCs. Depending upon the actual application, the particle volume fraction is varied in MMCs and is less than 30% in structural wear resistance applications and as high as 70% in electronic packaging applications. Compared with SFMMCs and CFMMCs, mechanical properties of PMMCs are inferior. However, their properties are better than the unreinforced alloys. As PMMCs are isotropic in nature, they can be subjected to a variety of secondary forming operations such as extrusion, rolling and forging.

2.3.3 Fabrication processes

MMCs can be prepared through a verity of processing techniques according to the temperature of the metallic matrix. The fabrication methods of MMCs are generally classified into four categories, which are liquid state processes, solid state processes, deposition processes and vapour state processes (Guniputi et al. 2013). In this section, liquid state processes and solid state processes for fabricating MMCs are reviewed because they are the main processes to produce PMMCs which are more relevant to the fabrication of metal matrix syntactic foams.

Liquid phase processes involve incorporation of reinforcement into a molten metal matrix, followed by its solidification. Liquid metal mixing processes and liquid metal infiltration processes are currently the two major methods for fabricating MMCs.

Liquid metal mixing processes are based on a stir casting technique, which incorporates the reinforcement particles or short fibres into a molten matrix by stirring and allows the mixture to solidify (see Figure 2-10). The critical point of stir casting is to ensure good wettability between the reinforcement and the liquid metal alloy. Stir casting is suitable for manufacturing composites with up to 30% volume percentages of reinforcement (Pal et al. 2015).

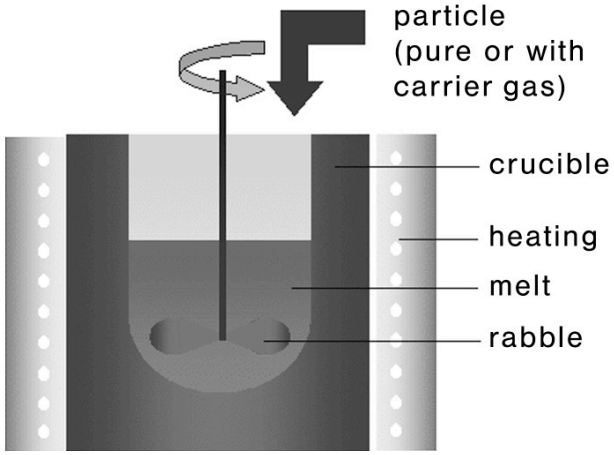

Figure 2-10 Schematic diagram of stir casting method (Kainer 2006).

Liquid metal infiltration refers to a molten alloy being introduced into a porous preform of reinforcement by pressure. Figure 2-11 shows the infiltration casting processes schematically, which use either inert gas or a mechanical device as a pressuring medium. In infiltration casting, the infiltration pressure, which is required to overcome the wetting and capillary resistance of the preform of reinforcement, needs to be properly applied, thereby reduce the porosity of the MMC (defects) and improve the mechanical properties. This method is also useful to fabricate MMCs of which the reinforcement volume is above 50%. For example, Lee and Hong (2003) successfully used infiltration casting to fabricate Al matrix composites containing 50~70% volume of SiC particles.

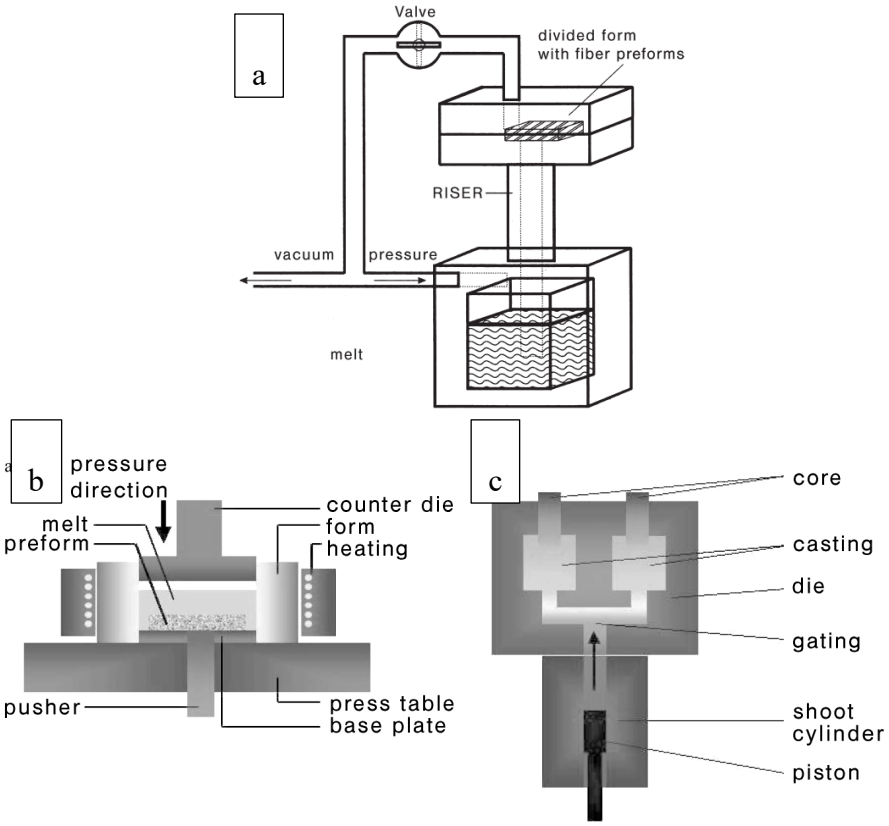

Figure 2-11 Schematic diagram of (a) gas pressure infiltration casting, (b) squeeze infiltration casting and (c) die infiltration casting (Kainer 2006).

The solid state processes involve the mixing of reinforcement into a solid state matrix. Diffusion bonding and powder metallurgy are currently two principal methods for fabricating MMCs.

In diffusion bonding, the metal matrix in the form of foils and the reinforcement in the form of long fibres are stacked in a particular order and then pressed at elevated temperature. The finished MMC is a laminate plate with a multilayer structure. However, this process is commonly used in the fabrication of simple shape parts (tubes and plates) as it is a cumbersome process.

In powder metallurgy (P/M), a powder mixture of a metal matrix and reinforcements is prepared and subsequently pressed to approximately 75% density, and then sintered

to its final consolidation (Ibrahim et al. 1991). Sintering is a process where the metal particles are bounded to the neighbouring powder particles by diffusion. The temperature of sintering is usually below the melting point of the metal matrix (approximately 0.7 to 0.9 melting temperature), which can depress undesirable reactions on the boundary between the matrix and the reinforcement. Sintering can also be combined with a deformation operation, such as hot isostatic pressing (HIP) and hot powder extrusion, to minimise the machining of MMC products (Nturanabo et al. 2019). The P/M method is suitable for fabricating MMCs which have a high melting point matrix, because it can avoid segregation and formation of brittle reaction products that are prone to occur in liquid state processes (Guniputi et al. 2013).

2.3.4 Mechanical properties

Considering that the microstructure of particle reinforced MMCs is more relevant to metal matrix syntactic foams, only mechanical properties of PMMCs are reviewed in this part. PMMCs provide significantly enhanced properties over conventional monolithic materials, such as higher strength, stiffness and weight savings. However, the mechanical properties of PMMCs are affected by the size, shape and volume fraction of the reinforcement, matrix material and reaction at the interface.

Aghajanian et al. (1993) fabricated Al_2O_3 particulate reinforced Al matrix composites with various particulate volume percentages to study the mechanical behaviours. The elastic modulus, tensile strength, compressive strength and fracture properties are significantly improved with an increase in the reinforcement content. According to the fractography, the tensile failure mechanism of this composite was transgranular

fracture of the Al_2O_3 particulates followed by ductile rupture of the Al matrix, with no debonding at the interface between reinforcement and matrix.

Chawla and Shen (2001) summarized that the strengthening mechanisms in particulate reinforced metals include direct and indirect strengthening. Direct strengthening in particulate reinforced metals is fundamentally the same as in continuous fibre reinforced composites (Chawla 2012). The strengthening is caused by load transfer from the matrix to the reinforcement of which stiffness is higher. Indirect strengthening results from the effect that the reinforcements may have on the matrix microstructure or deformation mode (Chawla et al. 1999).

San Marchi et al. (2002), Liu et al. (2012) and Liu et al. (2019) studied the effect of reinforcement particle size on quasi-static and dynamic mechanical properties of particle reinforced Al composites. Although the Al composites in these studies are fabricated with different particle materials, the results showed similar behaviours. The quasi-static and dynamic stress-strain curves all showed that the compressive strength of composites is sensitive to the size of the reinforcing particles. It is a consequence of matrix hardening by dislocations. The impact velocity (strain rate) does not affect the compressive strength of composites significantly in both low and high-speed impact.

Tahamtan et al. (2014) studied the effect of bonding strength at the particle interface on tensile properties and fracture behaviour of Al-A206/alumina composites. It was found that tensile properties of the Al-A206/alumina composites were improved by controlling the alumina/matrix interface. The interface was considered to have a reaction layer in view of its ability to enhance bonding strength and, hence, proper transfer of load to the reinforcing particles.

Besides the monotonic stress-strain behaviour of particle reinforced metal matrix composites, a large number of studies have also examined the cyclic stress-strain behaviour of these materials (Cavaliere 2005; Chawla et al. 1998; Llorca et al. 1992; Srivatsan 1995; Vyletel et al. 1991). In these reports, low-cycle fatigue properties and cyclic fracture characteristics of metal matrix composites were experimentally and numerically studied. In cyclic loading, hysteresis loops, which represent an energy dissipation, are found in the stress-strain response of metal matrix composites. However, these studies mainly discussed the effect of the volume fraction of reinforcement and the testing temperature on low-cycle fatigue properties of metal matrix composites. The energy dissipation of metal matrix composites represented by the hysteresis loop is less discussed. Xu and Schmauder (1999) used a numerical method to study the plastic energy dissipation in metal matrix composites during cyclic loading. Their results showed that the efficiency of dissipated energy is sensitive to the loading level, Young's modulus and volume fraction of reinforcing particles. The shape of the particles also has an effect on the efficiency of dissipated energy but the influence is not as significant as the other parameters.

2.3.5 Applications

Due to the superior mechanical, thermos-mechanical and tribological properties, MMCs have been used in high-tech structural and functional applications. Among the various types of MMCs, aluminium based particle reinforced composites (PAMC) can replace some components of monolithic materials and have several applications in aerospace, automotive and thermal management sectors.

The Al/SiC composite has been used to make the optical mirror substrates of a satellite and the airborne optoelectronic platform of aircrafts (Yan et al. 2008). It not only significantly saves the weight but also prevents resonance vibration to protect the devices mounted on the component. The Al/graphite composite, whose friction coefficient is as low as 0.2, has been used to make piston and cylinder liners in the automotive industry (Rohatgi et al. 1992). They enable the lightweight aluminium engine to reach operating temperatures more quickly while providing superior wear resistance, improving cold start emission and reducing weight (Gumus 2009). PAMCs with a high volume fraction of reinforcement are attractive materials for electronic packaging and can potentially be applied to make heat sinks due to their good thermal properties (Nturanabo et al. 2019).

2.4 Polymeric syntactic foams

2.4.1 Fabrication processes

The raw materials required to fabricate polymer syntactic foams include three constituents, which are the matrix material (epoxy resin), hardener and microspheres. In addition, a diluent is sometimes used for lowering the viscosity of the resin (Karthikeyan et al. 2001; Kim & Plubrai 2004; Woldesenbet 2005). Although different types of resins, such as modified epoxies, phenolic, polyurethanes, urethane acrylates, and polyester and vinyl ester resins, have been used to fabricate syntactic foams. Polymer syntactic foams are commonly fabricated with the epoxy resin DER-332 and hardener DEH 24 (Gupta et al. 2004; Woldesenbet et al. 2005).

The hollow microspheres of glass, carbon and phenolic resin can be used in fabricating syntactic foams. Their diameter and density are commonly in ranges 10-250 μm and 150-500 kg/m^3, respectively. These low density microspheres contribute lightweight to the fabricated syntactic foams (Gupta et al. 2013a). 3M Scotchlite glass hollow microspheres are representative microspheres popularly used in many polymer syntactic foams. Several studies have also used hollow fly ash microspheres, which are waste by-products of coal firing, as filler materials (Kulkarni 2003; Rohatgi et al. 2009). Compared to fly ash, hollow glass microspheres have better mechanical properties due to their controlled and better material quality. However, using industrial wastes can save the cost of their treatment and disposal.

Syntactic foams are commonly fabricated by the stirring method, which includes mixing and casting. The resin and diluent are mixed, and the hardener is then added by stirring thoroughly. The microspheres are added at last. Finally, the mixture slurry

is cast in a metal mould and cured at room temperature. Although this method is easy to operate, its limitation is also obvious. In most studies, the syntactic foams fabricated by this method have a microsphere volume percentage in the range 30~60%. This is because the microspheres tend to float and segregate in the top part of the foam slab during curing if less than 30%; the microspheres tend to break during stirring and their wetting and clustering become issues during processing if over 60% (Gupta et al. 2013a). Gupta and Nagorny (2006) also reported that using a stirrer made of a soft material can effectively prevent the breakage of microspheres during the stirring process.

2.4.2 Microstructure

Figure 2-12 shows a SEM micrograph of a vinyl ester/glass hollow microsphere syntactic foam fabricated by Gupta et al. (2010). Except microspheres and the resin matrix, some air voids were observed. Gupta and Ricci (2006) studied the porosity issue in polymer syntactic foams. Figure 2-13 schematically represents the microstructure of the syntactic foam, in which microsphere porosity and matrix porosity coexist. The microsphere porosity is desired and can be tailored by varying particle wall thickness and volume fraction. The matrix porosity caused by the air entrapped in the matrix resin during the mixing process is undesired. Polymer syntactic foams contain up to 5% matrix porosity in most published studies (Gupta et al. 2013a). Applying a shaker or vacuum during the curing process can effectively reduce the matrix porosity, which has a negative effect on mechanical properties of polymer syntactic foams. Gupta and Ricci (2006) used the following equation to evaluate the porosity (P_{p}) :

$$P_{\mathrm{p}} = \frac{\rho_{\mathrm{th}} - \rho_{\mathrm{me}}}{\rho_{\mathrm{th}}} \tag{2-3}$$

where ρ_{th} and ρ_{me} are the theoretical and measured densities of the syntactic foam, respectively.

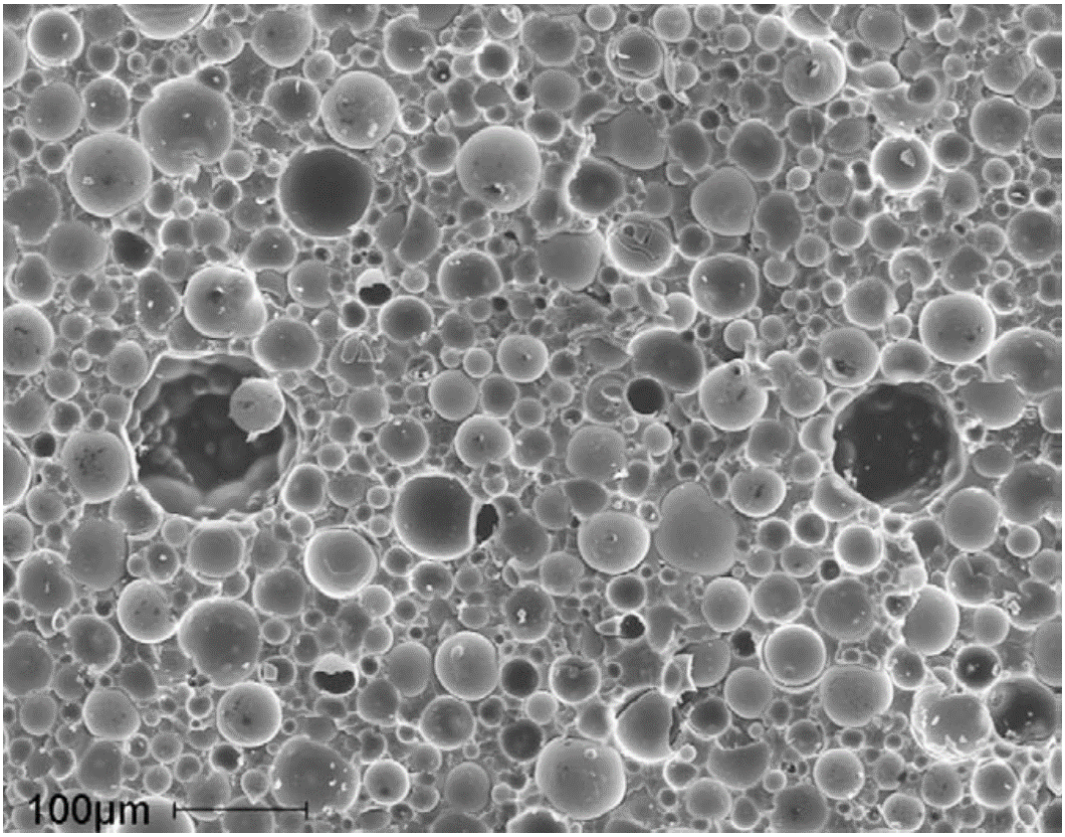

Figure 2-12 SEM of vinyl ester/glass hollow microsphere syntactic foam (Gupta et al. 2010).

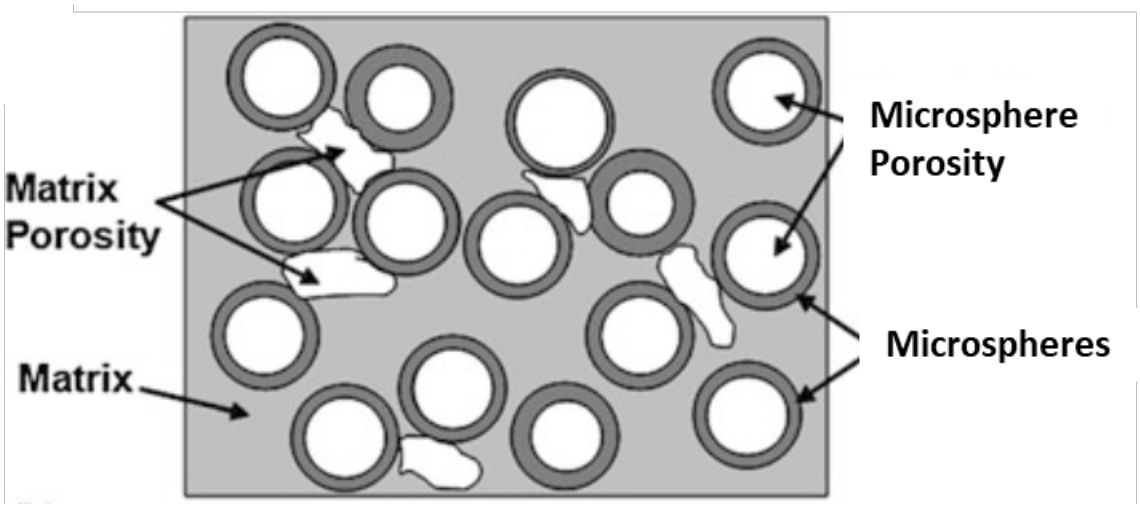

Figure 2-13 A schematic representation of phases present in a syntactic foam.

2.4.3 Mechanical properties

The compressive properties of polymer syntactic foams have been studied extensively. The compressive stress-strain behaviour of polymer syntactic foams is similar to cellular polymers and has an initial linear elastic region, a stress plateau region where stress remains nearly constant and a densification region where stress starts rising again (Bunn & Mottram 1993). However, polymer matrix syntactic foams contain load bearing elements (microspheres) so that their compressive strength, plateau stress and energy absorption are enhanced. Many researchers have studied the effect of microspheres, such as size, volume fraction, wall thickness and material type of particles on the compressive properties of polymer syntactic foams.

Bunn and Mottram (1993) fabricated syntactic foam samples with volume percentages of microspheres between 0% and 53% and studied their compressive properties. The bulk density of the sample is related to the volume percentage of microspheres, as expected from the rule of mixture. The results showed that the sample having the highest microsphere concentration has the lowest compressive strength and modulus.

The compressive strength and modulus of the samples had a nearly linear relationship with the bulk density of the samples. In short, the microsphere concentration significantly affects the compressive properties.

D'Almeida (1999) studied the influence of the diameter of the glass microspheres on the mechanical properties of syntactic foams. The results of this study agreed with the previous study (Bunn & Mottram 1993) that when the volume fraction of the microspheres increased, the compressive strength and elastic modulus of the syntactic foam decreased. At a fixed microsphere concentration, the syntactic foam containing small microspheres (greater relative wall thickness) has a higher compressive strength and elastic modulus, because small microspheres are advantageous in resistance to crack propagation.

The effect of microsphere wall thickness on the compressive properties of syntactic foams has been studied by Gupta et al. (2004). Syntactic foams with the same outer radius but different inner radius of microspheres have different compressive strengths and moduli, although the surface area of microspheres and microsphere/matrix interfacial strength do not change. All the syntactic foams have the same strain at the peak compressive stress because this strain mainly depends on the property of the resin matrix. Gupta et al. (2004) also studied the effect of specimen aspect ratio (width/thickness) on the compressive properties of polymer syntactic foams. Specimens tested in flatwise orientation (lower aspect ratio) have higher compressive strength and modulus compared to edgewise orientation (higher aspect ratio), because there are more lateral expansion and barrelling in flatwise orientation.

Dimchev et al. (2010) studied the effect of carbon nanofibers on compressive characteristics of polymer syntactic foams. Syntactic foams with different volume percentages of microspheres and fixed volume percentage of carbon nanofibers (0.25wt.%) were fabricated and tested. Compared with the plain syntactic foam, the nanofibers have limited effect on the compressive property of syntactic foams, because extensive particle crushing was observed under compression in these specimens. The fracture of the specimens was dominated by particle crushing, with only a small role played by the matrix and nanofibers.

Gupta and Nagorny (2006) fabricated polymer syntactic foams with different volume percentages (in range of 30%-60%) and wall-thickness-to-diameter ratios of glass microspheres, and studied their tensile behaviour. The tensile strengths of the syntactic foams were 60%-80% less than that of the pure resin. For syntactic foams fabricated with the same type of microspheres, the tensile strength decreased with increasing microsphere concentration. The tensile strengths of the syntactic foams were enhanced by increasing the density of the microspheres. The tensile modulus of the syntactic foams fabricated from a low density microsphere was sensitive to microsphere concentration. However, the tensile modulus of the syntactic foams fabricated from a higher density microsphere was not affected significantly by the microsphere concertation.

Dimchev et al. (2010) studied the effect of adding carbon nanofibers on tensile characteristics of polymer syntactic foams. By adding 0.25% volume of carbon nanofibers into the syntactic foam, the tensile properties of the syntactic foam were significantly enhanced, because the matrix played a more positive role in the deformation and fracture of the composite under tensile loading conditions.

2.4.4 Applications

Polymer syntactic foams are a lightweight porous composite material and have been applied in many areas. The initial application of syntactic foams was low density marine structures due to their naturally buoyant behaviour and low moisture absorption. Their unique microstructure provides hydrostatic compressive strengths significantly higher than conventional foams. The syntactic foams have been applied in many parts of submarines, e.g., the eyebrows, rudders, flaps, forward and aft free-flood areas of submarines.

Weight-sensitive aerospace structures take advantage of the lightweight property of syntactic foams. Airbus and Boeing have both reported that syntactic foams can be used to reinforce the hollow areas within the aircraft, such as fillers for propellers and guide vanes. The applications of polymer syntactic foams also include sports equipment, furniture, food containers, blast and fire protection (Gupta et al. 2013b).

2.5 Metal matrix syntactic foams

2.5.1 Fabrication processes

Metal matrix syntactic foam consists of two essential constituents, which are the matrix alloy and hollow particles. The properties of these two constituents can directly determine the properties of the MMSF. Additional materials are added in some cases, e.g., coating of particles which hinders reaction between matrix and particle.

Most MMSFs have used aluminium alloy as the matrix material, such as A356, A380, 6061 and 7075. This is because Al alloys are lightweight and have relatively low melting points. Recently, some studies focused on magnesium matrix syntactic foams whose matrix is even lighter. MMSFs fabricated with iron, titanium and nickel alloys have also been studied (Gupta & Rohatgi 2014).

Hollow microspheres are commonly used as the filler material for MMSFs in many studies. These microspheres are made from metals, glasses or ceramics (Al_2O_3, SiC and SiO_2). Both the size and wall thickness of engineered microspheres are controllable, leading to a variety of MMSFs. Some studies used fly ash microspheres to fabricate MMSFs (see Figure 2-14). Fly ash microspheres are an industrial waste by-product recovered from coal combustion. Their dominant constituents are SiO_2, Al_2O_3 and Fe_2O_3. Using fly ash microspheres in fabricating syntactic foams takes advantage of their low and environmental friendliness. The density of fly ash microspheres is usually between 0.35 g/cm^3 and 0.90 g/cm^3, and their sizes can vary from 5 to 500 microns (Kutchko & Kim 2006).

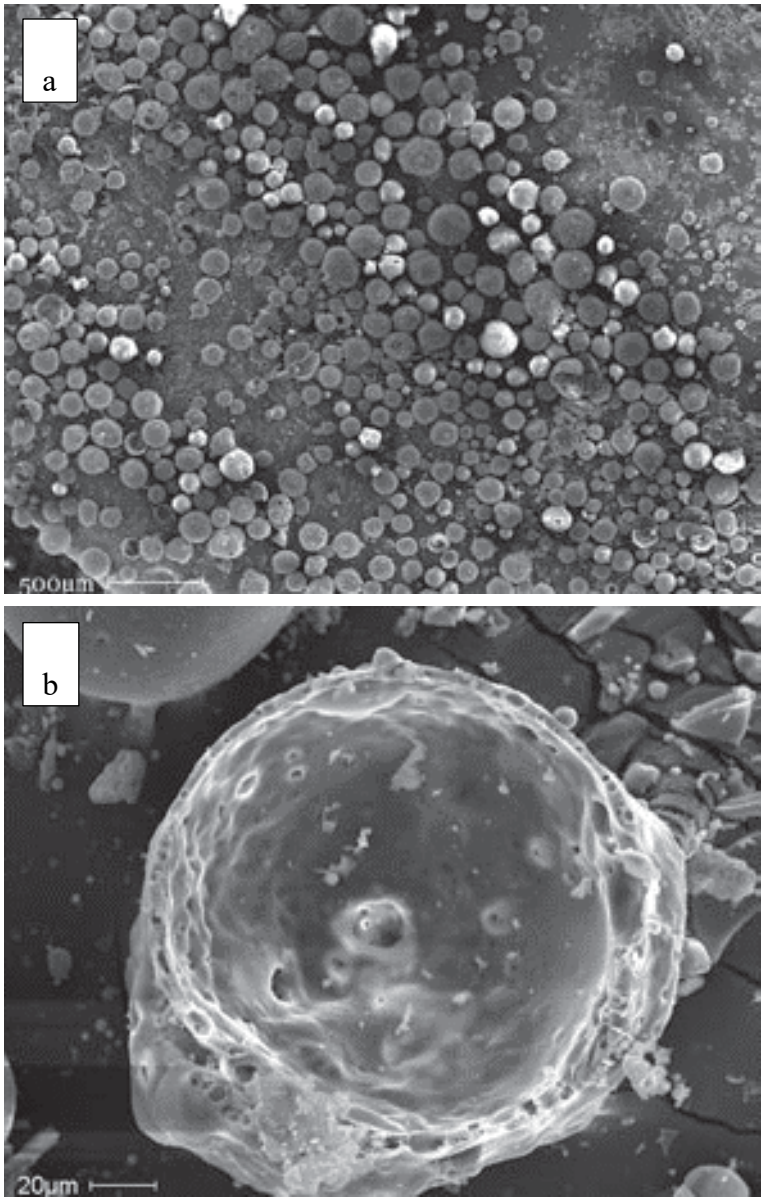

Figure 2-14 Micrographs of fly ash microspheres under (a) low magnification and (b) high magnification (Rohatgi et al. 2011).

Infiltration casting and stirring casting are two common methods used to fabricate metal matrix syntactic foams. Infiltration casting refers to forcing the molten metal into a microsphere preform so that the narrow interstices of the microsphere preform are filled with metal. Hartmann et al. (1999b) reported that the voids between packed spheres of equal size are about 37%, so the microsphere volume percentage of the syntactic foam fabricated by infiltration casting is about 63%. The pressure of the

infiltration casting is commonly supplied by gas (Balch et al. 2005; Orbulov et al. 2008) or mechanical pressure (Orbulov et al. 2008; Zhang & Zhao 2007; Zhao & Tao 2009). Figure 2-15 shows schematically a typical infiltration casting unit for fabricating metal matrix syntactic foam.

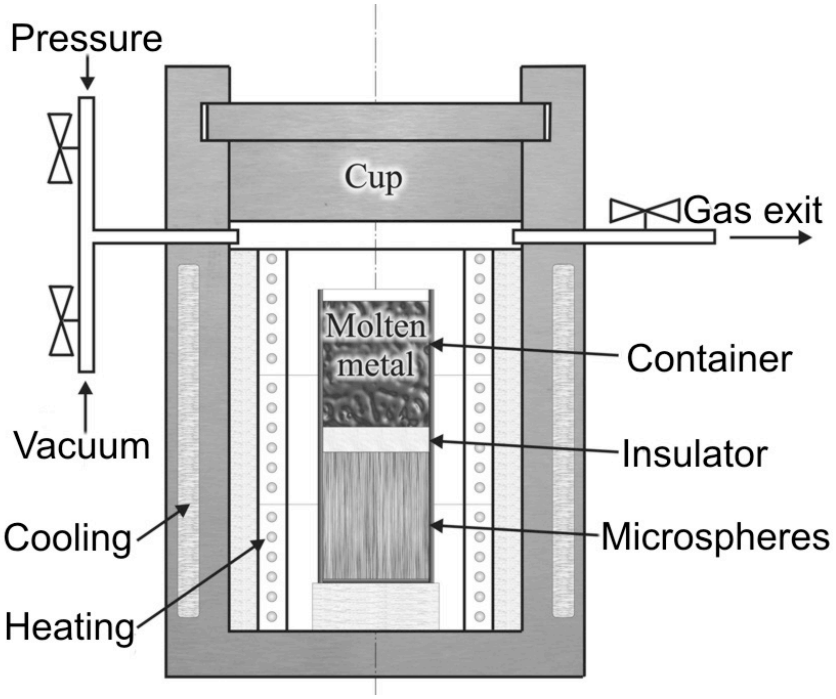

Figure 2-15 Schematic structure of the infiltration casting unit (Orbulov & Dobránszky 2008).

In stirring casting, the microspheres are added into the molten metal and then stirred in order to disperse the microspheres throughout the metal. This method is beneficial for controlling the volume percentage of microspheres, which can be varied from 30% to 50%. Daoud (2008) and Mondal et al. (2009) used stirring casting to fabricate Mg/fly ash syntactic foams and Al/fly ash syntactic foams respectively.

Xue et al. (2012) and Mondal et al. (2012) chose powder metallurgy to fabricate Ti alloy based syntactic foams. The mixture of metal powder and spheres is first prepared and then pressed into shape, outgassed and sintered to obtain a near fully dense part

(Gupta & Rohatgi 2014). Compared with the casting methods, powder metallurgy is limited to relatively simple geometries. However, it offers several advantages in fabrication, such as improved control of volume percentage and dispersion of the microspheres.

2.5.2 Microstructure

Figure 2-16 shows a typical microstructure of an Al syntactic foam fabricated by infiltration casting (Balch et al. 2005). The microspheres are randomly distributed in the Al matrix that results in isotropic properties in the syntactic foam. It is also observed that some microspheres are infiltrated by the Al alloy. Balch et al. (2005) believed that microspheres have been fractured either when received or during packing or infiltration. Orbulov (2013) studied the effect of infiltration pressure on the syntactic foam. The microstructure of syntactic foam is sensitive to the infiltration pressure, which cannot be over the compressive strength (crushing) of the hollow microspheres.

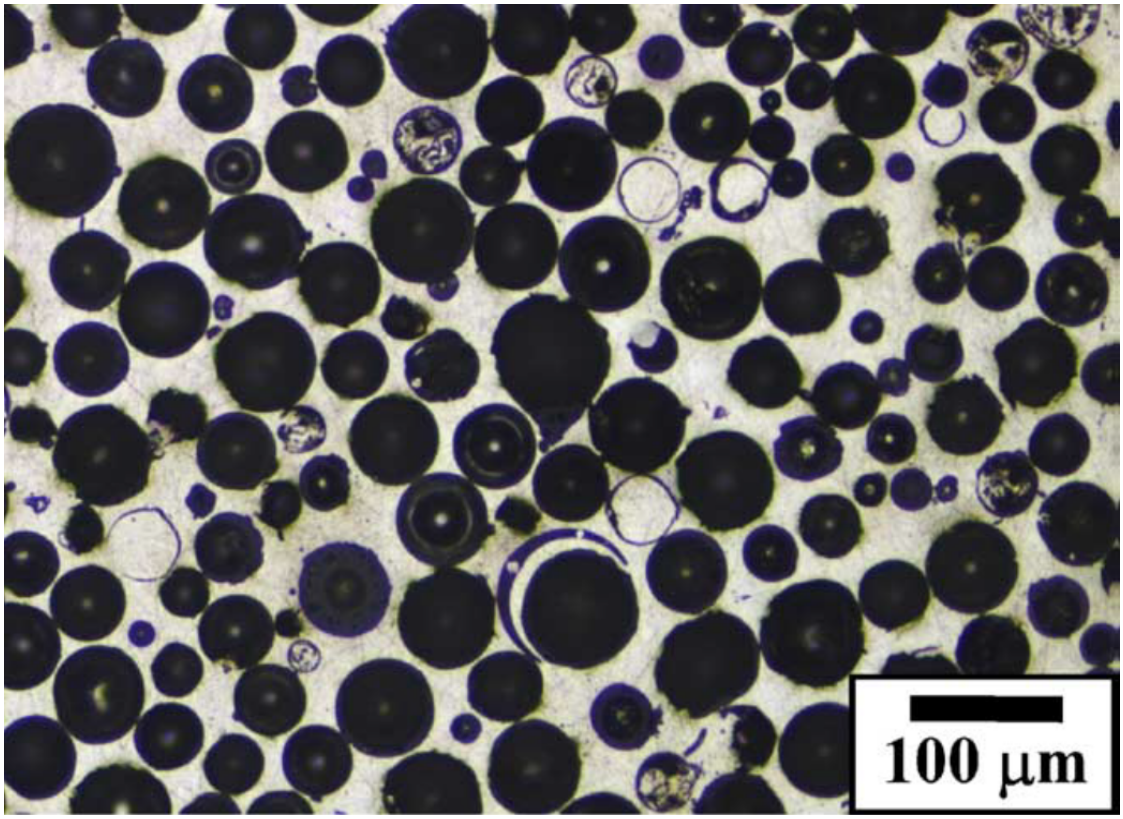

Figure 2-16 Typical microstructure of Al syntactic foam fabricated by infiltration casting (Balch et al. 2005).

The porosity of metallic syntactic foams is determined mainly by the porosity of the microspheres because there are normally no voids in the metal matrix compared with polymer matrix syntactic foams. Zhang and Zhao (2007) developed a formula to calculate the porosity of metal matrix syntactic foams (P_p) suitable for all types of microspheres:

$$P_p = \frac{\rho_m - \rho_f}{\rho_m - \rho_{eff}}\left(1 - \frac{\rho_{eff}}{\rho_{sm}}\right) \quad (2\text{-}4)$$

where, ρ_m, ρ_f and ρ_{sm} are the densities of metal matrix, syntactic foam and solid part of the microsphere, respectively, and ρ_{eff} is the effective density of the microspheres.

2.5.3 Static compressive properties

The static compressive behaviour of metal matrix syntactic foams is similar to those of cellular solid materials and the polymer matrix syntactic foams. Figure 2-17 shows a representative stress-strain curve of MMSFs under static compression (Cox et al. 2014). Their stress-strain curve includes three regions, which are initial linear elastic region, plateau region and densification region. The effects of metal matrix and particle material, particle wall thickness, diameter and volume fraction, and heat treatment on compressive properties of metal matrix syntactic foams have been extensively studied.

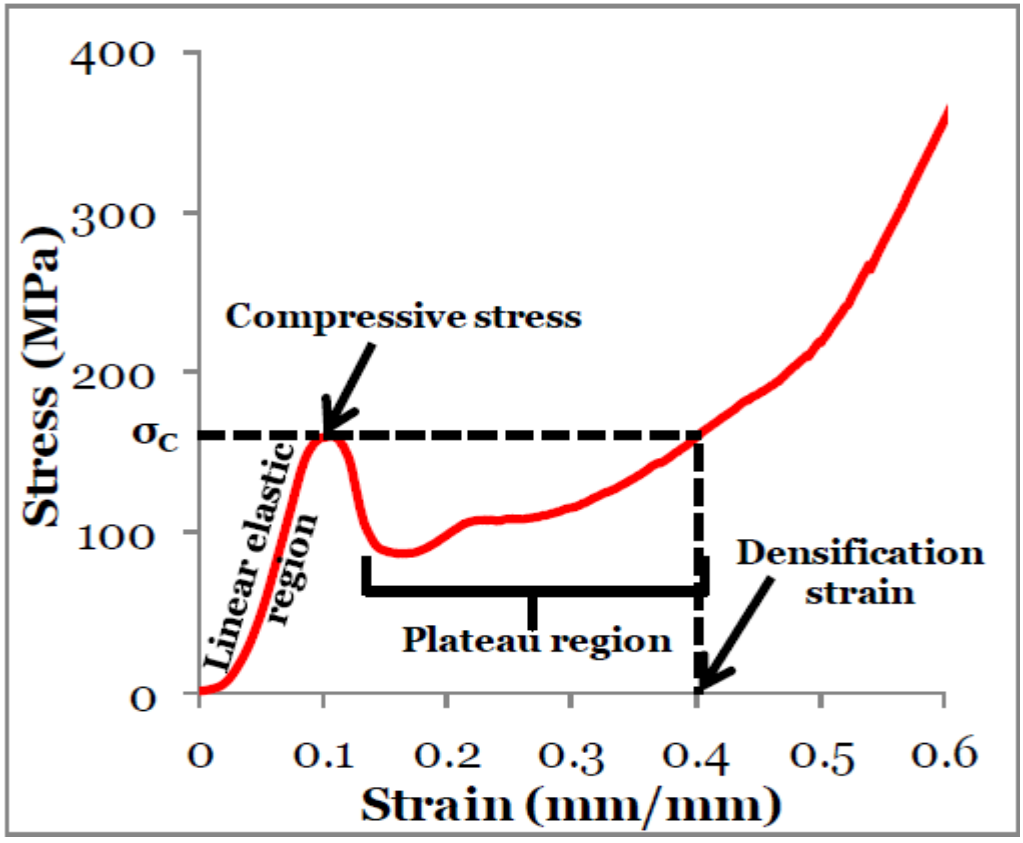

Figure 2-17 A representative quasi-static compressive stress-strain curve of MMSFs (Cox et al. 2014).

The compressive properties of MMSFs are dependent upon the metal matrix. Balch et al. (2005) studied the compressive behaviour of an Al syntactic foam fabricated from

commercially pure Al and Al 7075 alloy. The compressive strength of Al 7075 syntactic foam is much higher than pure aluminium syntactic foam. Orbulov and Ginsztler (2012) reported the compressive properties of the syntactic foams fabricated from four different types of Al alloy. The compressive properties of the syntactic foams are all slightly different. It indicates that the compressive properties of the MMSFs can be tailored by adjusting the alloy matrix. Rocha Rivero et al. (2013) compared the compressive properties of Al-A206/SiC and Mg-AZ91/SiC syntactic foams with microspheres of a similar size and volume fraction. The results showed that the peak strength, plateau strength and toughness of the syntactic foams increase with increasing yield stress of the matrix material.

The compressive properties of MMSFs are also determined by the material of the microspheres. Lehmhus et al. (2014) studied the compressive performance of 316L stainless steel/glass and ceramic microsphere syntactic foams. At a same volume percentage of microspheres, the compressive properties of 316L stainless steel /ceramic microsphere syntactic foams are better than those of 316L stainless steel /glass microsphere syntactic foams. Szlancsik et al. (2015) studied the compressive properties of iron hollow spheres reinforced Al syntactic foams. Compared with Al alloy ceramic microsphere syntactic foams, the compressive and plateau stresses of Al alloy iron hollow sphere syntactic foams are much lower. However, the engineering stress-strain curves of the latter showed plastic yielding and a long, gradually ascending plateau region, which can provide a large energy absorption capability. Májlinger and Orbulov (2014) fabricated hybrid metal matrix syntactic foams with combined ceramic and iron hollow particles, and studied their compressive properties. The compressive strength, yield strength, structural stiffness and fracture strain of the

hybrid metal matrix syntactic foams were all affected by the ratio of the two hollow spheres.

The compressive properties of MMSFs are sensitive to the wall-thickness-to-radius ratio (t/R) and size of the microspheres. Kiser et al. (1999) conducted static compression tests on Al/ceramic microsphere syntactic foams. The compressive strength of the syntactic foams was found to be proportional to t/R of the microspheres. Rohatgi et al. (2006) studied compressive properties of Al syntactic foams with different microsphere sizes and found that the compressive strength increased with increasing microsphere size. They believed that large microspheres have a higher t/R and can withstand a higher stress prior to fracture. Zhang et al. (2016) compared compressive properties of Al syntactic foams containing microspheres of different sizes but the same t/R. The small microsphere reinforced syntactic foam has a much higher compressive strength than the large microsphere reinforced syntactic foam. They explained that this is because, for the same wall thickness or the same thickness-to-radius ratio, smaller ceramic microspheres produce a stronger strengthening effect.

Changing the volume ratio between the metal matrix and the ceramic particles can also vary the compressive strength of the syntactic foam. As mentioned in the pervious section, the volume ratio can be easily controlled in stir casting and powder metallurgy. However, it is difficult to vary the volume percentage of ceramic spheres in pressure infiltration casting, because of a nearly fixed volume percentage of the randomly packed ceramic spheres. Rohatgi (2006) and Tao (2009) fabricated Al syntactic foams with lower volume fractions of microspheres by infiltration casting, by mixing different ratios of Al particles to microspheres. These two studies show that the

compressive strength of syntactic foams is enhanced by increasing the volume fraction of the metal matrix.

2.5.4 Compressive failure modes

Most MMSFs reinforced with ceramic microspheres basically show a similar compressive failure mode. The failed samples display either single or X-shaped shear crevasses or cracks with angles about 45° to the loading direction (Balch et al. 2005; Tao et al. 2008; Zhang et al. 2016; Zhang & Zhao 2007; Zhang et al. 2017). Figure 2-18 shows a schematic of the compressive deformation process in quasi-static compression of MMSFs. The central and corner regions of the syntactic foam suffer a higher compressive and shear stress during compression. It leads to a shear band of collapsed microspheres nearly 45° to the loading direction, after the peak stress in the stress-strain curve is reached. In further compression, the specimen becomes drum shaped due to the ductility of the Al matrix. The microspheres adjacent to the shear band are gradually crushed, leading to shear cracks emerging in the corner and central parts. No significant deformation occurred in the region near the top and bottom ends of the specimen due to the restraining effect of the compression fixture platens. In the densification stage, most microspheres have been crushed and the specimen is compacted (Zhang et al. 2017).

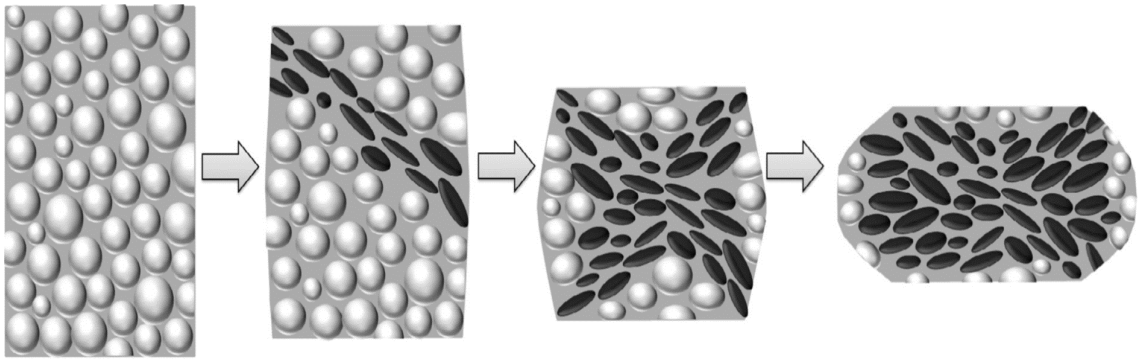

Figure 2-18 Schematic of quasi-static compressive deformation of metal matrix syntactic foam (Zhang et al. 2017).

Tao and Zhao (2012) studied the compressive failure of Al alloy matrix syntactic foams manufactured by melt infiltration casting and reported that the failure mechanisms of the Al syntactic foams are dependent upon the strength of the reinforcing ceramic microspheres. The syntactic foams reinforced with the stronger ceramic microspheres had the characteristics of Griffith rupture for brittle solids subjected to uniaxial compression. In Griffith rupture, tensile stress concentration at the tips of one or more cracks induces fracture. Griffith rupture has two characteristic features: the fracture cracks propagate at a preferred angle of 30° to the loading direction; the compressive strength is eight times of its tensile strength (Jayatilaka 1979; Lawn 1993). In Tao's study, the major cracks were inclined at an angle of 31.6±2.2° to the loading direction, and the compressive strength was eight times of its tensile strength which are also close to the theoretical ratio. Afterwards, the orientations of the cracks developed in the syntactic foams deviated significantly from 45°, which is characteristic of shear fracture. This suggested that Griffith rupture had precedence over shear fracture in these foams, although they had very low shear strengths. The syntactic foams reinforced with the weaker ceramic microspheres failed by a progressive collapse of the ceramic microspheres and had lower compressive

strengths. Thus, they concluded that stronger ceramic microspheres favour brittle fracture and weaker ceramic microspheres favour plastic collapse.

The results of hybrid metal matrix syntactic foams indicated that the failure mode of the syntactic foams can change from brittle shearing to plastic collapse, depending on the ratio between the ceramic and iron hollow spheres (Májlinger & Orbulov 2014).

2.5.5 Dynamic compressive properties

Many studies have investigated the dynamic compressive properties of MMSFs. Zhang and Zhao (2007) used the drop hammer test to study the low speed (4 m/s) impact response of Al matrix syntactic foams. Compared with static compression, the stress-strain curve of dynamic compression is different and has oscillations at low strains, because the impacting hammer experiences strong vertical vibrations when it hits the syntactic foam sample. Meanwhile, the impact peak strength is much higher than the compressive strength in static compression. Altenaiji et al. (2014) studied the characteristics of Al syntactic foams under drop weight impact and reported that impact peak strength is proportional to impact energy. Balch et al. (2005), Dou et al. (2007), Zhang et al. (2016) and Zhang et al. (2017) studied the impact response of Al matrix syntactic foams using Split-Hopkinson bars with high strain rates. The dynamic stress-strain curve is similar to that of static compression, but the compressive strength is much higher and strain rate dependent.

2.5.6 Energy absorption

Metal matrix syntactic foams have advantages in energy absorption because of the relatively higher plateau stress and extensive plateau regime. The former is mainly dependent upon the strengths of the metal matrix and microspheres, as well as upon the volume ratio between the two. The latter relates to the densification strain which is determined by the porosity of the syntactic foam. The specific energy absorption of CP Al matrix and Al 7075 matrix syntactic foams were about 39 J/g and 49 J/g respectively, which are significantly higher than those observed for unreinforced aluminium foams of similar density and are comparable to steel foams fabricated by powder metallurgy (Balch et al. 2005).

2.6 Damping capacity

The damping capacity of a material is an evaluation of the energy dissipation property of the material under a cyclic stress. When a material is subjected to excitation by an external force, it vibrates at certain amplitude which decreases as the external force is removed. This phenomenon results from the resistance that occurs in various microscopic and macroscopic processes in the materials. The damping of materials is usually referred to as internal damping (De Silva 1999). This section introduces the common measurement methods of damping and types of damping. Damping behaviours of, MMCs, PMSFs and MMSFs under either free or forced vibration modes are also reviewed.

2.6.1 Measurement of damping capacity

Damping capacity can be represented by various parameters, such as specific damping capacity, loss factor, Q-factor and damping ratio, and can be measured by different methods (De Silva 1999). Generally, damping measurement methods can be divided into time-response methods and frequency-response methods. The former includes logarithmic decrement method, step-response method and hysteresis loop method, based on a time-response record of the system to estimate damping. The latter include magnification-factor and bandwidth methods, using a frequency-response record. The logarithmic decrement, step-response, magnification-factor and bandwidth methods measure damping in a single-degree-of-freedom oscillatory system. The hysteresis loop method measures system damping under a cyclic stress. Figure 2-19 summarises the measurement methods and the relevant formulas for damping measurement. Among these methods, a large number of testing techniques have been developed, such

as the torsion pendulum method, suspended beam method, dynamic mechanical thermal analyser technique and piezoelectric ultrasonic composite oscillator technique (Lu et al. 2009).

Method	Measurements	Formulas
Logarithmic decrement method	A_i = first significant amplitude A_{i+r} = amplitude after r cycles	Logarithmic decrement $\delta = \frac{1}{r}\ln\frac{A_i}{A_{i+r}}$ (per cycle) $\frac{\delta}{2\pi} = \frac{\zeta}{\sqrt{1-\zeta^2}}$ (per radian) or $\zeta = \frac{1}{\sqrt{1+(2\pi/\delta)^2}}$ *For low damping:* $\zeta = \frac{\delta}{2\pi}$ $\zeta = \frac{A_i - A_{i+1}}{\pi(A_i + A_{i+1})}$
Step-response method	M_p = first peak value normalized w.r.t. steady-state value PO = percentage overshoot (over steady-state value)	$M_p = 1 + \exp\left[\frac{-\pi\zeta}{\sqrt{1-\zeta^2}}\right]$ $PO = 100\exp\left[\frac{-\pi\zeta}{\sqrt{1-\zeta^2}}\right]$
Hysteresis-loop method	ΔU = area of displacement–force hysteresis loop x_0 = maximum displacement of the hysteresis loop k = average slope of the hysteresis loop	Hysteretic damping constant: $h = \frac{\Delta U}{\pi x_0^2}$ Loss factor: $\eta = \frac{h}{k}$ Equivalent damping ratio: $\zeta = \frac{h}{2k}$
Magnification-factor method	Q = amplification at resonance, w.r.t. zero-frequency value	$Q = \frac{1}{2\zeta\sqrt{1-\zeta^2}}$ *For low damping:* $\zeta = \frac{1}{2Q}$
Bandwidth method	$\Delta\omega$ = bandwidth at $1/\sqrt{2}$ of resonant peak (i.e., half-power bandwidth) ω_r = resonant frequency	$\zeta = \frac{\Delta\omega}{2\omega_r}$

Figure 2-19 Summary of methods for damping measurement (De Silva 1999).

2.6.2 Types of material damping

The internal damping of materials, especially metal matrix composites, has been widely studied. Material damping is normally associated with microstructure defects, such as thermal mismatch-induced dislocation damping, interface damping, interaction damping and the rule of mixture damping (De Silva 1999; Lu et al. 2009).

Thermal mismatch between reinforcements and matrix leads to an enhancement of dislocation density, thereby increasing energy dissipation sources. Sliding of the interfaces between reinforcements and matrix can dissipate energy under cyclic loading. The interactions between reinforcements and dislocations or grain boundaries may lead to changes in damping response, such as dislocation pinning or viscous sliding of grain boundaries. Although the intrinsic damping of the reinforcements and the matrix is independent, a rule of mixture may affect the overall damping behaviour of the material (Lavernia et al. 1995; Mitra & Mahajan 1995; Zhang et al. 1994a). These established damping mechanisms in MMCs are helpful to understand the internal damping existing in metal matrix syntactic foams.

2.6.3 Damping behaviours of MMCs, PMSFs and MMSFs

The damping property of PMMCs has attracted considerable attention. Lavernia et al. (1995) reported that adding SiC and Al_2O_3 particles into the Al matrix can affect not only the specific stiffness and strength of the alloy but also the damping capacity of the alloy. The damping capacity of a material can be significantly enhanced by adding graphite particles but at the expense of stiffness. Wei et al. (2002) and Wei et al. (2007) demonstrated that the damping capacity of the macroscopic graphite particle reinforced Al composite is linked to the volume fraction of the reinforcement. Srikanth and Gupta (2002) tested the damping capacity of SiC particle reinforced Mg composites with various concentration of reinforcement. The results agreed with Wei et al. (2002) that the damping capacity of the pure magnesium matrix was improved in the presence of SiC particles, and it increased with increasing the proportion of the SiC particulates.

Sankaran et al. (2006) studied the damping characters of the epoxy syntactic foams fabricated from glass microspheres and three different binder matrix formulations. The damping of these syntactic foams was measured by dynamic mechanical analysis in the single cantilever mode. The damping factors of the syntactic foams measured at 30°C are different, and they are all less than the damping factors of the respective neat resins. Sankaran et al. (2006) explained that the composition of the polymer composite is the key factor in determining the damping behaviour, although other factors such as the interaction between reinforcement and matrix also affect damping characteristics.

The damping properties of metal matrix syntactic foams have studied either under the free and forced vibrations. Wu et al. (2006) tested damping of Al syntactic foams under both the free and forced vibrations, and compared with the pure Al alloy. The Al syntactic foams have a better damping capacity than pure Al alloy. The damping capacity of Al syntactic foam reinforced by small particles is higher than Al syntactic foam reinforced by large particles at both free and forced vibration modes. Luong et al. (2013) and Cox et al. (2014) used a dynamic mechanical analyser (DMA) to measure the damping capacity of Al syntactic foams at varying temperatures. Both of them reported that the damping parameter of Al syntactic foams links to the testing temperature. Although previous studies have measured damping of metal matrix syntactic foam, the actual damping mechanism of metal matrix syntactic foams has not been well explained yet.

2.7 Behaviour of materials under shockwave

The understanding of material behaviour under shockwave is usually based on empirical observations of actual explosive testing. The explosion can generate a high-

pressure shockwave which propagates from the surface of the explosive out into the surrounding medium (assumed here to be air). The shockwave is characterised by its peak value at the shock front followed by an immediate decay. The material may generate some interesting responses excited by the shockwave. However, due to the dangerous, expensive and uncertain nature of blast experiments, the body of experimental blast data is very limited and many aspects of blast response of materials remain unknown. Therefore, the shock tube test, which was originally designed for aerodynamic studies, is frequently applied to the study of material behaviour under shockwave, because it takes advantage of the safety, cost, range and repeatability of the experiment and the ease of operation (Lloyd et al. 2011; Stewart & Pecora 2015).

The shock tube consists of two major sections, which are the driver section and the driven section. The shock wave can usually be driven by either a compressed gas or an explosive.

Schleyer et al. (2007) used a large shock tube facility to conduct the shock pressure testing of a blast wall panel. The shock tube was configured to deliver a variety of blast pressure and impulse combinations, with a maximum possible peak blast pressure of 45 psi (3 bar) with a maximum impulse greater than 1000 psi*ms (660 ba*ms). The results showed that large permanent plastic deformations were produced in the blast wall panel without rupture.

Hua et al. (2014) designed a 28-inch square shock tube apparatus with a length of 10 m to study the structural response of carbon fibre sandwich panels subjected to shockwave. Their experimental results showed that the incident peak overpressure and maximum impulse increased with shockwave intensity, while the positive duration

remained almost unchanged. A much larger reflected peak overpressure and maximum impulse, as well as faster pressure decay, were observed in comparison to the incident overpressure profile. The sandwich panel oscillated in an elliptic manner and the peak oscillation frequency decreased with higher blast intensity. The influence of blast intensity and panel geometry on the maximum deflection of its back facesheet was further studied through a parametric analysis. It was observed that a higher peak overpressure induced a larger deflection on the back facesheet. The growth rate of deflection decreasing with the increased peak overpressure.

Colombo et al. (2015) studied the dynamic response and energy absorption of a mineral–phenolic foam subjected to shock loading. The shock wave generated by the shock tube impinged on a steel plate diffuser that was directly in contact with two prismatic foam specimens allowing to reach medium strain rate in the material (50~100 s^{-1}). The experimental investigation showed the strain rate insensitivity of the material in the range considered. The shock tube tests showed that the material was characterized by a good specific energy absorption (about 300 kJ/m^3) compared with other polymeric foams.

Louar et al. (2015) applied a high-speed 3D digital image correlation (DIC) system to compare the structural response of aluminium plates under shockwave excited by shock tube and free air blast. In the free air blast loading, three phases were observed. A linear elastoplastic deformation was followed by damped elastic vibrations and, finally, a stabilisation in a deformed state. In the shock tube loading, elastic vibrations were barely obtained due to high plastic deformation. The stress/strain wave propagation patterns were also different. More localised effects resulted from the shock tube load, and as a result, a stress/strain wave was generated at the borders of

the loaded area and propagated towards the edges and the centre of the plate. For the free air blast, the stress/strain wave was generated at the edges and propagated towards the centre. Chen et al. (2016) applied a similar experimental method to investigate the dynamic deformation of clamped circular plates subjected to confined blast loading.

Chapter 3 EXPERIMENTAL PROCEDURE

This chapter describes the raw materials and the processes used for fabricating the aluminium matrix syntactic foam. The experimental procedures for density measurement, microstructure observation, mechanical test, internal friction test and shock tube test are described in detail.

3.1 Raw materials

3.1.1 Al alloy

The alloy (metal matrix) used for fabricating the Al syntactic foam samples is the Aluminium 6082 alloy (Al 6082), which is a common commercial aluminium alloy for structural applications due to the medium strength with excellent corrosion resistance. The chemical composition of Al 6082 is shown in Table 3-1 (BSI 2013). With a high Si content, liquid Al 6082 has a good fluidity which offers an advantage in melt infiltration casting (Kalhapure & Dighe 2015). Al 6082 is also one of the strongest 6000 series alloys because of the high content of Mg. Figure 3-1 shows the two forms of the Al 6082 alloy used in the syntactic foam fabrication. The cylindrical block (ϕ70 mm) was always used in the manufacture of the syntactic foam samples, while the irregular shaped Al 6082 powder (particle size range of 0.5-1 mm) was used to control the Al volume fraction of the syntactic foam.

Table 3-1 Chemical composition of Al 6082

Chemical Element	Percentage %
Manganese (Mn)	0.40-1.00
Iron (Fe)	0.0-0.50
Magnesium (Mg)	0.60-1.20
Silicon (Si)	0.70-1.30
Copper (Cu)	0.0-0.10
Zinc (Zn)	0.0-0.20
Titanium (Ti)	0.0-0.10
Chromium (Cr)	0.0-0.25
Other (Each)	0.0-0.05
Others (Total)	0.0-0.15
Aluiminium (Al)	Balance

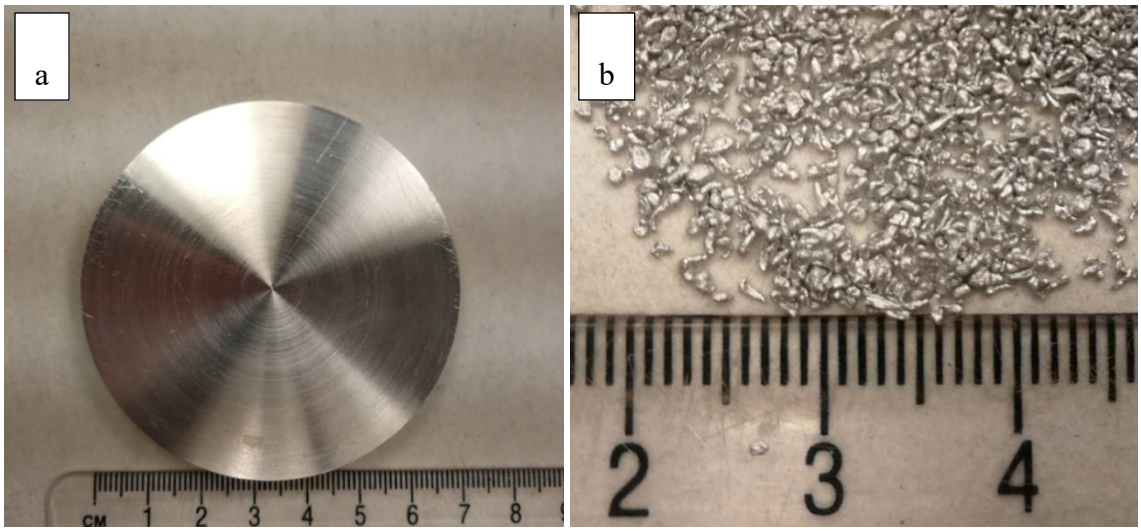

Figure 3-1 The Al 6082 in the forms of (a) cylindrical block and (b) powder.

3.1.2 Ceramic microsphere

The ceramic microsphere (CM) powder used to fabricate the syntactic foam samples was provided by Envirospheres Pty Ltd (Linfield, Australia) and its chemical composition is listed in Table 3-2. The CM powder was separated into three size groups with the particle size ranges of 75-150 μm, 125-250 μm and 250-500 μm for the evaluation of the effect of CM particle size on the mechanical response of the syntactic foam.

Table 3-2 Chemical composition of the CM powder

Chemical Element	Percentage %
Silica (SiO_2)	55-65
Alumina (Al_2O_3)	30-36
Iron Oxide (Fe_2O_3)	1-2
Titanium Dioxide (TiO_2)	0.5-1

3.1.2.1 Microstructure

Figure 3-2 shows the optical images of the three CM powder with different particle size ranges. The surface texture of the CMs can be either smooth or rough. There are two different kinds of inner structure in the CMs, either hollow or porous, as indicated in Figure 3-3. The hollow CMs are nearly perfect spheres with a smooth surface texture and a solid shell with an average thickness-to-radius ratio of 1:10. The porous CMs also have a regular spherical shape with a very coarse surface texture and a spongy inner structure, which contains either spherical, nearly-spherical or irregular pores with varied sizes.

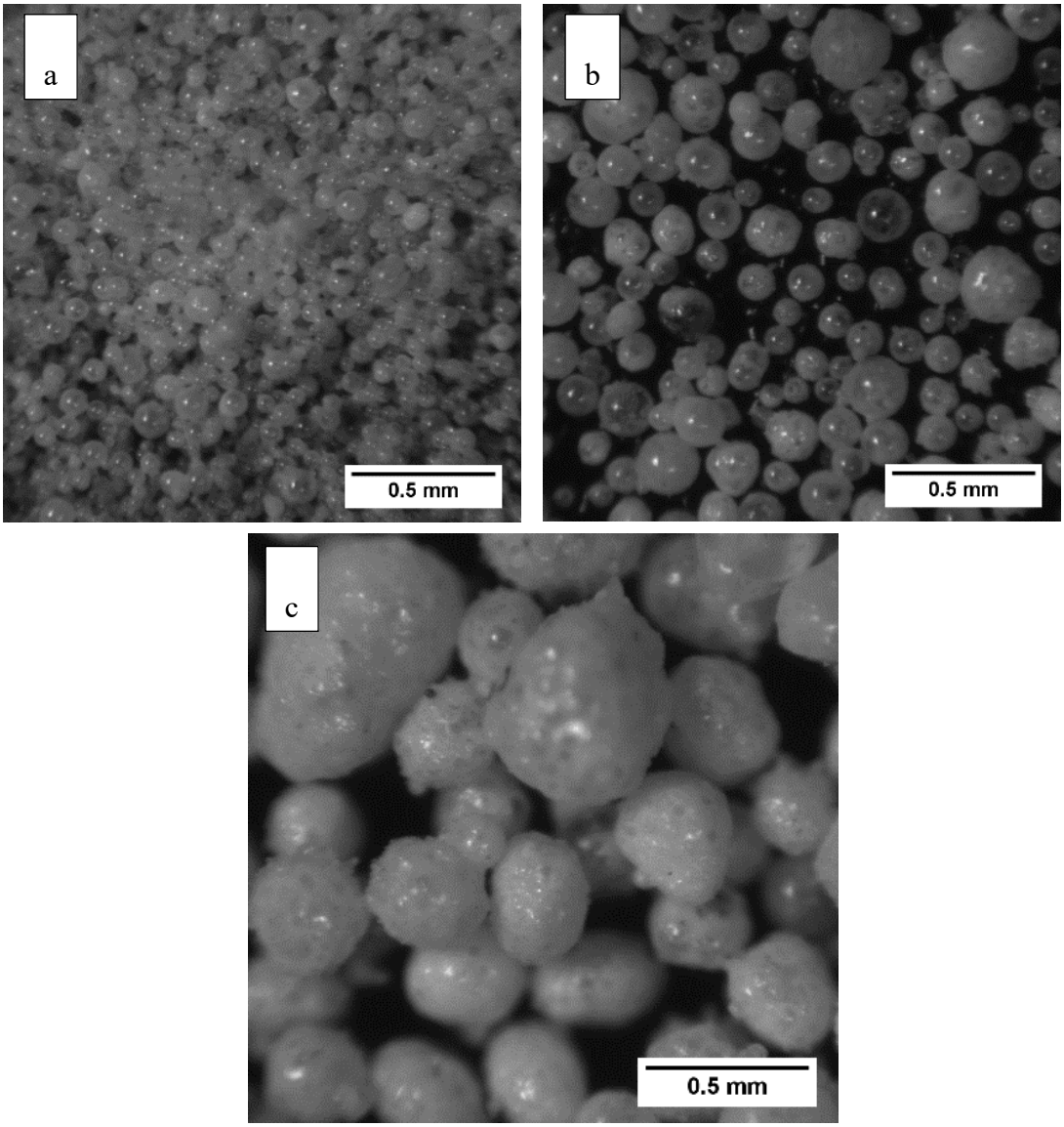

Figure 3-2 Optical images of the three of CM powders with different particle sizes: (a) 75-150 µm, (b) 125-250 µm and (c) 250-500 µm.

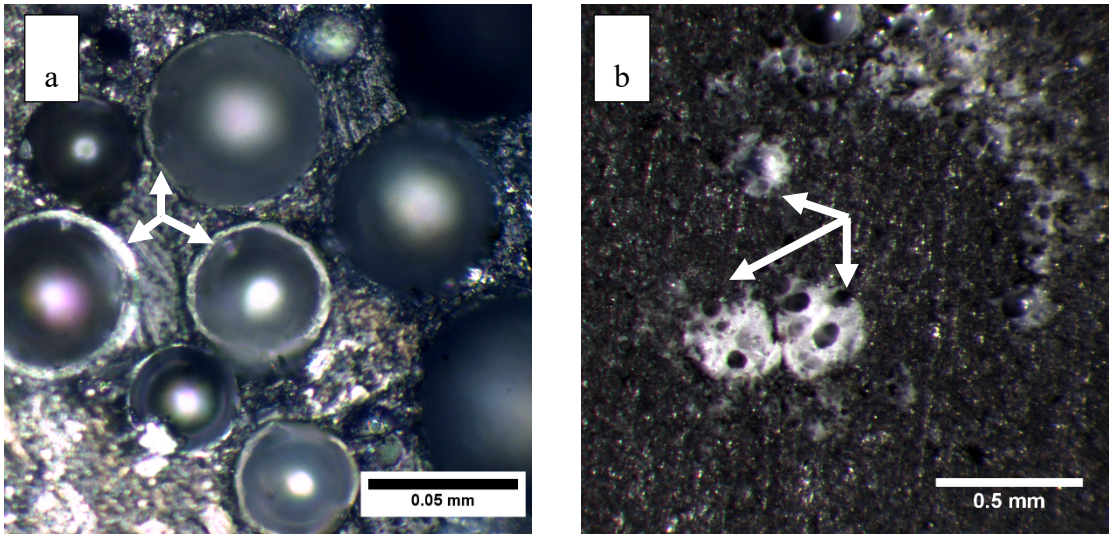

Figure 3-3 Optical micrographs of the cross sections of two different inner structures: (a) hollow CMs and (b) porous CMs.

3.1.2.2 Density and porosity

The effective densities of the three particle size groups of CM, i.e., the total mass of the CM particles divided by the total volume of the CM particles were measured using the Archimedes method. Water was used as the working medium in the Archimedes method. Because the CMs are lighter than water and water can infiltrate defective ceramic microspheres, the pure wax was used as a sealing material for measuring the effective density of the CMs. An amount of pure wax was first melted in a steel container and, after cooling and solidification, the total volume of the wax, the steel container and a steel stirrer wire was measured by the Archimedes method. The wax was subsequently re-melted at a temperature of less than 80°C to avoid any evaporation. An amount of the CMs which had been weighed, was mixed into the liquid wax by the steel wire stirrer to eliminate any air bubbles. After full solidification, the total volume of the wax together with the CMs, the steel wire stirrer and the steel container was measured again by the Archimedes method. The volume of the CMs

was the difference between the two measurements. The density of the CMs was calculated by the measured mass and volume of the CMs.

The effective density of each particle size group was measured three times and the average values for the three CM size groups are shown in Figure 3-4. The variations in effective density among the three measurements of each particle size group and among the three particle size groups are very small, in spite of the different particle sizes and inner structures. The effective density of the CMs was therefore regarded as a constant and the average value of approximately 0.66 g/cm^3 was used throughout the thesis. Given the chemical composition of the CMs, the density of the solid ceramic shell can be estimated to be ≈3.00 g/cm^3. The porosity of the CMs is thus estimated to be about 78%.

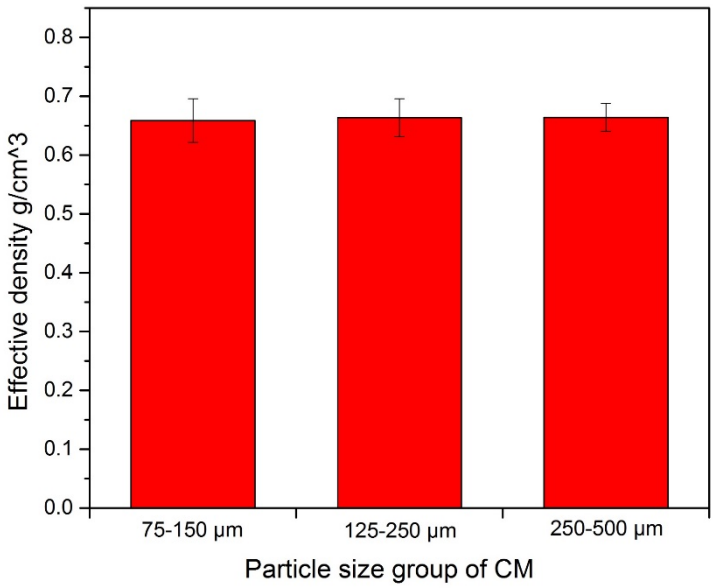

Figure 3-4 Measured effective densities of the three size groups of the CMs.

3.1.2.3 Particle size distribution

The particle size distribution of each of the three size groups of CMs was measured by placing the CM particles under a microscope and measuring the diameters of 1000 particles. Figure 3-5 shows that the particle sizes of the three CM size groups have a nearly normal distribution. Table 3-3 lists the surface weighted mean diameters (D (3,2)) of the three CM size groups, which is determined by:

$$D\ (3,2) = \frac{\sum_{i=1}^{k} n_i D_i^3}{\sum_{i=1}^{k} n_i D_i^2} \tag{3-1}$$

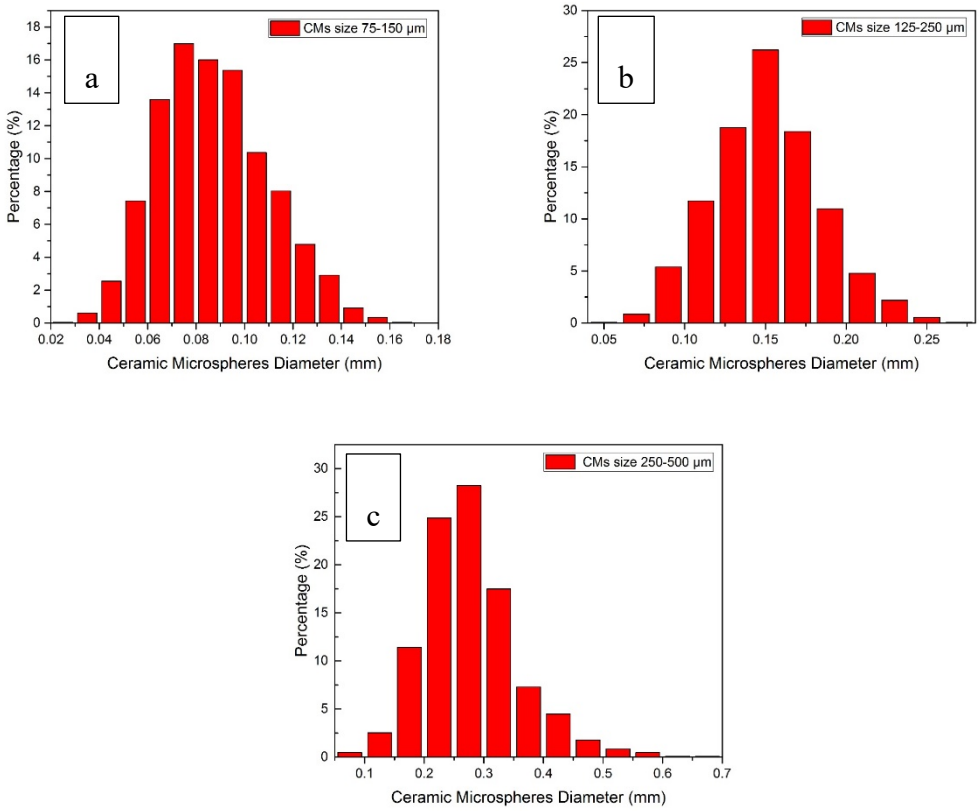

Figure 3-5 Particle size distributions of the CMs with particle size ranges of (a) 75-150 µm, (b) 125-250 µm and (c) 250-500 µm.

Table 3-3 Surface weighted mean diameters of the three size groups of CMs

CM size group	D [3, 2]
75-150 µm	99 µm
125-250 µm	166 µm
250-500 µm	326 µm

3.1.2.4 Compressive behaviour

The compressive load-displacement curves of the CMs are shown in Figure 3-6. For each particle size group, the curve has three characteristic regions corresponding to packing, crushing and densification. The load increases relatively rapidly with displacement in the packing region where CM particles undergo reordering and deform elastically with insignificant damage. The displacement then increases steadily with increasing load in the crushing region because the particles are gradually crushed. With the majority of the particles being crushed, the curve finally enters densification region where the broken pieces of the particles become densified and the load-displacement curve becomes steep again.

The average crushing load, which is taken as the mean load in the crushing region of the curve, of the small size group of CMs is slightly higher than the medium size group, but both are considerably higher than the large size group of CMs. The starting point of densification can be treated as the intersection between the tangents of the crushing and densification regions in the curves. The large, medium and small particle size groups of CMs have densification loads of 2.39, 3.45 and 4.22 kN, respectively. In other words, the smaller the CMs, the stronger they are. The corresponding

densification displacements of the three size groups of CMs are very similar, which are 16.6, 16.6 and 16.8 mm, respectively. This is because they have a similar porosity.

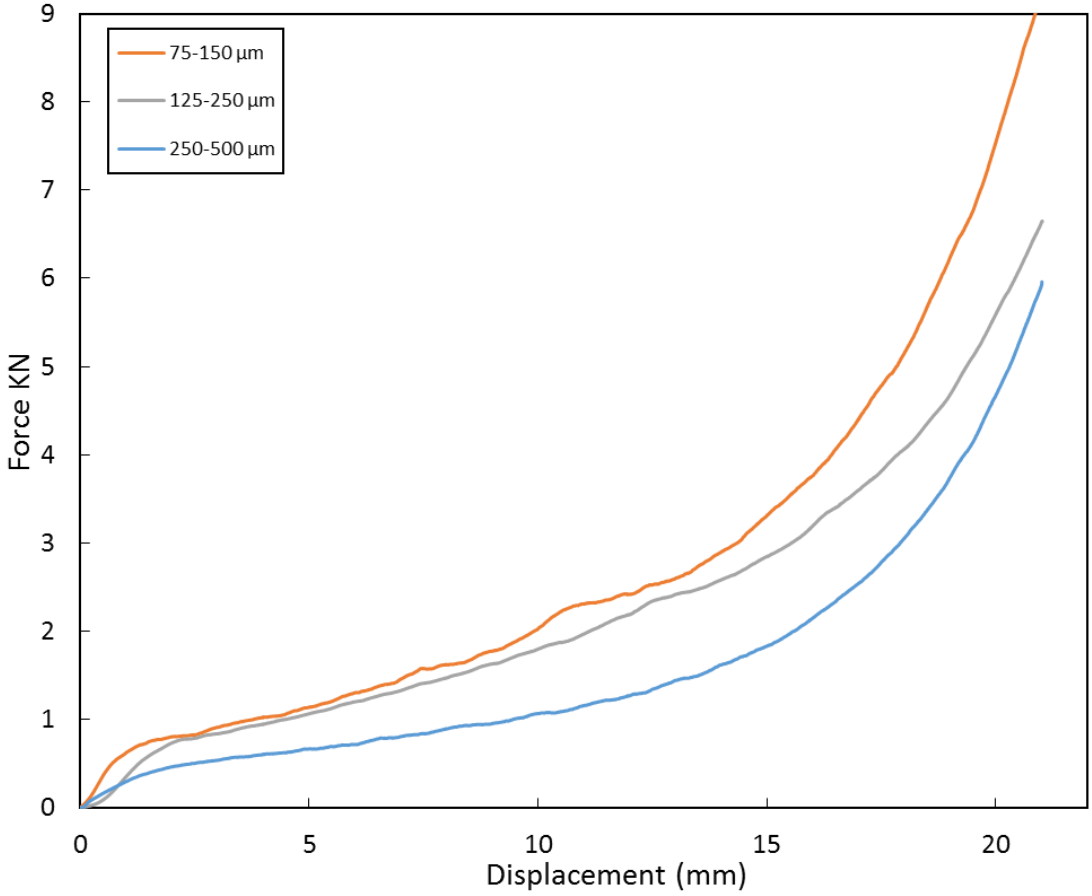

Figure 3-6 Compressive behaviours of the CMs.

3.2 Fabrication processes

The Al matrix syntactic foam samples were fabricated by melt pressure infiltration casting. Various types of syntactic foam samples were made by infiltrating liquid Al into packed beds of the monomodal (single particle size range) or bimodal (two particle size ranges) CMs, or a mixture of CMs and Al particles.

3.2.1 Melt infiltration into CMs

The melt infiltration casting process used for fabricating the syntactic foam samples is illustrated schematically in Figure 3-7. The process mainly included the following steps:

- A steel tube with a diameter of 70 mm and a length of 55 mm, with the bottom blocked with an inserted circular steel disc, was prepared as a mould. The bottom of the tube was not fully sealed. Instead, tiny gaps between the inner surface of the tube and the steel disc existed for air to escape during liquid infiltrating.

- A predetermined amount of the CMs was poured into the tube mould. An ultrathin Kaowool filter paper was placed on top of the packed bed of CMs. This paper was used to prevent direct contact between the Al melt and the CMs before pressure was applied and also to partially filter the aluminium oxide layer during infiltration. An Al ingot was then placed on the top of the filter paper. The volume ratio of Al to CMs was maintained at 1:2, to ensure that the Al was slightly more than the amount required for complete infiltration into the packed bed of CMs. Another circular steel disc, which was slightly smaller than the inner diameter of the tube, was finally placed above the Al ingot.

- The whole assembly was heated and maintained at 730°C for 30 minutes in an electric furnace in order to fully melt the Al ingot.

- The whole assembly was moved from the furnace to a hydraulic press, and the molten Al was rapidly compressed to infiltrate into the interstices within the packed bed of CMs.

- After complete solidification of the Al, as-produced syntactic foam sample was removed from the steel tube mould.

Table 3-4 shows the compositions of the as-fabricated syntactic foams, where M series samples were manufactured with different monomodal CMs and the B series samples were fabricated with bimodal CMs.

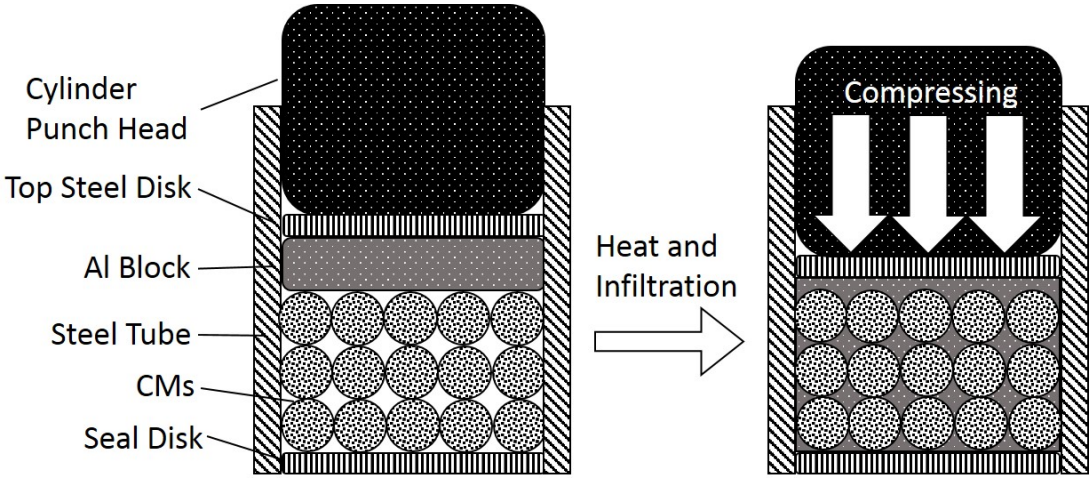

Figure 3-7 Schematic of melt infiltration casting.

Table 3-4 Volume percentages of CM particle size groups in the syntactic foams

Sample ID No.	Type and volume percentage of CM
M1	75-150 µm(100%)
M2	125-250 µm(100%)
M3	250-500 µm(100%)
B1	75-150 µm (70%) 250-500 µm (30%)
B2	75-150 µm (50%) 250-500 µm (50%)
B3	75-150 µm (30%) 250-500 µm (70%)

3.2.2 Melt infiltration into Al/CM mixtures

Syntactic foam samples toughened with additional Al 6082 particles were also produced using the melt infiltration casting method. Four sets of samples were fabricated by infiltrating molten Al 6082 into a mixture of Al 6082 powder and the CMs, with the target volume fractions of CMs of 50%, 40%, 30% and 20%. A mixture consisting of predetermined amounts of Al powder and CMs (the volume ratios shown in Table 3-5), with a small amount of ethanol as the binder, was prepared and then poured into the steel tube mould. An Al block was placed on the top of the Al/CM mixture. The volume of the Al block is predetermined about half of the volume of the CMs as the molten Al majorly infiltrates interstices between CM particles (Tao & Zhao 2009), while the interspaces within Al particles will become smaller by compression as Al particles are softened by heating process. The assembly was moved to an electric furnace preheated to 650°C and was then heated to 710°C and maintained for 10 min. Afterwards, the assembly was moved from the furnace to the hydraulic press, and the molten Al was instantly pressed to infiltrate into the Al/CM bed. After solidification, the syntactic foam sample was removed from the steel tube mould. The compositions of the syntactic foams toughed with Al particles, named as T series, are presented in Table 3-5.

Table 3-5 Compositions of the syntactic foams toughed with Al particles

Sample ID No.	Volume percentage of CM (%)	Volume percentage of Al ingot (%)	Volume percentage of Al powder (%)
T1	20	10	70
T2	30	15	55
T3	40	20	40
T4	50	25	25

3.2.3 Heat treatment

The syntactic foam samples were machined and ground to desired shapes and dimensions for different experiments. A number of syntactic foam samples were subjected to the standard T6 heat treatment (ASM 1991) before mechanical tests for investigations into the effect of heat treatment. Figure 3-8 is the T6 heat treatment procedure. The samples were initially heated to 540°C for 100 mins for solutionising, quenched in water and then aged at 180°C for 10 hours.

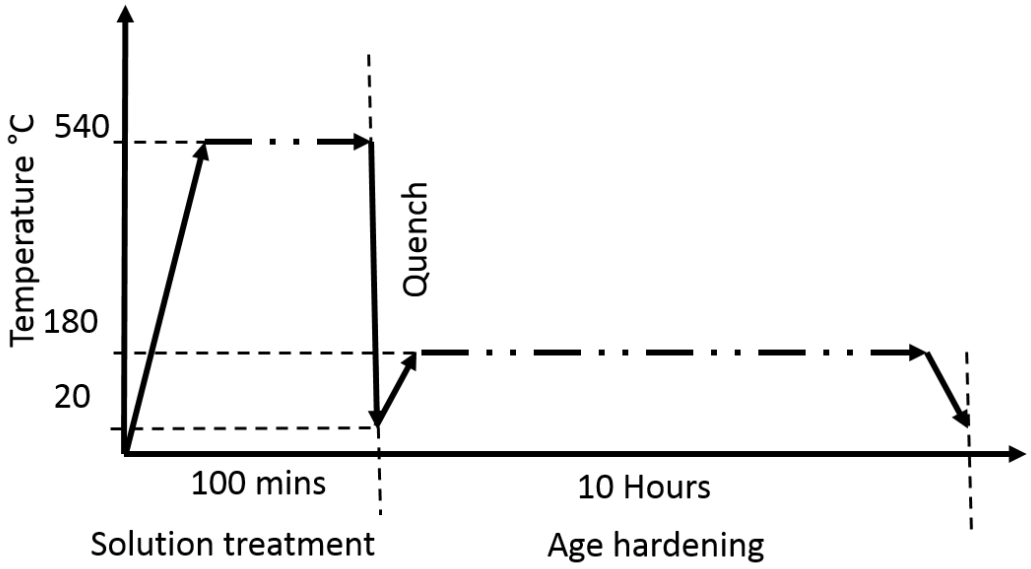

Figure 3-8 T6 Heat treatment procedure.

3.3 Density measurement and microstructural observations

The density of all syntactic foam samples was measured by the Archimedes method, the operating procedure of which has been introduced in detail in section 3.1.2.2. All the syntactic foam samples were heavier than 1 g/cm^3 so water was used as the working medium in the Archimedes method in this density measurement.

To investigate the microstructure of the syntactic foam, the samples were ground, polished and observed using a Nikon optical microscope and a Hitachi S-2460 scanning electron microscope (SEM). The chemical compositions of both the CMs and the syntactic foams were analysed by Energy Dispersive X-Ray Spectroscopy (EDS), a function of the SEM. The fracture surfaces of the samples after compression, three-point bending and Charpy tests were also studied by SEM.

3.4 Quasi-static compressive tests on syntactic foams

All of the quasi-static compression tests, including the monotonic, intermittent cyclic and repetitive cyclic compression tests, were conducted at room temperature on an Instron 4045 machine, supplied by Instron Corporation, Canton, USA. The Instron 4045 test system was equipped with a 50 kN load cell and the crosshead speed was chosen to give a nominal strain rate of $10^{-3}s^{-1}$ to ensure quasi-static compression. All the syntactic foam specimens were machined to a cubic form with dimensions $15\times15\times15$ mm^3 except one specimen used in the intermittent cyclic compression to study the energy dissipation due to internal friction, which had a height of 30 mm. The specimens were polished prior to testing and a thin layer of lubricant was applied on the surface of the specimens to minimise friction with the platens during compression. The load and displacement data were acquired with the Bludhill 2.0 software and processed by Excel. The final results of the compression tests are represented in the form of stress-strain curves.

3.4.1 Monotonic compression

In the monotonic compression tests, the syntactic foam specimens were compressed uniaxially to a nominal strain of 0.7 or until the specimens were completely crushed. For each type of syntactic foam, three specimens were tested and the compressive properties were characterised by the average values of the three tests.

3.4.2 Intermittent cyclic compression

In the intermittent cyclic compression tests, the specimens were compressed uniaxially first to a strain of 0.01, unloaded (to zero force) and then reloaded to the strain of 0.02.

The unloading-loading cycles were repeated six more times at different strains up to 0.08 with an interval of 0.01.

3.4.3 Repetitive cyclic compression

In the repetitive cyclic compression tests, the specimens were compressed uniaxially to a predetermined stress of 30, 60 or 80 MPa, unloaded and then reloaded to the same stress amplitude. The unloading-loading cycles were repeated for 50 times in each predetermined stress level.

3.5 Charpy impact test

The Charpy impact fracture tests were carried out based on the standards ASTM E23(ASTM 2016) for V-notched bar impact testing of metallic materials. Figure 3-9 shows the schematics of the Charpy V-notch impact test and the striker position relative to the specimen. The aim of this experiment is to measure the energy absorption of the specimen using a moving mass of sufficient energy to break the specimen placed in its path.

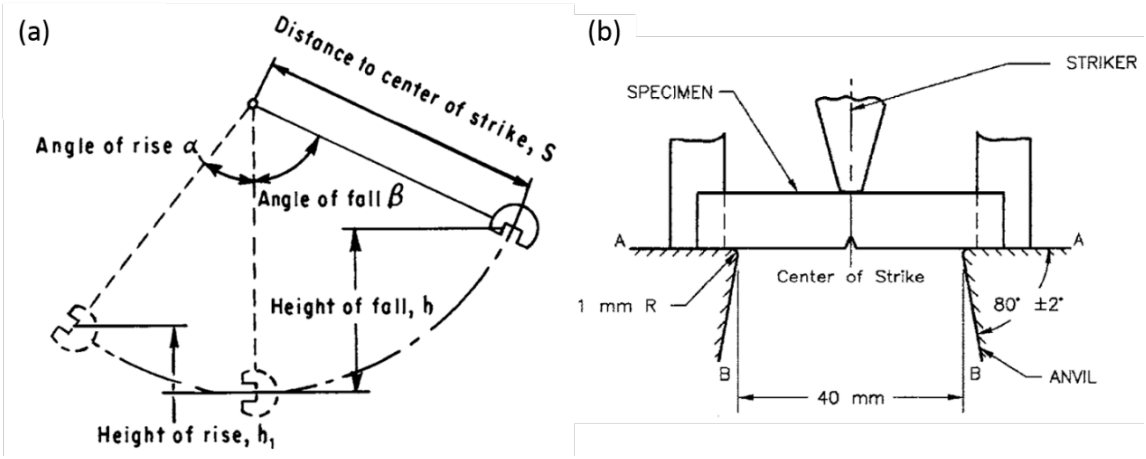

Figure 3-9 Schematics of (a) Charpy V-notch impact test and (b) Charpy striker position (ASTM 2016).

The specimens were machined to the standard dimensions as shown in Figure 3-10. The V-notch of the specimen, which was used to concentrate the stress during the impact process, was precisely manufactured. The procedure of the Charpy test can be summarised as follows:

(1) The specimen was placed in the correct position so that the V-notch was against the anvil and aligned to the centre of the striker.

(2) A pendulum hammer was lifted up to the starting angle (β) to provide a potential energy, which was converted to the equal amount of kinetic energy to impact the specimen when the pendulum hammer was released.

(3) After the sample was fractured, the pendulum hammer continued to swing until the kinetic energy transferred to a potential energy. The finish swing angle (α) of the pendulum was measured.

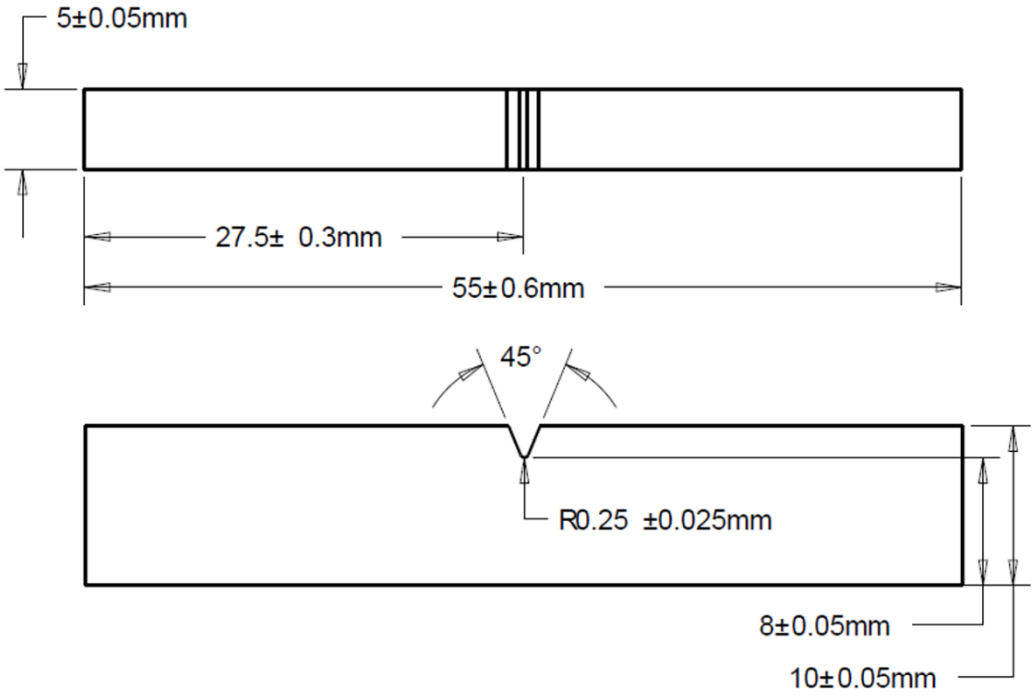

Figure 3-10 Drawings of Charpy impact test specimen.

The absorbed energy during the fracture of the specimen, i.e., Charpy impact energy (E_a), is equal to the difference in the energy of the hammer between the initial and follow-through positions:

$$E_a = \mathrm{m}_p \mathrm{g} \times \mathrm{R}_p(\cos\beta - \cos\alpha) \tag{3-2}$$

where m is the pendulum hammer mass (3.7 kg), g is the gravitational acceleration (9.81 m/s^2), R is the radius of the pendulum hammer arm (0.347 m), α is the starting angle (150°) and β is the follow-through swing angle.

3.6 Shock tube test

3.6.1 Shockwaves

A pressure pulse (or blast wave) created by, e.g., the sudden rupture of a vessel containing high-pressure gas or detonation of an explosive propagates readily in a compressible fluid to form a shockwave. The development of a shockwave is not instantaneous but forms over a finite distance as this pressure pulse expands outwards from the explosive source.

The process of forming a shockwave begins with the sudden release of energy that, typically, is propagated outwards from the surface of a detonating explosive into the surrounding medium. Figure 3-11 illustrates schematically the formation of a shockwave from an arbitrary high-amplitude pressure pulse to a fully shocked waveform after some distance (Ling et al. 2009). The initial high-pressure pulse, as idealised in Figure 3-11 (a), compresses and travels into the medium at the local speed of sound (Stewart & Pecora 2015). Due to the highly compressive state (i.e., elevated temperature and pressure) in the centre portion of the pulse, the localised speed of sound is higher than that at the leading edge of the pulse. This higher pressure portion then moves toward the leading edge of the pulse and away from the trailing edge as shown Figure 3-11 (b). As the pressure pulse propagates further away from the source, this higher pressure region of the pulse moves further towards the leading edge until it becomes a complete shockwave that is characterised by the well-known Friedlander waveform, which has a steep pressure wave front followed by an exponential decay as shown in Figure 3-11 (c).

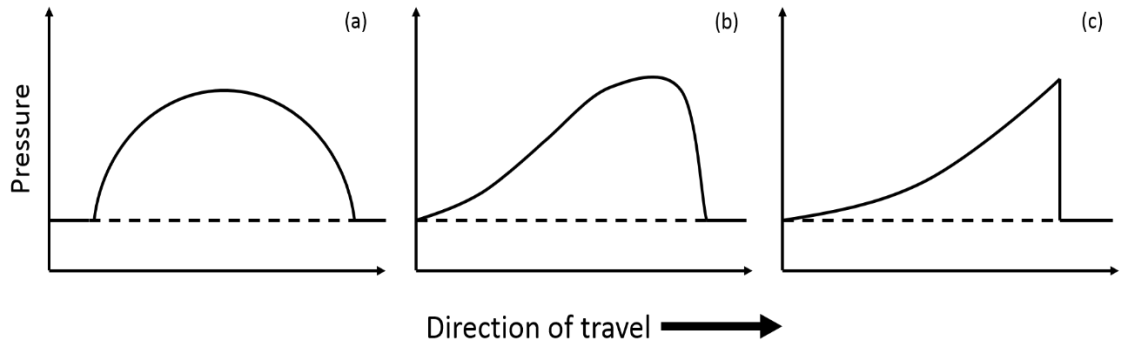

Figure 3-11 Schematic of shockwave forming process from an explosion.

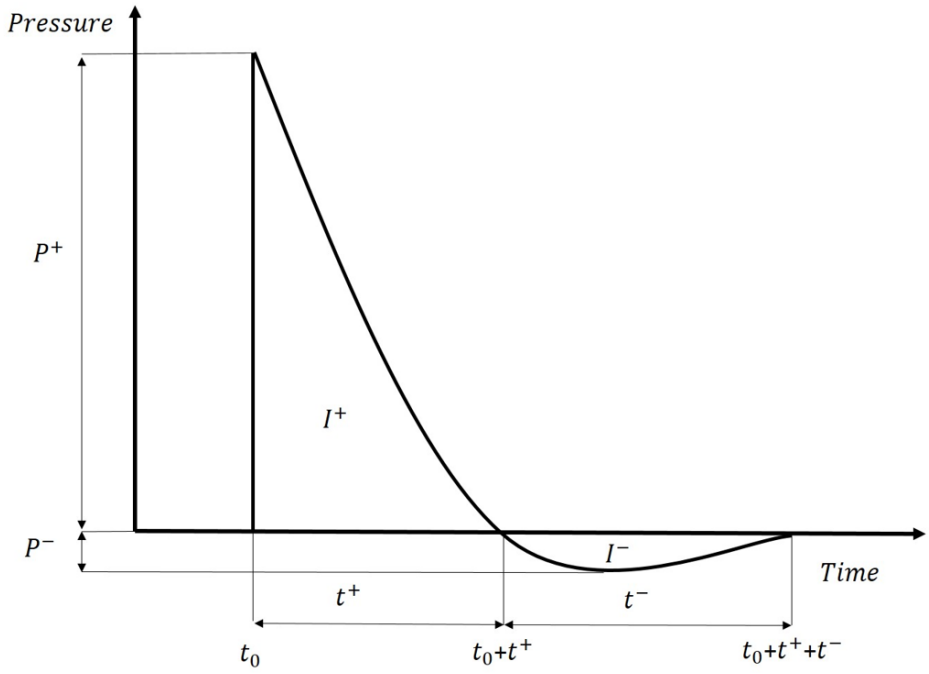

Figure 3-12 Schematic of an ideal Friedlander wave showing impulses and duration.

The Friedlander waveform (Figure 3-12) is the simplest schematic diagram used to represent a shockwave (Chavko et al. 2007; Courtney & Courtney 2010) in a compressible medium such as a gas. The shockwave front arrives at the time t_0 with a rapid rise in positive pressure P^+. The area under the first part of the curve with duration t^+ is considered a positive impulse, I^+, due to the pressure being above the local ambient state. This compression is followed by an over-expansion where the shocked gas

pressure falls below the local ambient pressure after t^+. Similar to the positive phase, the area between the pressure curve and the abscissa between t_0+t^+ and $t_0+t^++t^-$ represents the negative impulse, I^- (Louar et al. 2015). The positive impulse of the Friedlander waveform is represented by the following equation:

$$I^+ = \int_{t_0}^{t_0+t^+} P^+ \, dt \tag{3-3}$$

while the negative impulse is given by:

$$I^- = \int_{t_0+t^+}^{t_0+t^++t^-} P^- \, dt \tag{3-4}$$

Essentially, even though a real shockwave (blast wave) usually lasts only a few milliseconds, it can cause severe damage to surrounding. A shock tube is a well-known apparatus for producing shockwaves in the laboratory to investigate the effect of this type of impulse loading on materials and structures. Typically, shock tubes are driven either by the release of high-pressure gas or explosive device to produce the initial pressure pulse. In this study, an explosive driven shock tube (EDST) was used to investigate response of syntactic foam under impulsive loading.

3.6.2 Shock tube apparatus

A schematic of the EDST apparatus used in this investigation is presented in Figure 3-13. The apparatus was designed to be driven by the detonation of a small explosive charge in a pulse generator but could also be driven by a compressed gas and quick

release valve system. The shock tubes were manufactured from commercial PVC tubing with outer and inner diameters of 75 mm and 60 mm and a safe working pressure of 16 bar (230 PSI). The fundamental design of the shock tube system comprises two pieces of PVC tubing each of 3 meters long joined together using a bolted flange sealed with rubber at the contact surfaces to ensure no leakage at the joint. The flange also acted as a holder in which a specially machined syntactic foam test specimen (see Figure 3-14) was clamped rigidly. The pulse generator, which was mounted at one end, used standard commercial blank nail gun ammunition as explosive driver charge. Four different types of ammunition were used and their performance will be discussed in the next section. A rigid end cap was used to close the other end of the shock tube arrangement.

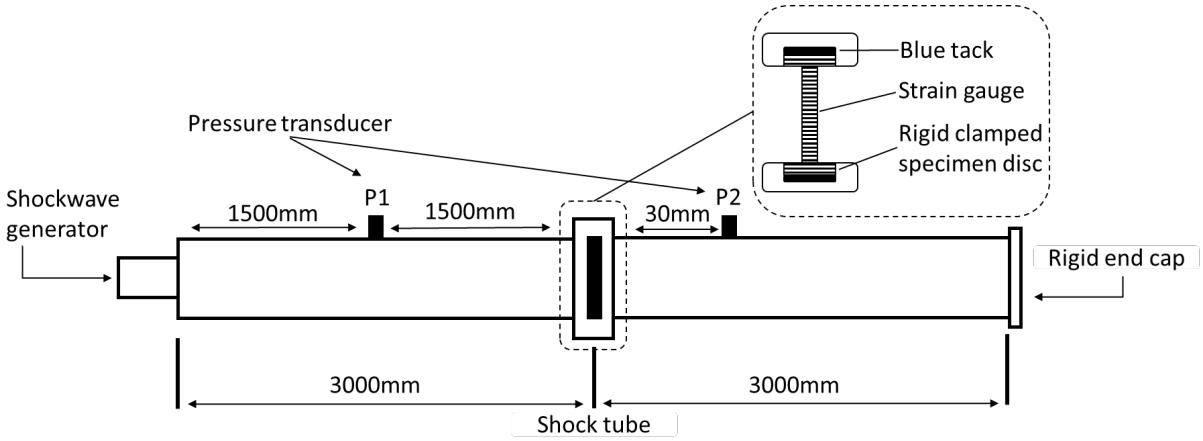

Figure 3-13 Schematic diagram of shock tube system.

a

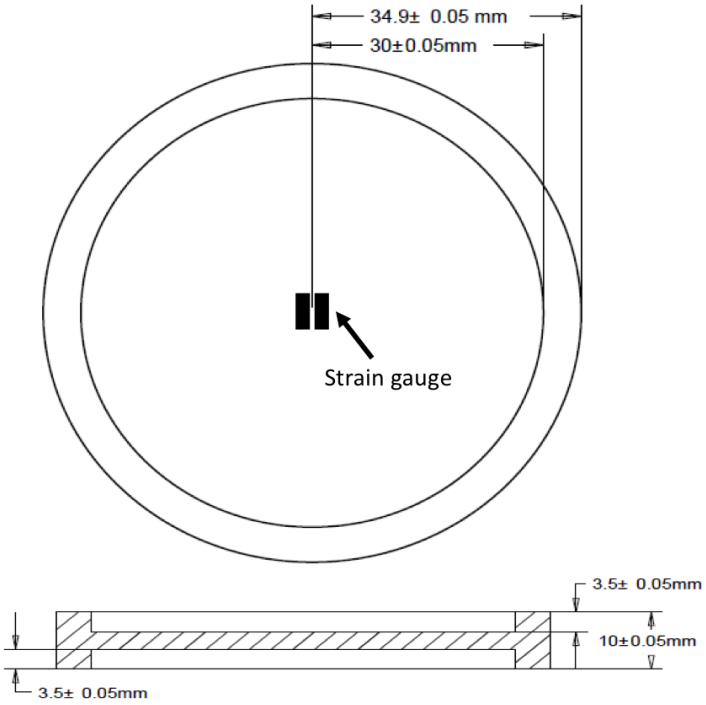

b

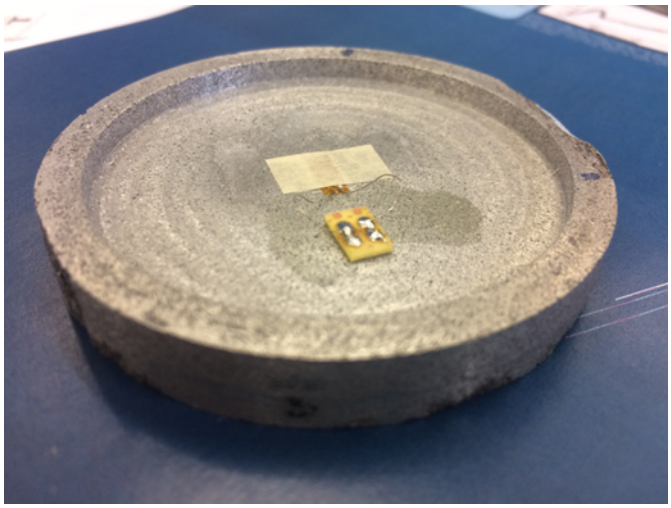

Figure 3-14 (a) Drawing of shock tube test specimen and (b) Photo of test samples.

Figure 3-14 shows the geometry of the syntactic foam test specimen. The machined inner recessed area of the disc is the test area and has the same internal diameter of the shock tube. The thicker outer rim, which is clamped into the connection flange, acts to provide a rigid boundary support. During a test the inner area is fully impinged by the

shockwave which excites a vibrational response that is measured using a single axis centrally mounted strain gauge.

Two piezo-resistive pressure transducers, P1 and P2, are mounted at the predetermined positions along the shock tube. The pressure vs. time history profile of the incident shockwave is measured by P1 as it propagates towards the specimen. After the shockwave impinges onto the specimen disc the flexural displacement of the inner area is measured by the strain gauge. Any transmitted impulse is measured by a second pressure transducer, P2, behind the specimen. These three measurements go to a Fylde amplifier then captured on a TRA800 data capture system (digital transient recorder), and are analysed later to provide information about the energy absorption, transmission and response characteristics of the material under impulsive loading.

3.6.3 Test procedure

Prior to carrying out a test, the shock tube apparatus was fully assembled as described in the previous section. The experimental operation procedures are introduced in detail as below. These include the calibration of the pressure transducers, shockwave test and pressure and strain measurements.

The pressure transducer calibration test was carried out as follows: a compressed air supply with a high-resolution pressure gauge was connected to the shock tube and the system was pressurised statically in steps of 20 PSI (≈ 0.138 MPa) up to 120 PSI (≈ 0.827 MPa). The stable voltage output from the pressure transducer was recorded at each step and compared with the high-resolution pressure gauge to establish a calibration factor. After the calibration test, the air supply was replaced by the

shockwave generator and the performance of each type of commercial blank ammunition was evaluated for shock tube test.

For the actual shockwave tests, a syntactic foam specimen disc was carefully mounted into the holder and all gaps between disc and specimen holder were sealed with a sealing compound (Blue Tack) (see Figure 3-13). The electrical signals from pressure transducers and strain gauge were zeroed and the transient data capture system stabilised prior to firing the generator. After each test, the shockwave generator was disassembled for reloading explosive charges and the shock tube was purged with compressed air to remove combustion gas particulates.

The shockwave and response of the syntactic foam disc under impulsive loading were measured by the pressure transducer P1 and the strain gauge, respectively. Their voltage outputs were converted to pressure and strain, with the former using the calibration factor as described previously and the latter using the following standard Wheatstone bridge conversion:

$$\varepsilon_f = \frac{4 \times Volt_{out}}{BV \times GF} \tag{3-5}$$

where ε_f is strain amplitude, BV is the bridge excitation voltage which is 5 V, GF is the gauge factor which is 2, $Volt_{out}$ is the output voltage which is the measured voltage ($Volt_m$) amplified with a gain of 1000 from the amplifier. Therefore, the equation can also be written as:

$$\varepsilon_f = \frac{4 \times \frac{Volt_m}{1000}}{BV \times GF} \quad (3\text{-}6)$$

3.6.4 Behaviour of impulsive loading

3.6.4.1 Pressure transducer calibration

The pressure transducer produces an electrical output signal measured in voltage (millivolt), so a calibration is required to convert the signal from voltage to pressure. The calibration process measured signals of the pressure transducers under known static pressures. Figure 3-15 plots the measured voltages of both pressure transducers P1 and P2 at a series of actual pressures. It shows that there in a linear relationship between voltage and pressure. Therefore, the measured voltage can be simply converted to pressure by applying the gradient of the line obtained in Figure 3-15 for each pressure transducer.

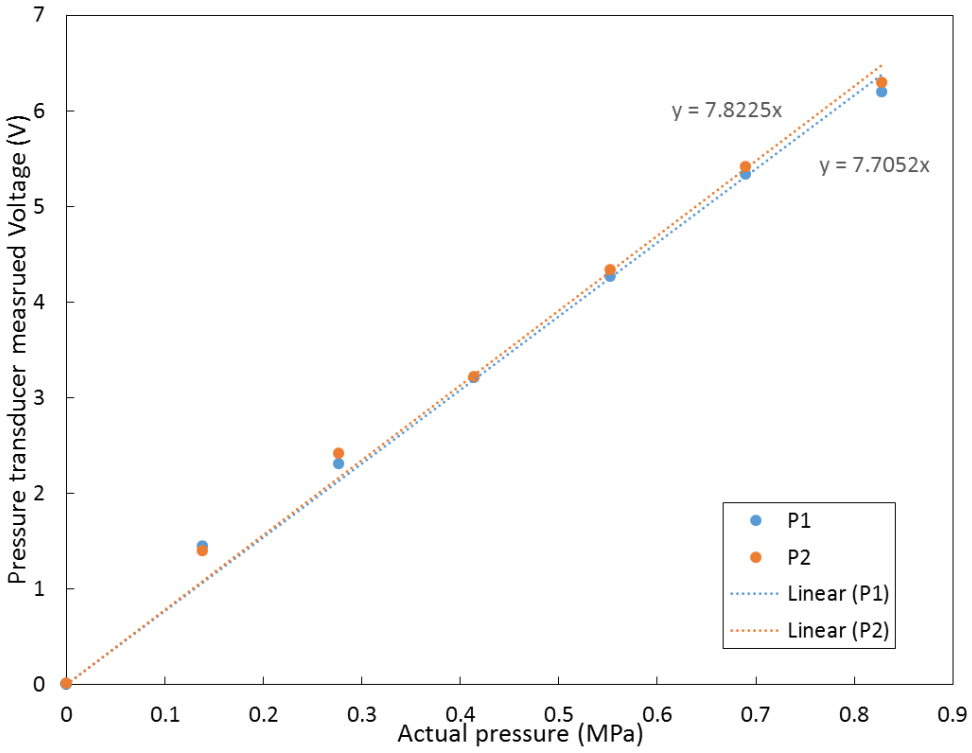

Figure 3-15 Calibration of pressure transducers.

3.6.4.2 Reliability of impulsive loading

Four types of commercial blank ammunition, which contain different amount of dynamite, were used to generate the shockwave in the shock tube. These are shown in Figure 3-16 and are identified as A-6mm, A-0.22L, A-0.22H and A-7mm. The performance and repeatability of each type of ammunition were investigated prior to conducting the actual tests on syntactic foam samples. The pressure pulses generated from at least three consecutive firings of each type of ammunition were measured by the piezoelectric pressure transducer P1.

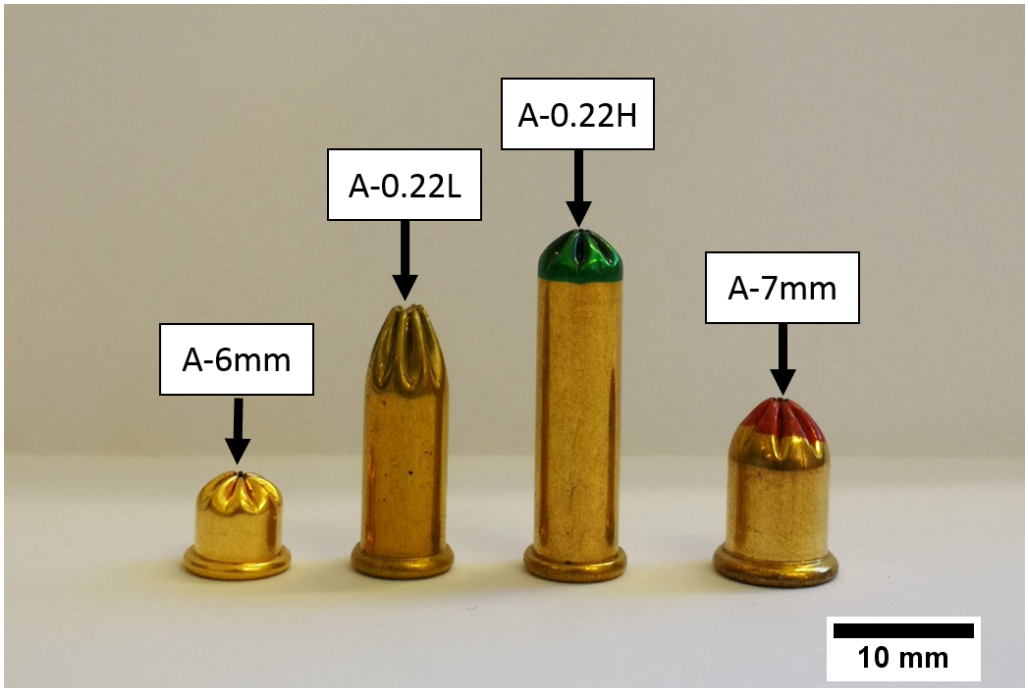

Figure 3-16 Photo of commercial blank ammunitions.

Figure 3-17 shows the individual pressure-time profiles (shockwaves) produced for the four types of ammunition. Although there were noises in the signals, likely due to the vibrations in the tube wall from the explosion, the shockwave produced by each type of ammunition is the typical Friedlander waveform, i.e., a plane wave front with an exponential decay (see 3.6.1). By comparing the shockwaves generated over several firings of each type of ammunition, it can be seen that the generated shockwaves had a good level of repeatability.

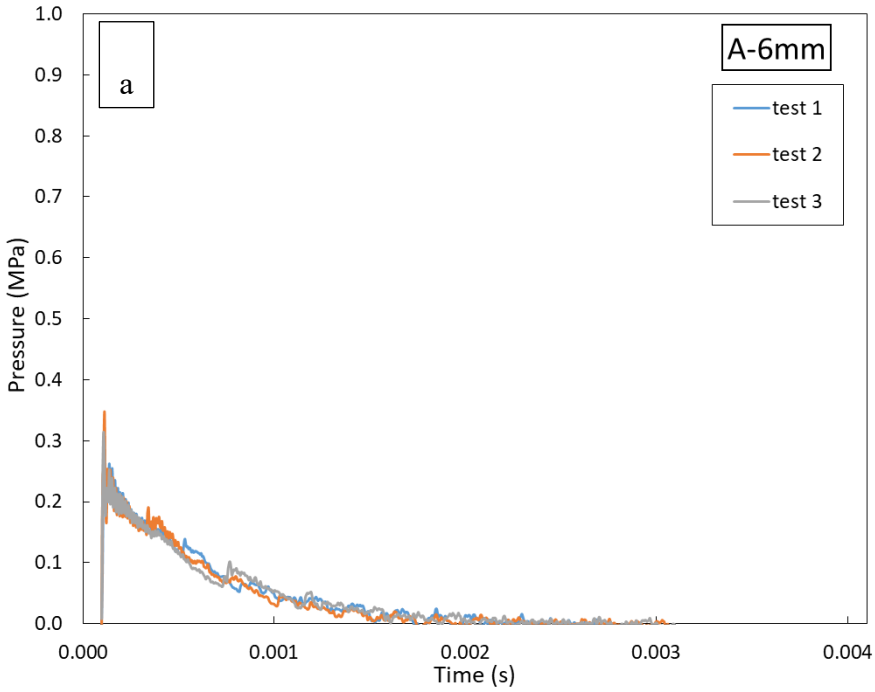
a
A-6mm
test 1
test 2
test 3
Pressure (MPa)
Time (s)
0.0
0.1
0.2
0.3
0.4
0.5
0.6
0.7
0.8
0.9
1.0
0.000
0.001
0.002
0.003
0.004

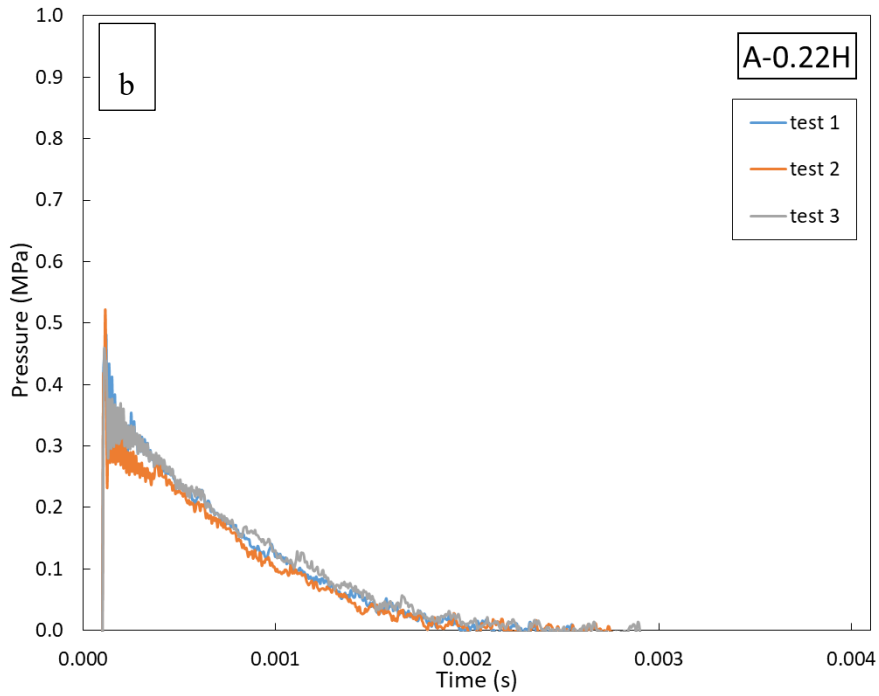
b
A-0.22H
test 1
test 2
test 3
Pressure (MPa)
Time (s)
0.0
0.1
0.2
0.3
0.4
0.5
0.6
0.7
0.8
0.9
1.0
0.000
0.001
0.002
0.003
0.004

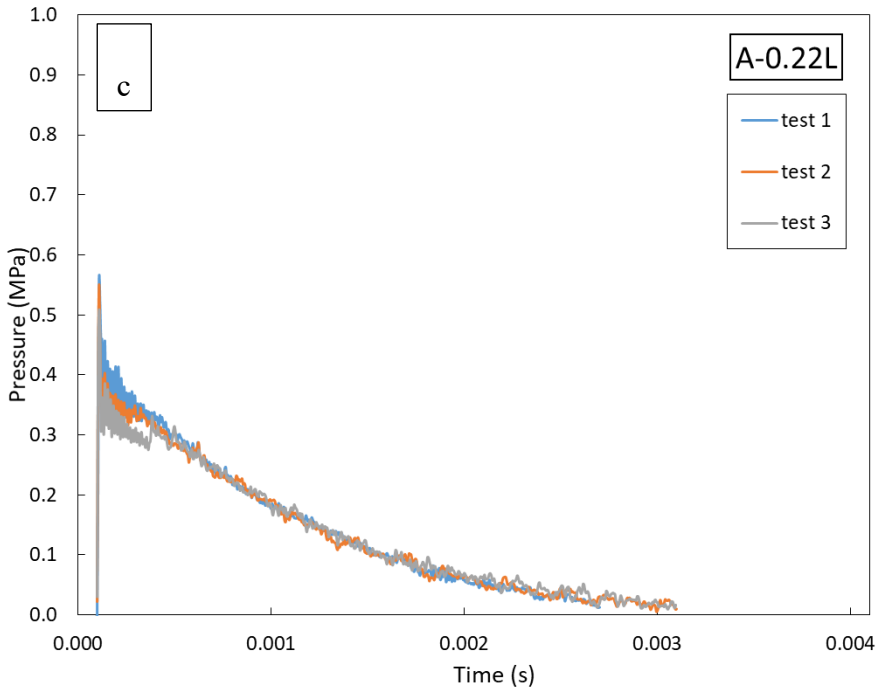

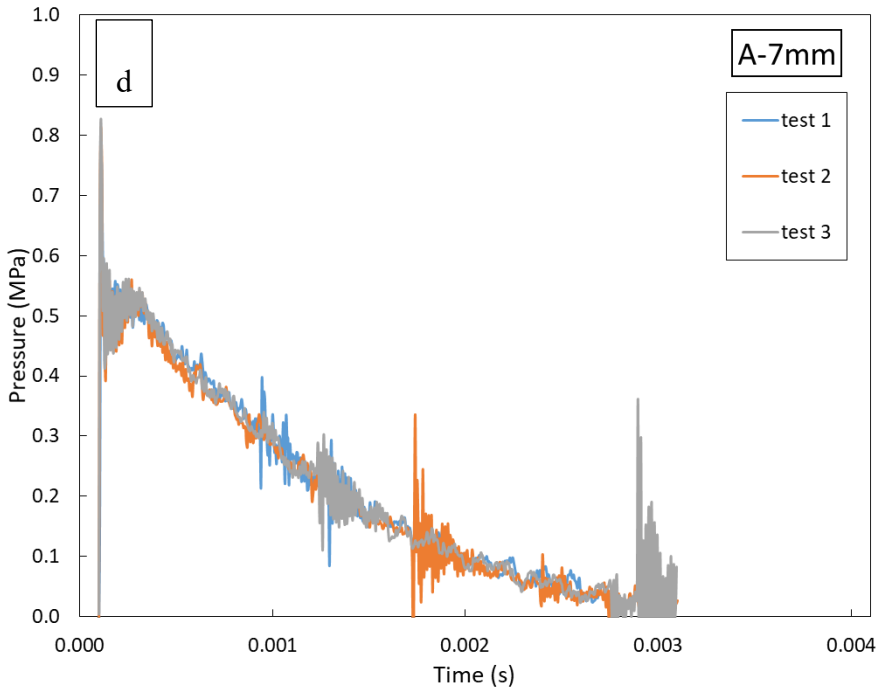

Figure 3-17 Pressure-time signals of shockwave generated by (a) A-6mm, (b) A-0.22H, (c) A-0.22L, and (d) A-7mm

3.6.4.3 Characters of impulsive load

The pressure-time profiles of the shockwaves produced by the four types of ammunition are compared in Figure 3-18. The parameters of these shockwaves such as the positive impulse energy and overpressure, were evaluated. The wave energy was characterised by the positive impulse value which was calculated by equation (3-3). Figure 3-19 shows variation of the positive impulse value with respect to the type of ammunition. It can be concluded that these four types of commercial blank ammunition were able to provide predictable shockwaves of four different energy magnitudes. Moreover, as the distance between the firing point and the pressure transducer P1 is known, the exact speed of shockwave can also be calculated. The shockwave parameters were obtained by averaging the measured values of three shockwaves and these are listed in Table 3-6. The variations in these results are less than 10%.

In the shock tube test, the monomodal syntactic foams were subjected to all the shockwaves with different impulsive loads. The shockwaves were applied to each specimen in an order of low to high impulsive loads, and the tests were repeated three times. The shock tube test of the syntactic foams toughened with Al particles was conducted under the shock wave of ammunition A-7mm.

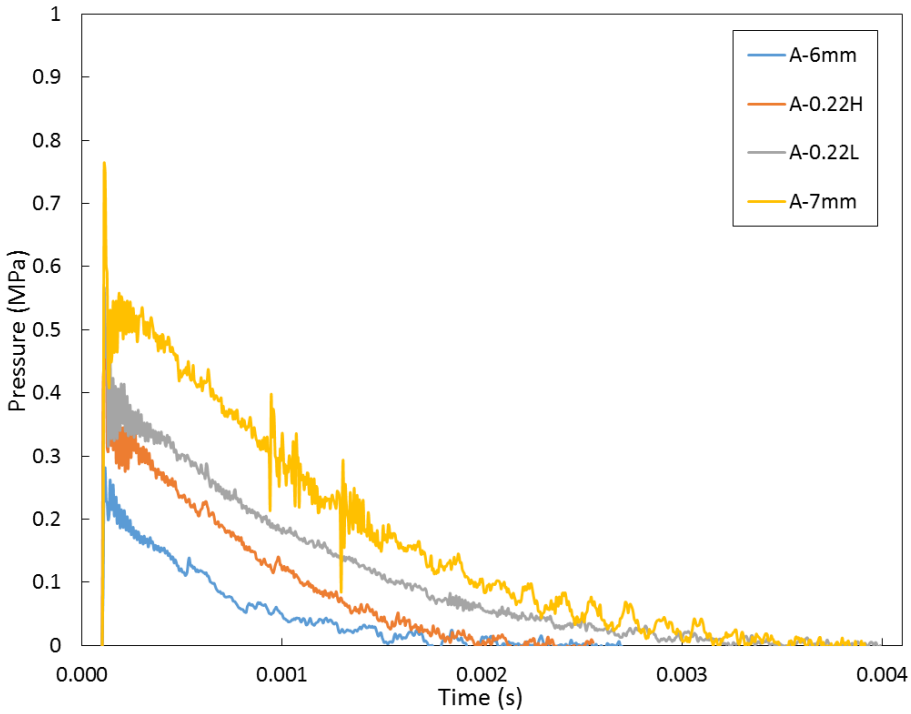

Figure 3-18 Comparison of shockwaves generated by ammunitions.

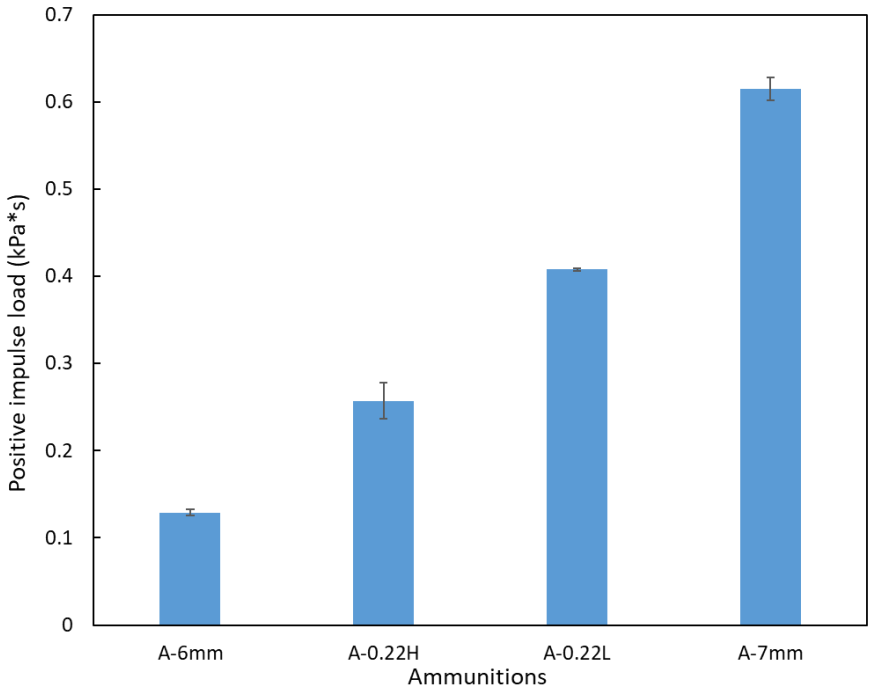

Figure 3-19 Comparison of the positive impulse of each shockwave.

Table 3-6 Specifications of shockwaves generated by the ammunitions

Ammunitions	Over-pressure (MPa)	Average pressure (positive impulse divided by time) (MPa)	Positive pulse duration (ms)	Wave speed (m/s)
A-6mm	0.314±0.033	0.045±0.005	2.87±0.23	371±0.3
A-0.22H	0.486±0.033	0.097±0.009	2.64±0.17	385±2.4
A-0.22L	0.540±0.028	0.102±0.005	4.01±0.21	389±2.8
A-7mm	0.801±0.033	0.161±0.007	3.83±0.09	407±0.3

3.6.4.4 Transmission of shockwave

In the shockwave tests, all shockwaves were successfully captured by the pressure transducer P1. However, the pressure transducer P2 measured no impulsive signals, e.g., as shown in Figure 3-20, which is the measured signal of pressure transducer P2 after the shockwave of ammunition A-7mm was loaded on the syntactic foam specimen. That means there is almost no transmitted signal through the syntactic foam sample. Therefore, it can be confirmed that all the shockwaves used in this experiment did not have enough energy to make penetrable leakages or damages on the syntactic foam specimens. This research mainly investigated on the response of the syntactic foam samples excited by the shockwaves.

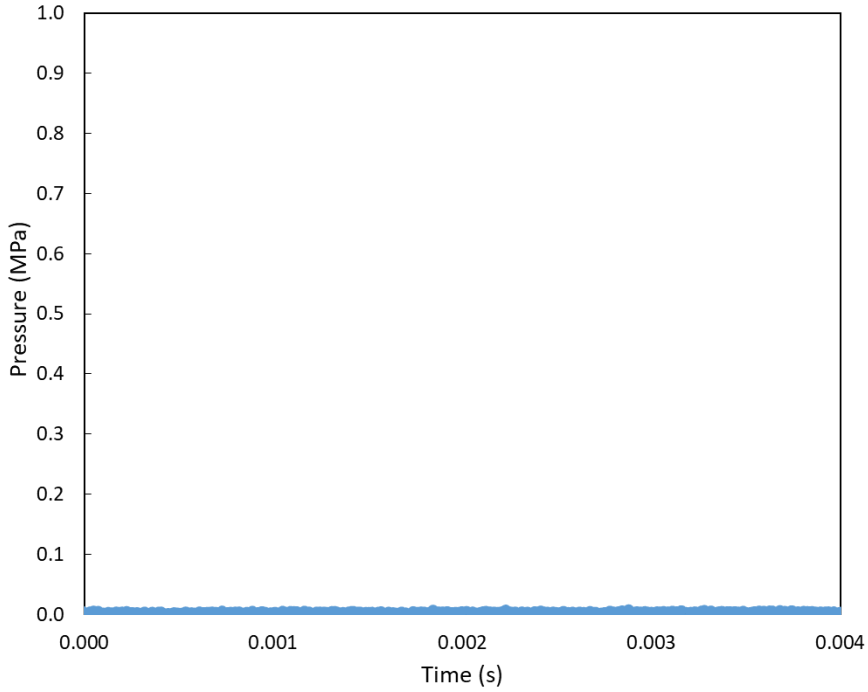

Figure 3-20 Signal of pressure transducer P2 after shockwave of ammunition A-7mm loaded on a syntactic foam sample.

3.7 Calculation of damping capacity

3.7.1 Dissipated energy and specific damping capacity in cyclic compression

The hysteretic dissipated energy and specific damping capacity of the syntactic foams were calculated from the hysteresis loops formed by the unloading-loading cycles in cyclic compression. The sequence of the unloading-loading path in a hysteresis loop in the stress-strain curve is illustrated in Figure 3-21, where the arrows pointing upwards and downwards represent loading and unloading respectively. From the previous cycle (Point A), the new cycle starts from a predetermined strain of point B, unloads along the path B-C to point D where the stress reaches zero, and reloads along the path D-E-B. The hysteresis loop is captured by the unloading curve B-C-D and the reloading curve D-E-B.

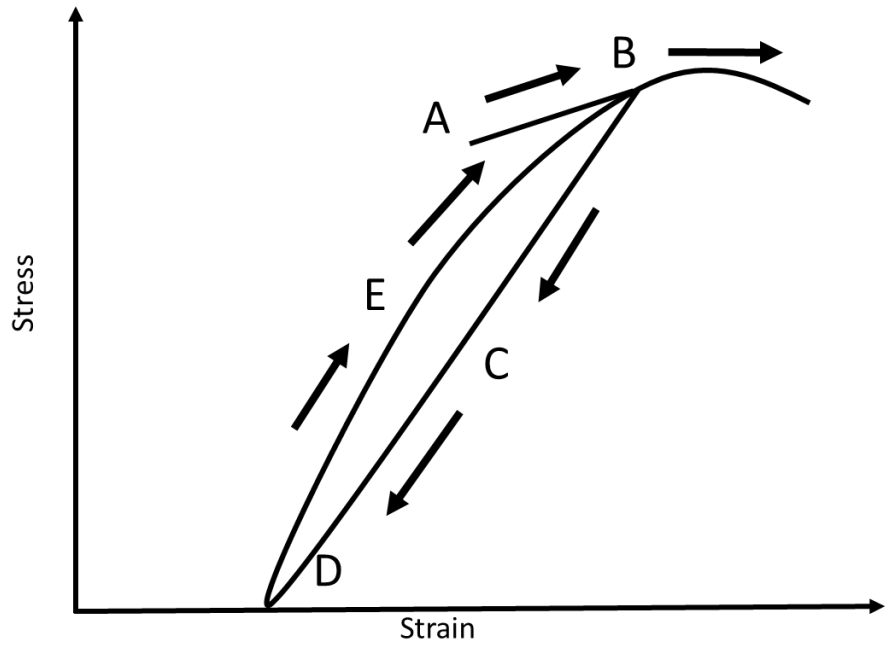

Figure 3-21 Schematic of an unloading-loading cycle.

The area enclosed by the hysteresis loop represents the energy absorbed or dissipated, which is also equal to the work done against the internal friction or other dissipation mechanisms in the syntactic foam. The hysteresis loop also involves an elastic deformation and a significant strain energy contribution (elastic energy). Figure 3-22 is a schematic diagram that clearly defines the dissipated and elastic energy of the hysteresis loop in the stress-strain curve. The specific dissipated energy (SDE) (W_D) corresponds to the area enclosed by the hysteresis loop; the area under the lower path (unloading part) of the hysteresis curve represents the specific elastic energy stored (W_E).

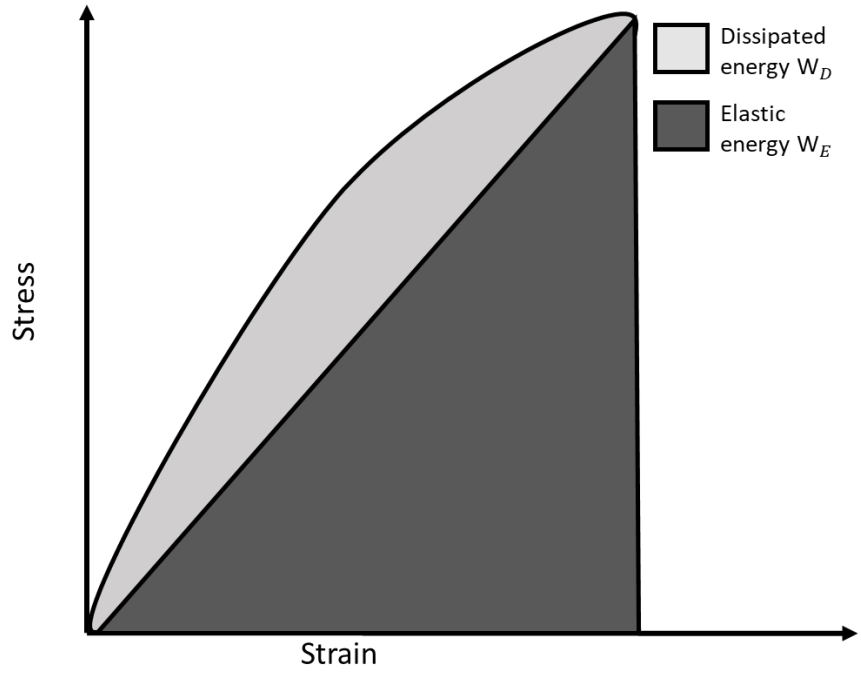

Figure 3-22 Schematic of potential energy and dissipated energy.

Both the specific elastic energy (W_E) and dissipated energy (W_D) can be calculated by integrating the stress over the corresponding strain in equations (3-7) and (3-8).

$$W_E = \int_0^{\sigma_{unloading}} \varepsilon d\sigma \tag{3-7}$$

$$W_D = \int_0^{\sigma_{reloading}} \varepsilon d\sigma - \int_0^{\sigma_{unloading}} \varepsilon d\sigma \tag{3-8}$$

This hysteresis loss can also be defined as a damping property of the material. The damping capacity of the material can be characterized by the specific damping capacity (SDC), which is the ratio of the energy dissipated in a cycle (W_D) to the elastic energy stored per cycle (W_E). Therefore, specific damping capacity (ψ) is written as:

$$\psi = \frac{W_D}{W_E} \tag{3-9}$$

3.7.2 Loss factor in free vibration

The damping properties of the syntactic foams were determined from the measured strain response of the syntactic foams in the shockwave tests, where the shockwave excites an oscillation on the syntactic foam specimen. This oscillation belongs to a

damped free vibration because the shockwave acts on the syntactic foam specimen transiently and the specimen does not have a subsequent disturbance.

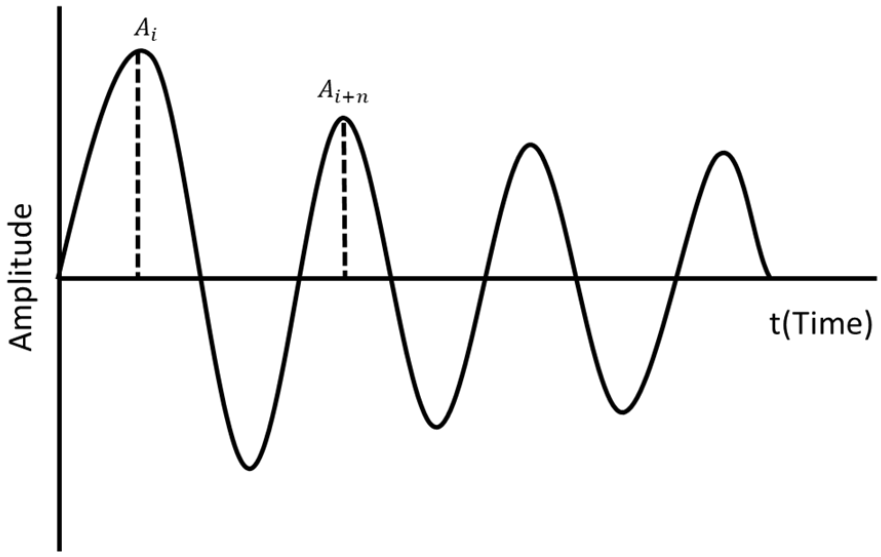

Figure 3-23 Schematic of the transient response of a classically under-damped system.

Figure 3-23 is a schematic diagram that presents a transient response of a classically under-damped system. The decay of amplitude of the oscillation indicates the energy loss in the syntactic foam. The damping property of the syntactic foam can be evaluated by the logarithmic decrement in the amplitude of the damped free vibration. The logarithmic decrement is described as the natural logarithm of the ratio of amplitudes of successive vibrations (Chawla 2012; Magalas 2006; Venkatanarayanan & Stanley 2012):

$$\delta = \frac{1}{n} In \frac{A_i}{A_{i+n}} \tag{3-10}$$

where n is the number of oscillations to decay from amplitude A_i to A_{i+n}.

In order to compare with the damping characteristics of the material measured by other methods, the logarithmic decrement is commonly converted to the loss factor (η) which is the ratio of the logarithmic decrement to π:

$$\eta = \frac{\delta}{\pi} \tag{3-11}$$

Chapter 4 RESULTS AND DISCUSSION

4.1 Structural properties of syntactic foams

The defects and microstructure of the syntactic foam samples are the fundamental factors which affect the investigation of the syntactic foam mechanical properties. In this section, the defects that can occur in syntactic foam samples, and affect structural properties, are first presented and discussed. The microstructure of the syntactic foam samples is then introduced through the micrographs of the polished cross-sections. The measured density of the syntactic foam samples is presented.

4.1.1 Defects formed during infiltration

During the infiltration casting process, some defects may form in the syntactic foam samples. These defects can directly affect the microstructure and mechanical properties of the syntactic foams. In fact, two typical defects occurred in the syntactic foam samples manufactured by infiltration casting: broken CM particles filled with Al and CM particle bed not well infiltrated by Al, as shown in Figures 4-1 and 4-2, respectively.

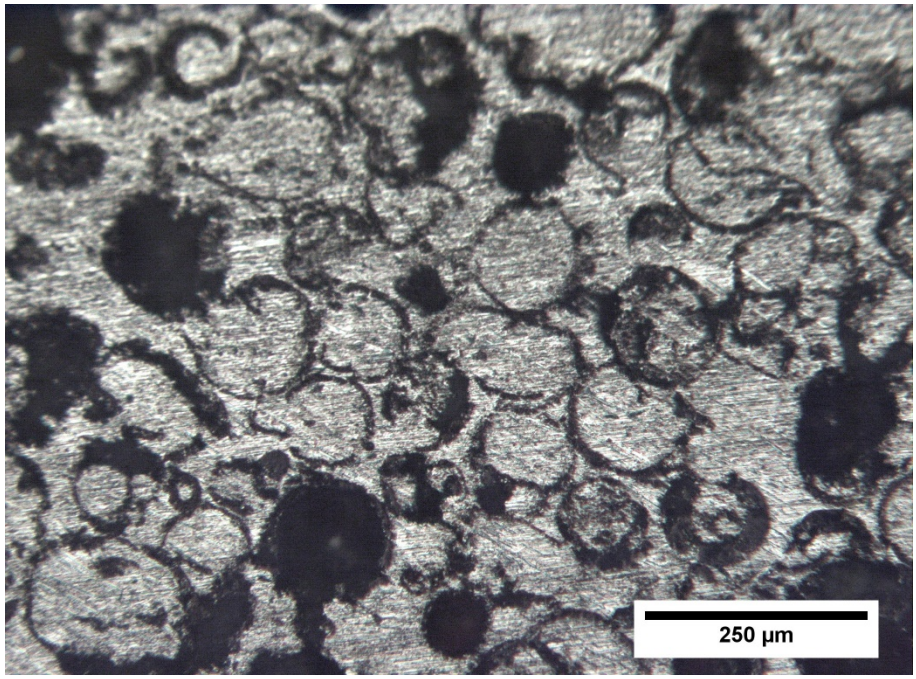

Figure 4-1 Cross-section of a syntactic foam sample showing broken CM particles infiltrated with Al.

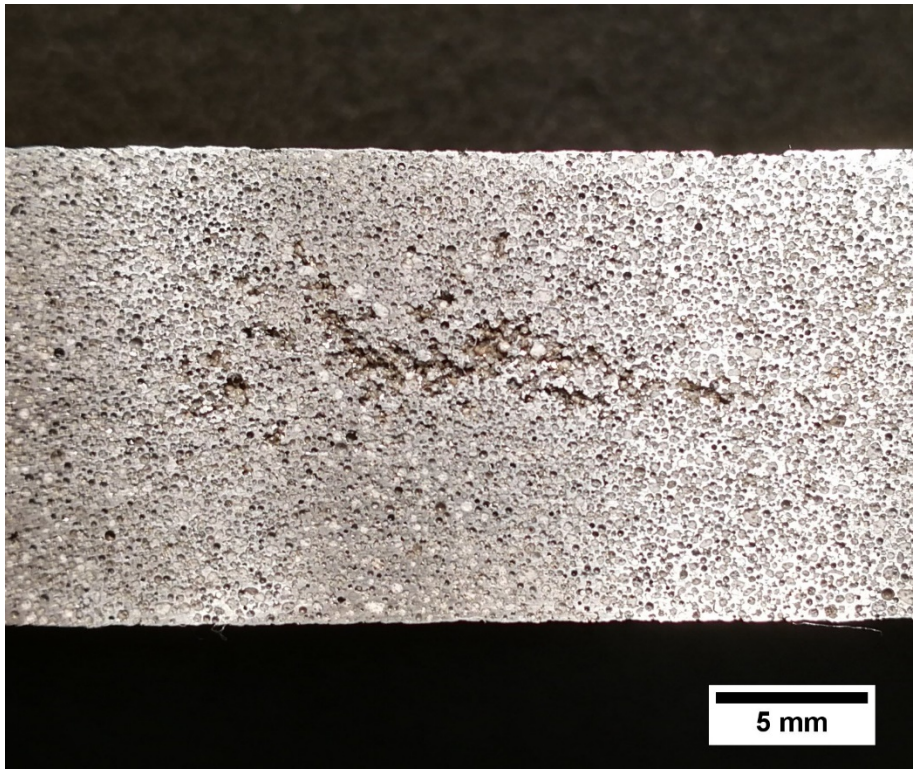

Figure 4-2 Cross-section of a syntactic foam sample showing a defective core not well infiltrated by Al.

4-1 shows a common type of defects in a syntactic foam sample, where Al infiltrated into a large number of broken CM particles. In addition to defective CM particles existing before processing, some defects are formed during infiltration when the applied infiltration pressure is higher than the strength of these weak CM particles, leading to damaged CM particles. Ideally, the infiltration pressure should be high enough to press the molten Al into the interstices within the packed bed of CM particles without causing any damages. Practically, however, the infiltration pressure is hard to be controlled precisely in our experimental conditions. Continuous compressing of the molten Al after the interstices within the packed bed of CM particles are fully infiltrated can result in the CM particles being crushed.

4-2 shows another typical type of defects, where the core region of the syntactic foam sample is not fully infiltrated with molten Al. It is formed due to the particular flow routes of molten Al during infiltration casting. Figure 4-3 schematically illustrates the representative flow routes of the molten Al infiltrating into the interstices within the packed bed of CM particles. With a low resistance near the inner surface of the steel tube, the molten Al preferentially goes through the packed bed of CM particles through these routes and, once reaching at the bottom, flows back up through the interior of the packed bed of CM particles. If the molten Al is solidified in the bottom region of the mould due to poor thermal insulation at the mould/press interface, some air can be trapped in the core region of the packed bed, resulting in no infiltration by the molten Al.

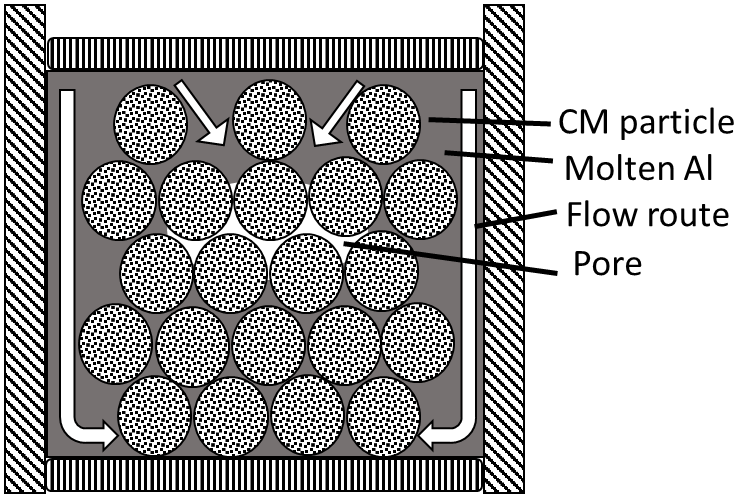

Figure 4-3 Schematic diagram showing the flow routes of the molten Al in infiltration process.

Both types of defects can have detrimental influences on the structure and properties. They also affect the density of the syntactic foam. Broken CMs result in an increase in Al volume percentage and thus a high density of the syntactic foam, as the broken CM particles are filled with Al. Trapped air in the core region leads to a low density of the syntactic foam. Hence, applying and maintaining a proper infiltration pressure and the temperature is extremely important during the infiltration process to eliminate the casting defects in the syntactic foams.

In this research, the preparation process was modified in order to minimise the amount of defects in the syntactic foams. Controlling the position of the punch head was found to be more effective than controlling the infiltration pressure to avoid over compression during infiltration casting. In the new procedure, a line was drawn on the punch head corresponding to the height of the Al block used. Compression was stopped immediately when the punch head reached this line to ensure that the molten Al fully infiltrated into the interstices between the CM particles without damaging the CM particles. All the syntactic foam samples used in this research were machined or cut to remove the parts that were not well infiltrated.

4.1.2 Microstructure

4.1.2.1 Monomodal syntactic foam

Figures 4-4 and 4-5 show the microscopic structures of the three types of monomodal syntactic foams (M1, M2, and M3) under different magnifications. All types of the monomodal syntactic foams have a homogeneous structure where the CM particles distributed randomly in the Al 6082 matrix. 4-5 (d) indicates a good bond at the matrix-CM particle interface.

A significant microstructural difference in the three types of syntactic foam is the inner structures of the CM particles as exhibited in 4-4. Syntactic foam M3 contains a much higher proportion of porous CM particles than syntactic foams M1 and M2. The proportions of porous and hollow CM particles in the syntactic foams were evaluated quantitatively by examining 1000 CM particles in the optical micrographs of each type of syntactic foam. The percentages of the porous ceramic microspheres in the syntactic foams M1, M2 and M3 were found to be 0.5%, 19.7%, and 77.2%, respectively.

A small number of CM particles in the syntactic foam samples were infiltrated with molten Al, as indicated by arrows in 4-5 (b) as an example. By examining 1000 CM particles in the cross-sections of each type of syntactic foam, the percentages of the infiltrated CM particles in the syntactic foams M1, M2 and M3 were determined to be 2.6%, 5.5% and 7.3% respectively. This type of defects seems to occur more frequently in porous CM particles than in hollow CM particles.

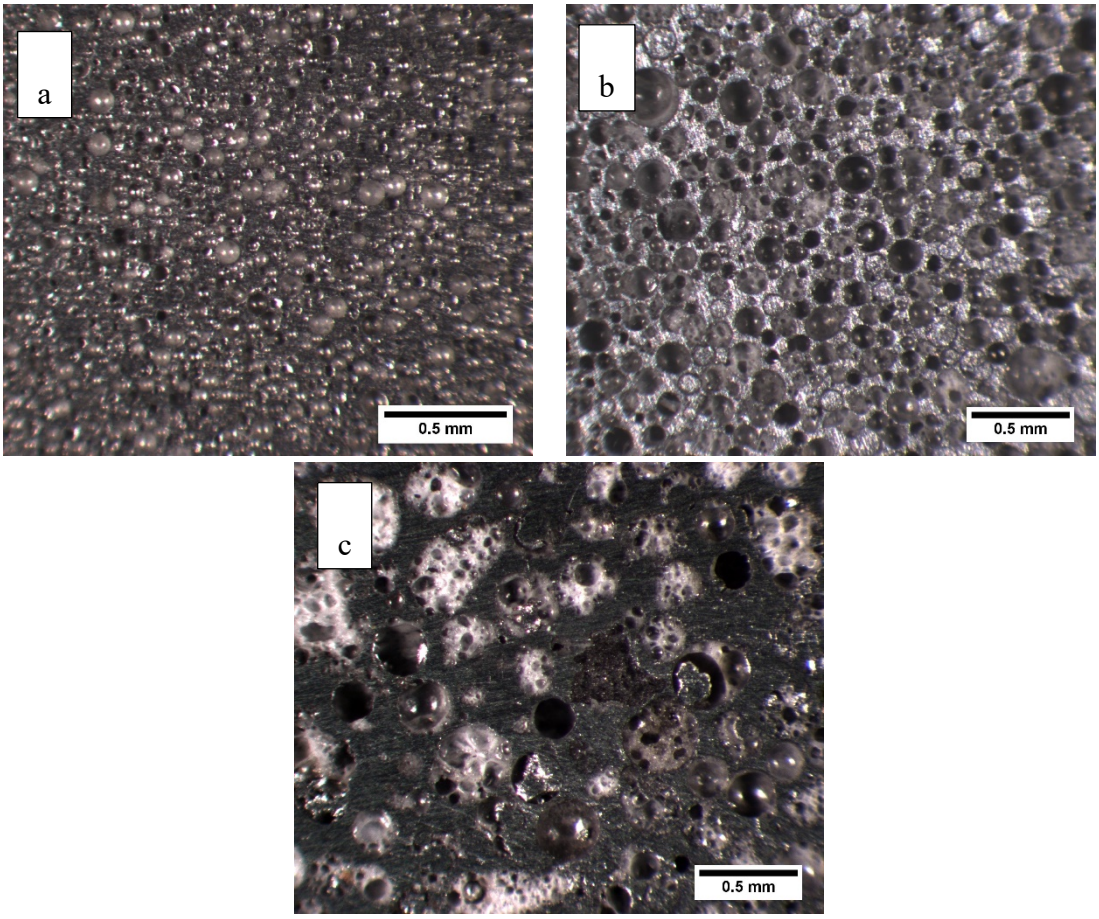

Figure 4-4 Low magnification micrographs of the cross-sections of the monomodal syntactic foams: (a) M1, (b) M2 and (c) M3.

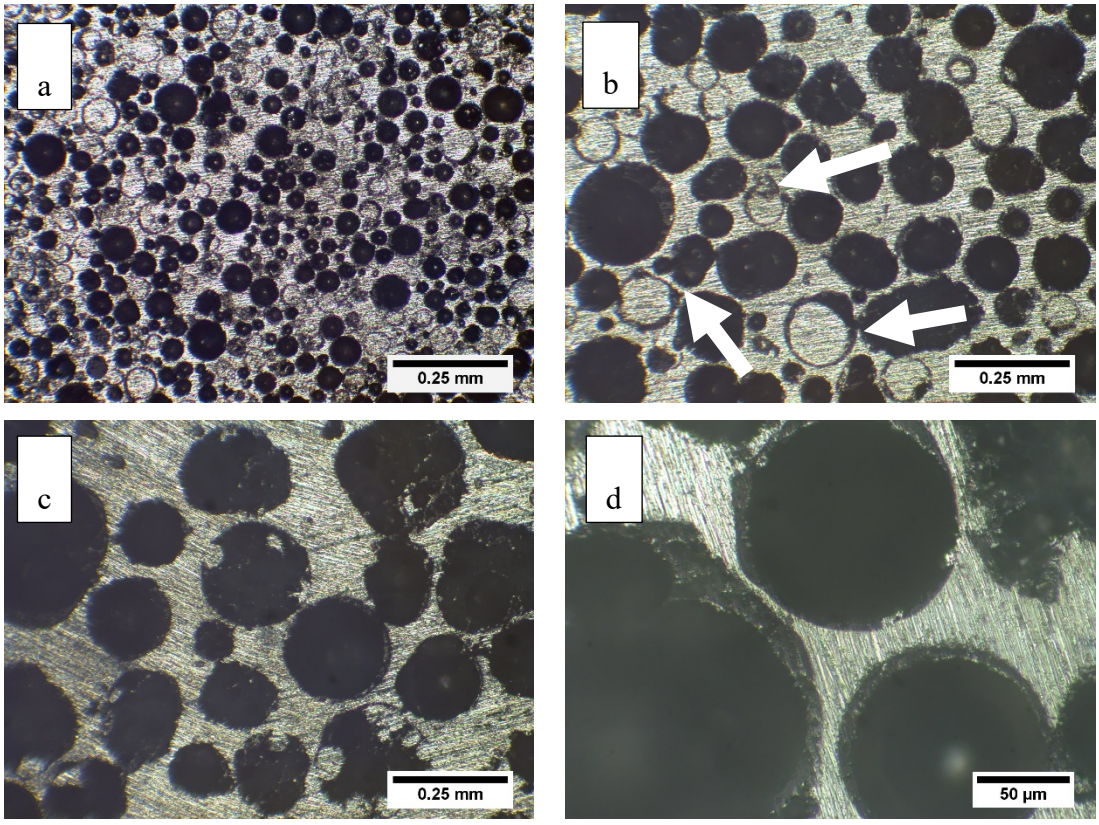

Figure 4-5 Higher magnification optical micrographs of the cross-sections of the monomodal syntactic foams: (a) M1, (b) M2 and (c) M3. (d) A higher magnification micrograph showing the interface between the matrix and the CM particles.

4.1.2.2 Syntactic foams toughened with Al particles

Figure 4-6 shows the microstructure of the syntactic foams manufactured by infiltrating molten Al 6082 into the mixture of CM and Al particles. In all the syntactic foams toughened with Al particles (T1~T4), the Al particles are randomly distributed in the syntactic foam, indicating that the Al particles do not move or diffuse during the infiltration casting process. Two factors may have ensured that the Al particles stay in fixed locations in the mixture during infiltration. First, due to the poor thermal conductivity of the surrounding CM particles, the Al particles are mainly either in the solid or in a semisolid state in the heating process. Second, even though the Al particles

are in the molten state, the liquid Al may still be wrapped up by a solid alumina shell, which may not rupture easily during the compressing process. In either case, the Al particles cannot flow into the interstices between the CM particles during the infiltration process. However, the Al particles are intimately fused with the infiltrating molten Al, as shown in Figure 4-7. Figure 4-7 also shows the alumina skin at the interface between an Al particle and the Al matrix.

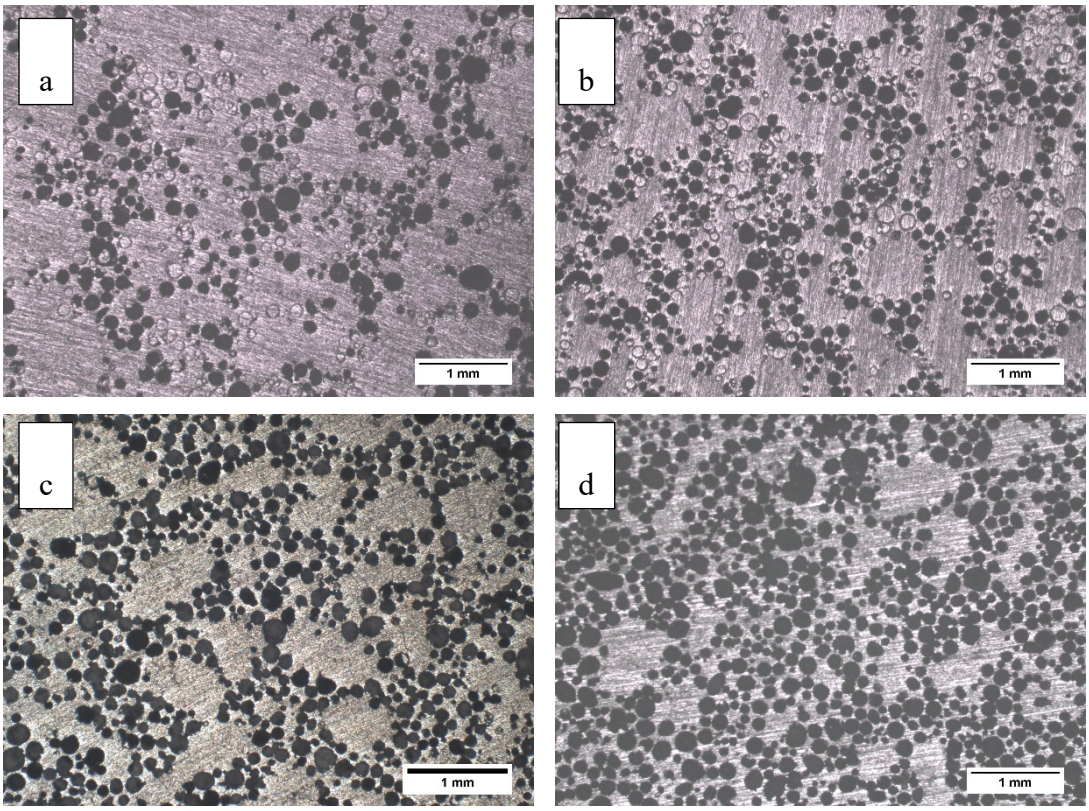

Figure 4-6 Polished cross-sections of the syntactic foams toughened with additional Al particles: (a) T1, (b) T2, (c) T3 and (d) T4.

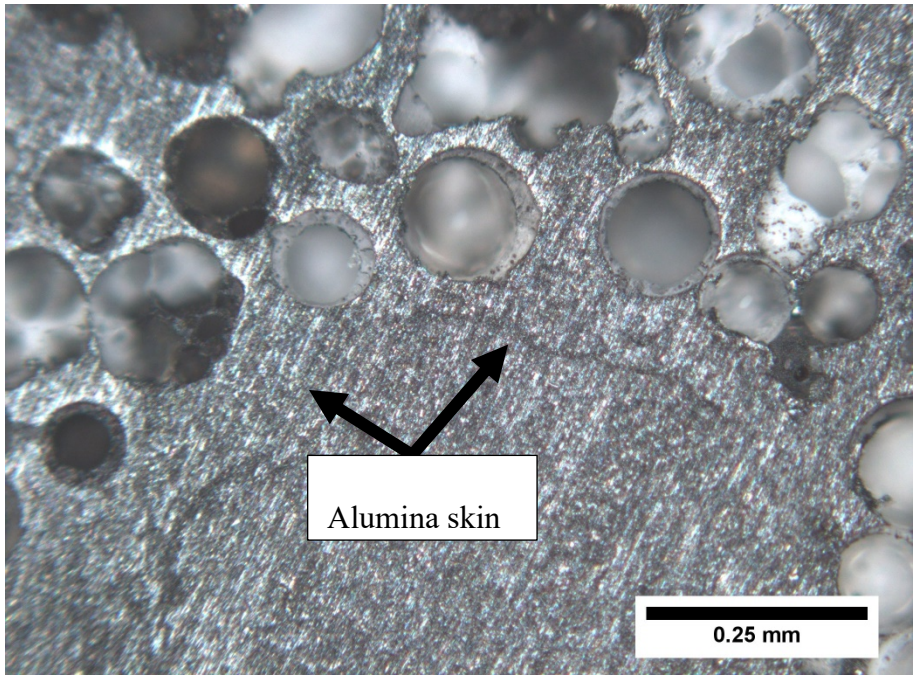

Figure 4-7 Polished cross-section of the syntactic foam T1 showing the interface between an Al particle and the Al/CM region.

4.1.2.3 Bimodal syntactic foams

Figure 4-8 shows the microstructure of the bimodal syntactic foams (B1, B2 and B3) whose CM particles consist of large and small size groups with different ratios. Overall, the CM particles are randomly distributed in all bimodal syntactic foams, which have a different microstructure from the monomodal syntactic foams.

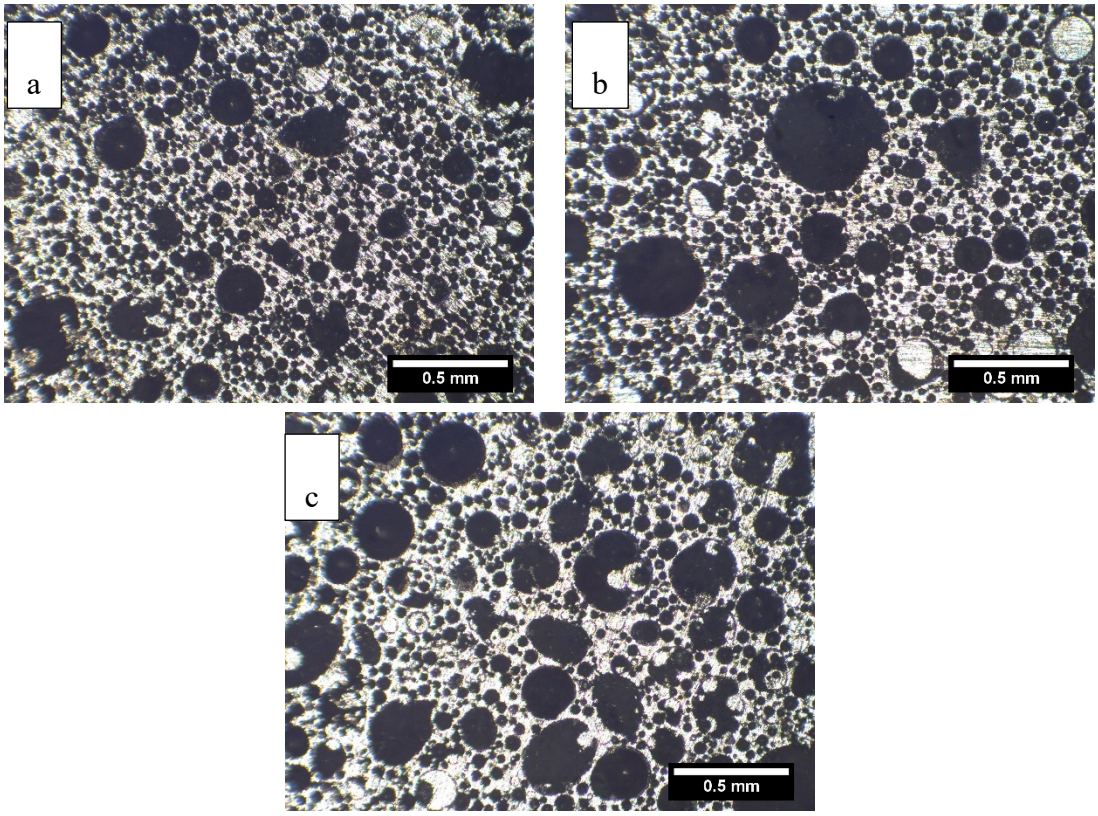

Figure 4-8 Polished cross-sections of the bimodal syntactic foams: (a) B1, (b) B2 and (c) B3.

The microstructure of the monomodal syntactic foams fabricated with either small or large size groups of CM particles (Figure 4-5) is essentially the same but in different scales. The network structure of the Al matrix in the syntactic foam M1 is thin due to the narrow interstices of the small CM particles. Likewise, the wide interspaces between the large CM particles make the syntactic foam M3 have a thick network structure of Al matrix. The bimodal syntactic foams, however, can be viewed as a combination of the syntactic foams M1 and M3. The thick network of the Al matrix in M3 is replaced with the M1. The network of the Al matrix in the bimodal syntactic foams becomes thin.

In the syntactic foams B1 and B2 (Figure 4-8 (a) and (b)), whose proportions of small CM particles are 70% and 50% respectively, the small CM particles are distributed not

only in the interstices between the neighbouring large CM particles but also in the wide regions further from the sparsely populated large CM particles. For syntactic foam B3 (Figure 4-8 (c)), which contains a relatively low volume percentage (30%) of small CM particles, the small CM particles are distributed nearly close-packed in the interstices between the large CM particles. The network structure of the Al matrix becomes fine as the wide interstices, which are used to be occupied by pure Al matrix, are partly replaced by the small CM particles.

4.1.3 Density

4.1.3.1 Monomodal syntactic foam

Figure 4-9 shows the densities of the monomodal syntactic foams M1, M2, and M3. The density of each type of monomodal syntactic foam was measured by the Archimedes method and obtained by averaging the measured values of four specimens. The variations among each set of four specimens are less than 4%.

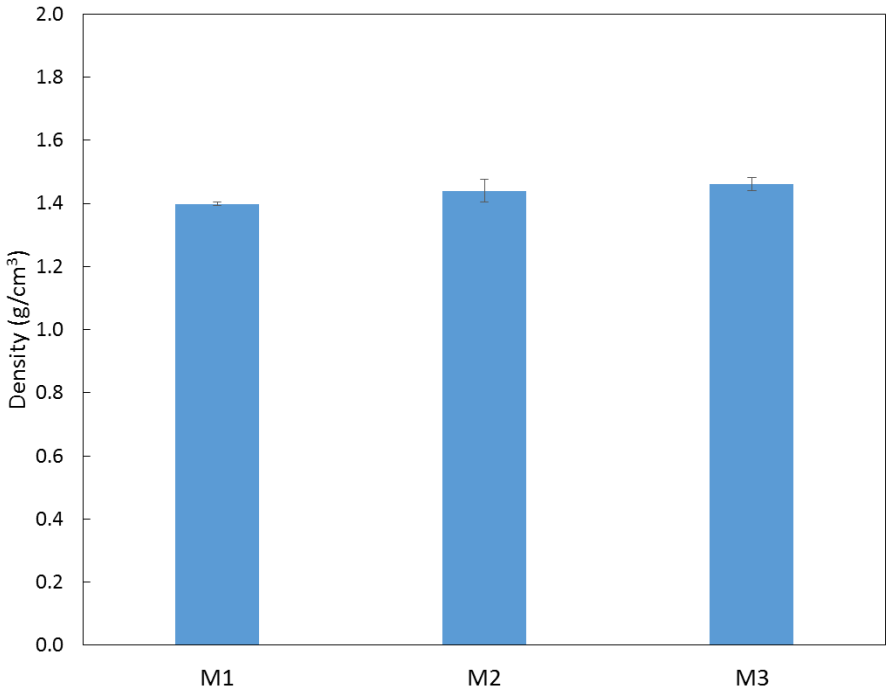

Figure 4-9 Densities of monomodal syntactic foams.

The results show that the measured densities of the syntactic foams are in a narrow range of 1.40~1.43 g/cm^3, because the same volume percentage of CM particles was used in the fabrication of all the monomodal syntactic foams. However, all the monomodal syntactic foams have a density slightly higher than the theoretical value of 1.38 g/cm^3, calculated based on a randomly packed spherical powder with approximately 63% of the total volume (Hartmann et al. 1999a). The difference

between the measured and theoretical density values is mainly due to some CM particles being infiltrated with molten Al. The variations in the density of the syntactic foams result from the different proportions of infiltrated CM particles in these syntactic foams. The syntactic foam M3 fabricated using the large of CM powder has the highest density. This is because the large of CM powder contains mainly porous particles, which have thin surface membranes and therefore are more apt to break during delivery, packing and melting infiltration, compared with the other CM powders.

Although the manufacturing process for the Al/CM syntactic foams in this study used the same raw materials, facilities, and infiltration procedures as in two previous studies, the density of the Al/CM syntactic foam samples in the present study is more consistent. The Al/CM syntactic foams made by Zhang and Zhao (2007), and Tao and Zhao (2012) have a large variation in density between 1.4~1.8 g/cm^3, which was caused by poor control over the compressing pressure as discussed in 4.1.1. Orbulov and Ginsztler (2012) also fabricated Al/CM syntactic foams by the infiltration process with a controllable pressure under a vacuum condition. The density of their syntactic foams is comparable to ours. It confirms that using the modified infiltration process can reduce removing defects in the Al/CM syntactic foams.

4.1.3.2 Syntactic foams toughened with Al particles

Table 4-1 compares the theoretical and measured values of the density of syntactic foams T1, T2, T3, and T4. The measured densities of all the syntactic foams are slightly less than the theoretical values estimated from the designed proportions of the CM particles and Al. Reducing CM volume percentage or adding Al particles in the syntactic foam makes its density higher than the monomodal syntactic foam embedded with the same of CM powder.

The densities of these syntactic foams toughened with Al particles are comparable to but slightly higher than those reported in a previous study (Tao & Zhao 2009). The syntactic foam samples used in the present study were fabricated by the modified infiltration process which reduced defects in the Al/CM syntactic foam and resulted in more representative results. The study further confirms that different densities of metal matrix syntactic foams can be achieved in infiltration casting by embedding additional metal particles in the syntactic foams.

Table 4-1 Theoretical and measured density values of syntactic foams toughened with Al particles.

Sample ID	T1	T2	T3	T4
Theoretical density (g/cm^3)	2.29	2.09	1.89	1.68
Measured density (g/cm^3)	2.15±0.03	1.96±0.01	1.85±0.01	1.58±0.06

4.1.3.3 Bimodal syntactic foams

Figure 4-10 shows the measured densities of syntactic foams B1, B2, and B3, which are 1.43 g/cm^3, 1.36 g/cm^3, and 1.29 g/cm^3, respectively. Overall, all the bimodal syntactic foams are lighter than the monomodal syntactic foams (M1~M3). The densities vary among the three bimodal syntactic foams B1, B2, and B3, because the density of the syntactic foam depends on the volume percentage of the CM particles which in turn is dependent upon the proportions of the small and large CM powders in the bimodal syntactic foams. The CM volume percentage increases when the proportion of the small CM particles is reduced from 70% (B1) to 50% (B2), and then to 30% (B3).

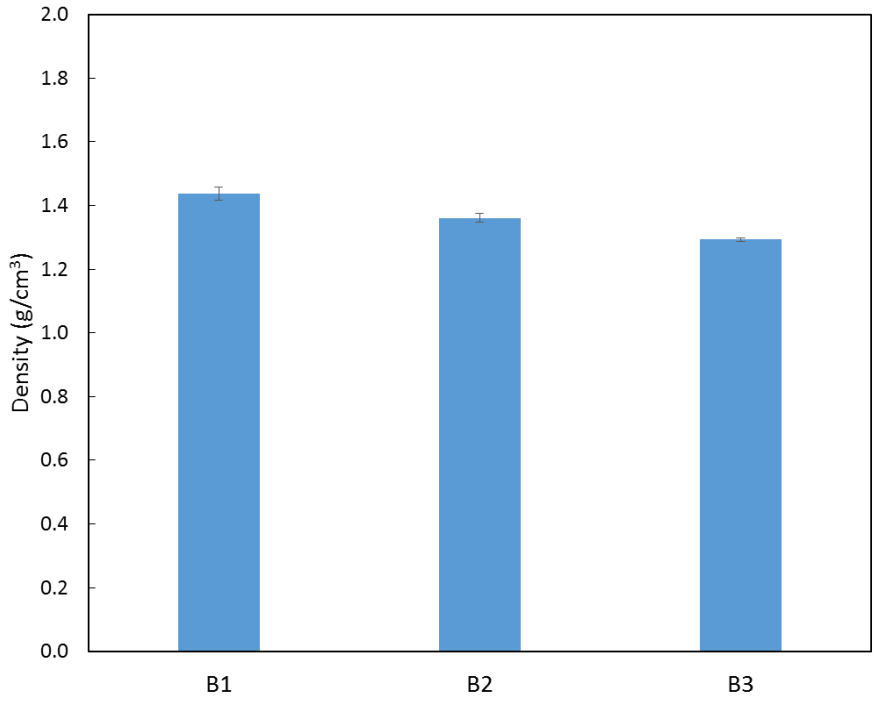

Figure 4-10 Densities of bimodal syntactic foams.

Figure 4-11 shows a schematic diagrams of representative arrangements of the small and large CM particles which can explain the influence of bimodal structure on the

density of the syntactic foam (Tao et al. 2009). The lower density of a bimodal syntactic foam is due to the fact that the overall CM volume percentage is increased by adding small CM particles, which can be accommodated in the interstices between the large CM particles, as shown in Figure 4-11 (a). To increase the CM volume percentage substantially, however, the amount of small CM particles in the mixture should be considerably less than the amount of large CM particles. Otherwise, the small CM particles will separate the large CM particles apart and regions of randomly packed small CM particles are formed (Figure 4-11 (b)). The resultant structure is almost equivalent to the monomodal structure, which results in the bimodal syntactic foam having a density comparable to the monomodal syntactic foam.

The optimum proportions of the small and large CM particles for the highest porosity in the bimodal syntactic foam can be evaluated from a geometrical consideration. For a randomly packed spherical powder, the highest CM particle volume percentage in a bimodal syntactic foam is obtained when the large CM particles occupy approximately 2/3 of the volume of syntactic foam while the small CM particles occupy 2/3 of the remaining 1/3 of the volume of the syntactic foam, i.e., 2/9. The ratio between the small and the large CM particles is therefore 1:3.

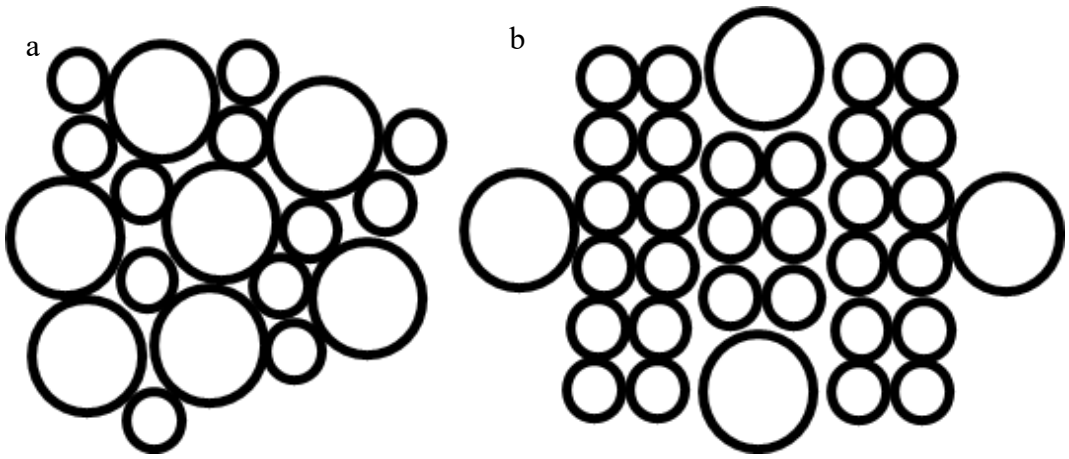

Figure 4-11 Schematic arrangements of bimodal CM particles with (a) less small CMs and (b) more small CMs.

All the bimodal syntactic foams B1, B2, and B3 in the present study have higher densities than those reported in the previous study (Tao et al. 2009). This is because the modified infiltration process reduced the defects in the Al/CM syntactic foams.

4.1.4 Summary

The defects in the syntactic foams are broken CM particles filled with Al and CM particle bed not well infiltrated by Al. These manufacturing defects of syntactic foams can be minimised by modifying the infiltration casting process. The microstructure features of three types of syntactic foam foams, i.e., monomodal, toughened with Al particles, and bimodal, were studied and all showed a good bond at the Al matrix-CM particles interface. All the monomodal syntactic foams have a nearly fixed density. The syntactic foams toughened with Al particle result in a higher density. The bimodal syntactic foams have lower densities than the monomodal syntactic foams.

4.2 Static compressive and impact behaviour

4.2.1 Compressive behaviour of monomodal syntactic foams

4.2.1.1 Non-heat treated syntactic foam

Figure 4-12 shows the representative quasi-static compressive stress-strain curves of the non-heat treated monomodal syntactic foams M1, M2 and M3. Although the stress-strain curves of the syntactic foams present different characteristics, such as stress level, they have qualitatively a similar behaviour to the cellular solids and exhibit three typical regions, namely linear elastic region, plateau region and densification region. Simply put, each curve initially increases linearly in the elastic region until reaching the peak stress, followed by plastic deformation associated with a sharp stress drops due to the onset of particle crushing. Afterwards, the stress is nearly unchanged over an extensive strain range, which is known as the plateau region. The CM particles densify plastically (crushing) in this region. Following the plateau region, the stress increases rapidly again as the material densification has completed.

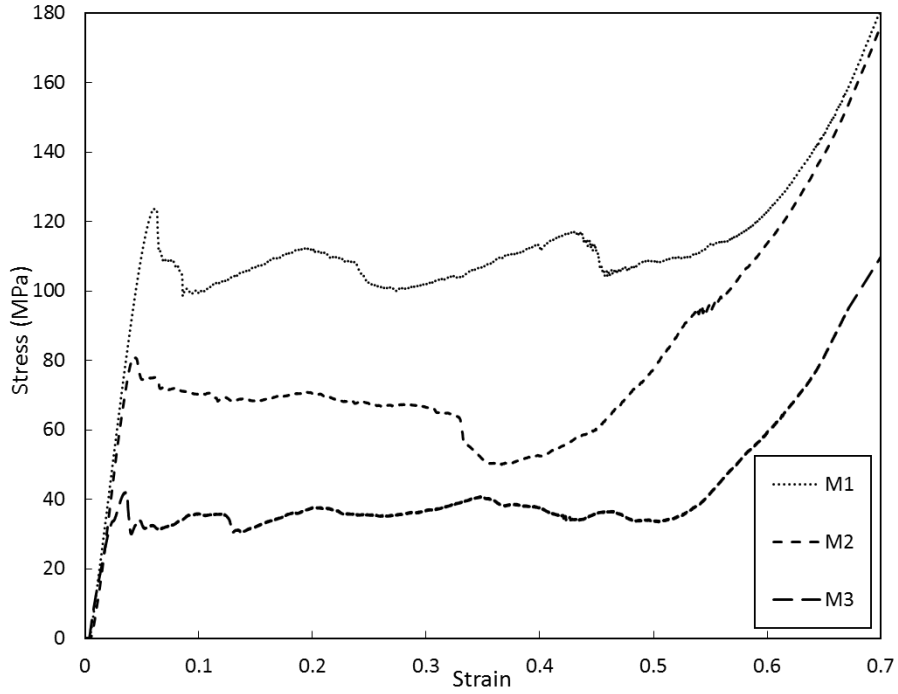

Figure 4-12 Quasi-static compressive stress-strain curves of monomodal syntactic foams M1, M2 and M3.

The exteriors of the monomodal syntactic foams, M1, M2 and M3, which were compressed to 0.15 strain, are shown in Figure 4-13. All samples apparently display either single or X-shaped shear crevasses or cracks with angles about 45° to the loading direction.

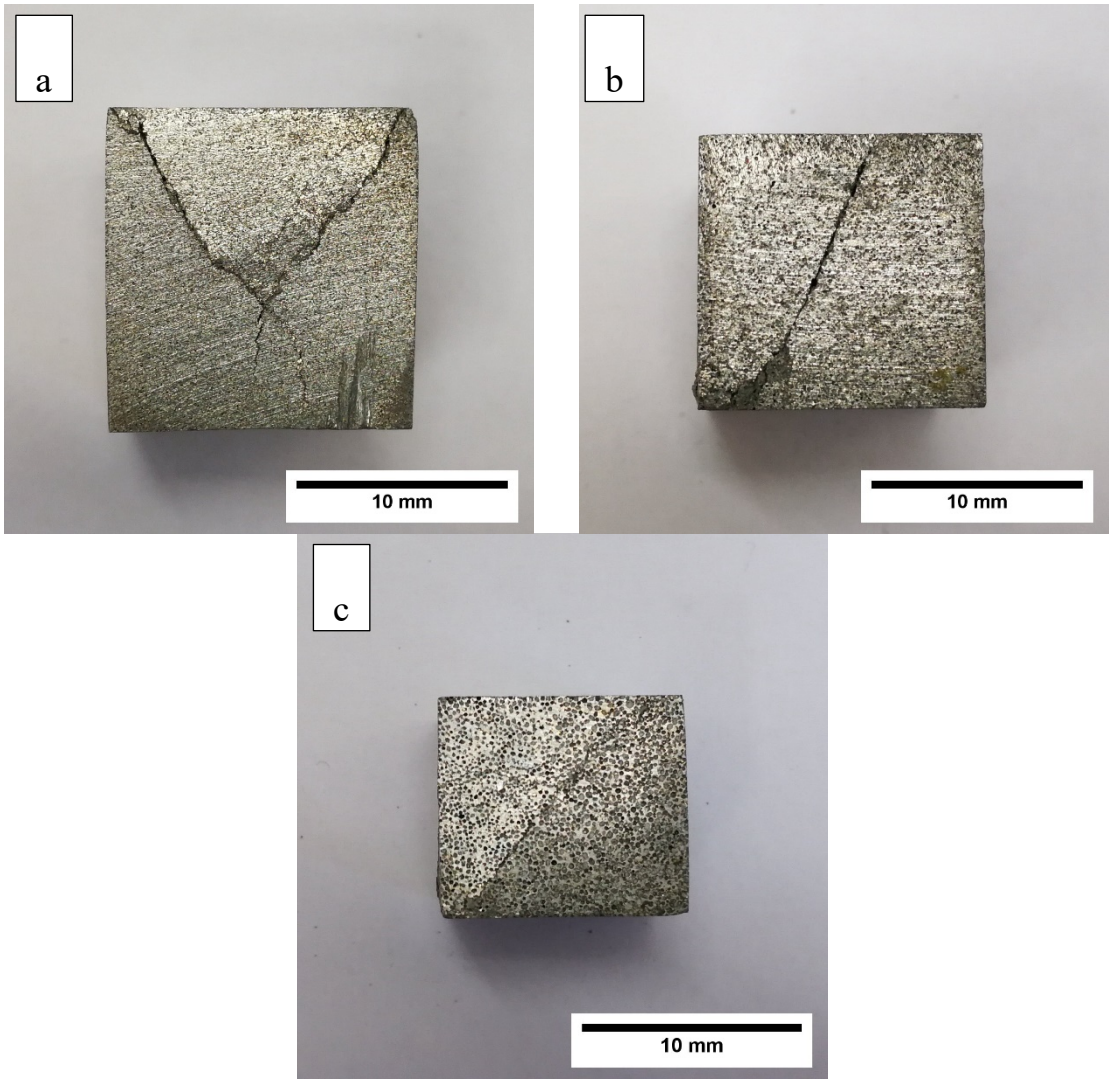

Figure 4-13 Exterior photos of syntactic foams: (a) M1, (b) M2 and (c) M3, compressed to 0.15 strain.

The characteristic compressive properties of the monomodal syntactic foams under the quasi-static compression, obtained by averaging the values of three specimens, are summarized in 4-2. The compressive strength is defined according to ISO 13314 as the maximum stress at fracture or collapse of the foam and the plateau stress is the mean of the stress in the plastic deformation region after the initial drop until the densification strain (ISO 2011). The yield strain is the strain corresponding to the yield stress. The densification strain is defined as the intersection of the tangents to the plateau region and the densification region (Nieh et al. 2000). The specific energy

absorption, which quantifies the energy absorption capacity of the syntactic foam, is the area under the stress-strain curve up to the densification strain.

Table 4-2 Compressive properties of the non-heat treated monomodal syntactic foams

Sample	Compressive strength (MPa)	Yield strain	Plateau stress (MPa)	Densification strain	Specific energy absorption (MJ/m^3)
M1	123.2±8.5	0.06	108.5±5.6	0.60±0.05	62.5±2.1
M2	80.9±5.1	0.05	65.3±0.9	0.58±0.02	36.7±0.4
M3	41.9±1.1	0.02	35.7±1.0	0.59±0.01	19.6±0.5

Table 4-2 shows that the compressive strength, yield strain, and plateau stress are gradually decreasing with the embedded CM particles size varying from small to large. The syntactic foam M1, which was made by small CM particles, has the highest compressive stress and plateau stress, which are about 123.2 MPa and 108.5 MPa respectively. The compressive stress and plateau stress of the syntactic foam embedded with the large CM particles (M3) are 41.9 MPa and 35.7 MPa, which are the lowest among the monomodal syntactic foams.

The yield strain follows the same pattern as the compressive strength because their stress-strain curves in the linear region indicate that all three syntactic foams have a comparable elastic modulus, as evidenced in Figure 4-12. All the three syntactic foams have a comparable densification strain which is independent of the CM particle size.

The specific energy absorptions of the syntactic foams are also presented in Table 4-2. The specific energy absorption is evaluated as the absorbed energy by a unit volume of syntactic foam from the start of compression up to the onset of densification. The calculated specific energy absorption also indicates that the energy absorption

capability of the syntactic foams decreases gradually with the embedded CM particle size varying from small to large.

4.2.1.2 Heat treated syntactic foam

Figure 4-14 shows the representative quasi-static compressive stress-strain curves of the heat treated (T6) monomodal syntactic foams, HT-M1, HT-M2 and HT-M3. The overall characteristics of the stress-strain curves of the heat treated syntactic foams are similar to the non-heat treated samples. Compared with syntactic foams M1, M2 and M3, the heat treated samples present higher stress levels, and the curves are also more flat and stable in the plateau region (except syntactic foam HT-M1). Meanwhile, the exterior fractures of these heat treated syntactic foam samples after failure are also similar to those of the non-heat treated samples. X-shaped shear crevasses or cracks with angles about 45° to the loading direction are present on the surface of the samples.

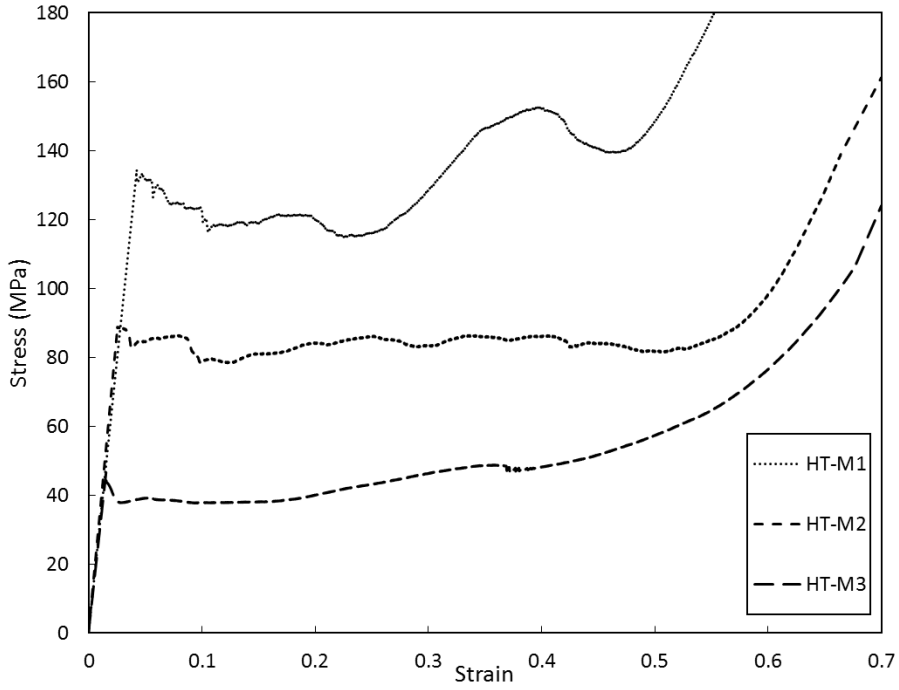

Figure 4-14 Quasi-static compressive stress-strain curves of heat treated monomodal syntactic foams HT-M1, HT-M2 and HT-M3.

Table 4-3 Compressive properties of the heat treated monomodal syntactic foams

Sample	Compressive strength (MPa)	Yield strain	Plateau stress (MPa)	Densification strain	Specific energy absorption (MJ/m^3)
HT-M1	133.1±6.5	0.05	131.0±9.3	0.53±0.04	67.5±3.6
HT-M2	88.6±2.6	0.03	83.8±4.6	0.57±0.04	46.0±2.0
HT-M3	46.7±3.5	0.02	45.9±2.5	0.55±0.01	25.0±1.4

The characteristic compressive properties of the monomodal syntactic foams under the quasi-static compression, obtained by averaging the values of three specimens, are summarized in 4-3. The compressive behaviour of the heat treated syntactic foams is similar to that of the non-heat treated syntactic foam samples. The compressive strength, yield strain and plateau stress also decrease gradually with the embedded CM particle size varying from small to large. However, these heat treated syntactic foams are slightly stronger than the non-heat treated samples. The compressive strength and

plateau stress are increased by approximately 10% and 30%. Furthermore, the specific energy absorption of each heat treated syntactic foam is also enhanced by approximately 20% due to the higher plateau stress.

4.2.2 Compressive behaviour of syntactic foams toughened with Al particles

Figure 4-15 shows the representative quasi-static compressive stress-strain curves of the syntactic foams T1, T2, T3 and T4, whose CM particle volume percentage are about 20%, 30%, 40% and 50%, respectively. The deformation of all the syntactic foams embedded with Al particles also involves three typical regions, which are the elastic region, plateau region and densification region. However, they have different behaviours from the monomodal syntactic foams in some regions.

The behaviours of syntactic foams, T1~T4, in the elastic region are nearly the same, while the behaviours in the plastic region are varied. All the syntactic foams have the different compressive strengths although the variation is small. The curves of syntactic foams T2, T3 and T4 show an obvious stress drop after reaching the compressive strength and then enter into the plateau region. The curve of the syntactic foam T1, however, does not show a drop. The compressive behaviour is closer to that of pure aluminium. The curves of all the syntactic foams in the plateau region are smoother than the untoughened syntactic foams although the range of the plateau region in each syntactic foams is varied as shown in the stress-strain curves.

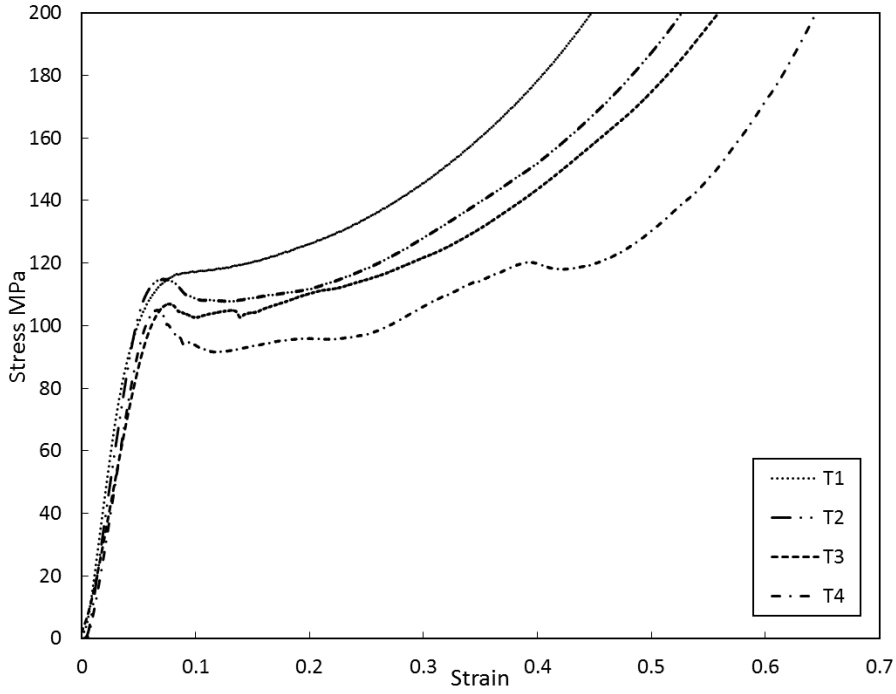

Figure 4-15 Quasi-static compressive stress-strain curves of syntactic foams toughened with Al particles T1, T2, T3 and T4.

Figure 4-16 shows the photos of the exterior of the syntactic foams, T1~T4, compressed to 0.15 strain. In syntactic foams T1 and T2, although small cracks are present, mainly surrounding the Al particles, the barrelling plastic deformation is dominant. The syntactic foams T3 and T4 have the same shear crevasses with angles about 45° to the loading direction.

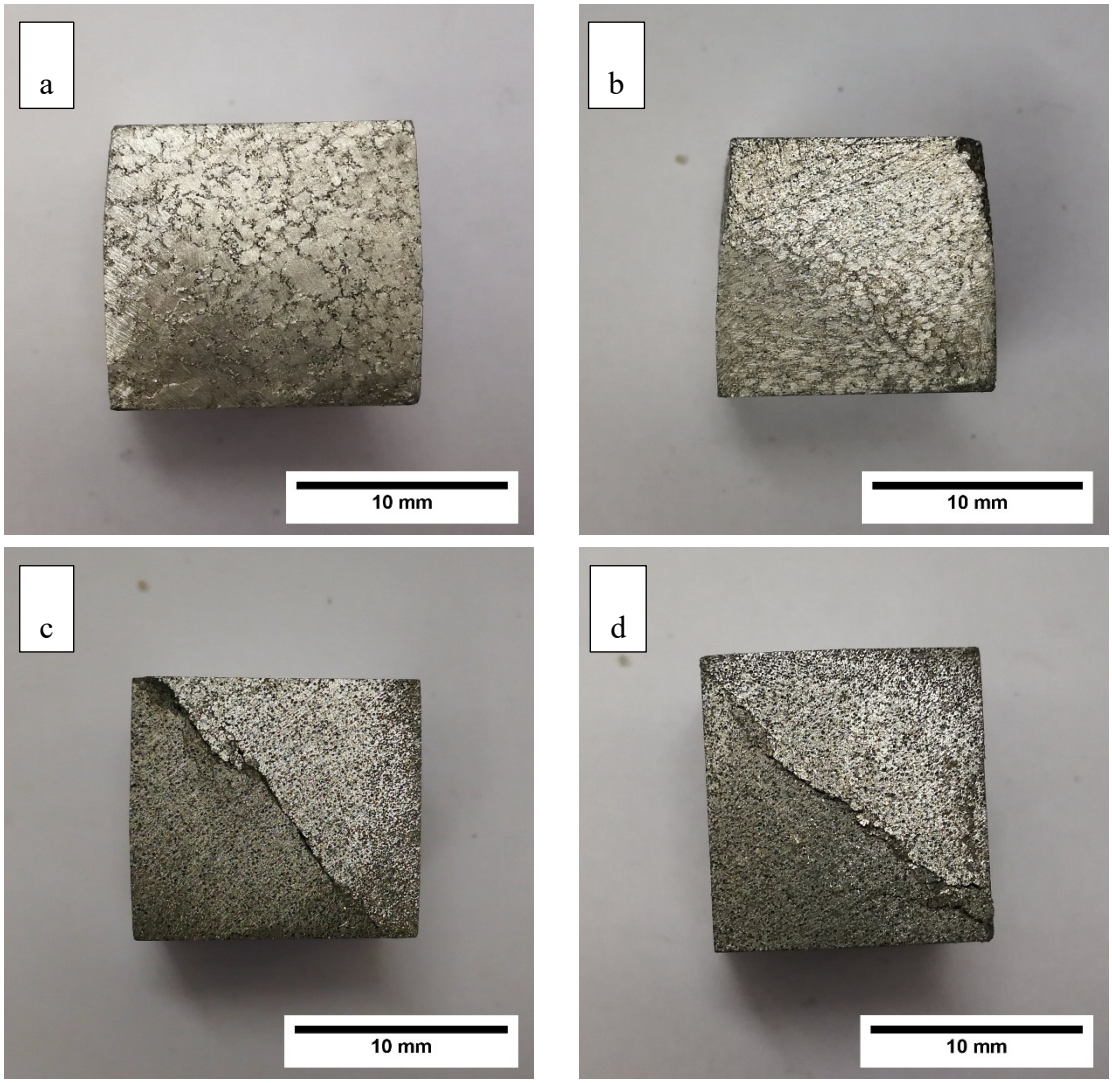

Figure 4-16 Exterior photos of syntactic foams: (a) T1, (b) T2 (c) T3 and (b) T4, compressed to 0.15 strain.

Table 4-4 Compressive properties of the syntactic foams toughened with Al particle

Sample	Compressive strength (MPa)	Yield strain	Plateau stress (MPa)	Densification strain	Specific energy absorption (MJ/m^3)
T1	116.5±1.7	0.08	128.6±1.0	0.33±0.06	38.5±0.2
T2	115.1±1.5	0.08	120.0±1.7	0.38±0.06	41.8±0.8
T3	107.1±1.8	0.08	117.4±1.8	0.43±0.06	47.0±0.8
T4	105.2±2.0	0.08	107.0±1.4	0.51±0.07	51.1±0.1

Table 4-4 summarises the characteristic compressive properties of these four syntactic foams toughened with Al particles under quasi-static compression. The values of the properties are based on the averages of the measurements of three samples. Compared with the monomodal syntactic foams fabricated using the same CM particle size, the compressive strength, yield strain, plateau stress and specific energy absorption in these syntactic foams with lower CM volume percentages are significantly improved. However, the improvement of the compressive strength is small in syntactic foams T1~T4, which only increases about 10 MPa when the CM volume percentage drops down from 50% to 20%. On the contrary, the densification strain and specific energy absorption are decreased evidently.

4.2.3 Compressive behaviour of bimodal syntactic foams

Figure 4-17 shows the representative quasi-static compressive stress-strain curves of the bimodal syntactic foams B1, B2 and B3 manufactured using mixtures of the small and large CM particle sizes with three different volume proportions. The classic compression characteristics of cellular solid, i.e., linear region, plateau region and densification region, are still present in the stress-stress curves of all the bimodal syntactic foam samples.

The curves of bimodal syntactic foams B1 and B3, having the higher and lower proportions of small CM particles, have a significant stress drop after the linear elastic region, with syntactic foam B3 being steeper than B1. The stress fluctuated in the plateau region. The curve of bimodal syntactic foam B2, having 50% small CM particles, only shows a relatively small stress drop following the elastic deformation

and the curve is stable in the plateau region. All the bimodal syntactic foams are found to densify at a strain about 0.6.

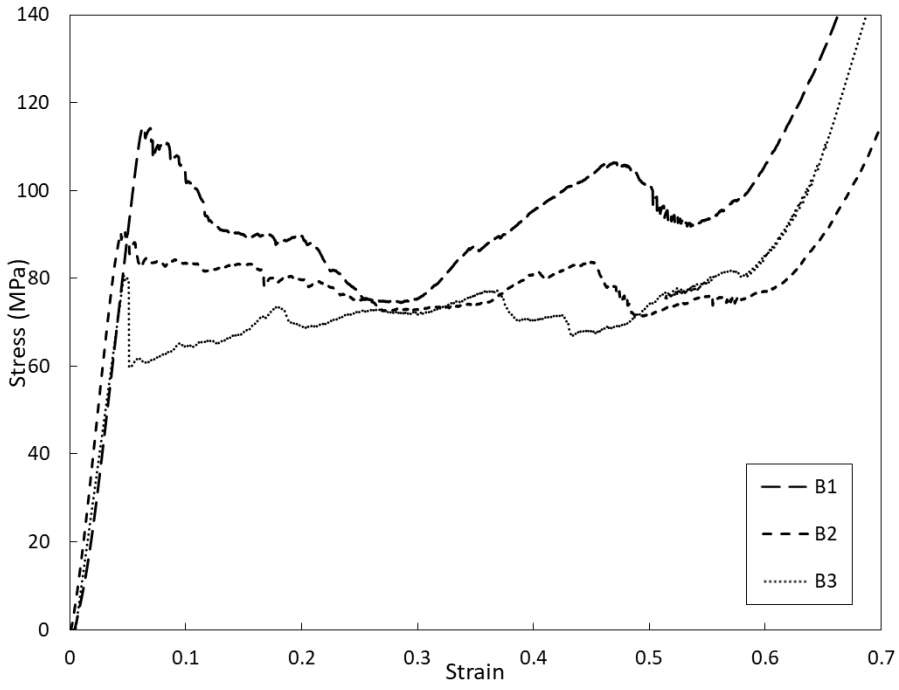

Figure 4-17 Quasi-static compressive stress-strain curves of bimodal syntactic foams B1, B2 and B3.

The exteriors of syntactic foams B1, B2 and B3 compressed to 0.15 strain are shown in Figure 4-18. All the bimodal syntactic foams have the same behaviour, i.e., samples crack at angles about 45° to the loading direction.

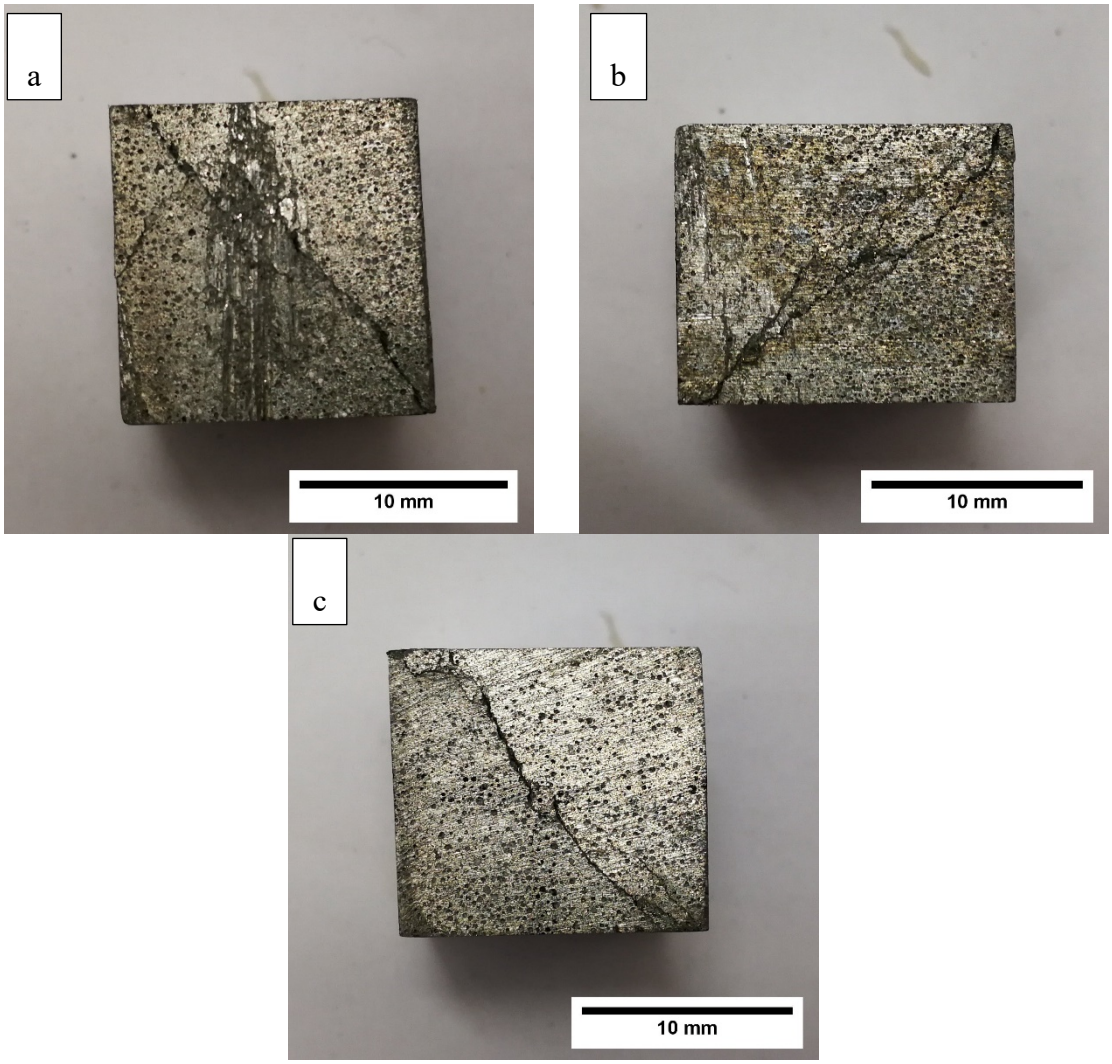

Figure 4-18 Exterior photos of syntactic foams: (a) B1, (b) B2 and (c) B3, compressed to 0.15 strain.

The characteristic compressive properties of the three bimodal syntactic foams under quasi-static compression, obtained by averaging the values of three specimens, are listed in Table 4-5. The three bimodal syntactic foams have a comparable densification strain, while the compressive strength, plateau stress and specific energy absorption decrease significantly with reducing the amount of small CM particles in the mixture. The compressive strength, plateau stress and specific energy absorption of the bimodal syntactic foams are higher than the monomodal syntactic foams fabricated with the

large CM particles but lower than the monomodal syntactic foam fabricated with the small CM particles.

Table 4-5 Compressive properties of the bimodal syntactic foams

Sample	Compressive strength (MPa)	Yield strain	Plateau stress (MPa)	Densification strain	Specific energy absorption (MJ/m^3)
B1	114.1±3.4	0.06	92.3±2.8	0.59±0.05	52.8±0.3
B2	91.1±3.1	0.05	81.7±1.3	0.62±0.04	47.2±1.4
B3	80.6±2.8	0.05	71.6±0.4	0.61±0.05	41.4±1.0

4.2.4 Effects of Al and CM particle on compressive behaviour

4.2.4.1 Al matrix

Comparing the compressive properties of non-heat treated and heat treated syntactic foams (see Tables 4-2 and 4-3) shows that, the strength of the metal matrix syntactic foam is sensitive to the strength of the metal matrix. The compressive strength of the heat treated syntactic foams has an apparent enhancement, agreeing with two previous studies (Balch et al. 2005; Orbulov & Ginsztler 2012). This is because the heat treatment modifies the mechanical property of the metal matrix, which in turn enhances the strength of the syntactic foam. In other words, a stronger metal matrix will result in a higher compressive strength of the resultant syntactic foam. For example, Castro and Nutt (2012) reported that the medium carbon steel syntactic foam has significantly higher compressive strength than the low carbon steel syntactic foam.

The metal matrix also has a significant influence on the energy absorption capability of the syntactic foam. The energy absorption capability of the syntactic foam under quasi-static compression is evaluated by the specific energy absorption, which is a

function of both the plateau stress and the densification strain. All the monomodal syntactic foams have a similar densification strain. The heat treatment enhances but the plateau stress and therefore the energy absorption. The specific energy absorption of the heat treated syntactic foam is approximately 20% higher than the non-heat treated sample. This increment of specific energy absorption is comparable to Balch's results where the matrix of the syntactic foam is Al 7075 (Balch et al. 2005).

4.2.4.2 CM particle size

According to the compressive behaviour of monomodal syntactic foams shown in section 4.2.1, the size of the CM particles has a critical influence on the compressive strength and plateau stress of the metal matrix syntactic foams, with the compressive strength and plateau stress decreasing significantly with increasing CM particle size. Santa Maria et al. (2014) ascribed this behaviour to the higher thickness-to-radius ratio of the small particles within the syntactic foam, while Cox et al. (2014) also confirmed that even using the same diameter particles, particles with thicker wall particles significantly increased the compressive strength of the resultant syntactic foam.

Nevertheless, the three sizes of the CM particles have the same chemical composition and the same effective density in the present study. The effect on the compressive strength in the three syntactic foams seems to be related to the structure of the CM particles. As introduced in the experimental procedure section, two internal structures exist in the CM powder particles, with the large CM powder consisting of mainly porous particles. Meanwhile, compressing the CM powders showed that the large CM powder had the lowest strength compared to the medium and small CM powders. It indicates that the porous CM particles are significantly weaker than the hollow ones.

As the monomodal syntactic foams have a very similar CM volume percentage, their compressive strength decreases with increasing ratio of porous CM particles in the embedded CM particles. Syntactic foam M1, which has nearly 100% hollow CM particles, therefore, has the highest compressive strength, while syntactic foam M3 has the lowest compressive strength due to approximately 77% of porous CM particles. This behaviour is also evident in bimodal syntactic foams where compressive strength decreases with adding large CM particles consisting of more porous particles.

The compressive behaviour of the heat treated Al/CM syntactic foams is comparable to that reported in two previous studies on syntactic foam samples fabricate from the same raw materials (Tao & Zhao 2012; Zhang & Zhao 2007). However, with a higher proportion of the stronger hollow particles in each CM particle size group, the syntactic foam samples in the present study have a relatively higher compressive strength. In addition to the effect of the CM particles, the syntactic foam embedded with the smallest CM particles has the highest compressive strength and plateau stress because the small CM particles produce a stronger strengthening effect (Zhang et al. 2016).

The CM particle size also has a significant influence on the energy absorption capability of the syntactic foam. This is because the CM particle size has a significant effect on the plateau stress of the syntactic foam. When the syntactic foams have the same densification strain, the energy absorption capability is mainly determined by the magnitude of the plateau stress.

4.2.4.3 CM volume percentage

It is very hard to manufacture syntactic foams with various volume percentages CM particles by normal pressure infiltration casting. Different CM volume percentages are

achieved either by embedding additional Al particles or applying bimodal CM powders. Toughening with Al particles can successfully reduce the CM volume percentage to a desirable value in the syntactic foams. Compared with the monomodal syntactic foam (M2), the compressive strength of the syntactic foams toughened with Al particles (syntactic foam T1~T4) is improved by 26~35 MPa. This improvement of compressive strength, however, can be attributed to the different failure modes between the normal and the Al particle toughened syntactic foams. As shown in Figure 4-16, the syntactic foam toughened with Al particles failed by collapse and crushing of the CM particles, while the normal syntactic foams failed by shear or cracking (Figure 4-13).

However, the compressive strength is less sensitive to the CM volume percentage. Reducing the CM volume percentage from 50% to 40%, to 30%, and to 20% by increasing the amount of Al particles in the syntactic foam samples has limited effect on the compressive strength, in particular in syntactic foams T1 and T2 in which the compressive strength remains almost constant. The compressive behaviour of the syntactic foams agrees with that reported in a previous study of syntactic foams toughened with Al particles (Tao & Zhao 2009). The compressive strength of the syntactic foams is slightly difference in the between the two studies due to the different CM particle size. Overall, in the syntactic foams with lower CM volume percentages fabricated by embedding Al particles, the compressive strength is dominated by the compressive strength of the CMs rather than by the volume percentage of the CM particles.

In bimodal syntactic foams, the syntactic foam B1 with the lowest CM volume percentage has the highest compressive strength than those with a higher CM volume

percentage. As there is a big difference in the strength between the large and small CM powders, the compressive strength of the bimodal syntactic foams seems to be determined by the volume percentage of the stronger CM particles rather than by the total volume percentage of the CM particles. The compressive behaviour of the bimodal syntactic foam agrees with the previous study (Tao et al. 2009). The actual compressive strength of each bimodal syntactic foam sample, however, is higher in this study, because the modified infiltration casting process results in less manufacturing defects. It seems that defects in the syntactic foam has a significant effect on the mechanical properties.

The CM volume percentage also has a significant influence on the energy absorption capability of the syntactic foam. The CM volume percentage essentially determines the densification strain of the syntactic foam under the compression, which is one of the major parameters to evaluate the specific energy absorption. Syntactic foams toughened with Al particles have higher plateau stress, but their densification strain also becomes smaller due to reduced CM volume percentage. Therefore, toughening with Al particles does not always improve the specific energy absorption.

Although the CM volume percentage in bimodal syntactic foams can be varied with different proportions of small CM particles, the difference is not enough to change their densification strain significantly. The energy absorption capability of bimodal syntactic foams mainly depends on the plateau stress. Nevertheless, adding relatively stronger particles into a weaker particle powder is a good approach to improve the energy absorption capability of the syntactic foam, because it enhances the plateau stress without reducing the densification strain.

4.2.5 Impact behaviour

The impact toughness of the monomodal syntactic foams is evaluated by the Charpy impact energy, which is shown in Figure 4-19. The Charpy impact energy for each syntactic foam was obtained by averaging the values of three samples. The fracture surface of each syntactic foam sample after the Charpy impact test is shown in Figure 4-20.

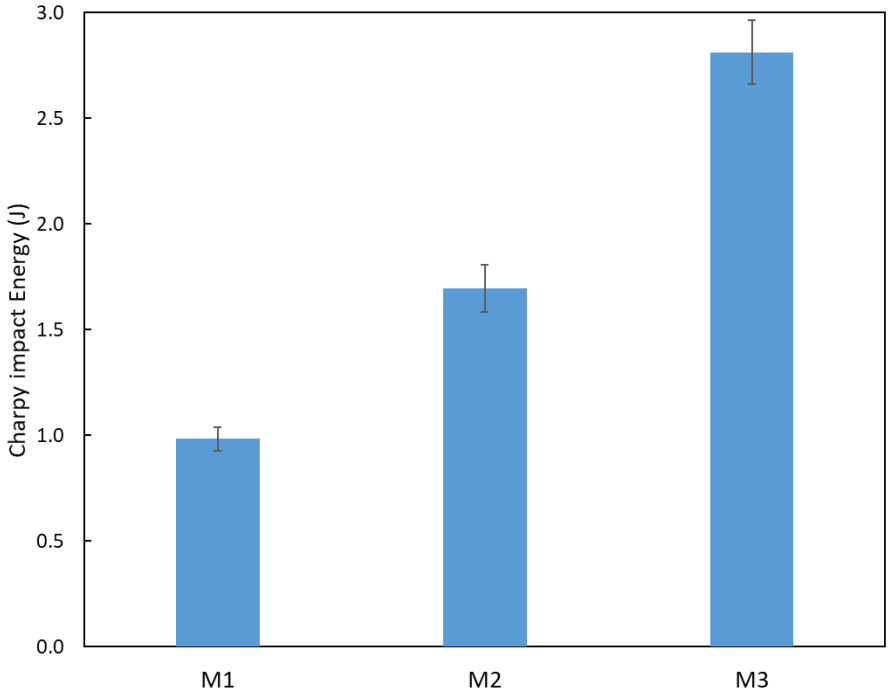

Figure 4-19 Charpy impact energy of monomodal syntactic foams.

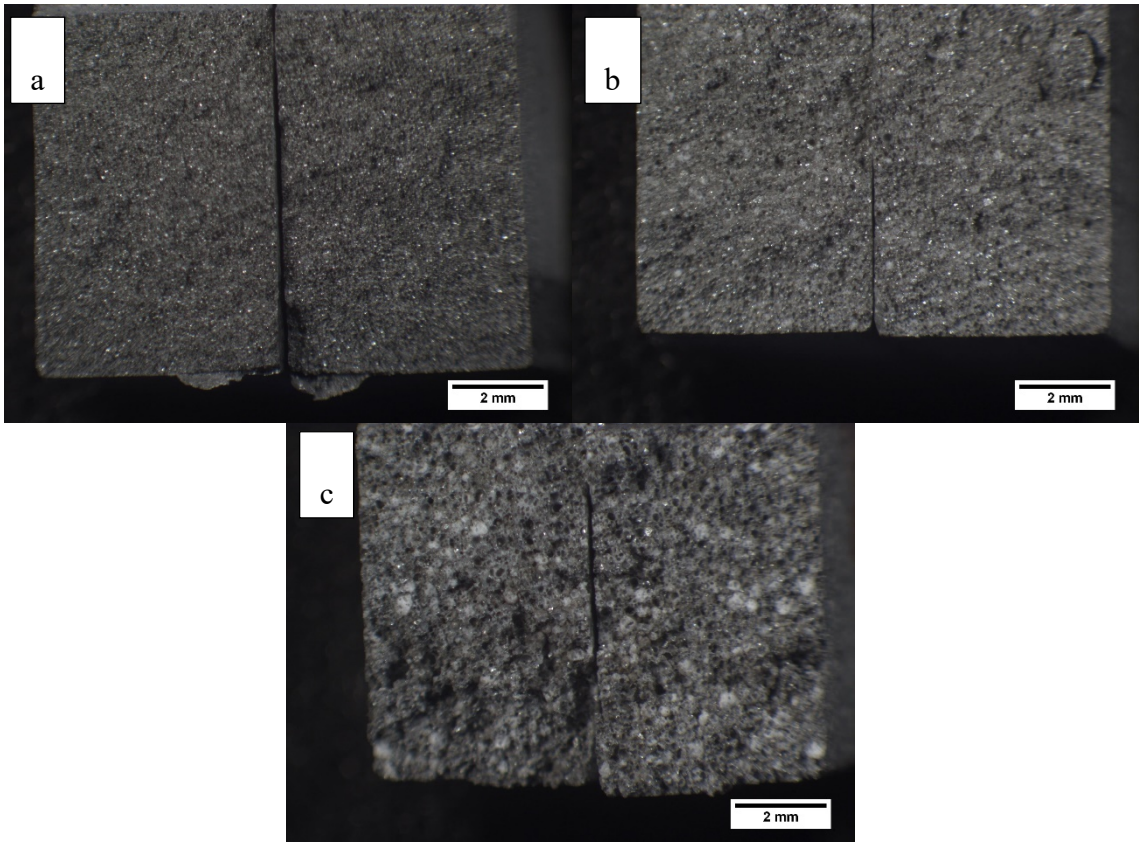

Figure 4-20 Charpy impact fracture surfaces of the syntactic foams: (a) M1, (b) M2 and (c) M3.

Figure 4-19 clearly indicates that the Charpy impact energy of the syntactic foam is affected by the size of the embedded CM particles, with the syntactic foam fabricated with the largest particles has the highest Charpy impact energy. By observing the Charpy impact fracture surface in Figure 4-20, the CM particle size seems to influence the fracture mechanism in the syntactic foam. The fracture surface of syntactic foam M1 is smooth and flat, indicating a straight crack path. It is because M1 has a relatively fine metal network structure and brittle hollow CM particles. When the fracture occurs, crack propagation is directly through the matrix and the CM particles. The rough fracture surface of syntactic foam M3, however, indicates a different crack path. The large CM particles lead to a relatively thick metal network structure, which needs more energy for fracture. Meanwhile, the large CM particles are porous and do not break

easily. The crack propagates along the particle surface, making the crack path more tortuous. Consequently, the increased total distance of crack path in syntactic foam M3 may have led to the higher Charpy impact energy.

4.2.6 Summary

The compressive stress-strain curves of all the syntactic foam specimens show a linear elastic region, a plateau region, and a densification region. The compressive behaviours of the monomodal and the bimodal syntactic foams and syntactic foams toughened with Al particle showed that the compressive strength, plateau stress, densification strain and energy absorption capability are significantly influenced by the metal matrix and the size and volume percentage of the CM particles. The compressive strength of the monomodal syntactic foams is dependent on the Al matrix and the size of CM particles. The compressive strength of syntactic foams toughened with Al particles is enhanced by increasing the volume of the Al particles while the densification strain is reduced. The compressive strength of the bimodal syntactic foams is affected by the volume percentage of the stronger CM particles. The energy absorption capability of the syntactic foams is affected by both the plateau stress and the densification strain. The syntactic foam M3 has the highest Charpy impact energy due to a longer crack path.

4.3 Intermittent cyclic compressive behaviour

4.3.1 Monomodal syntactic foams

Figure 4-21 shows the stress-strain curves of the monomodal Al matrix syntactic foams with different CM particle sizes under intermittent cyclic compression. Some interesting features are exhibited in all these stress-strain curves. The general trend of each curve broadly coincides with the stress-strain curve of the corresponding syntactic foam under monotonic compression, with comparable strength and yield strain. It can be confirmed that the strength of the syntactic foams is not affected by the intermittent cyclic compression. However, appreciable hysteresis loops are present in the stress-strain curves of the syntactic foams under cyclic unloading-loading compression. The syntactic foams M1, M2, and M3 have differently sized hysteresis loops under the intermittent cyclic loading, because of their different strengths. In each syntactic foam, the hysteresis loops also vary with the starting strain, there is a gradually increase in the elastic region and remains almost the same plastic region.

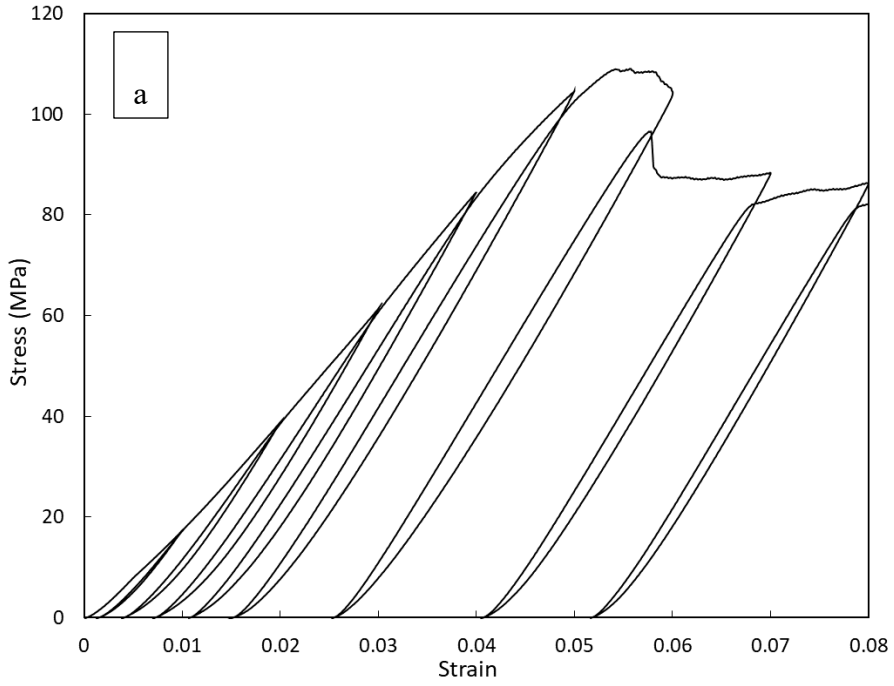
a
Stress (MPa)
Strain
0
20
40
60
80
100
120
0
0.01
0.02
0.03
0.04
0.05
0.06
0.07
0.08

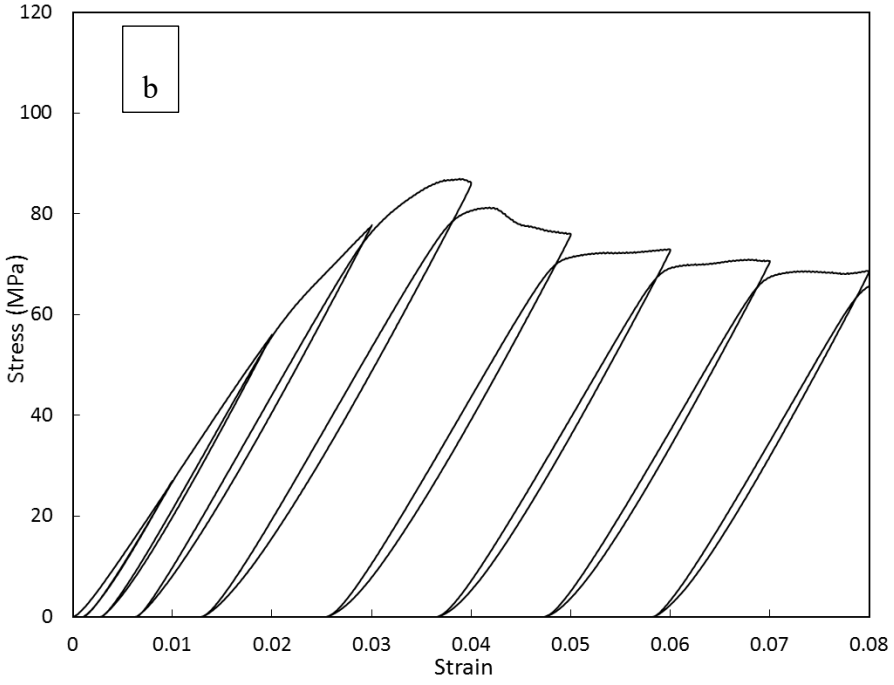
b
Stress (MPa)
Strain
0
20
40
60
80
100
120
0
0.01
0.02
0.03
0.04
0.05
0.06
0.07
0.08

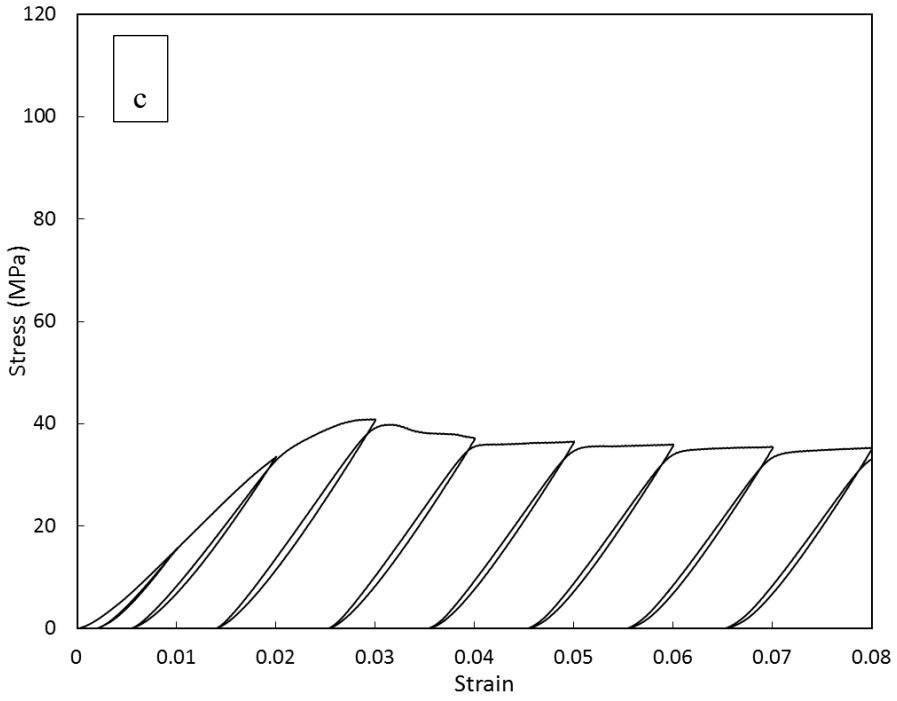

Figure 4-21 Stress-strain curves of the Al matrix syntactic foams (a) M1, (b) M2 and (c) M3 under intermittent cyclic compression.

Figure 4-22 compares the specific dissipated energy or hysteresis loss at different strains for the syntactic foams with different CM particles sizes. It shows that the specific dissipated energy increases with the strain in the elastic region and fluctuates in the plateau region. The highest SDE value is obtained at the 4^{th} or 5^{th} intermittent loading cycle in each syntactic foam, when the starting strain of the hysteresis loops is close to the yield strain of the syntactic foams. Among the three syntactic foams, syntactic foam M1 has the largest specific dissipated energy, because it has the highest strength, allowing the unloading-loading cycle to produce a large hysteresis loop during intermittent cyclic compression. Apparently, the energy dissipation is related to the stress at which the cyclic loading was conducted.

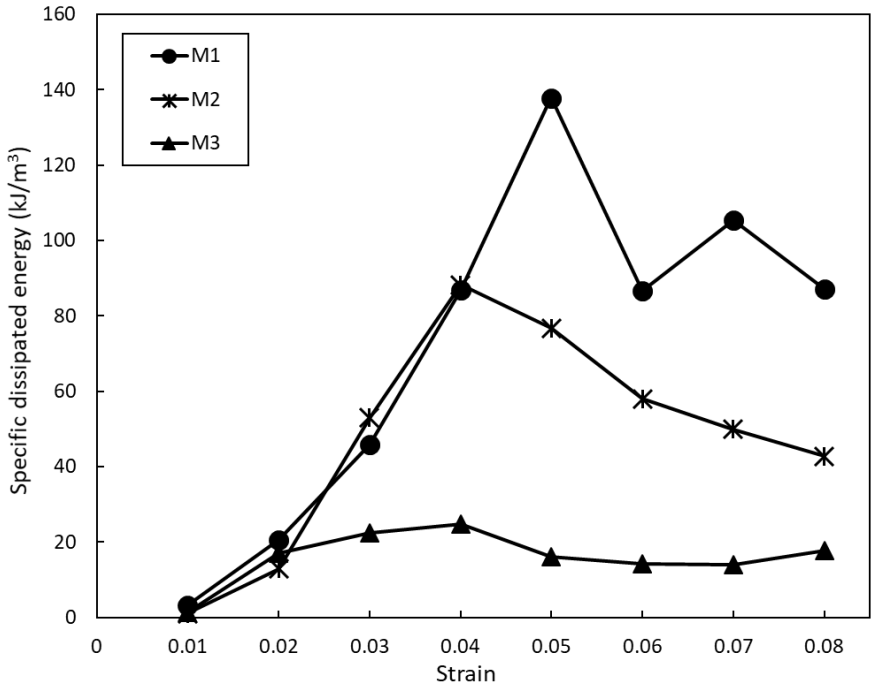

Figure 4-22 Hysteretic dissipated energy of each unloading-loading cycle of the syntactic foams with different CM particle sizes.

The specific dissipated energy describes the energy that can be dissipated in each cycle at any given strain and is dependent upon the applied stress at the strain. The higher the applied stress, the larger the SDE. In order to compare the damping capacity of the three syntactic foams with different CM particles sizes, Figure 4-23 shows the specific damping capacity values at different strains. Excluding the first unloading-loading cycle at the strain of 0.01, where the specific damping capacity is small, the specific damping capacity remains nearly constant in the subsequent unloading-loading cycles for any particular syntactic foam. Thus, the three syntactic foams have similar performance in terms of the specific damping capacity (SDC), which is approximately 0.085.

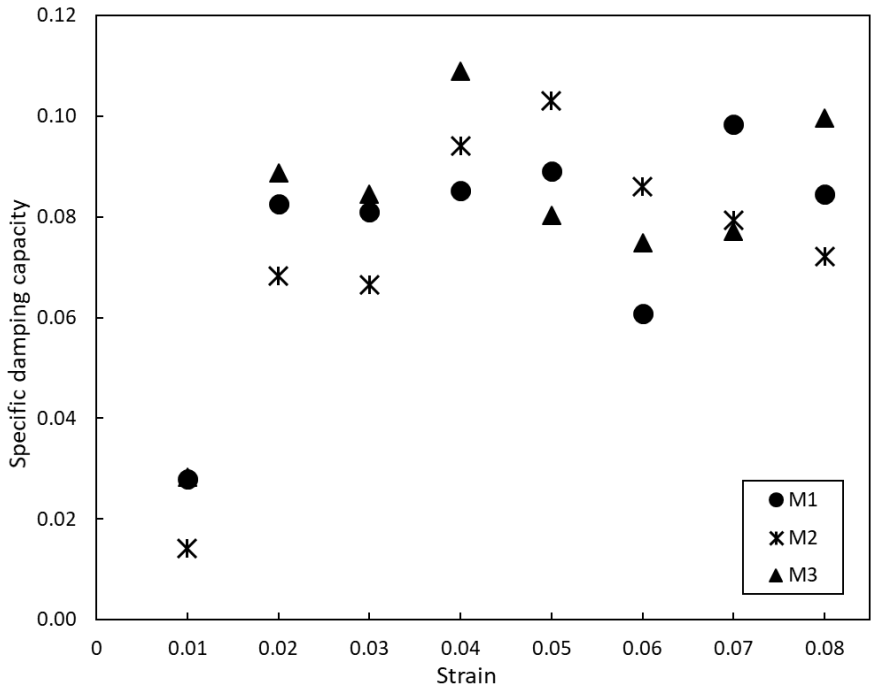

Figure 4-23 Specific damping capacity of each loading-unloading cycle of the syntactic foams with different CM particle sizes.

In order to confirm that the hysteresis loops are caused by internal dissipation in the syntactic foams rather than due to experimental errors, such as the sliding friction between the specimen and the platen in cyclic loading, the same intermittent cyclic compression test was conducted on a syntactic foam specimen with twice the height (30 mm). The stress-strain curve of this specimen is shown in Figure 4-24. Basically, the stress-strain curve is similar to the curve of the ordinary size syntactic foam M2 under the intermittent cyclic compression and also exhibits a hysteresis loop in each unloading-loading cycle. Both the SDE and SDC of the specimen are also evaluated and compared with the ordinary size specimen, as shown in Figures 4-25 and 4-26. The two specimens with different heights show similar SDE and SDC values, except for a relatively high SDC value for the large specimen at the strain of 0.01. Therefore, the measured hysteresis loss can be ascribed to the internal energy dissipation in the syntactic foam.

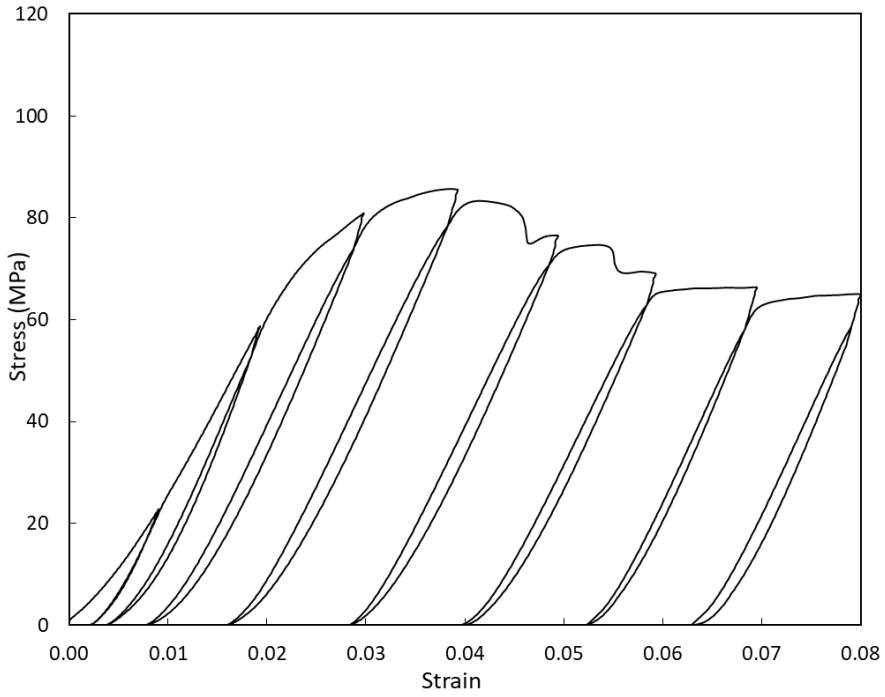

Figure 4-24 Stress-strain curve of the Al matrix syntactic foam M2 with a height of 30 mm under intermittent cyclic compression.

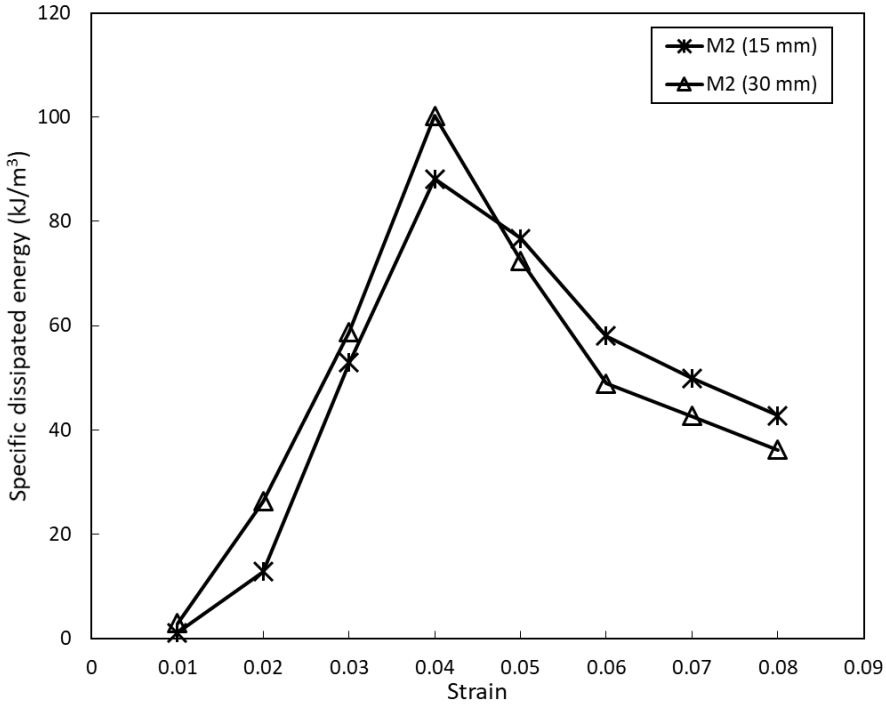

Figure 4-25 Comparison of specific dissipated energy of syntactic foam M2 between samples with different heights.

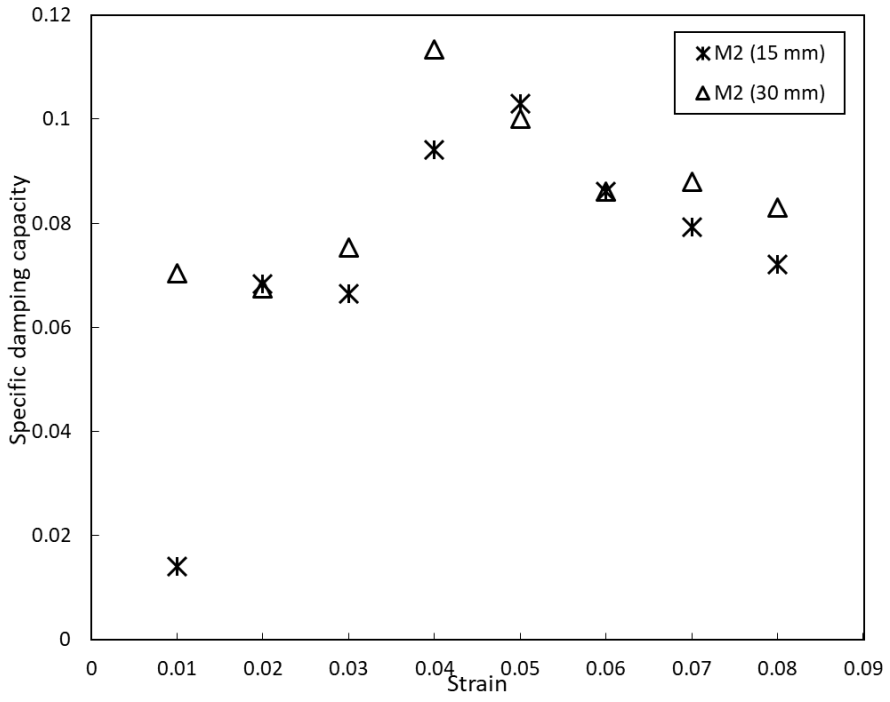

Figure 4-26 Comparison of specific damping capacity of syntactic foam M2 between samples with different heights.

4.3.2 Syntactic foams toughened with Al particles

Figure 4-27 shows the stress-strain curves of the Al matrix syntactic foams toughened with different percentages of Al particles under intermittent cyclic compression. According to the quasi-static compression, the yield strain of all the syntactic foams toughened with Al particles is about 0.08, so the intermittent cyclic compression is only conducted to the strain of 0.08. All the stress-strain curves of syntactic foams T1~T4 basically present a similar tendency and the envelop curves are similar to that of the syntactic foam M2. The hysteresis loops of these syntactic foams toughened with Al particles are thinner than those of M2 at the same given strains, even though some of them are formed at a higher stress level.

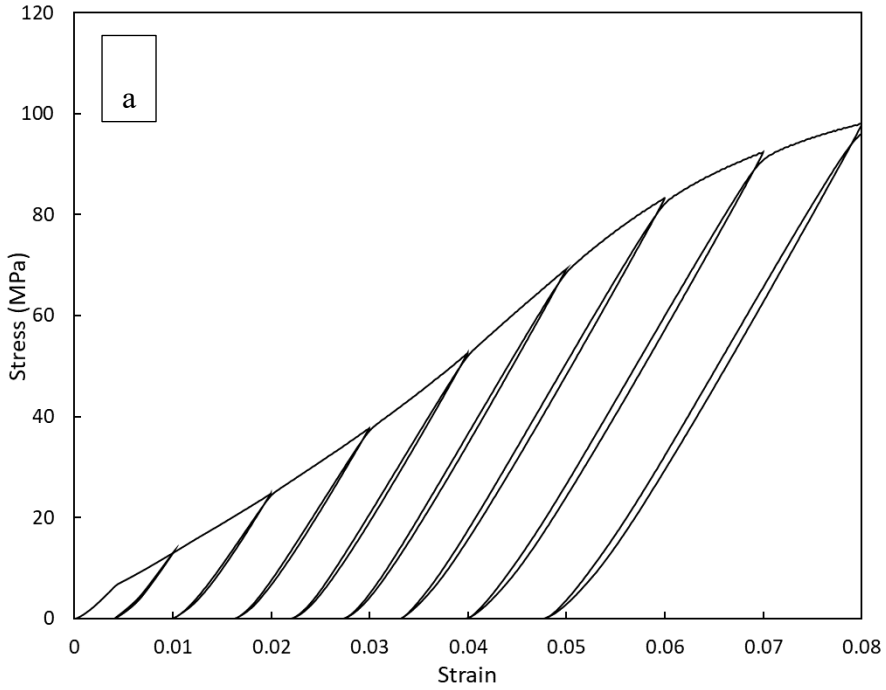
a
Stress (MPa)
Strain
0
20
40
60
80
100
120
0
0.01
0.02
0.03
0.04
0.05
0.06
0.07
0.08

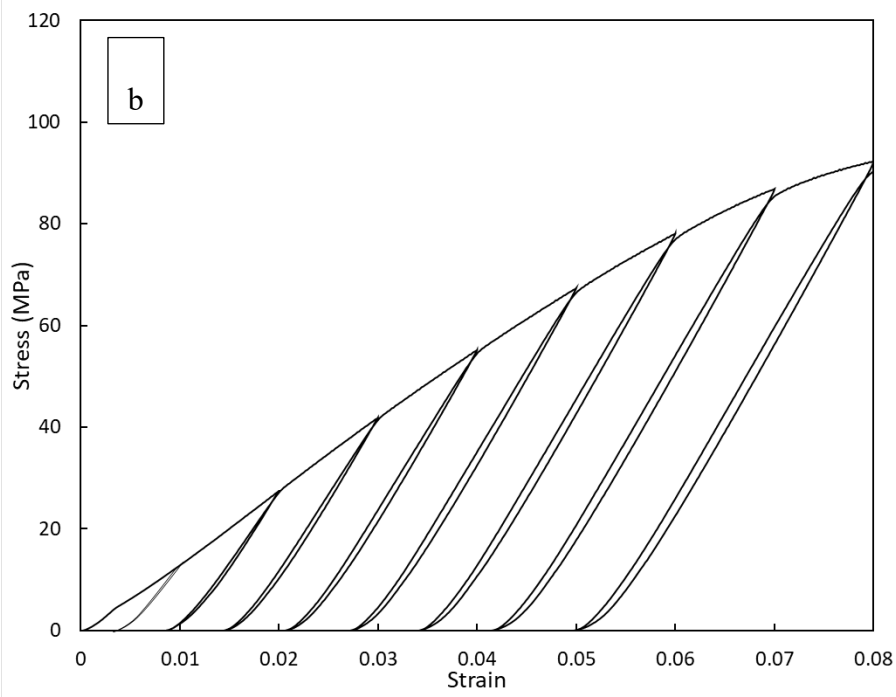
b
Stress (MPa)
Strain
0
20
40
60
80
100
120
0
0.01
0.02
0.03
0.04
0.05
0.06
0.07
0.08

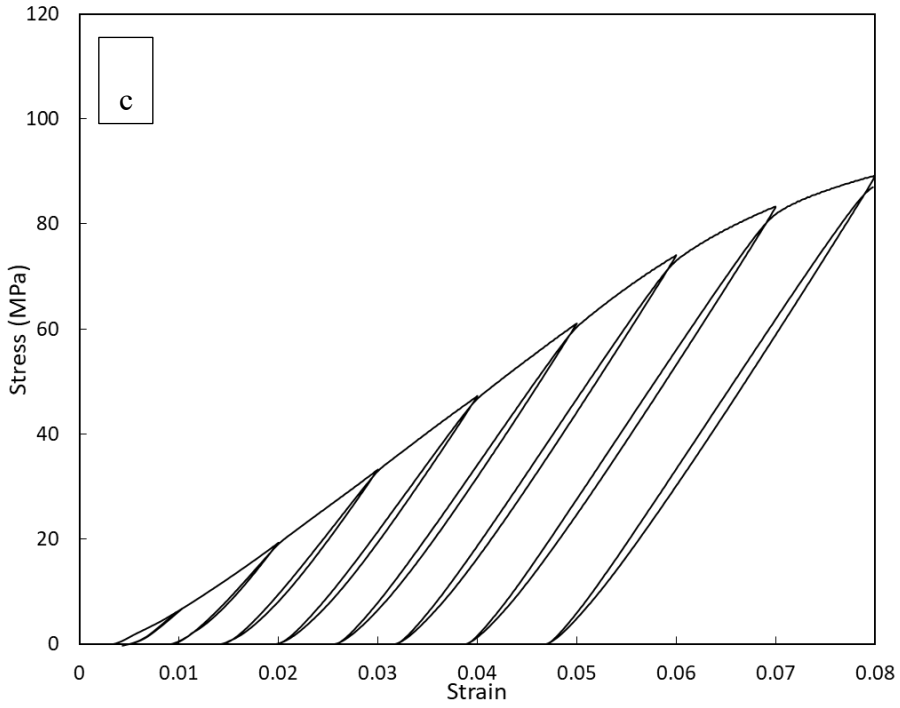

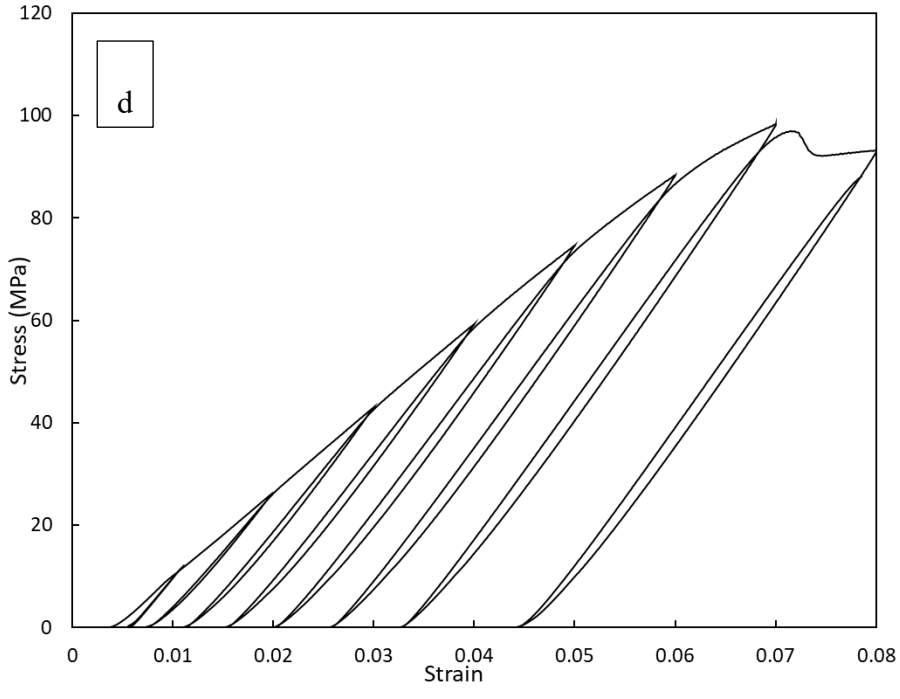

Figure 4-27 Stress-strain curves of the syntactic foams toughened with Al particles under intermittent cyclic compression (a) T1, (b) T2, (c) T3 and (d) T4.

Figure 4-28 shows the specific dissipated energy (SDE) of the syntactic foams toughened with different volume proportions of Al particles at different strains. Except for the last hysteresis loop of the syntactic foam T4, the SDE increases with the strain. The specific dissipated energy is apparently related to the stress at which the cyclic loading was conducted. Overall, the syntactic foam T1 toughened with more Al particles presents the lowest SDE value, while T4 toughened with less Al particles has the highest SDE value. Syntactic foams T2 and T3 show similar SDE values, which are in between.

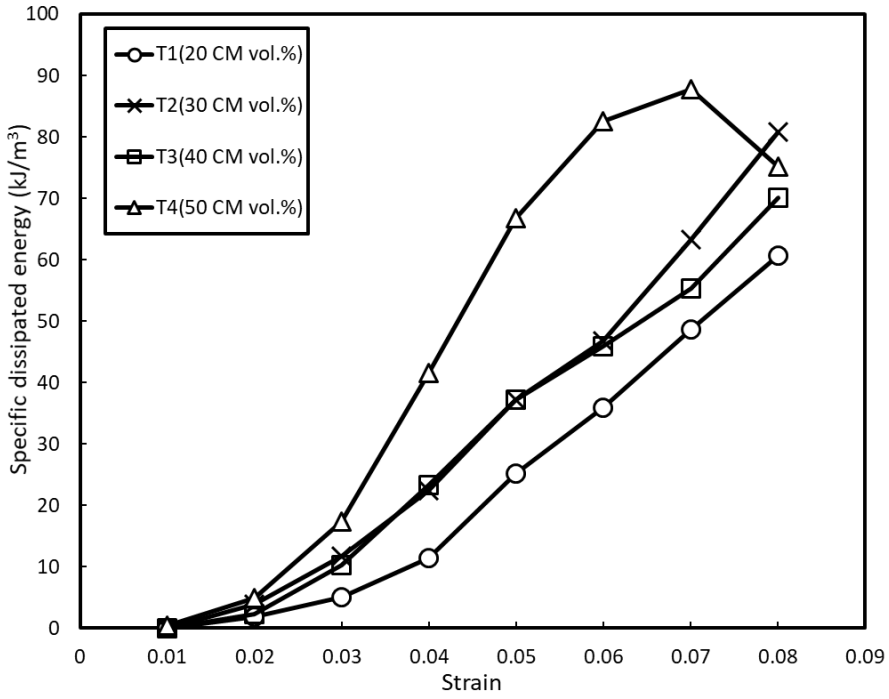

Figure 4-28 Hysteretic dissipated energy of each unloading-loading cycle of the syntactic foams with different CM particle volume percentages.

4-29 compares the specific damping capacity (SDC) of the syntactic foams T1~T4 in all the unloading-loading cycles. Their tendencies are similar to those of the monomodal syntactic foams M1~M3. Excluding the first unloading-loading cycle at the strain of 0.01, of which the SDC is small, the SDC does not change much for any

particular syntactic foam in the subsequent unloading-loading cycles. However, in contrast to the syntactic foams M1 ~ M3, which have nearly constant SDC, the SDC of the syntactic foams T1~T4 are gradually increasing, more markedly with decreasing the amount of toughening Al particles. Therefore, the damping capacity is somewhat related to the percentage of the toughening Al particles, which in turn determines the percentage of CM particles.

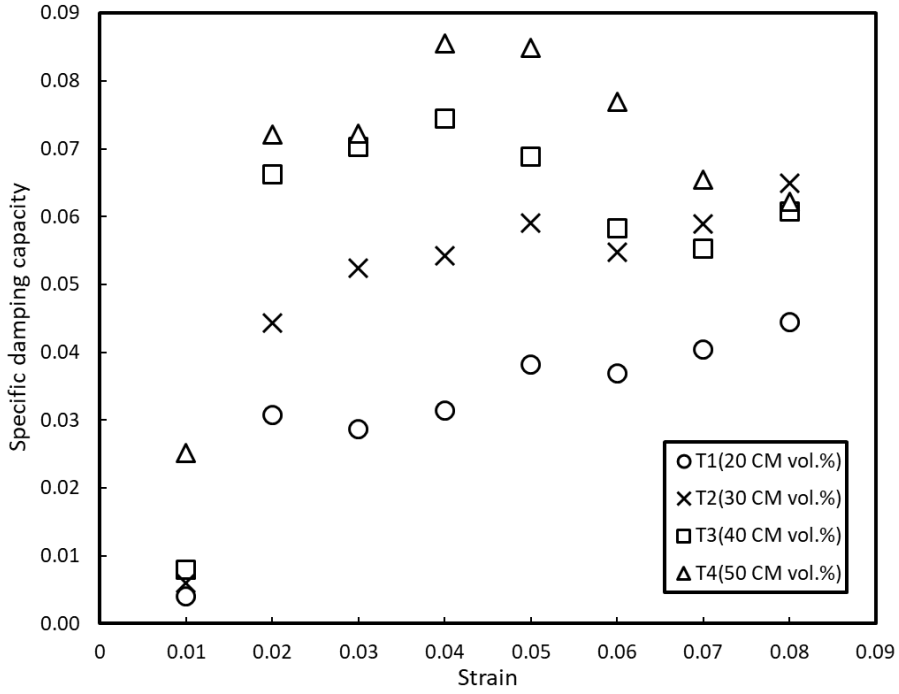

Figure 4-29 Specific damping capacity of each unloading-loading cycle of the syntactic foams with different CM particle volume percentages.

4.3.3 Bimodal syntactic foams

Figure 4-28 shows the stress-strain curves of the bimodal syntactic foams which contain various volume proportions of small and large CM particles, under intermittent cyclic compression. The general trend of each curve broadly coincides with the stress-strain curve of corresponding syntactic foam under monotonic compression, with comparable strength and yield strain. Meanwhile, appreciable hysteresis loops are

present in all the stress-strain curves of bimodal syntactic foams under the cyclic unloading-loading compression. The bimodal syntactic foams B1, B2, and B3 have different sized hysteresis loops under intermittent cyclic loading, because of their different strengths. In each syntactic foam, the hysteresis loops also vary with the starting strain, gradually increasing in the elastic region and remaining nearly the same in the plastic region.

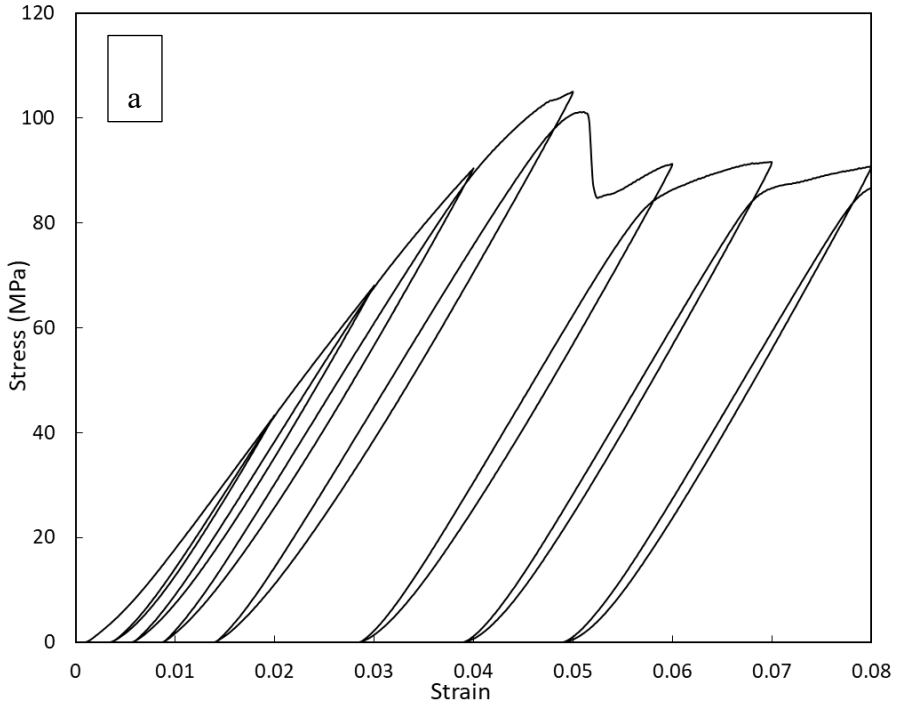

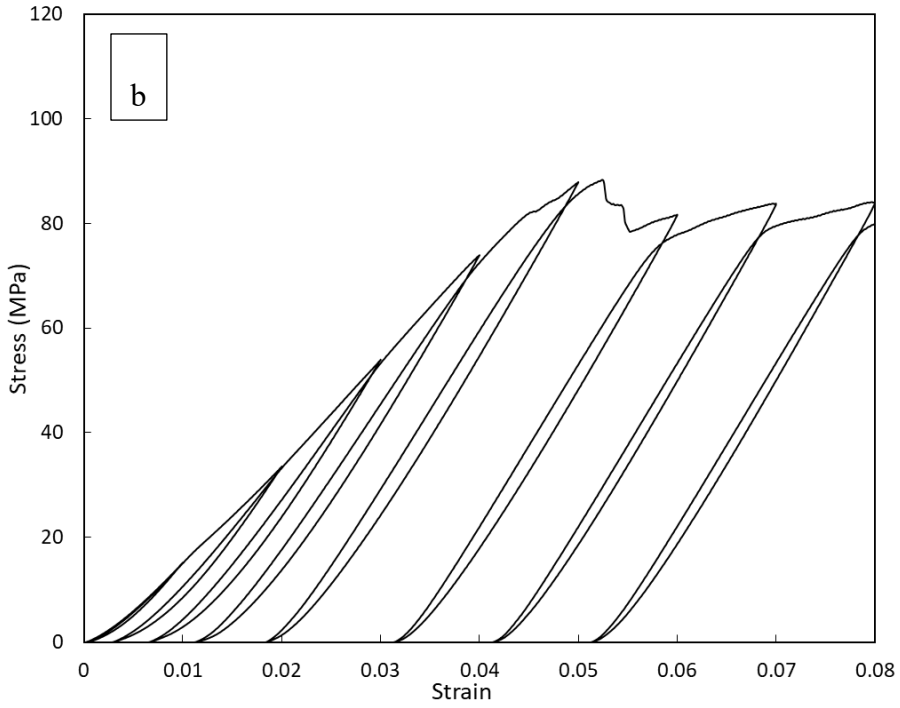

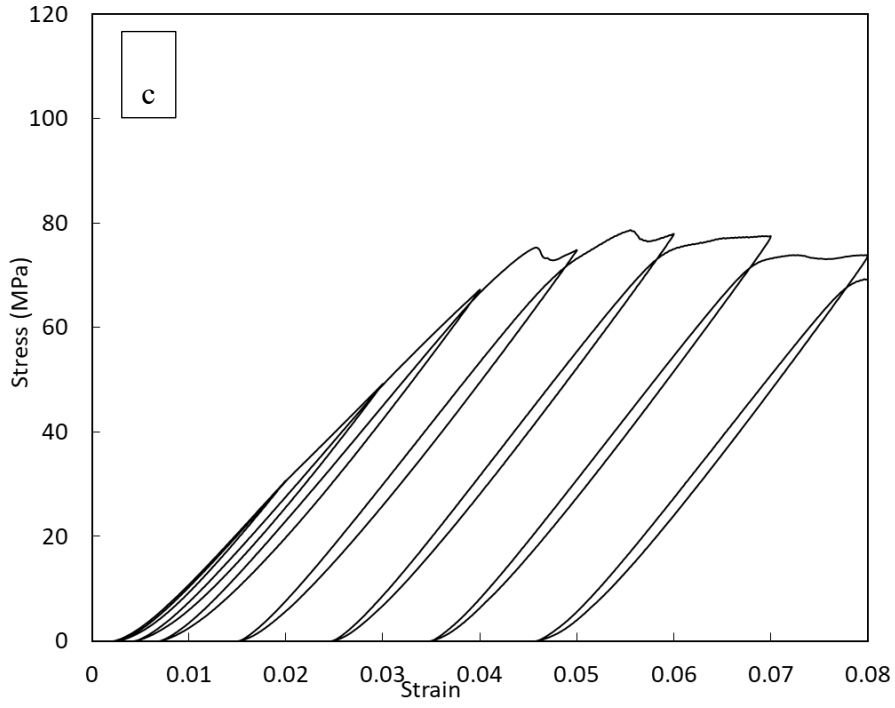

Figure 4-30 Stress-strain curves of the bimodal syntactic foams under intermittent cyclic compression (a) B1, (b) B2 and (c) B3.

Figure 4-31 compares the specific dissipated energy (SDE) at different strains for the bimodal syntactic foams with various proportions of small and large CM particles. It shows that the specific dissipated energy increases with the starting strain in the elastic region and fluctuates in the plateau region. The highest SDE value is also obtained at the 5th intermittent loading cycle in each syntactic foam, when the starting strain the hysteresis loops is close to the yield strain of the syntactic foams. Overall, the specific dissipated energy of the bimodal syntactic foam is apparently related to the strength of the syntactic foam. The strongest syntactic foam B1 presents the highest SDE, while the syntactic foams B2 and B3, with a similar strength present the comparable SDE values.

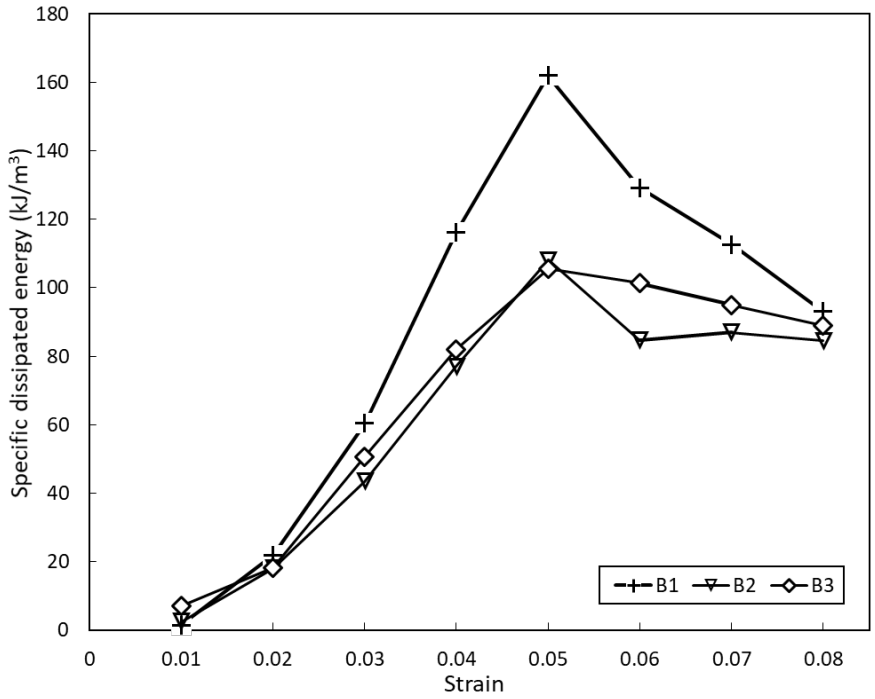

Figure 4-31 Hysteretic dissipated energy of each unloading-loading cycle of the bimodal syntactic foams.

4-32 compares the specific damping capacity (SDC) of the bimodal syntactic foams B1~B3 in all the unloading-loading cycles. Their tendencies are similar to those of the

monomodal syntactic foams and syntactic foam toughened with Al particles. Excluding the first unloading-loading cycle at the strain of 0.01, of which the SDC is small, the SDC does not change much for any particular syntactic foam in the subsequent unloading-loading cycles. Although these three bimodal syntactic foams have various volume proportions of small and large CM particles, their SDC values are nearly constant, which is approximately 0.09. This is because they have a similar total volume percentage of CM particles. Compared with syntactic foams M1~M3 and T1~T4, the bimodal syntactic foams have the highest volume percentage of CM particles, which lead to the highest SDC value. Hence, it further confirms that the damping capacity is somewhat related to the volume percentages of the Al matrix and the CM particles in the syntactic foam.

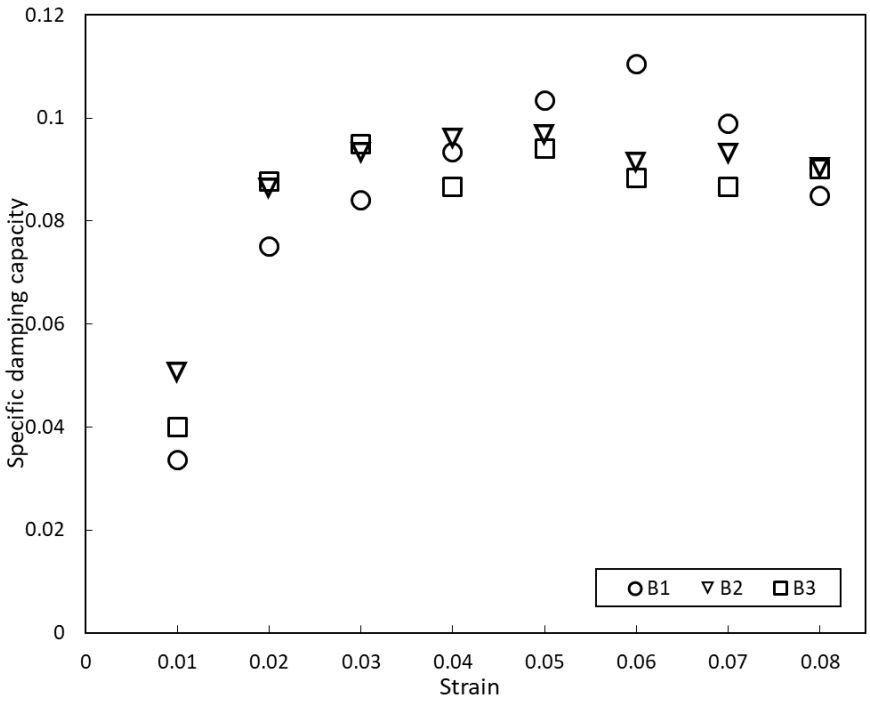

Figure 4-32 Specific damping capacity of each unloading-loading cycle of the bimodal syntactic foams.

4.3.4 Relationship between dissipated energy and applied stress

The specific damping capacity in cyclic loading describes the hysteretic energy dissipation relative to the elastic energy involved in the loading cycle. This elastic energy is the amount of recoverable energy in the unloading-loading cycle and can be expressed by:

$$W_E = \frac{1}{2}\sigma\Delta\varepsilon = \frac{\sigma^2}{2E} \quad (4\text{-}1)$$

where σ is the stress at which the unloading-loading cycle is conducted and $\Delta\varepsilon$ is the elastic strain produced in the cycle, which is approximately equal to the stress divided by the elastic modulus of the syntactic foam, E. As all the syntactic foam specimens have nearly the same elastic modulus (see 4.3.1 to 4.3.3), the elastic energy involved in cyclic loading is solely determined by the stress of the cyclic loading.

The specific damping capacity of any particular syntactic foam measured at strains between 0.02 and 0.08 does not vary much (see Figures 4-23, 4-29 and 4-32). It means that the ratio between the dissipated energy by hysteresis loss, W_D, and the elastic energy involved in the loading cycle, W_E, is nearly a constant. Like the elastic energy, the dissipated energy at strains between 0.02 and 0.08 is also proportional to the square of the applied stress of the cyclic loading, σ^2.

However, the specific damping capacity of the first hysteresis loop measured at the strain of 0.01 in the intermittent cyclic compression is considerably lower than those of the subsequent hysteresis loops (see Figures 4-23, 4-29 and 4-32). It is appreciated that the first compression cycle was conducted at a relatively low stress. It seems that

this low stress amplitude is not sufficient to initiate the main energy dissipation or damping mechanism prevalent at higher stress amplitudes in the subsequent hysteresis loops. This is because the low-stress amplitude does not cause enough damages in the CM particles in the syntactic foam for energy dissipation. The CM particles either survive at the low-stress amplitude without damage, or the low-stress amplitude is only sufficient to remove the micro-defects in the syntactic foam.

It is worth noting that the specific damping capacity is one of several parameters that are used to quantify the damping property of a material. Depending on the measurement methods (such as torsion pendulum, suspended beam, dynamic mechanical thermal analyser, piezoelectric ultrasonic vibration, decay and resonant vibration), a variety of parameters, including loss angle (φ), loss tangent (tan φ), inverse quality factor (Q^{-1}), loss factor (η), logarithmic decrement (δ) and specific damping capacity (ψ), are used to characterise the damping capacity. Although these parameters are sensitive to frequency and temperature, they are interchangeable with a proper conversion in cases of relatively small damping capacity (tan $\varphi < 0.1$) by the following equation (Lu et al. 2009):

$$\varphi \approx \tan\varphi = Q^{-1} = \eta = \frac{\psi}{2\pi} \approx \frac{\delta}{\pi} \qquad (4\text{-}2)$$

The order of magnitude of the damping capacity measured in this study is comparable to those measured by Cox et al. (2014), Licitra et al. (2015) and Katona et al. (2019) on Al matrix syntactic foams reinforced with hollow Al_2O_3, SiC or Al_2O_3-SiO_2 particles using dynamic mechanical analyser.

4.3.5 Effect of interfacial surface area

The damping at the CM particle/Al matrix interface is not considered to be a significant factor for the dissipated energy under cyclic loading. The interfacial area between the CM particles and the Al matrix is equal to the total surface area of the CM particles. Table 4-6 shows the total surface area of syntactic foams M1~M3, calculated from the surface weighted mean diameters (D (3. 2)). The interfacial area between the CM particles and the Al matrix in syntactic foam M1 is nearly twice and three times of that of syntactic foams M2 and M3, respectively. The average specific damping capacity values of syntactic foams M1, M2, and M3, however, are very similar. It demonstrates that the interface damping is not a significant damping mechanism in the syntactic foams under cyclic loading. Previous research has concluded that interface damping only plays a dominant role MMCs at elevated temperatures (Zhang et al. 1994a).

Table 4-6 Total surface area of CM particles in three monomodal syntactic foams

Syntactic foam	Surface area of CM particles (mm^2)
M1	20455
M2	12199
M3	6212

In fact, Figure 4-33 shows that the average specific damping capacity between the strains of 0.02 to 0.08 for each type of syntactic foam is proportional to the CM volume percentage. It confirms that the energy dissipation in cyclic loading mainly occurs inside the CM particles. The energy dissipation of metal matrix syntactic foam under intermittent cyclic loading is possibly due to the damage of the CM particles. Although this damping mechanism is seldom discussed in MMCs or MMSFs, it is discussed more commonly in the damping analysis of polymer composites under cyclic fatigue

loading, involving energy dissipation in matrix cracks, broken filter material and debonding (Idriss et al. 2013).

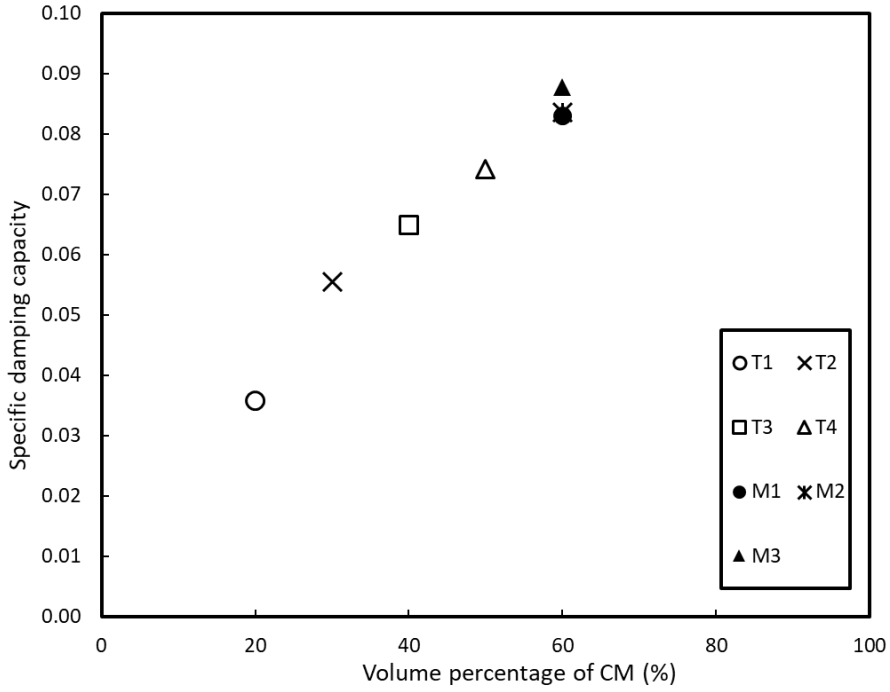

Figure 4-33 Specific damping capacity vs CM volume percentage for the syntactic foams.

4.3.6 Summary

Hysteresis loops are evident in the stress-strain curves of all the syntactic foams under the intermittent cyclic compression, confirming that there is an energy dissipation in cyclic compression of the syntactic foams. The energy dissipation property of the syntactic foams can be described by the specific damping capacity (SDC), which is the ratio of the hysteretic dissipated energy to the elastic energy. The experimental results showed that the energy dissipation is due to the CM particles rather than interfacial damping between the CM particles and the Al matrix. The SDC value for all the syntactic foams is very small at the strain of 0.01 but is nearly a constant at strains between 0.02 and 0.08. The dissipated energy of syntactic foam is proportional to the square of the applied stress of the cyclic loading. The SDC is dependent upon the volume percentage of the CM particles within the syntactic foam.

4.4 Repetitive cyclic compressive behaviour

4.4.1 One-stage cyclic compression

4.4.1.1 Monomodal syntactic foams

Figure 4-34 shows the stress-strain responses of the syntactic foams M1, M2 and M3 under the repetitive cyclic compression at the stress amplitude of 30 MPa for 50 loading cycles. In order to amplify and compare the evolution of the hysteresis loops during cyclic loading, the 1st, 25th and 50th hysteresis cycles are shown in Figure 4-35. The evolution of the hysteresis loops during 50 loading cycles in all the three syntactic foams is similar. The initial hysteresis loop is wider than the subsequent hysteresis loops.

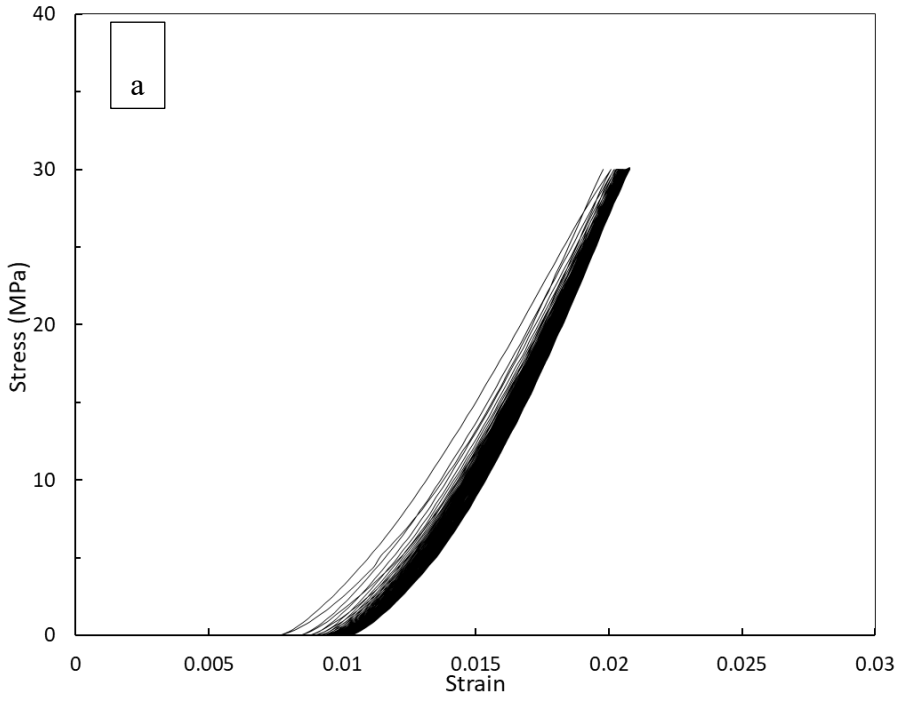

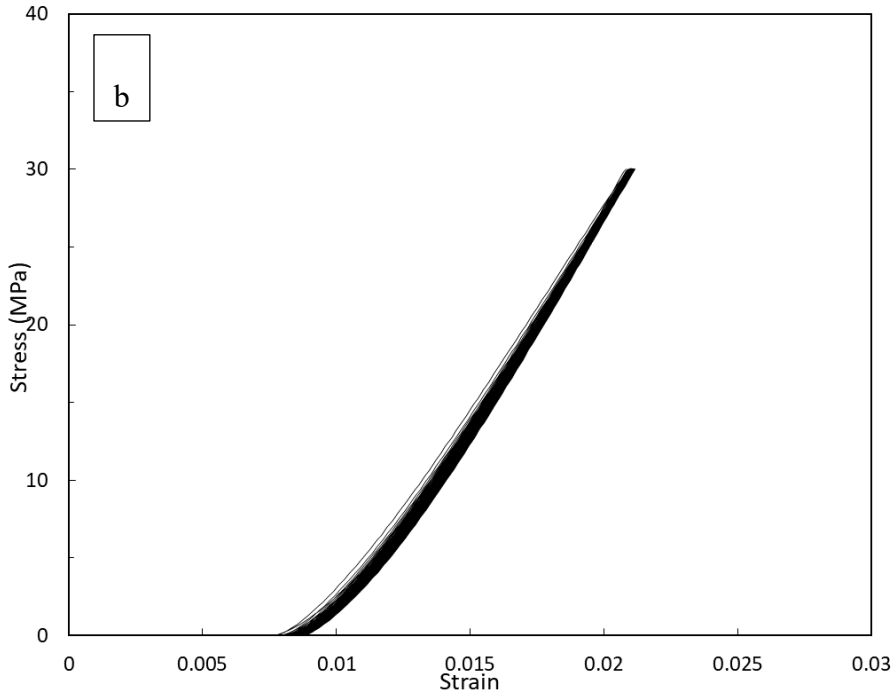

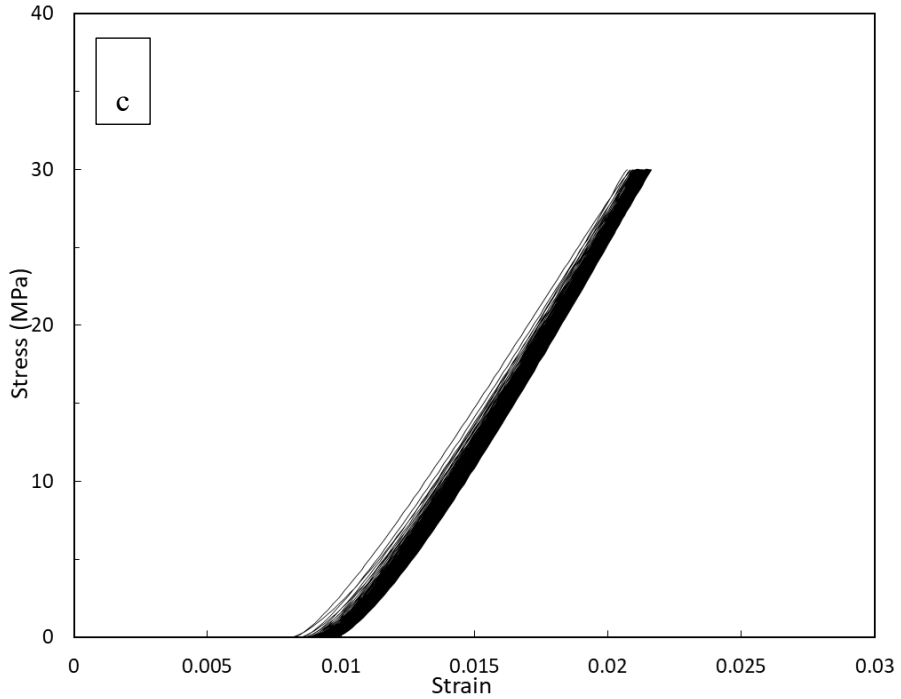

Figure 4-34 Stress-strain curves of the syntactic foams under repetitive cyclic compression at 30 MPa: (a) M1, (b) M2 and (c) M3.

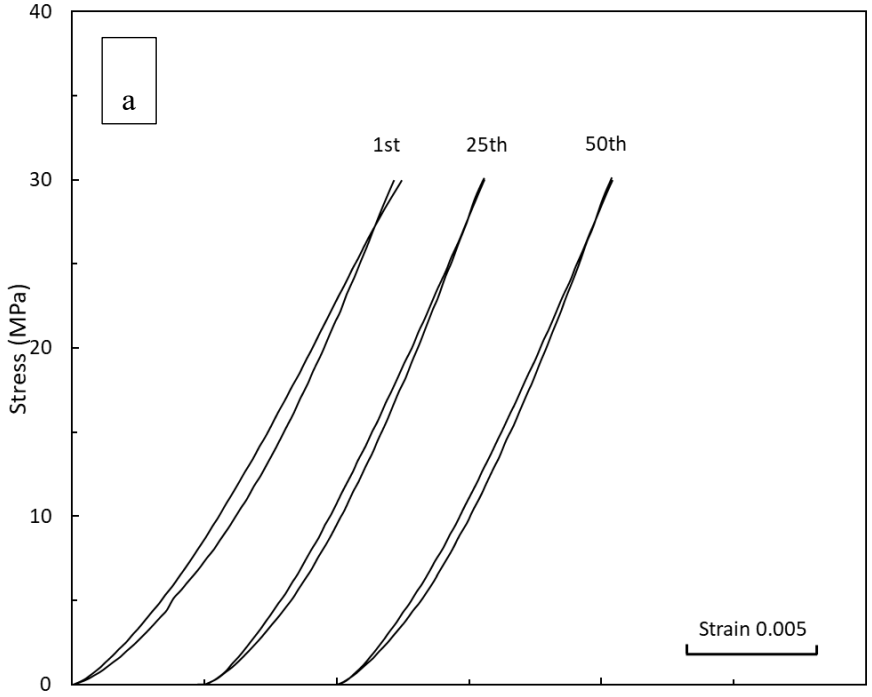
a
1st
25th
50th
Stress (MPa)
40
30
20
10
0
Strain 0.005

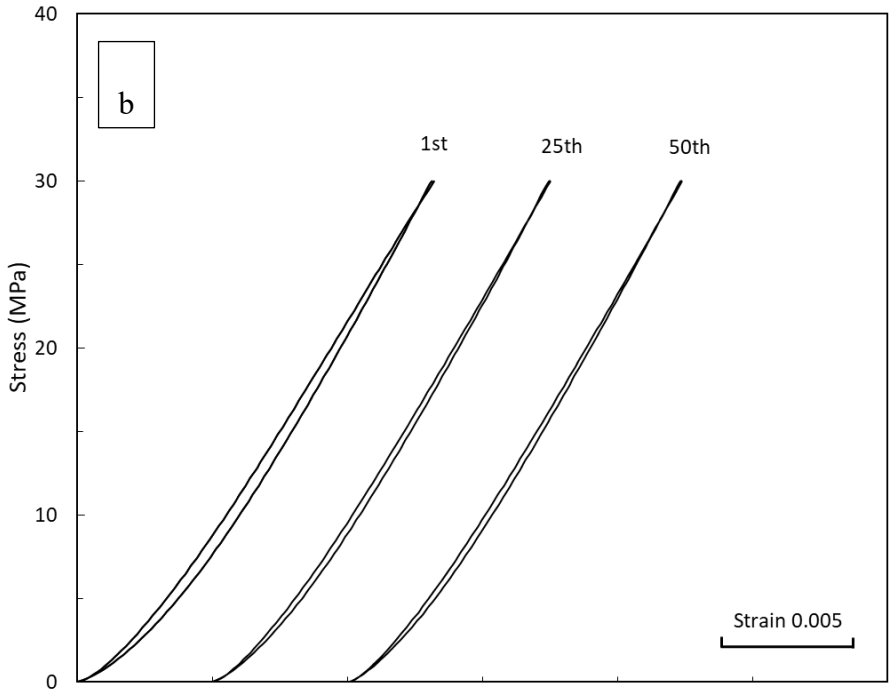
b
1st
25th
50th
Stress (MPa)
40
30
20
10
0
Strain 0.005

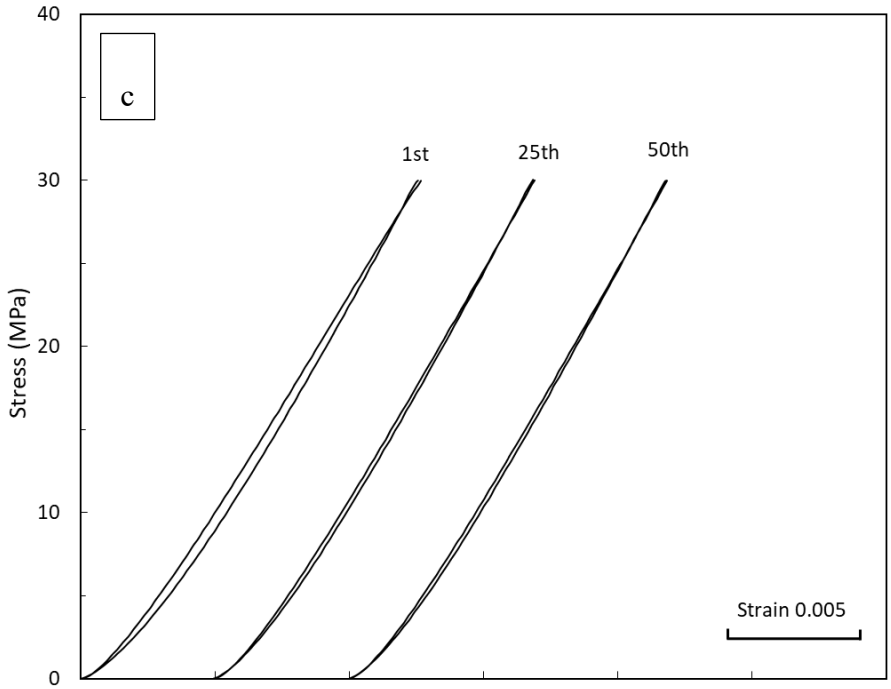

Figure 4-35 Hysteresis loops of the 1st, 25th and 50th cycles of syntactic foam: (a) M1, (b) M2 and (c) M3 in the repetitive cyclic compression, conducted at 30 MPa.

The specific dissipated energy and specific damping capacity of the 50 loading cycles at the stress amplitude of 30 MPa for the syntactic foams M1, M2 and M3 are compared in Figure 4-36 and Figure 4-37. All three syntactic foams have similar values of SDE and SDC at the initial loading cycle, approximately 12 kJ/m^3 and 0.08, respectively. These values matched well with the data of the syntactic foams obtained under intermittent cyclic compression. However, the SDE and SDC of syntactic foams decrease first rapidly in the subsequent loading cycles and then become nearly constant after the 20th loading cycle. The SDE values of the syntactic foams M1, M2 and M3 after 20th cycles are approximately 8, 5 and 3 kJ/m^3, respectively, and the SDC values are 0.065, 0.055 and 0.035, respectively. It is shown that the hysteretic energy dissipation in the repetitive cyclic compression is sensitive to the CM particles sizes.

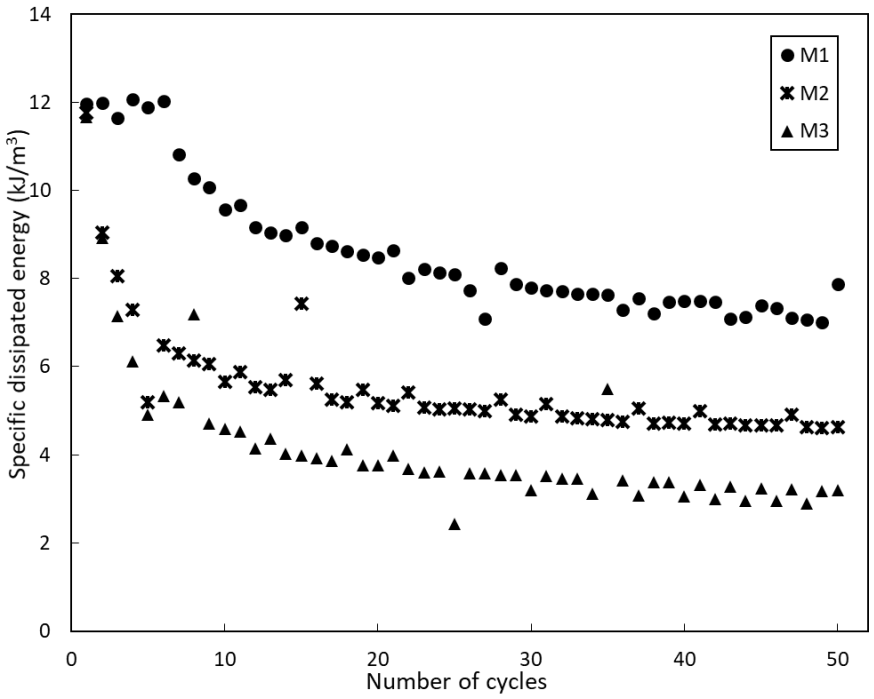

Figure 4-36 Evolutions of specific dissipated energy in repetitive cyclic compression at the stress amplitude of 30 MPa for different syntactic foams.

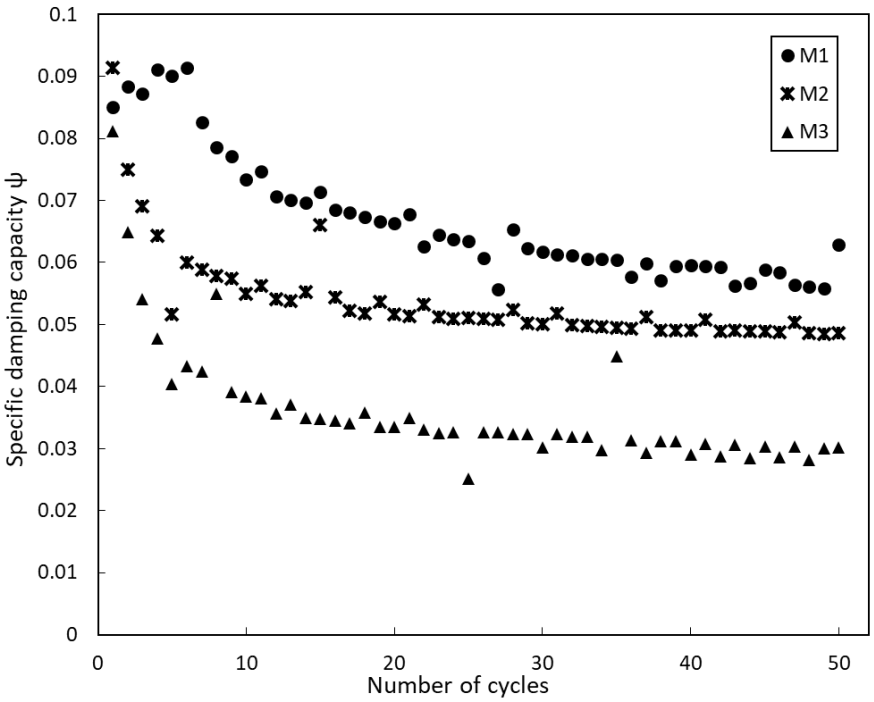

Figure 4-37 Evolutions of specific damping capacity in repetitive cyclic compression at the stress amplitude of 30 MPa for different syntactic foams.

The total strain produced after the 50 repetitive loading cycles in the three syntactic foams are shown in Figure 4-38. All three syntactic foams have a similar displacement after 50 repetitive loading cycles, although syntactic foam M2 has a slightly larger displacement.

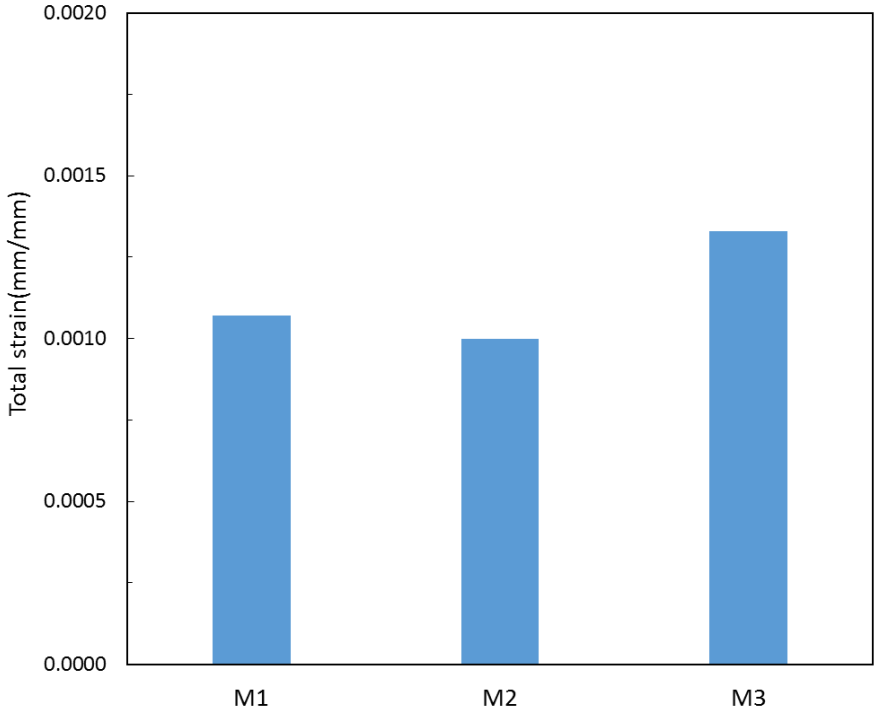

Figure 4-38 Total strain after 50 repetitive loading cycles at the stress amplitude of 30 MPa for different syntactic foams.

4.4.1.2 Syntactic foams toughened with Al particles

Figure 4-39 shows the stress-strain responses of the syntactic foams T1, T2, T3 and T4 under the repetitive cyclic compression at the stress amplitude of 60 MPa for 50 loading cycles. In order to amplify and compare the evolution of the hysteresis loops during cyclic loading, the 1st, 25th and 50th hysteresis cycles of the syntactic foams are shown in Figure 4-40. The evolution of the hysteresis loops during 50 loading cycles

in all the three syntactic foams is similar. The initial hysteresis loop is wider than the subsequent hysteresis loops.

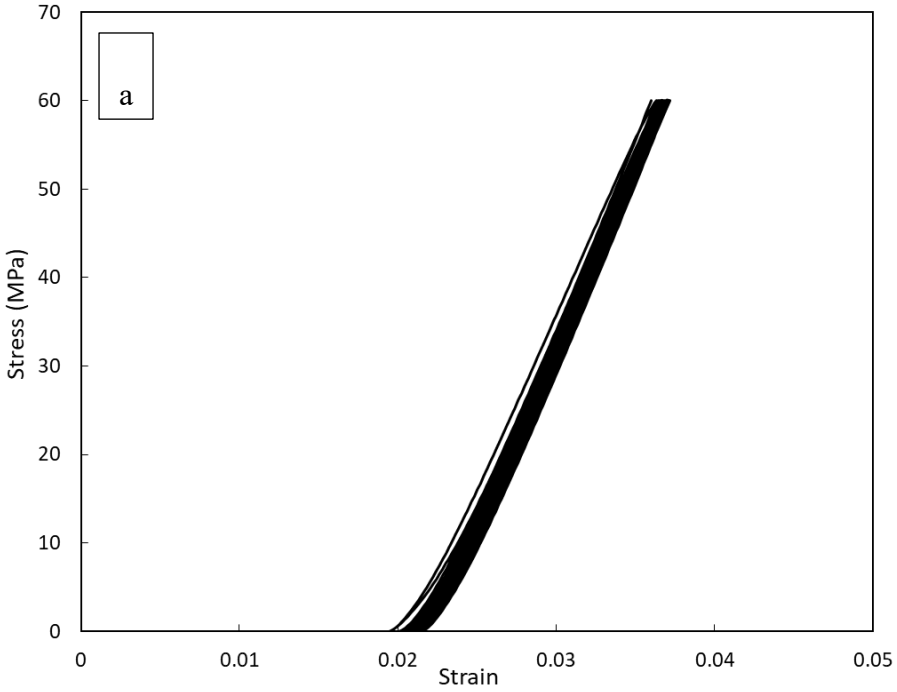

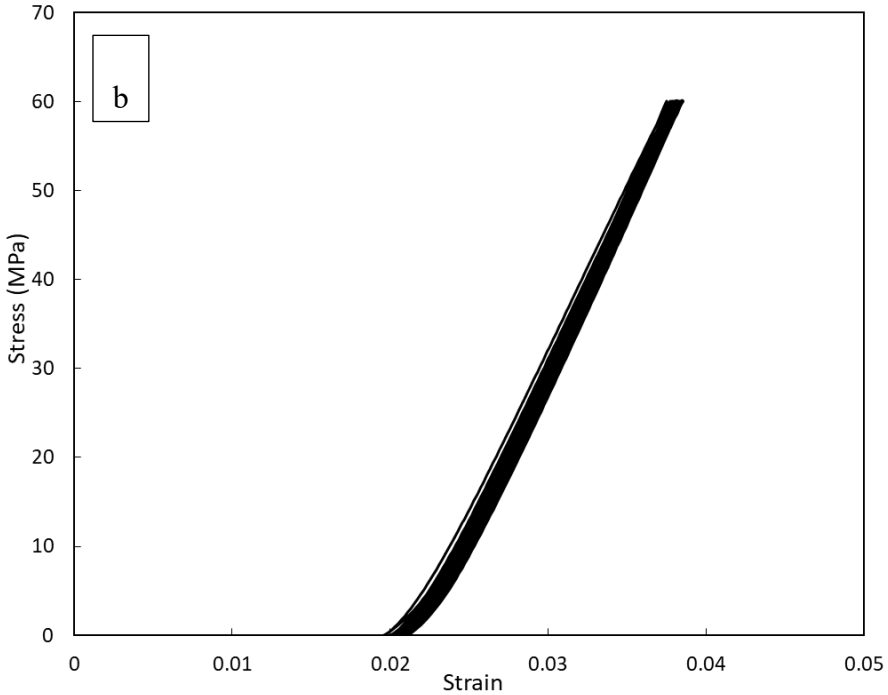

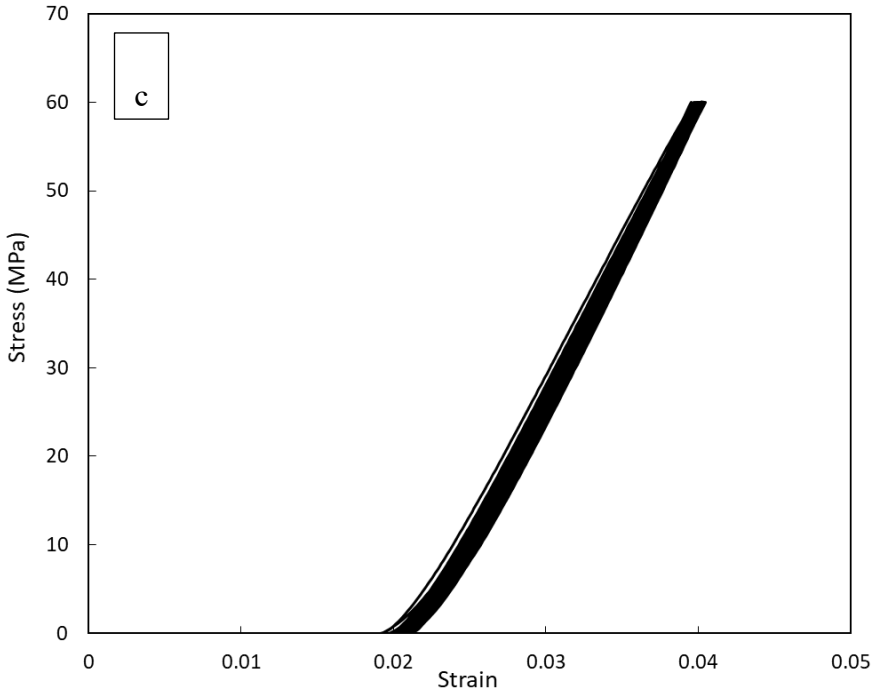

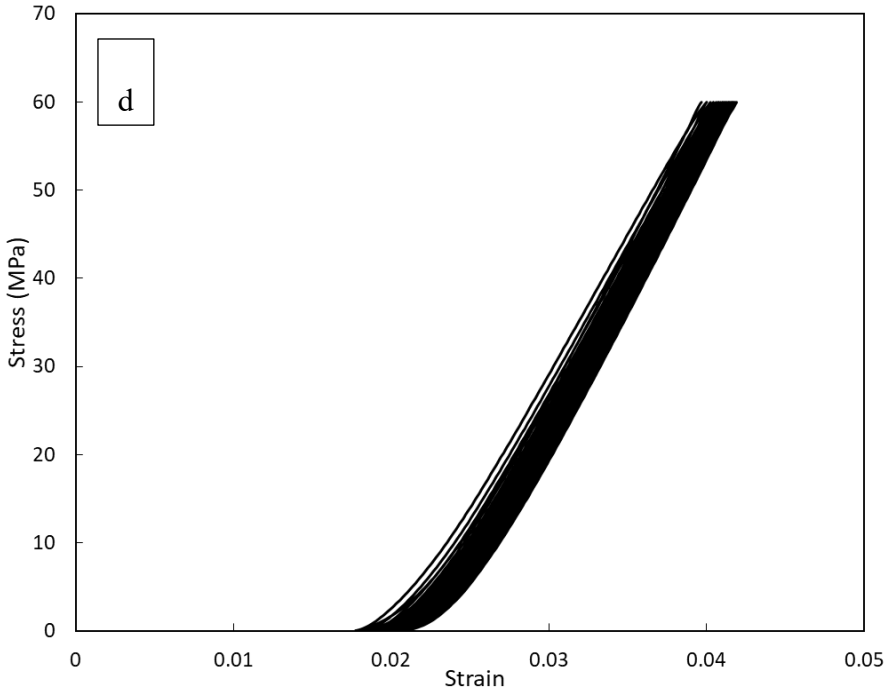

Figure 4-39 Stress-strain curves of the syntactic foams toughened with Al particles under repetitive cyclic compression at 60 MPa: (a) T1, (b) T2, (c) T3 and (d) T4.

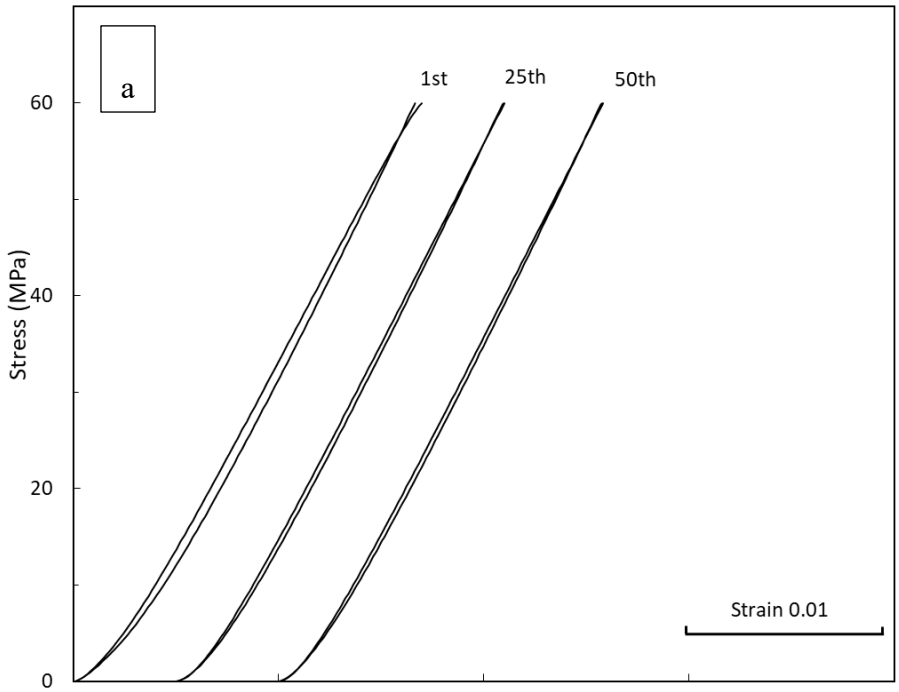
a
1st
25th
50th
60
40
20
0
Stress (MPa)
Strain 0.01

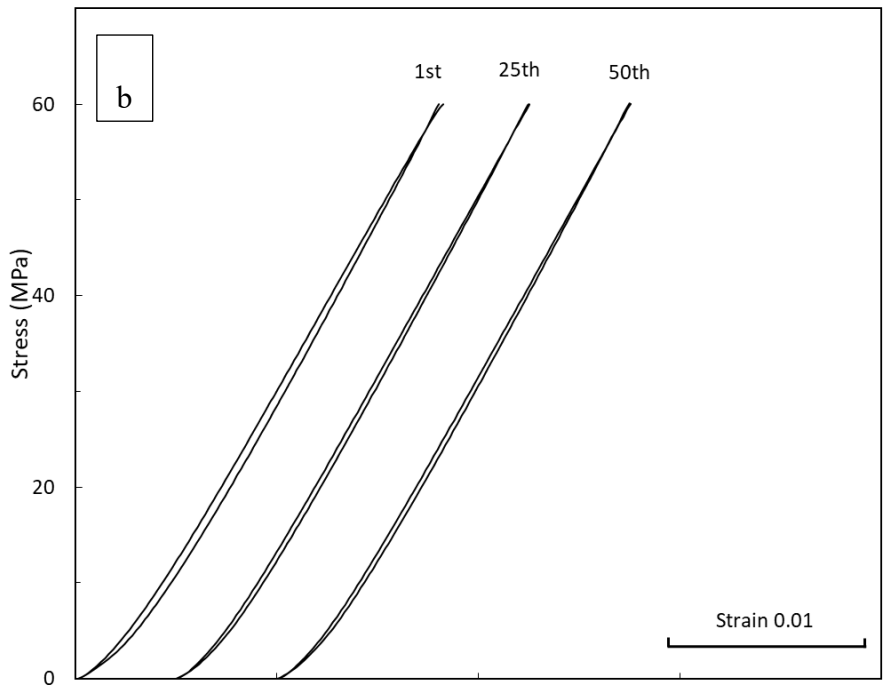
b
1st
25th
50th
60
40
20
0
Stress (MPa)
Strain 0.01

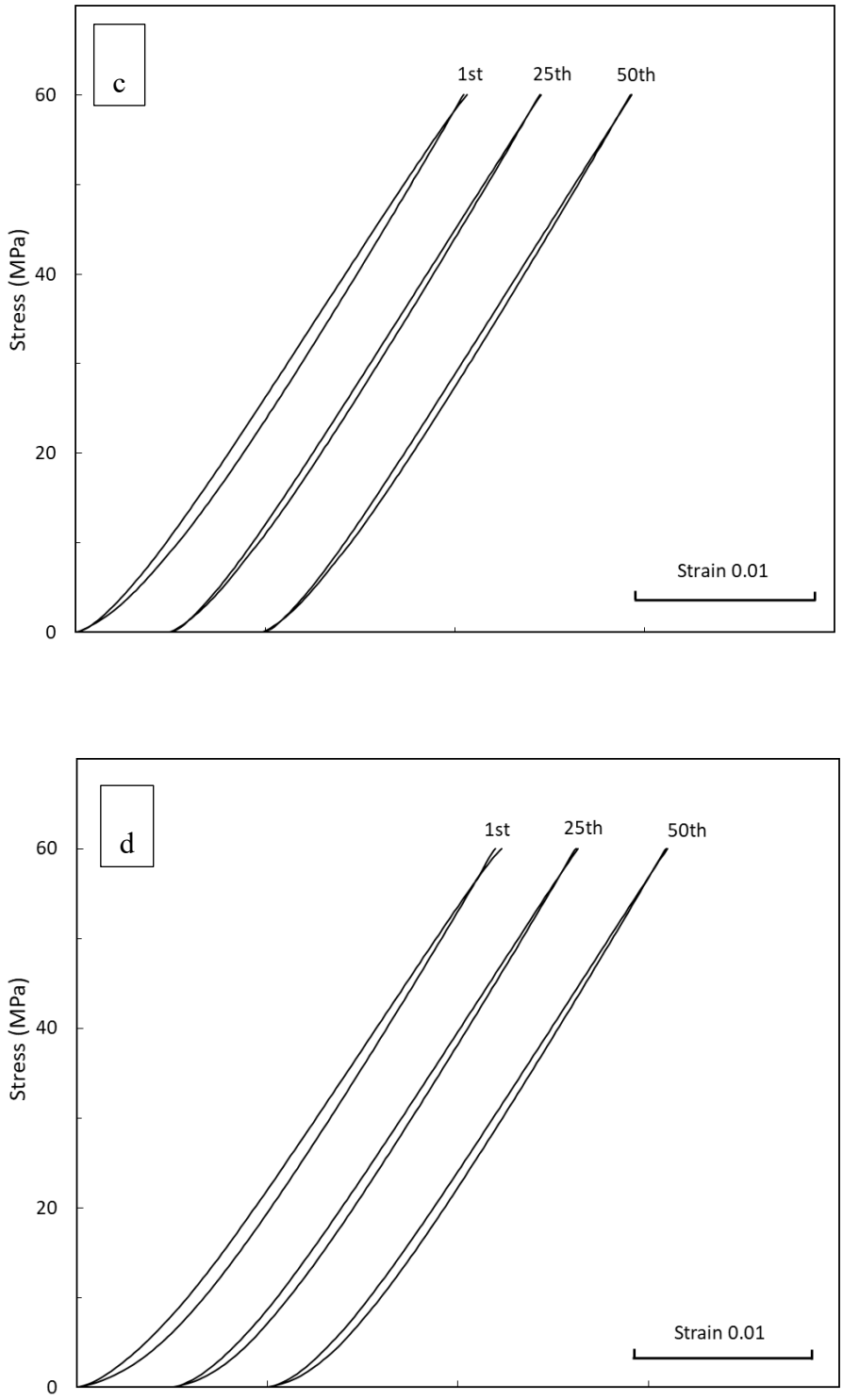

Figure 4-40 Hysteresis loops of the 1st, 25th and 50th cycles of syntactic foams: (a) T1, (b) T2, (c) T3 and (d) T4 in the repetitive cyclic compression, conducted at 60 MPa.

The specific dissipated energy and specific damping capacity of the 50 loading cycles at the stress amplitude of 60 MPa for the syntactic foams T1, T2, T3 and T4 are compared in Figures 4-41 and 4-42. Similar to monomodal syntactic foams, the SDE and SDC of the syntactic foam toughened with Al particles decrease approximately 30% in the first 20 loading cycles and then becomes nearly constant after the 20th loading cycle. The different SDE and SDC values between the syntactic foams T1, T2, T3 and T4 indicate that SDE and SDC are dependent upon the volume percentage of CM particles in the syntactic foam under repetitive cyclic compression. In addition, the total strain produced after the 50 repetitive loading cycles in the three syntactic foams are shown in Figure 4-43. It is shown that the total strain of the syntactic foam toughened with Al particles under the repetitive cyclic compression is related to the volume percentage of CM particles.

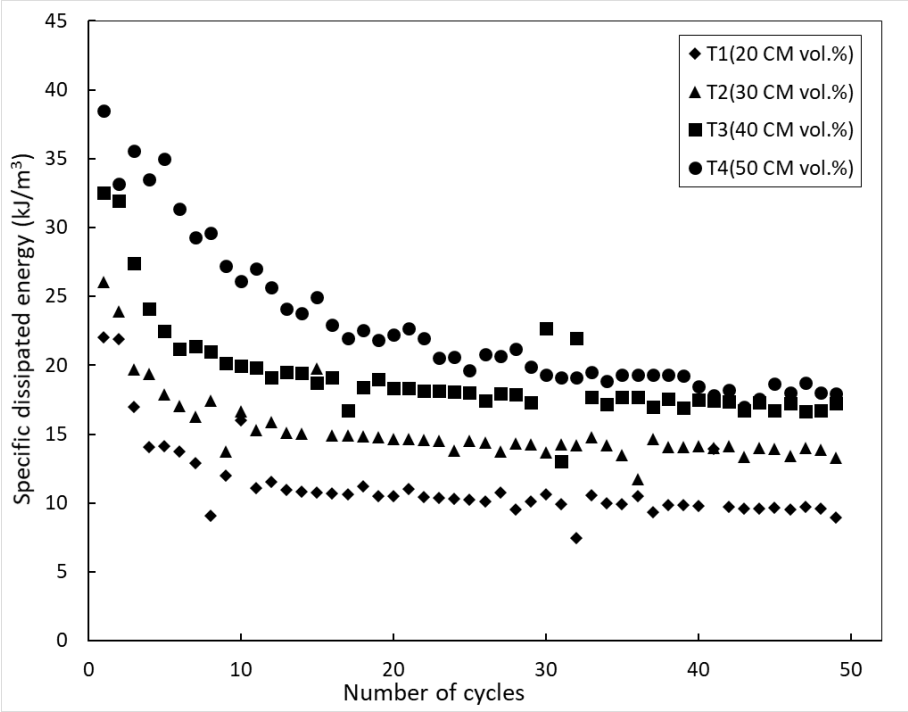

Figure 4-41 Evolutions of specific dissipated energy in repetitive cyclic compression at the stress amplitude of 60 MPa for different syntactic foams.

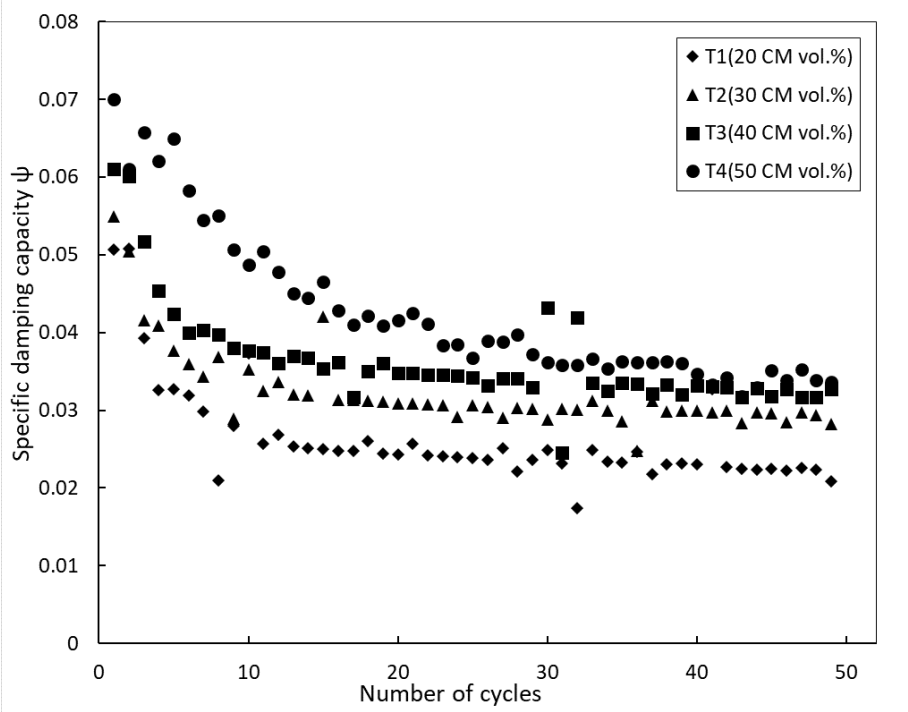

Figure 4-42 Evolutions of specific damping capacity in repetitive cyclic compression at the stress amplitude of 60 MPa for different syntactic foams.

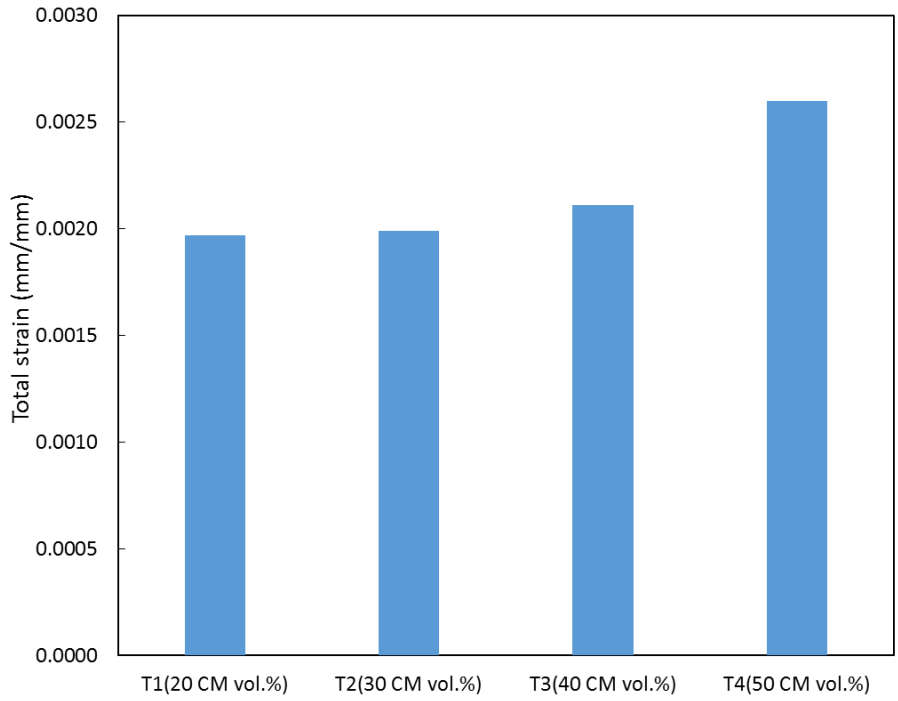

Figure 4-43 The total strain after 50 repetitive loading cycles at the stress amplitude of 60 MPa for different syntactic foams.

4.4.2 Two-stage cyclic compression

The stress-strain responses of the syntactic foam reinforced with the small CM particles (M1) under the repetitive cyclic compression are shown in Figure 4-44. The repetitive cyclic compression was conducted at the stress of 30 MPa, 60 MPa and 80 MPa in two stages. To amplify and compare the evolution of the hysteresis loops during cyclic loading in both stages, the 1st, 25th and 50th hysteresis cycles at each stress amplitude for both stage 1 and stage 2 loading are shown in Figure 4-45.

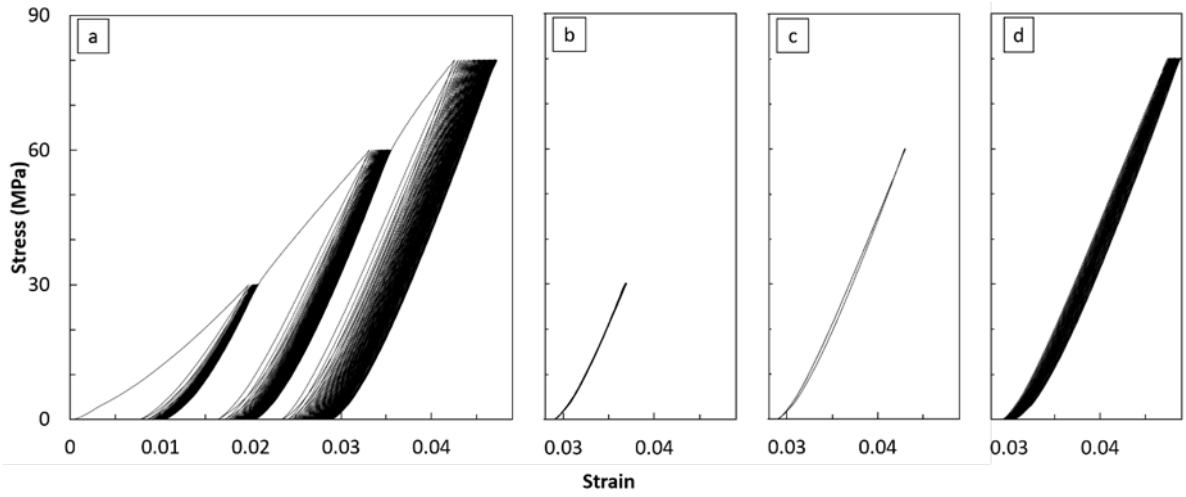

Figure 4-44 Stress-strain curves of the syntactic foam M1 under repetitive cyclic compression in (a) stage 1 and stage 2 at (b) 30 MPa, (c) 60 MPa and (d) 80 MPa.

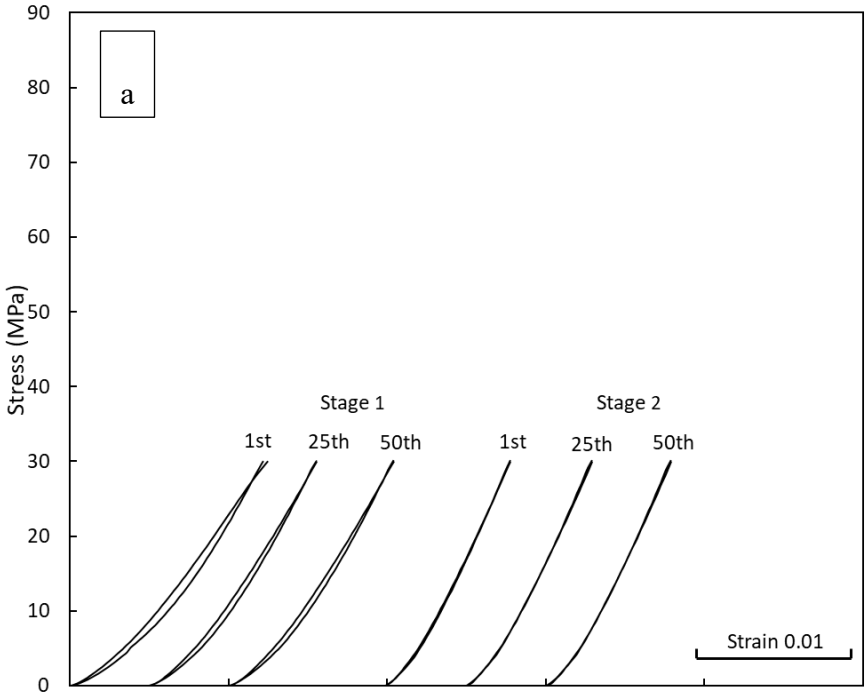
a
Stress (MPa)
0
10
20
30
40
50
60
70
80
90
Stage 1
Stage 2
1st
25th
50th
1st
25th
50th
Strain 0.01

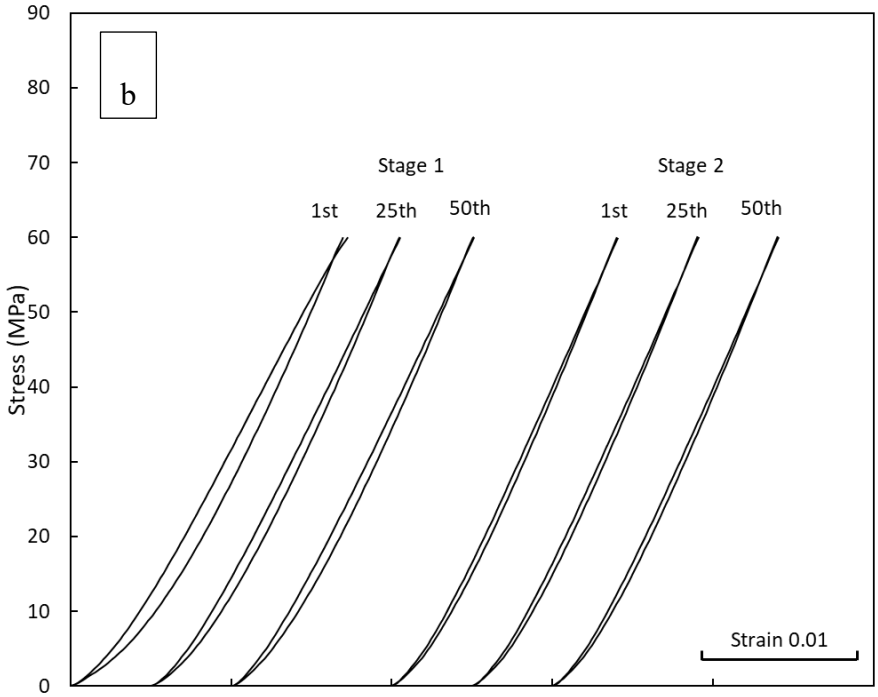
b
Stress (MPa)
0
10
20
30
40
50
60
70
80
90
Stage 1
Stage 2
1st
25th
50th
1st
25th
50th
Strain 0.01

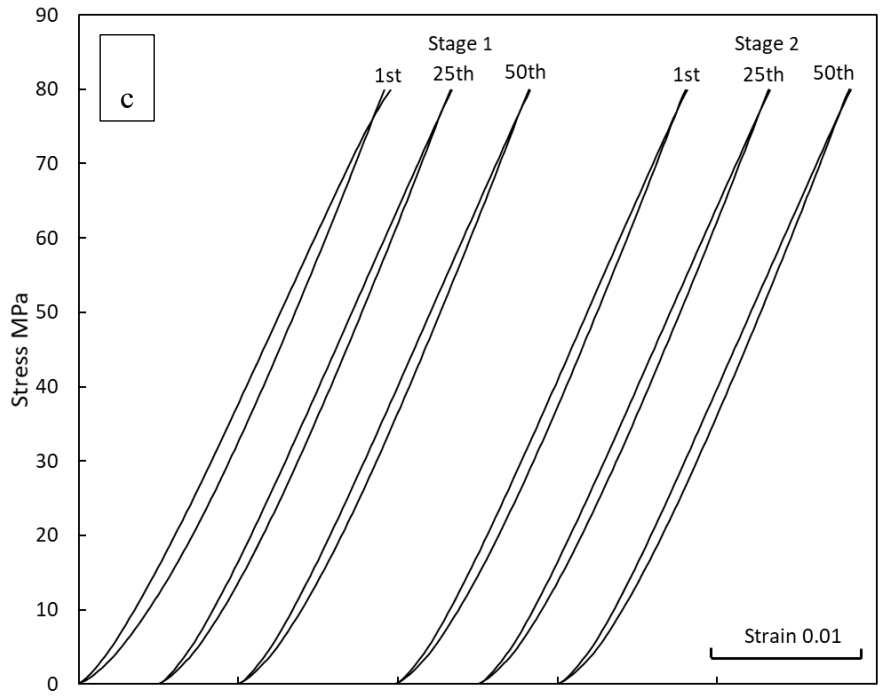

Figure 4-45 Hysteresis loops of the 1st, 25th and 50th cycles in the repetitive cyclic compression in stage 1 and stage 2, conducted at (a) 30 MPa, (b) 60 MPa and (c) 80 MPa.

Figure 4-44 shows that the behaviours of the hysteresis loops generated by the repetitive cyclic compression in stage 1 and stage 2 are significantly different, in spite of the same loading conditions. In stage 1, the displacements and the hysteresis loops are evident at all the three stress amplitudes of 30, 60 and 80 MPa. In stage 2, however, the large displacements and large hysteresis loops are only seen at the highest stress amplitude of 80 MPa in which the strain displacement is also less than those in stage 1 (see Table 4-7). Appreciable hysteresis loops are also exhibited at the intermediate stress amplitude of 60 MPa, but they are narrower than those in stage 1. The hysteresis loops at the lowest stress amplitude of 30 MPa in stage 2 are very small, with nearly overlapping unloading and loading paths.

Table 4-7 Strain after repetitive cyclic compression at different stress amplitudes.

	30 MPa	60 MPa	80 MPa
Stage 1	0.00107	0.0024	0.0047
Stage 2	0	0.0001	0.0031

The evolutions of the hysteresis loops in the two stages are demonstrated more clearly in terms of specific dissipated energy (Figure 4-46) and specific damping capacity (Figure 4-47). As a general observation, the specific dissipated energy tends to decrease with increasing number of cycles in stage 1 but remains unchanged in stage 2. In stage 1, the average magnitudes of the specific dissipated energy at the stress amplitudes of 30, 60 and 80 MPa are approximately 8, 30 and 50 kJ/m^3, respectively. They are similar to those observed in the intermittent cyclic compression. In stage 2, the average magnitudes of the specific dissipated energy at 30 and 60 MPa are reduced considerably to approximately 1 and 13 kJ/m^3, which are approximately 8% and 30% of the stage 1 values, respectively. The specific dissipated energy at 80 MPa in stage 2 follows the same trend as in stage 1, with a slightly lower average magnitude of 45 kJ/m^3.

The difference in energy dissipation behaviour between stage 1 and stage 2 is more visible in terms of the specific damping capacity (Figure 4-47). The specific damping capacity is not sensitive to the stress amplitude in stage 1. It varies in a relatively narrow range of 0.06~0.1. In stage 2, however, the specific damping capacity is very sensitive to the stress amplitude and has representative values of 0.005, 0.036 and 0.075 at the stress amplitudes of 30, 60 and 80 MPa, respectively.

The two-stage test results above demonstrate that the cyclic loading history has a direct influence on the hysteretic energy dissipation, depending on whether the stress amplitude is below, equal to or above the maximum stress the specimen has experienced previously. When the stress is above the previous stress levels experienced by the specimen (as shown in stage 1), the previous loading history has very little effect on the hysteretic energy dissipation; the specific dissipated energy and specific damping capacity are solely determined by the current stress amplitude. When the stress is equal to the maximum stress level experienced in the previous cycles (as shown in the case of 80 MPa in stage 2 vs stage 1), the current cyclic loading behaves as a continuation of the previous cyclic loading; the specific dissipated energy and specific damping capacity remain the same in both stages. When the stress is below the maximum stress level experienced in the previous cycles (as shown in the cases of 30 MPa and 60 MPa in stage 2), the previous loading history has a strong effect on the hysteretic energy dissipation; the specific dissipated energy and specific damping capacity become much lower than the previous stage; the lower the stress, the greater the reduction in the hysteretic energy dissipation.

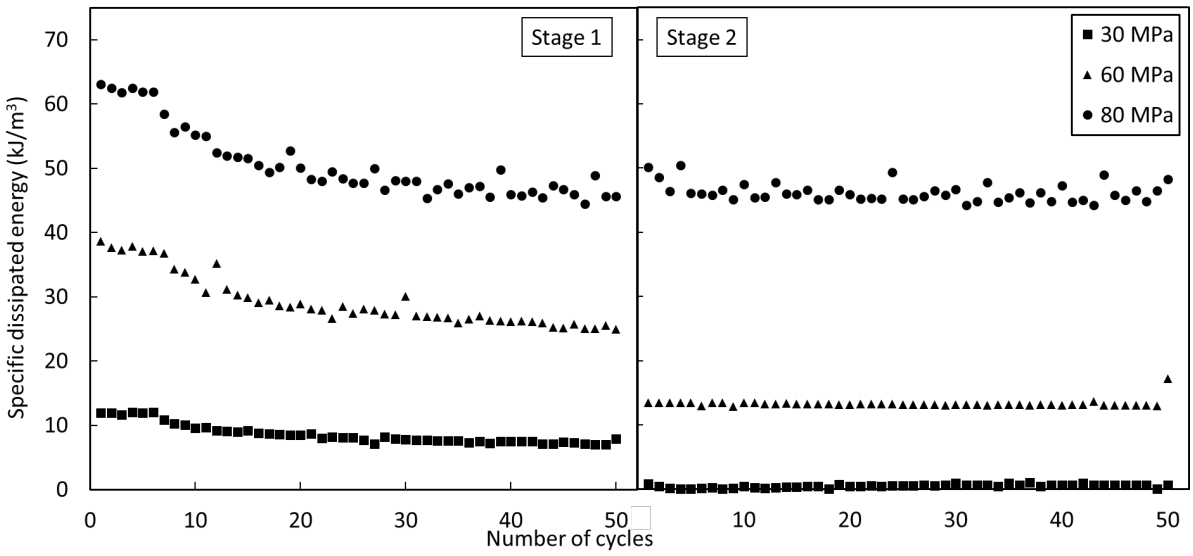

Figure 4-46 Evolutions of specific dissipated energy in repetitive cyclic compression at different stress amplitudes in stage 1 (left) and stage 2 (right).

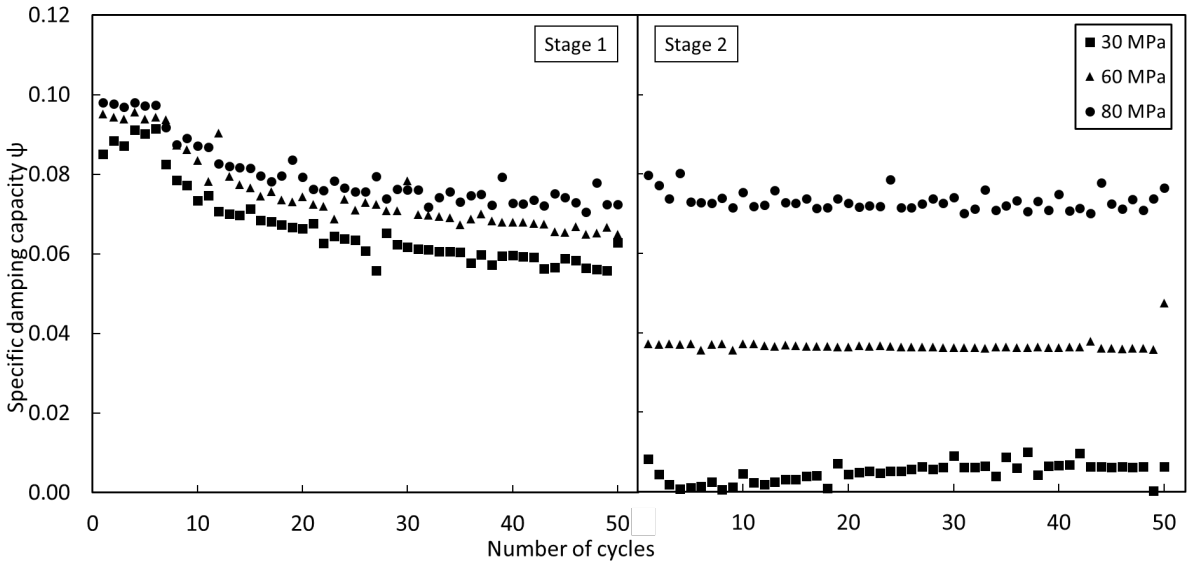

Figure 4-47 Evolutions of specific damping capacity in repetitive cyclic compression at different stress amplitudes in stage 1 (left) and stage 2 (right).

4.4.3 Damping mechanism

The damping behaviour of metal matrix syntactic foam (MMFS), is usually explained by applying the theory of internal friction in metal matrix composite (MMC), as MMFS can be classified as a kind of MMC. The internal friction of MMC is typically attributed to one or more of the following mechanisms: intrinsic damping of each constituent and the particulate/matrix interface damping (Lu et al. 2009). Previous research on the damping in aluminium matrix composite has suggested the dominant damping mechanisms as the dislocation damping (at low temperature) and grain boundary damping (at high temperature) of the metal matrix, intrinsic damping of the silicon carbide (SiC) particles, and the particulates/matrix interface damping (Li et al. 2016; Zhang et al. 1993a; Zhang et al. 1993b, 1994a; Zhang et al. 1994b). However, these mechanisms cannot explain the damping behaviour of MMFS in cyclic compression.

In the previous research, the damping measurement was conducted in the low-strain and low-stress conditions in the elastic region. The damping capacity can be defined as a material's ability to dissipate elastic strain energy during mechanical vibration. In the present study, the cyclic loading of syntactic foam was conducted at a large strain in which both metal matrix and CM particles deform plastically. The damping capacity of the syntactic foams indicates the ability to dissipate not only elastic strain energy but also plastic strain energy.

In section 4.3.5, the specific damping capacity of the syntactic foam is shown to be proportional to the CM volume percentage in the syntactic foam (Figure 4-33). It is also demonstrated that the energy dissipation in cyclic loading mainly occurs inside the CM particles such that the amount of the dissipated energy is directly correlated to

the volume percentage of the CM particles in the syntactic foam. Meanwhile, the interface between the CM particles and the matrix, which varies with the CM particle size, does not seem to play a part in the energy dissipation (Table 4-6). The repetitive cyclic compression shows that the mechanism of damping energy dissipated in the syntactic foam under cyclic compression is mainly due to damage, in particular the microcrack formation and propagation in the CM particles as reasoned below.

In the multiple repetitive cyclic compression of the syntactic foam M1, the stage 1 repetitive cyclic compression (Figure 4-44 a) shows that there is a permanent plastic deformation after each unloading-loading cycle and the amount of the plastic deformation is dependent on the stress at which the cyclic loading is conducted. The accumulative plastic strains after 50 cycles at the applied stresses of 30, 60 and 80 MPa are 0.0011, 0.0024 and 0.0047 (see Table 4-7), which correspond to plastic-deformation-caused energy absorptions of 33, 144 and 376 kJ/m^3, respectively. For each unloading-loading cycle, the average energy absorptions due to plastic deformation are 0.66, 2.88 and 7.52 kJ/m^3, respectively. In comparison, the average hysteretic energy dissipations at the stresses of 30, 60 and 80 MPa are 8, 30 and 50 kJ/m^3, respectively (Figure 4-46). Conversely, the hysteretic energy dissipations are approximately 12, 10 and 7 times of the plastic-deformation-caused energy absorptions, for the stresses of 30, 60 and 80 MPa, respectively.

Five observations on the hysteretic energy dissipation can be made from the above analyses:

1) The main contributor to the hysteretic energy dissipation is the CM particles.
2) The hysteretic energy dissipation is not due to permanent plastic deformation.

3) The process generating the hysteretic energy dissipation may contribute to the permanent plastic deformation.
4) The hysteretic energy dissipation is approximately proportional to the stress squared.
5) A higher stress results in a lower ratio between the hysteretic energy dissipation and the plastic-deformation-caused energy dissipation.

These observations indicate that the energy dissipation is caused by microcrack formation and propagation in the CM particles. Many microcracks have indeed been detected on CMs in the synaptic foam samples after repetitive cyclic loading (Figure 4-48). Cox et al. (2014) also observed cracks in the hollow SiC particles in an Al matrix syntactic foam after DMA test.

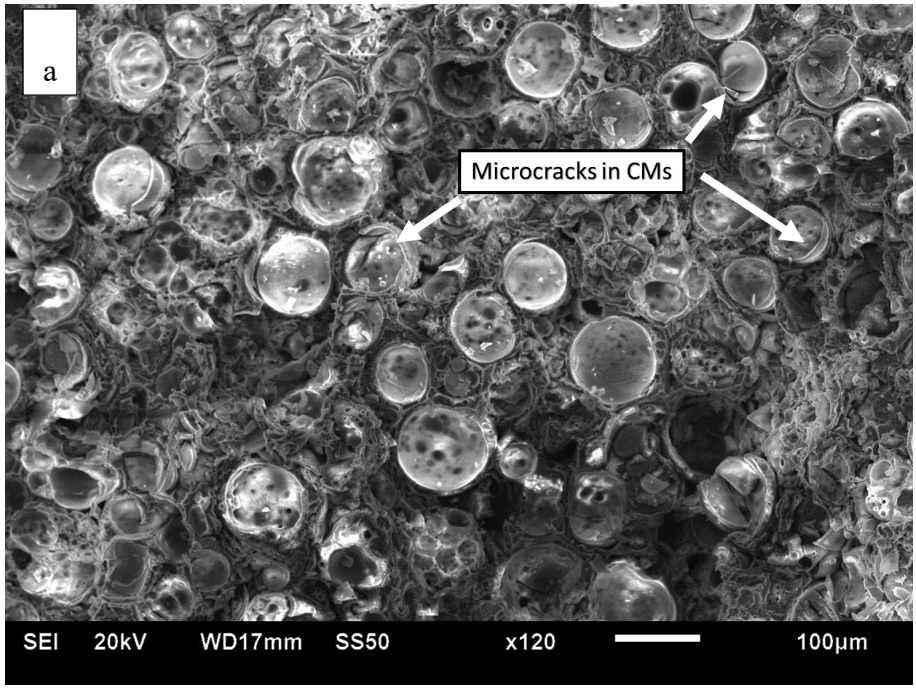

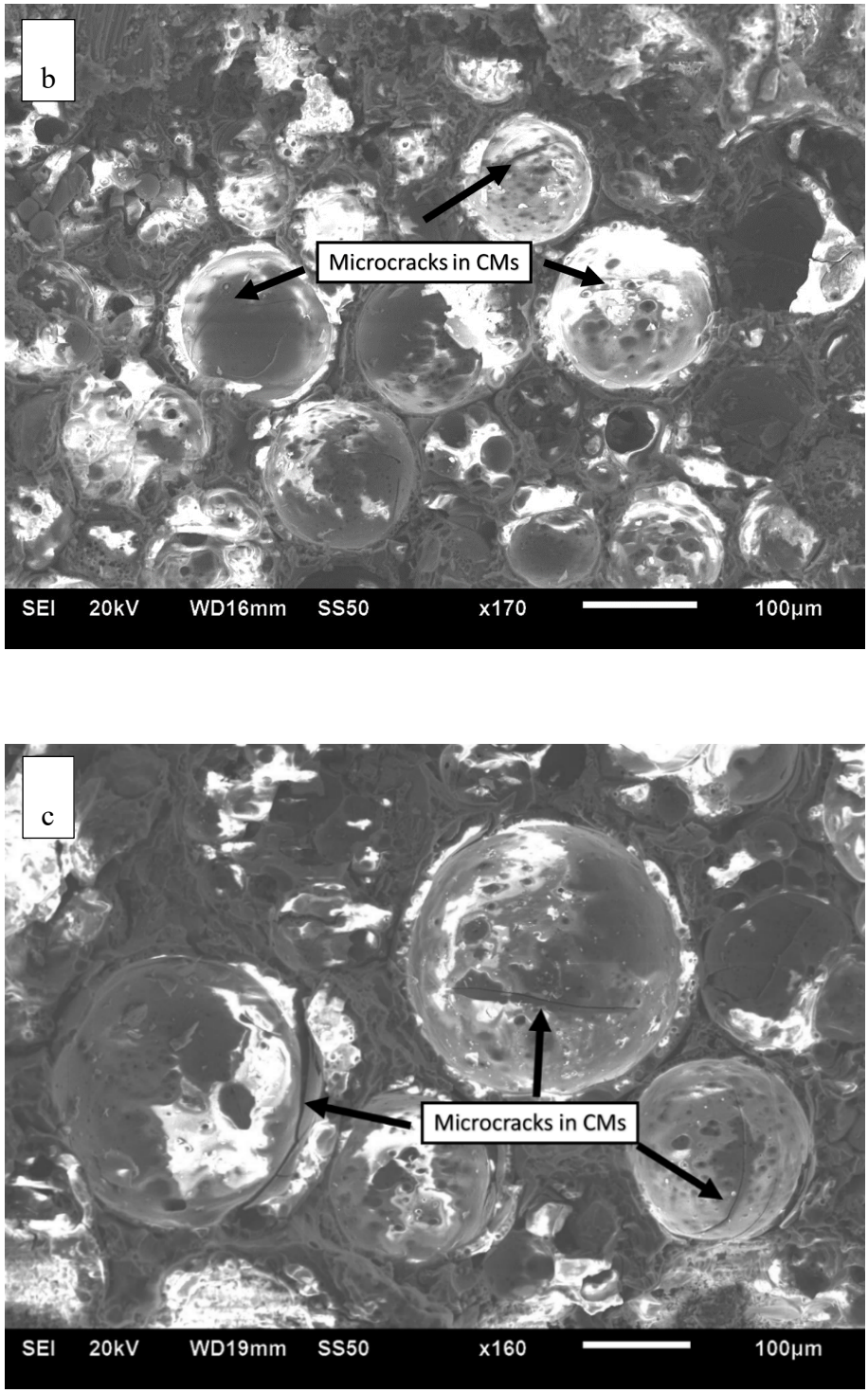

Figure 4-48 Scanning electron micrograph of an Al matrix syntactic foam with (a) 70-150 µm, (b) 125-250 µm , and (c) 250-500 µm CMs, after the cyclic compression.

According to the Griffith theory of brittle fracture, the critical stress required for crack propagation in a brittle material is proportional to the square root of the specific surface energy of the material, or the energy required to create the crack surfaces is proportional to the square of the applied stress, provided it is above the critical stress (Lawn 1993). The fact that the dissipated energy by hysteresis loss at strains between 0.02 and 0.08 is proportional to the square of the applied stress ($W_D \propto \sigma^2$) conforms to the Griffith theory. This provides a strong supporting evidence that the key mechanism of hysteretic energy dissipation is microcrack formation and propagation in the CM particles.

The microcrack formation and propagation in the CM particles during the cyclic loading can be described as follows. The metal matrix syntactic foam is essentially a cluster of inherently brittle CM particles interspersed with a metal matrix. As a characteristic of the infiltration casting process adopted in this work, most CM particles are in direct contact with their neighbouring CM particles. Stress concentrations will occur at these contact points and the local stress can be significantly higher than the global stress. When the global stress is above a certain level, say a third of the yield stress of the syntactic foam, the local stresses at some locations will reach the critical stress required for crack initiation and propagation in the CM particles. A higher global stress leads to more stress concentration and in turn more crack initiation and propagation. The energy absorbed in creating the crack surfaces is expected to be proportional to the square of stress, according to the Griffith theory. Once a microcrack develops across a CM particle during repetitive loading, fracture occurs and a small plastic deformation is formed. The permanent plastic deformation and the hysteretic energy absorption are the accumulative effects of

formation and propagation of all the microcracks inside CM particles. They are dependent on the local stress at the contact points between the CM particles, which in turn is dependent on the stress applied to the syntactic foam sample.

The different hysteretic energy dissipation behaviour in stage 2 from stage 1 cyclic loading at the low and intermediate stress levels can be well explained by the microcrack formation and propagation mechanism. After cyclic loading at 80 MPa for 50 cycles in stage 1, many stress concentration locations that can be activated at a stress below 80 MPa for microcrack propagation have disappeared due to localised plastic deformation. The numbers of microcracks that can form and propagate at stresses of 30 and 60 MPa are reduced, especially significantly at the lower stress. Only when the stress is equal to or above the maximum stress experienced in stage 1, more locations of stress concentration can be activated to form more microcracks and the new and existing microcracks can continue to propagate.

The microcrack formation and propagation mechanism of the CM particles under cyclic compression can also explain the fact that the syntactic foams M1, M2 and M3 have different damping decrements after 50 repetitive cyclic loading. Although the three syntactic foams have a similar CM volume percentage, different CM particle sizes lead to significantly different quantities of CM particles. In the early repetitive loading cycles, the three syntactic foams have comparable values of SDE and SDC because the numbers of microcracks in the CM particles are probably at the same level. However, with increasing repetitive loading cycles, some CM particles can no longer dissipate energy as the microcracks have propagated across the particles. Some new CM particles start to take part in microcrack propagations. The syntactic foam M1 has

a higher SDE and SDC at subsequent repetitive loading cycles because it has more CM particles, i.e., more potential microcracks for energy dissipation.

4.4.4 Summary

In one-stage cyclic compression, the monomodal syntactic foams and the syntactic foams toughened with Al particles conducted at different stress amplitudes show the same behaviour in their hysteresis loops. The 1st loop is larger than the subsequent loops. Their SDE and SDC also show a similar trend. They decrease rapidly in the first 20 cycles and then become nearly constant afterwards. The damping behaviour of the monomodal syntactic foams is sensitive to the CM particle sizes. The damping capacity of all the syntactic foams toughened with Al particles is determined by the volume percentage of the CM particles in the syntactic foams. The total strain of the monomodal syntactic foams after 50 repetitive compression cycles are comparable, while the total strain of the syntactic foams toughened with Al particles are dependent on the volume percentage of the CM particles.

In two-stage cyclic compression, both the SDE and SDC of syntactic foam M1 at the stress amplitudes of 30 and 60 MPa in the 1st stage are higher than that for the 2nd stage, while the SDE and SDC at the stress amplitude of 80 MPa are comparable in the two stages. The main damping mechanism of the syntactic foam during cyclic loading is microcrack formation and propagation in the CM particles.

4.5 Damping behaviour of syntactic foams under shockwaves

4.5.1 Strain response of monomodal syntactic foams

4.5.1.1 Strain amplitude

Figures 4-49~4-52 show the typical strain responses of the syntactic foams M1, M2 and M3, which were excited by the four different shockwaves caused by the different impulsive loads, respectively. The syntactic foam foams presented some interesting responses, even though the impulsive loads used to generate the shockwaves were small and limited. The strain responses of the syntactic foams indicated that the syntactic foams have been excited with vibrations by these four shockwaves. The strain amplitude of each syntactic foam was proportional to the impulsive load of the shockwave (see Figures 4-49~4-52). The three syntactic foams have a comparable strain amplitude under each shockwave due to the similar Young's modulus.

The shockwave is an excitation force that makes the syntactic foam specimen oscillate. The oscillation of the syntactic foam specimen decays exponentially over time, so it is a typical under-damped dynamic system. The behaviour is typical of a damped free oscillation. The time of the decay of the damping oscillation is dependent upon the strain amplitude for each syntactic foam. The damping ratio, however, is different among the syntactic foam specimens. Therefore, the damping capacity of the syntactic foams can be studied by systematically analysing the data of the damped free oscillations.

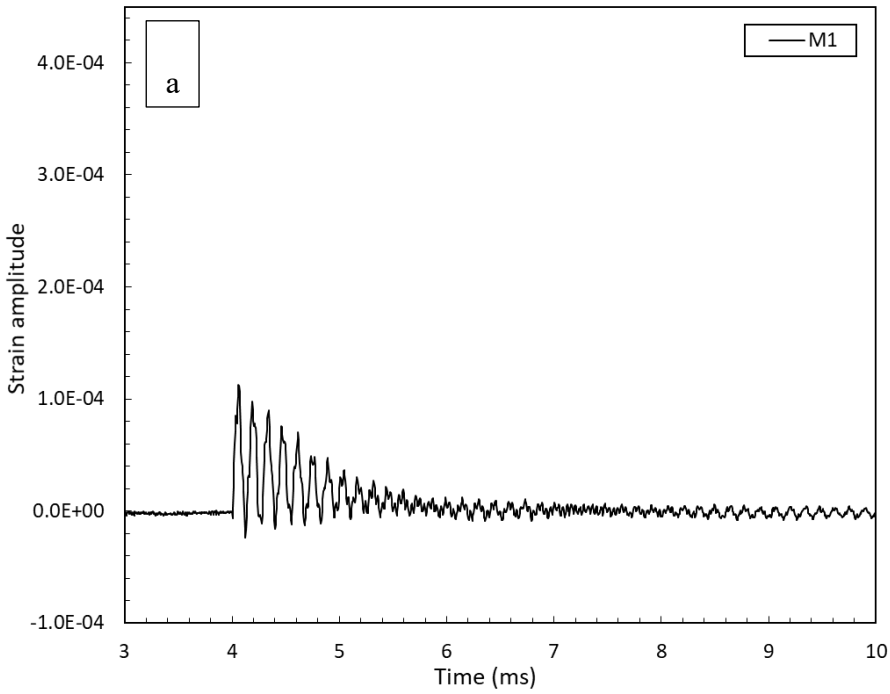
a
M1
4.0E-04
3.0E-04
2.0E-04
1.0E-04
0.0E+00
-1.0E-04
Strain amplitude
3
4
5
6
7
8
9
10
Time (ms)

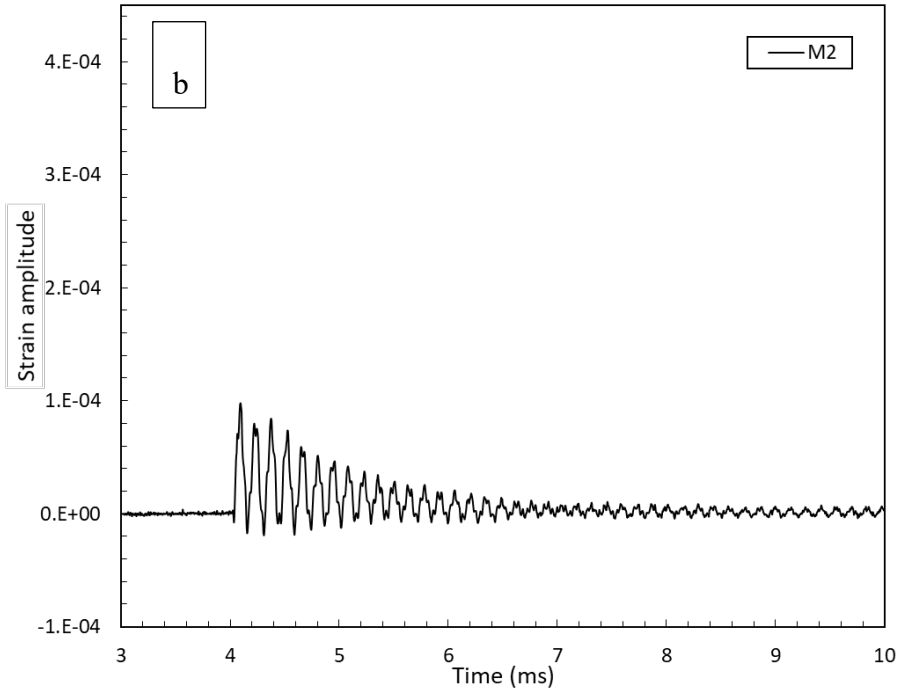
b
M2
4.E-04
3.E-04
2.E-04
1.E-04
0.E+00
-1.E-04
Strain amplitude
3
4
5
6
7
8
9
10
Time (ms)

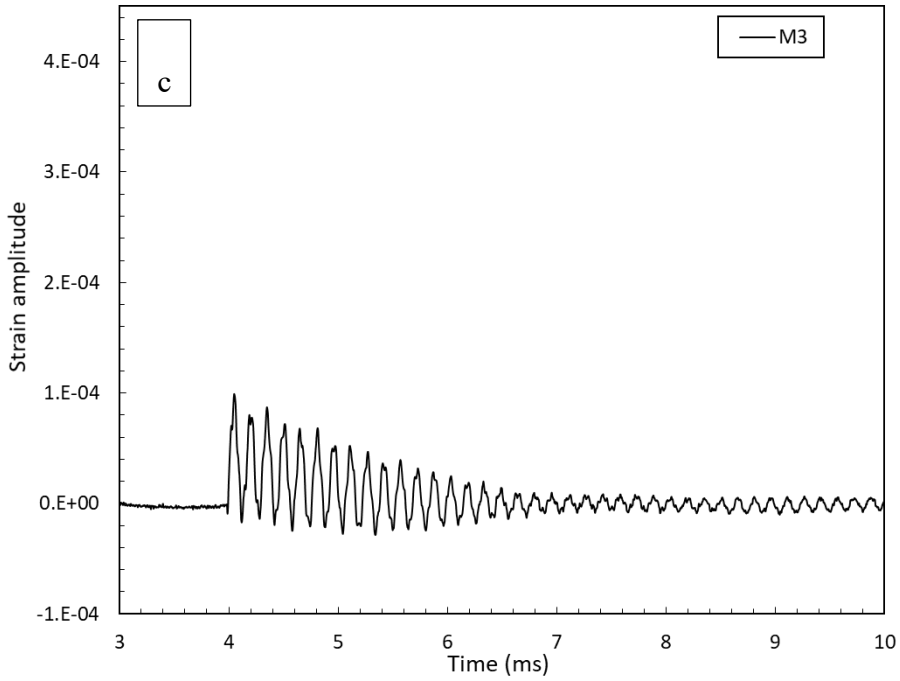

Figure 4-49 Typical strain responses of syntactic foams (a) M1, (b) M2 and (c) M3 excited by the shockwave A-0.6mm.

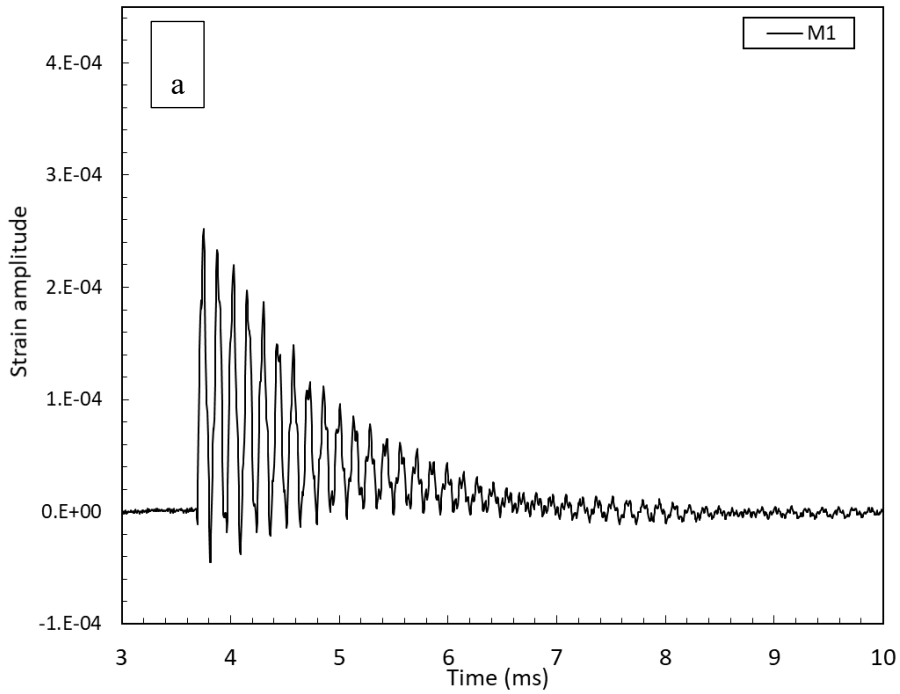

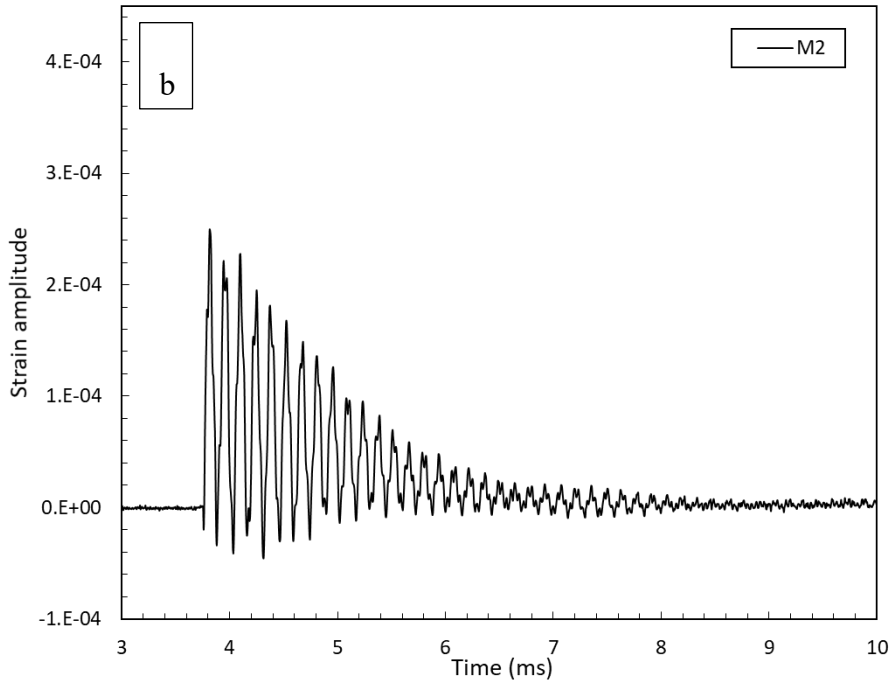

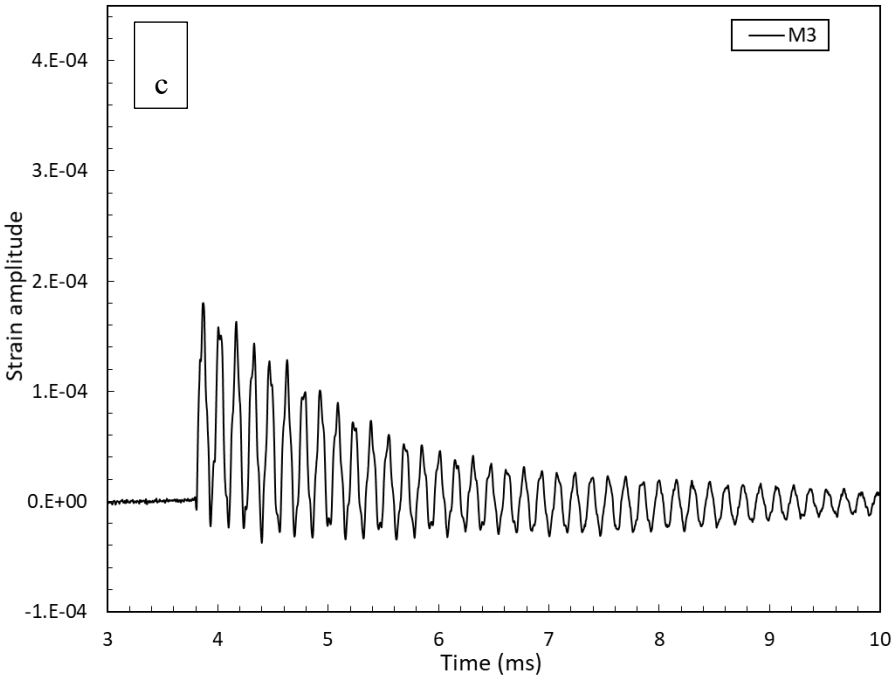

Figure 4-50 Typical strain responses of syntactic foams (a) M1, (b) M2 and (c) M3 excited by the shockwave A-0.22H.

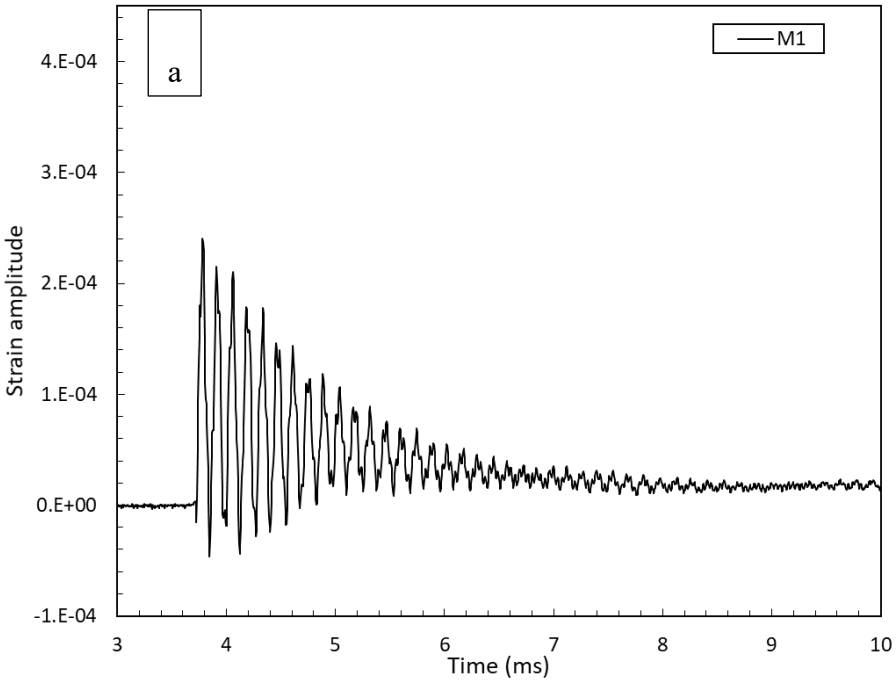
a
M1
4.E-04
3.E-04
2.E-04
1.E-04
0.E+00
-1.E-04
Strain amplitude
3
4
5
6
7
8
9
10
Time (ms)

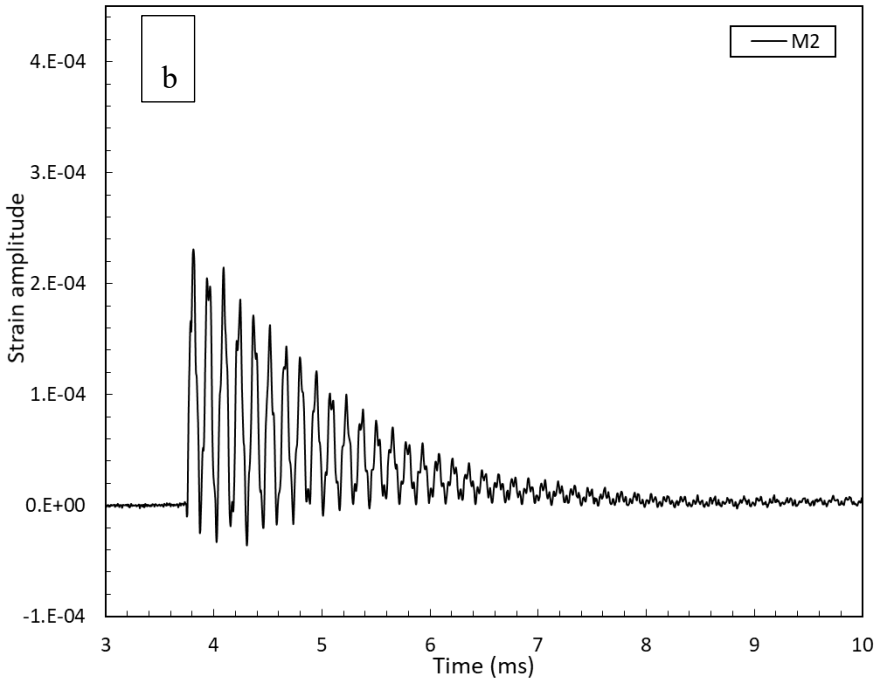
b
M2
4.E-04
3.E-04
2.E-04
1.E-04
0.E+00
-1.E-04
Strain amplitude
3
4
5
6
7
8
9
10
Time (ms)

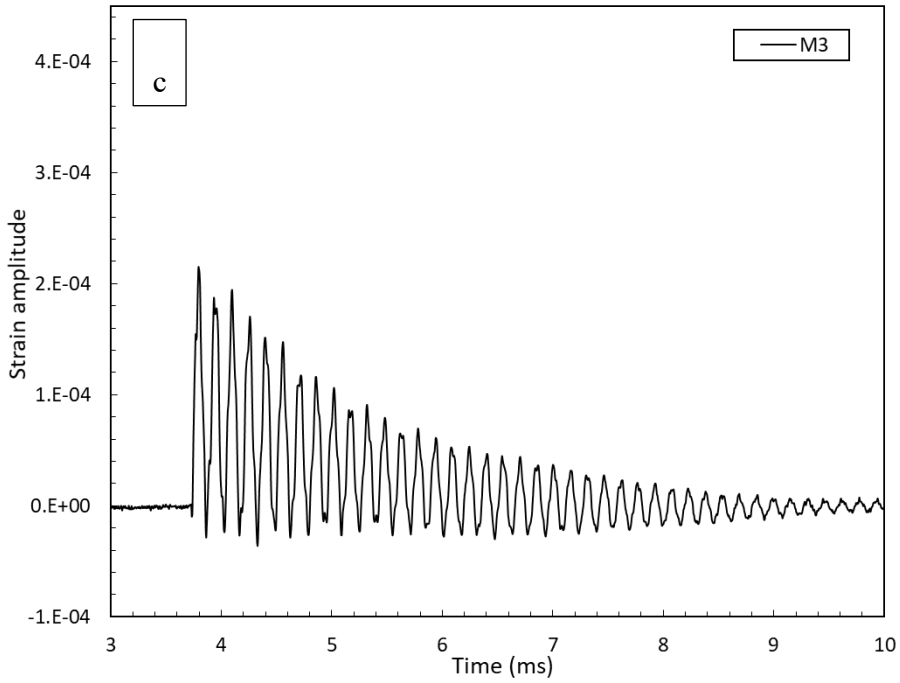

Figure 4-51 Typical strain responses of syntactic foams (a) M1, (b) M2 and (c) M3 excited by the shockwave A-0.22L.

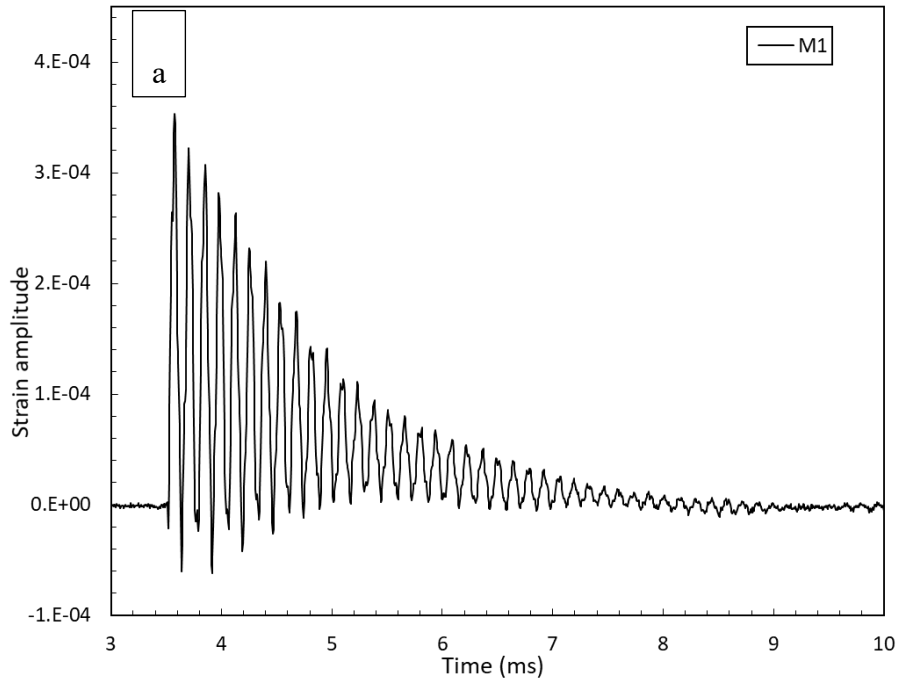

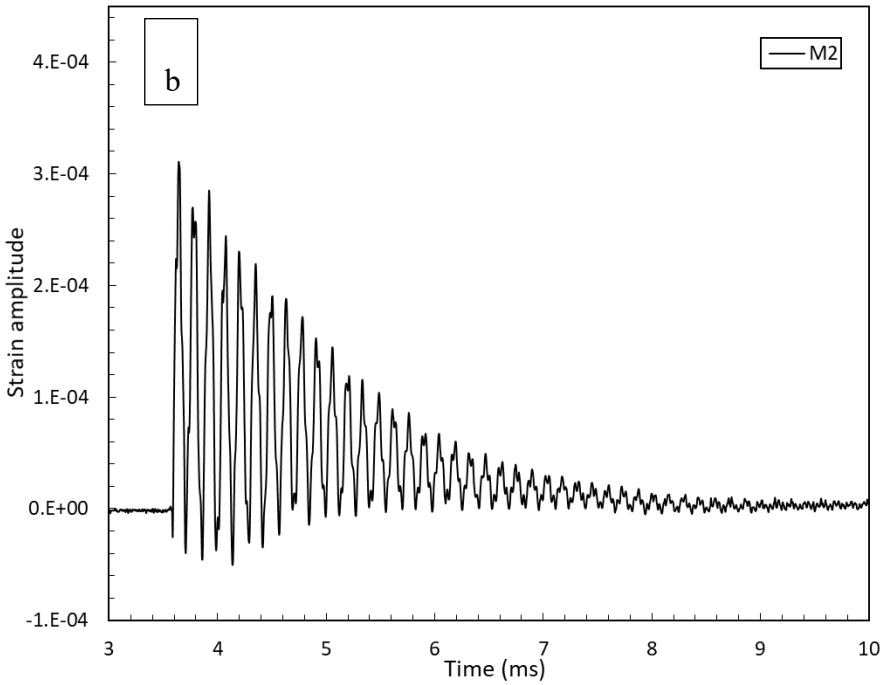

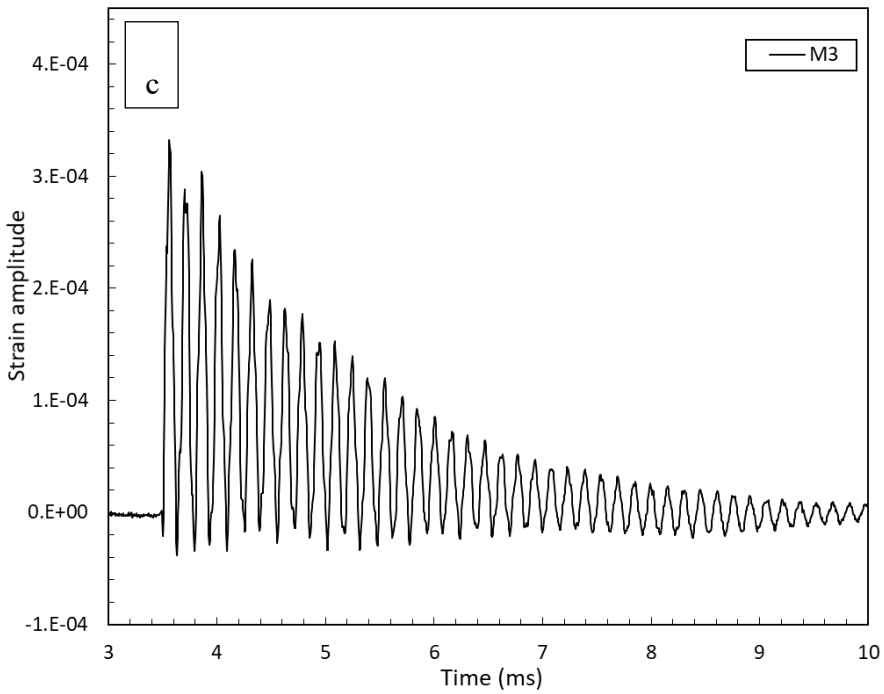

Figure 4-52 Typical strain responses of syntactic foams (a) M1, (b) M2 and (c) M3 excited by the shockwave A-7mm.

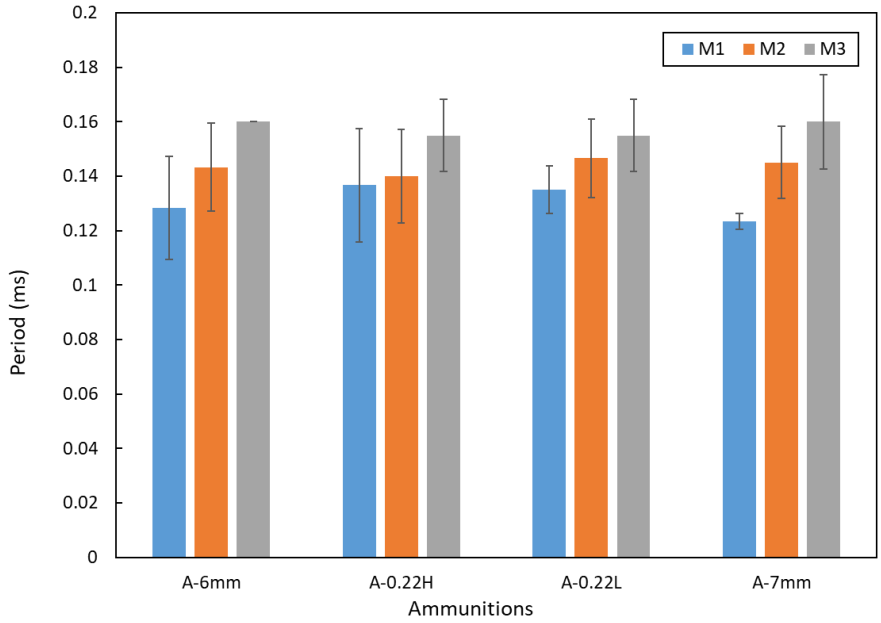

Figure 4-53 Oscillatory periods of syntactic foams M1, M2 and M3 excited by different shockwaves.

Figure 4-53 shows the average oscillatory periods of the three syntactic foams in different impulsive loads. The difference in the oscillatory period between the syntactic foams M1, M2 and M3 is small. Although it increases slightly from M1, M2 to M3, the impulsive load does not affect the oscillatory period.

4.5.1.2 Detrended strain amplitude

In order to analyse the damped free oscillation of the syntactic foam, the strain response was firstly deterended by removing the trend from the data. This enabled us to focus on the analysis of the fluctuations in the data about the trend. Figures 4-54~4-57 show the detrended strain responses of syntactic foams M1, M2 and M3, respectively, processed by MATLAB. The free decaying oscillations of the syntactic foams are shown more clearly in Figures 4-54~4-57. The three syntactic foams show apparently different behaviours in free decaying oscillation. The strain amplitude of syntactic foams M1 and M2 decayed rapidly while the strain amplitude of syntactic foam M3 decayed relatively slowly.

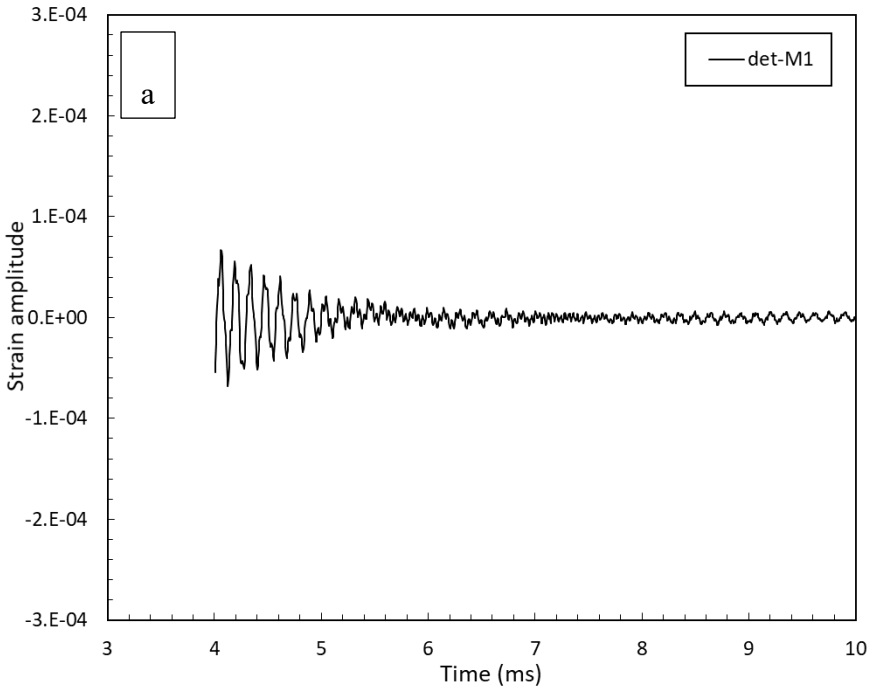

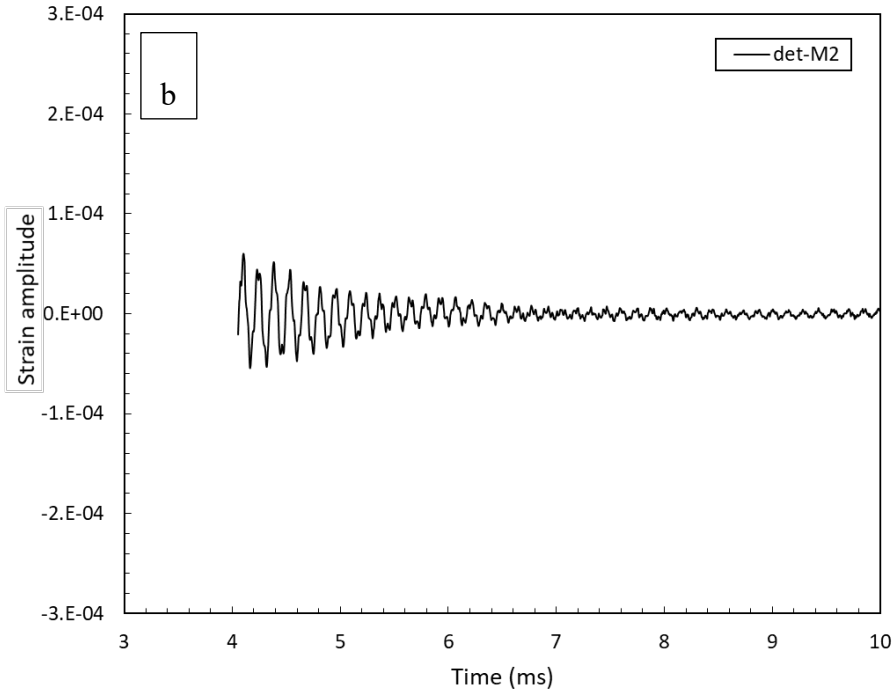

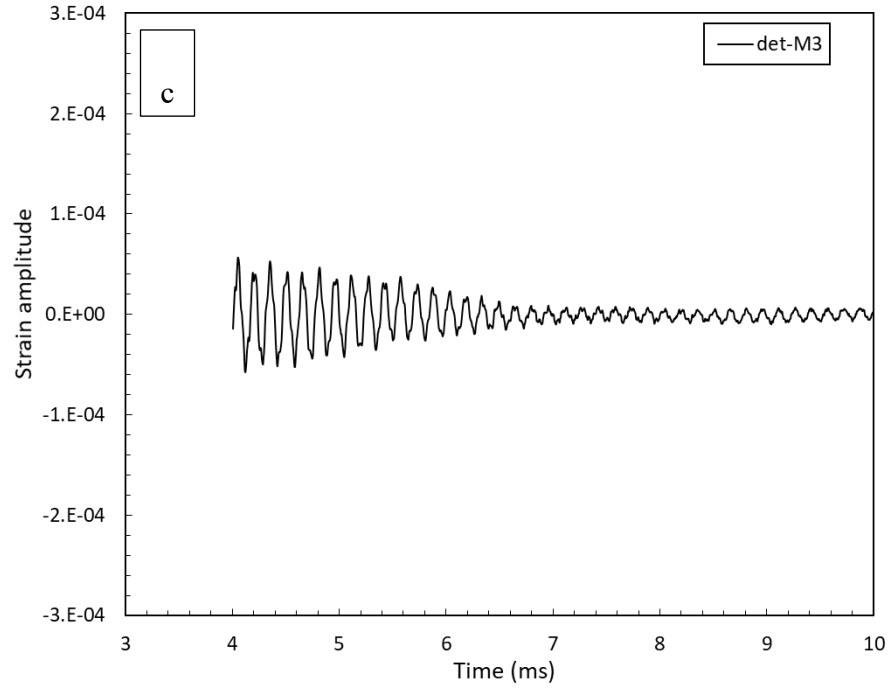

Figure 4-54 Detrended response amplitude of syntactic foams (a) M1, (b) M2 and (c) M3 excited by the shockwave A-6mm.

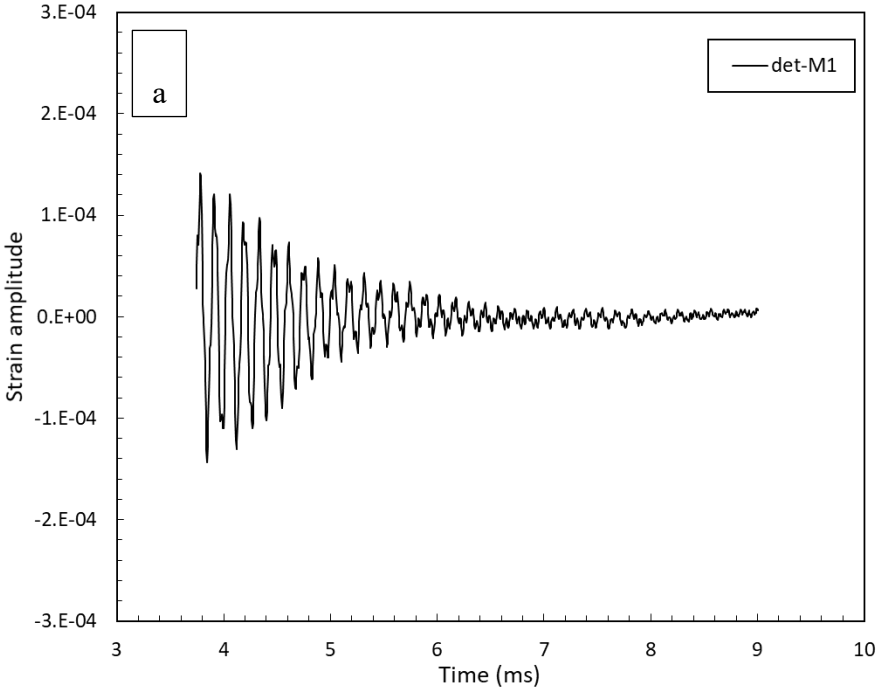
a
det-M1
3.E-04
2.E-04
1.E-04
0.E+00
-1.E-04
-2.E-04
-3.E-04
Strain amplitude
3
4
5
6
7
8
9
10
Time (ms)

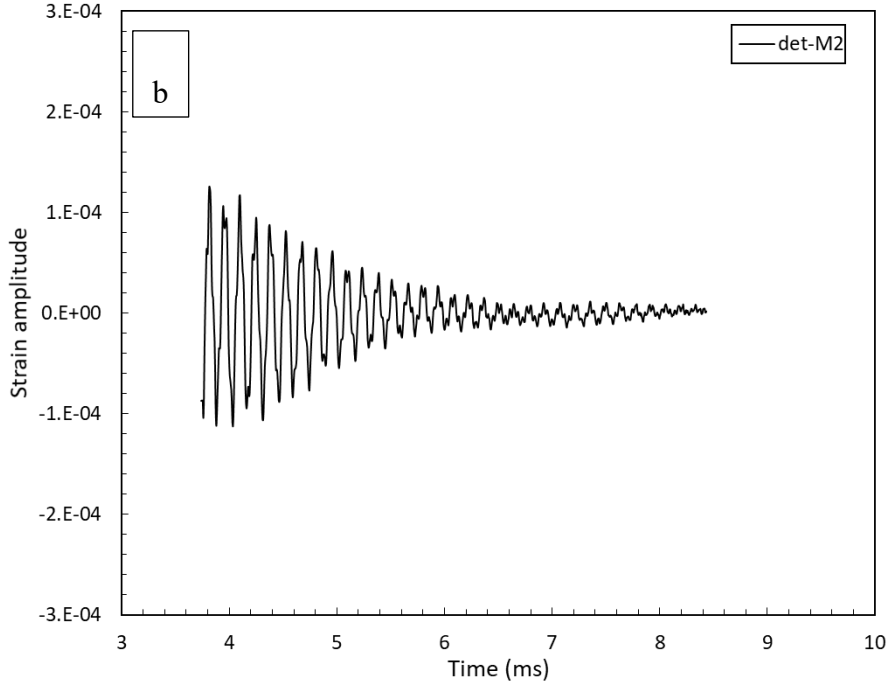
b
det-M2
3.E-04
2.E-04
1.E-04
0.E+00
-1.E-04
-2.E-04
-3.E-04
Strain amplitude
3
4
5
6
7
8
9
10
Time (ms)

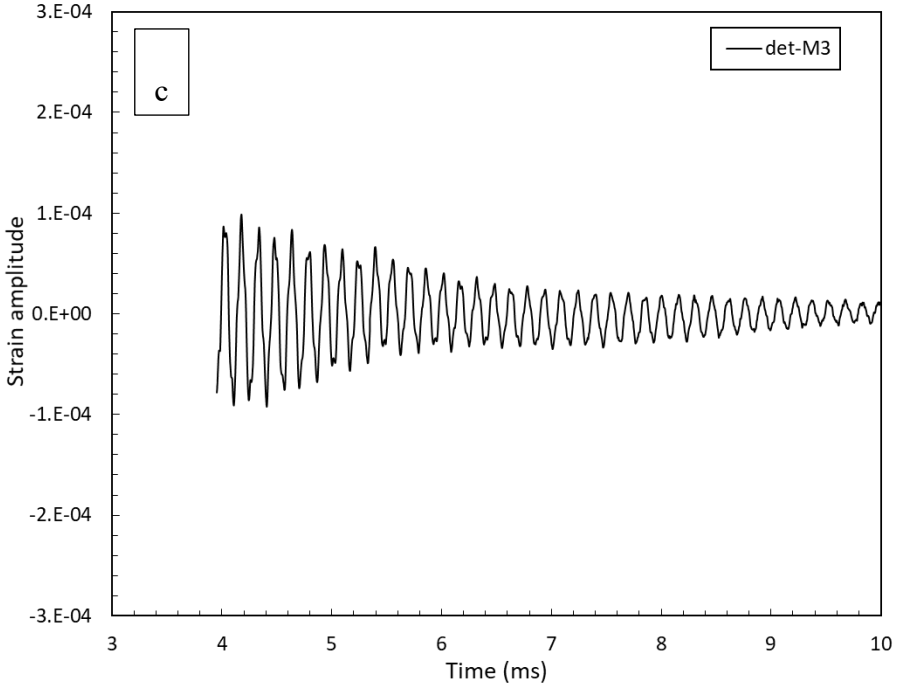

Figure 4-55 Detrended response amplitude of syntactic foams (a) M1, (b) M2 and (c) M3 excited by the shockwave A-0.22H.

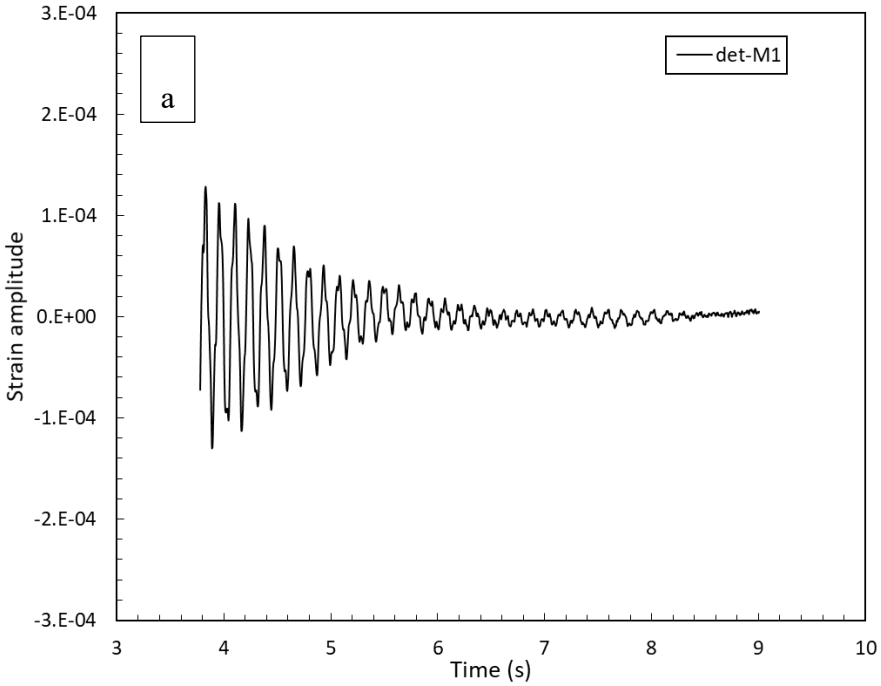

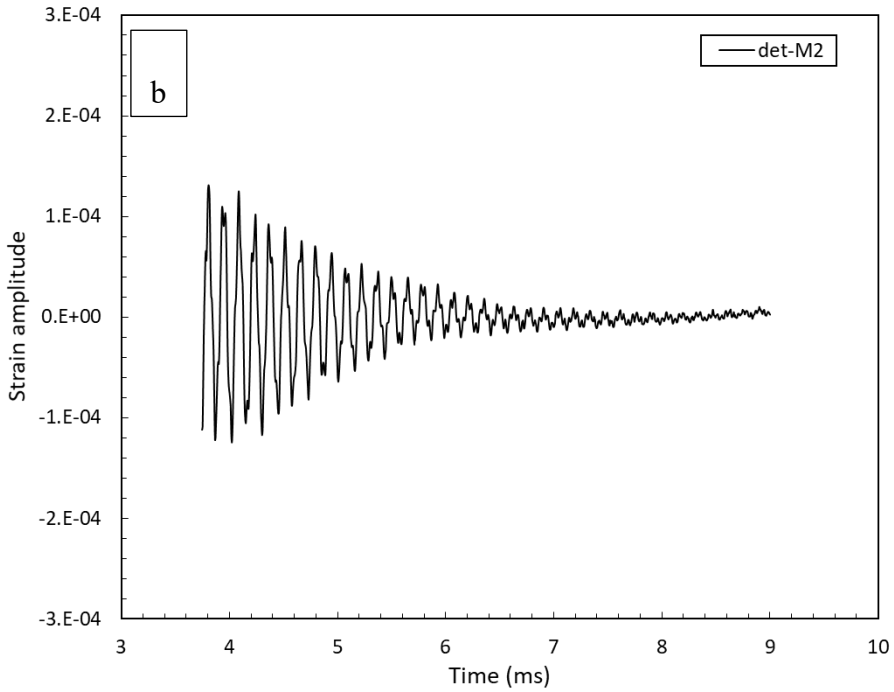

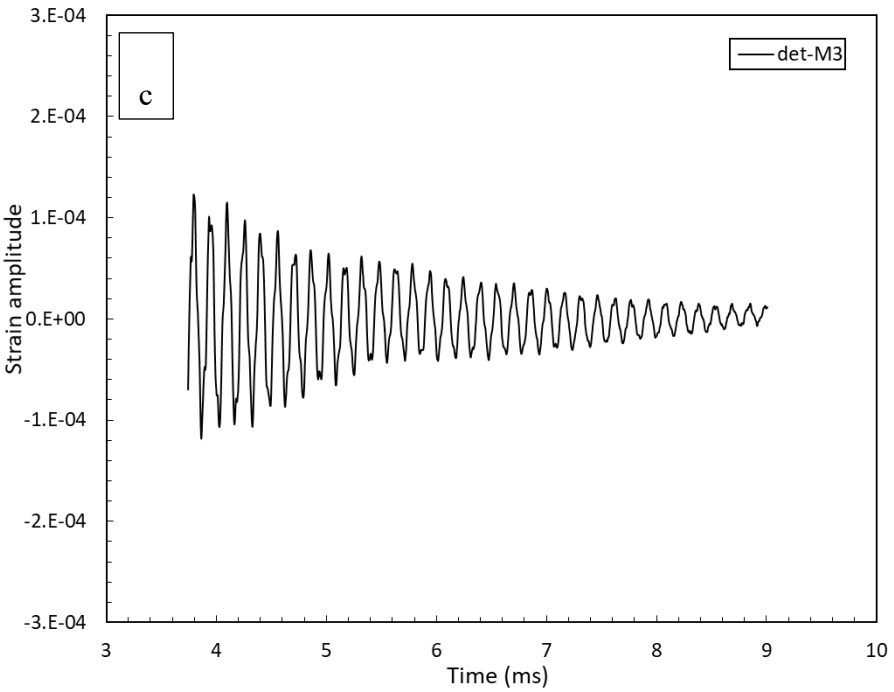

Figure 4-56 Detrended response amplitude of syntactic foams (a) M1, (b) M2 and (c) M3 excited by the shockwave A-0.22L.

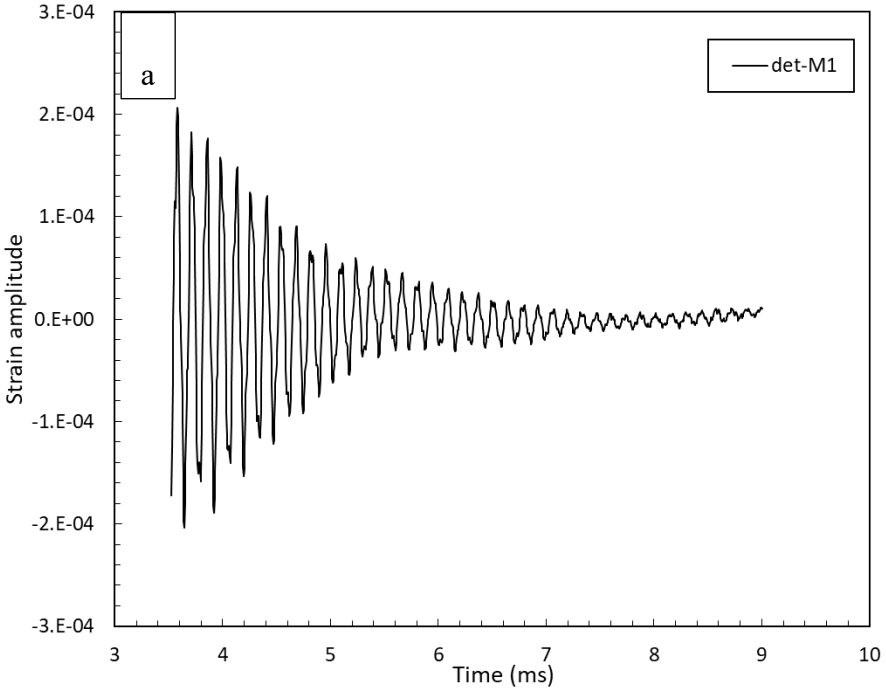
a
det-M1
3.E-04
2.E-04
1.E-04
0.E+00
-1.E-04
-2.E-04
-3.E-04
Strain amplitude
3
4
5
6
7
8
9
10
Time (ms)

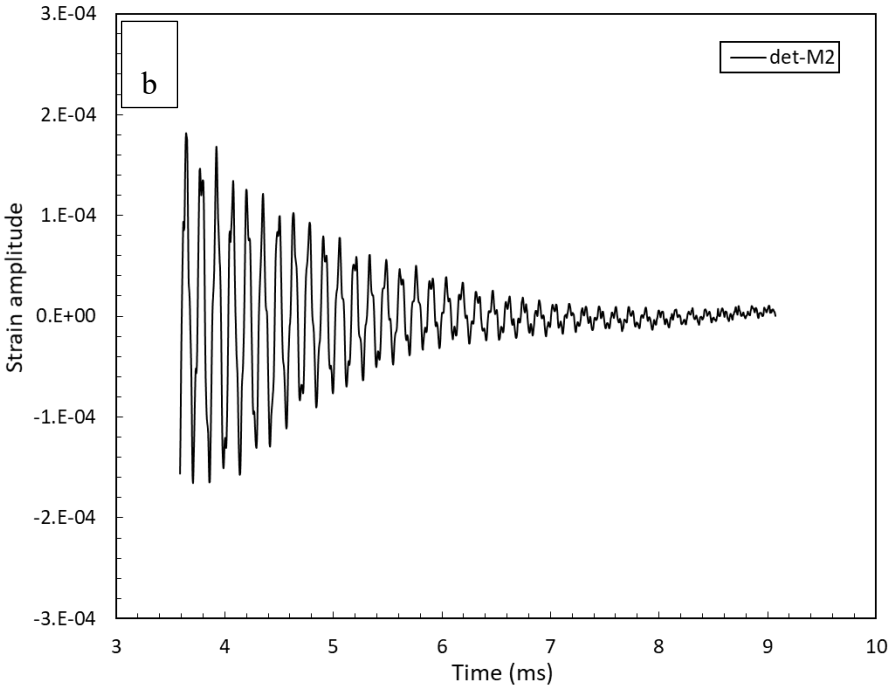
b
det-M2
3.E-04
2.E-04
1.E-04
0.E+00
-1.E-04
-2.E-04
-3.E-04
Strain amplitude
3
4
5
6
7
8
9
10
Time (ms)

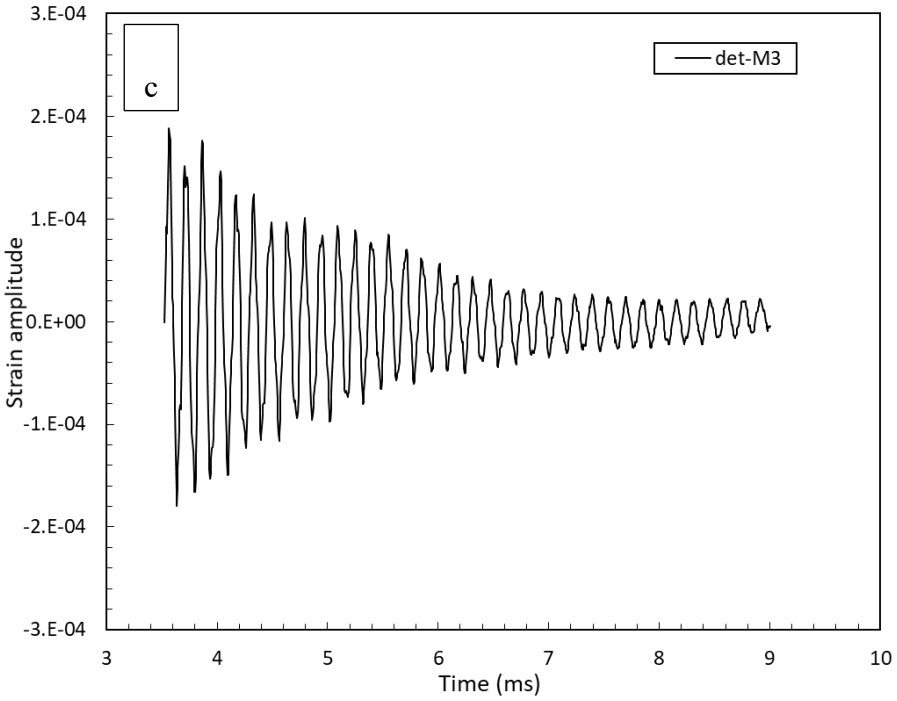

Figure 4-57 Detrended response amplitude of syntactic foams (a) M1, (b) M2 and (c) M3 excited by the shockwave A-7mm.

4.5.1.3 Logarithm of strain amplitude

To characterise the damping behaviours of the syntactic foams under free oscillation, the method of logarithmic decrement, as described in Chapter 3, was applied. The strain amplitudes of the oscillation were obtained using a MATLAB programme. The logarithmic decrements were calculated from the data using Excel. The logarithmic decrement of syntactic foam is normally obtained by using the mean logarithmic decrement of all the amplitudes. However, this method is not appropriate in this study, because of the scattered values of the logarithmic decrement. Figure 4-58 shows the logarithmic decrements of strain amplitude of each oscillation in syntactic foam M1 excited by the explosive charge A-6mm. It is evident that the data points scatter greatly, so using an average value does not represent the damping capacity of the syntactic foam well. Therefore, applying the formula directly to obtain the mean logarithmic decrement is not a good way to represent the behaviour.

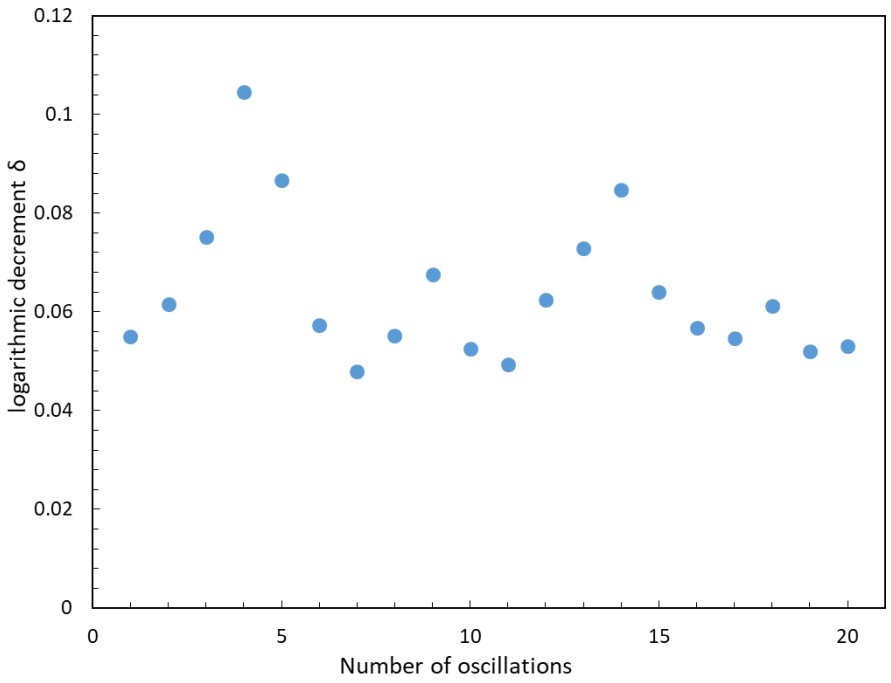

Figure 4-58 Logarithmic decrement of strain amplitude of syntactic foam M1 excited by the A-6mm.

In fact, the logarithmic decrement can be obtained by considering the overall trend of the natural logarithm of strain amplitude. Figure 4-59 shows the natural logarithm of strain amplitude of syntactic foam M1 under the A-6mm shockwave. It is evident that the natural logarithm of strain amplitude decreases nearly linearly with increasing time, although not a perfectly straight line due to measurement errors. The logarithmic decrement can be obtained from the gradient of the best-fit line.

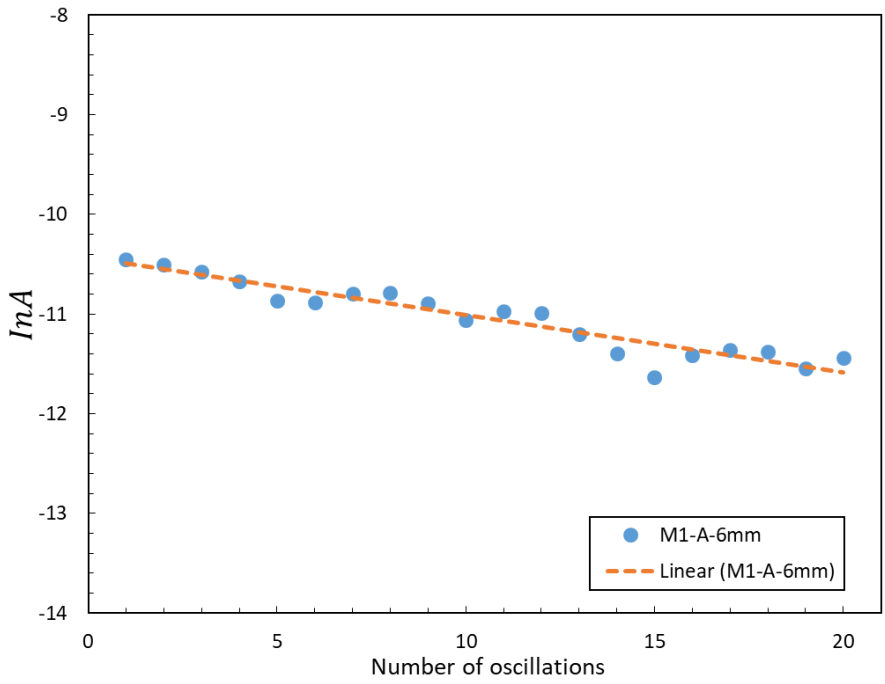

Figure 4-59 The logarithm of strain amplitude of syntactic foam M1 under the shockwave A-6mm.

Figure 4-60 shows the natural logarithms of strain amplitude of syntactic foams M1, M2 and M3 under different shockwaves. The natural logarithm of strain amplitude in all three syntactic foams under all the shockwaves largely has a nearly linear trend. The linear trend indirectly indicates that the oscillation of the syntactic foams is a free oscillation system and the shockwave does not interfere with the free damping of the syntactic foams. All the shockwaves have a short duration of positive impulse (about 3 milliseconds). Although it is larger than the period of the oscillation, the shockwave does not seem to interfere with the damping measurement.

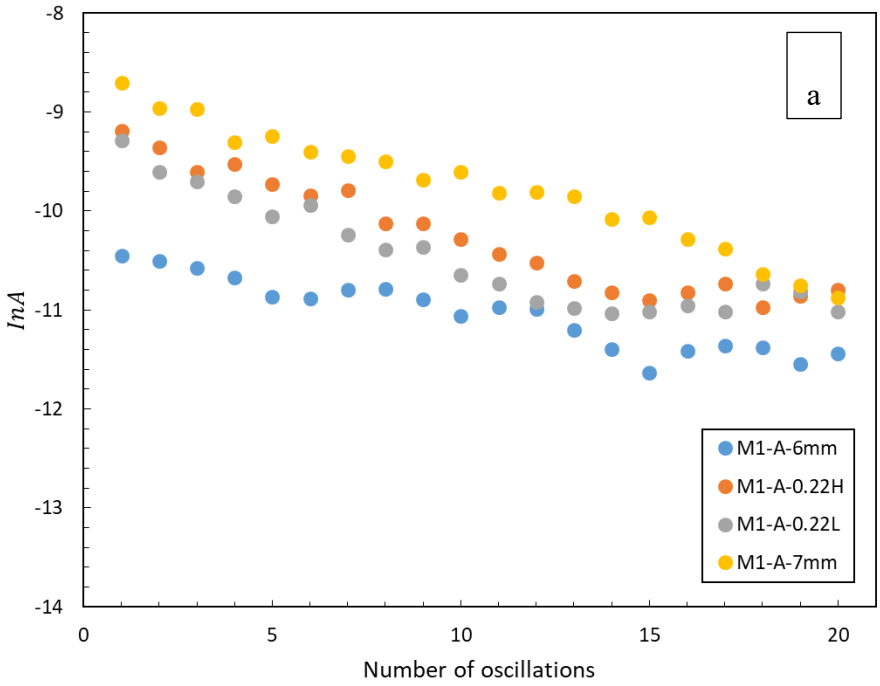
a
-8
-9
-10
-11
-12
-13
-14
lnA
0
5
10
15
20
Number of oscillations
M1-A-6mm
M1-A-0.22H
M1-A-0.22L
M1-A-7mm

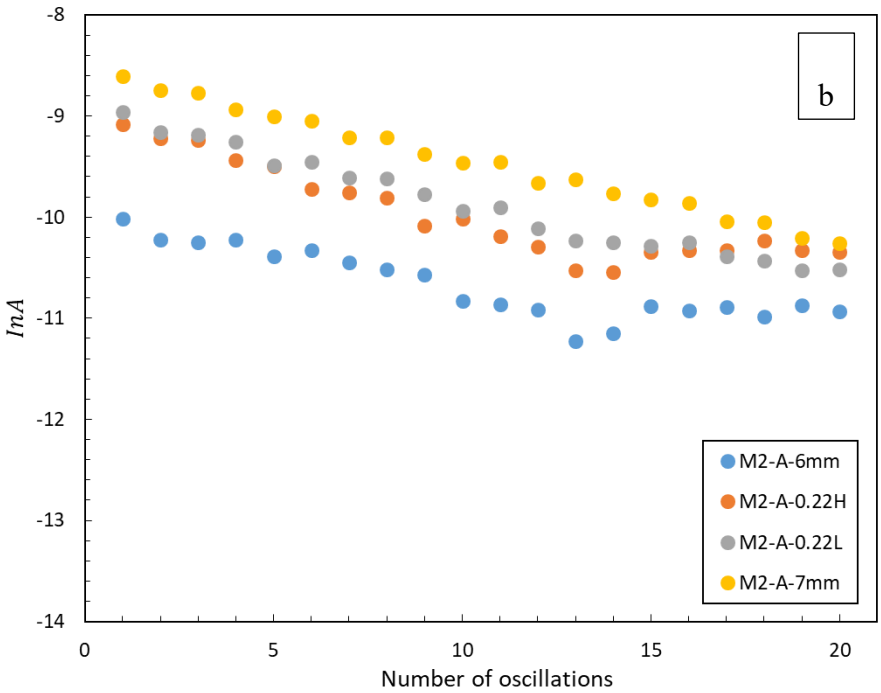
b
-8
-9
-10
-11
-12
-13
-14
lnA
0
5
10
15
20
Number of oscillations
M2-A-6mm
M2-A-0.22H
M2-A-0.22L
M2-A-7mm

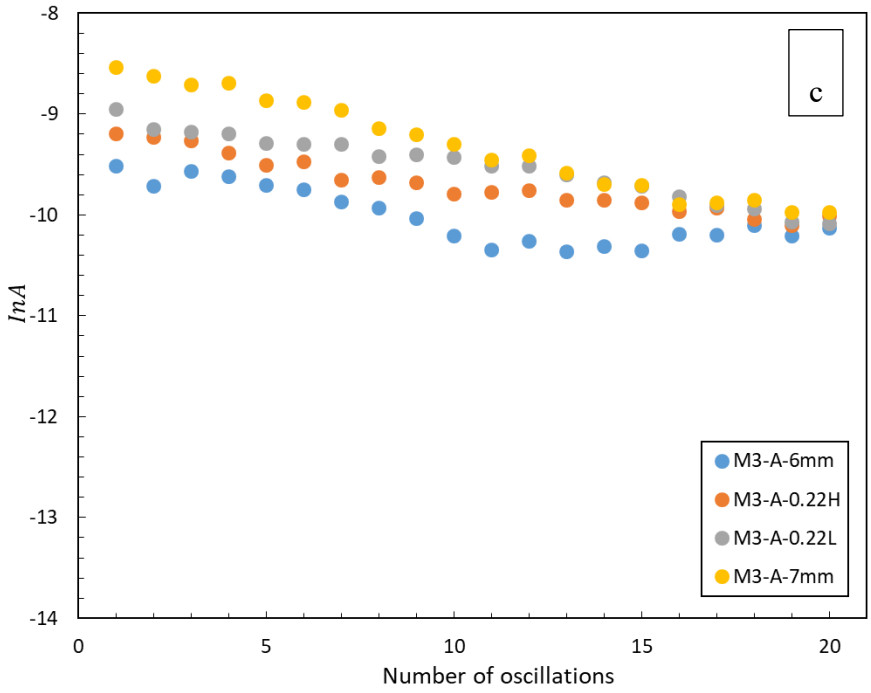

Figure 4-60 Logarithms of strain amplitude of syntactic foams (a) M1, (b) M2 and (c) M3 under four types of shockwaves.

4.5.1.4 Logarithmic decrement and loss factor

Figure 4-61 shows the loss factors and logarithmic decrements of the syntactic foams M1, M2 and M3 respectively under different impulsive loads of three shockwave tests. The loss factors of syntactic foam M1 have a similar trend in all the three shockwave tests, in which the loss factor increases with the impulsive load of shockwave (Figure 4-61 (a)). The behaviours of syntactic foams M2 and M3 in the first shockwave test were similar to syntactic foam M1. However, the behaviours of syntactic foams M2 and M3 in the second and third shockwave tests changed significantly (see Figure 4-61 (b) and (c)). The loss factors of syntactic foams M2 and M3 in the second and third shockwave tests became nearly constant for each impulsive load.

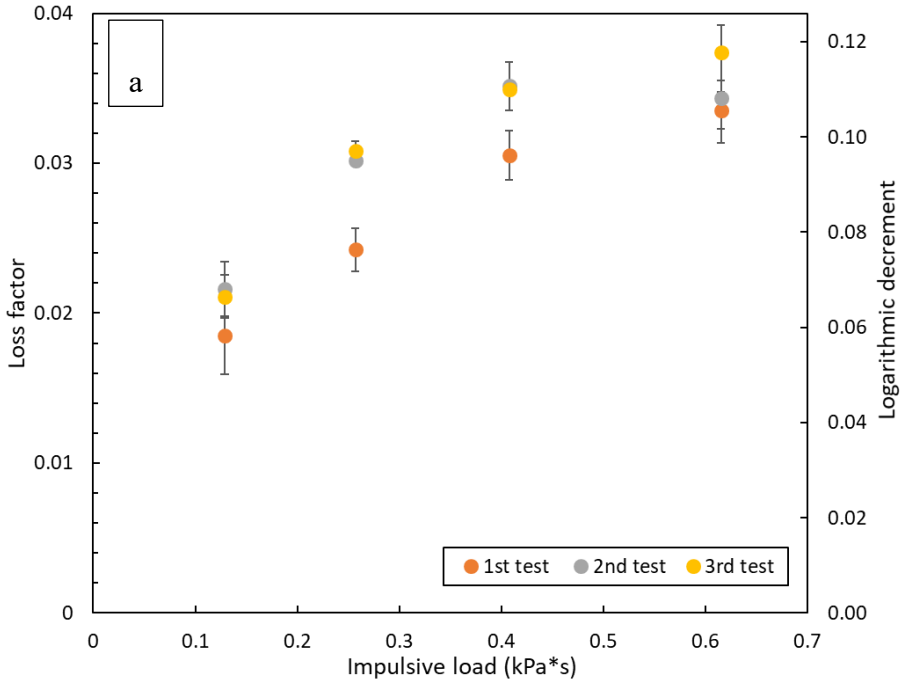

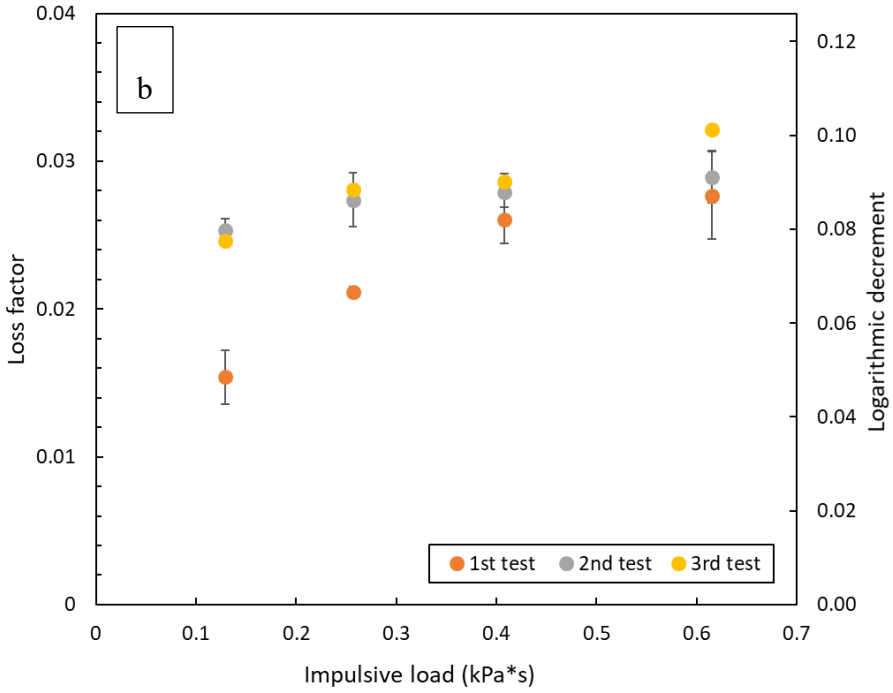

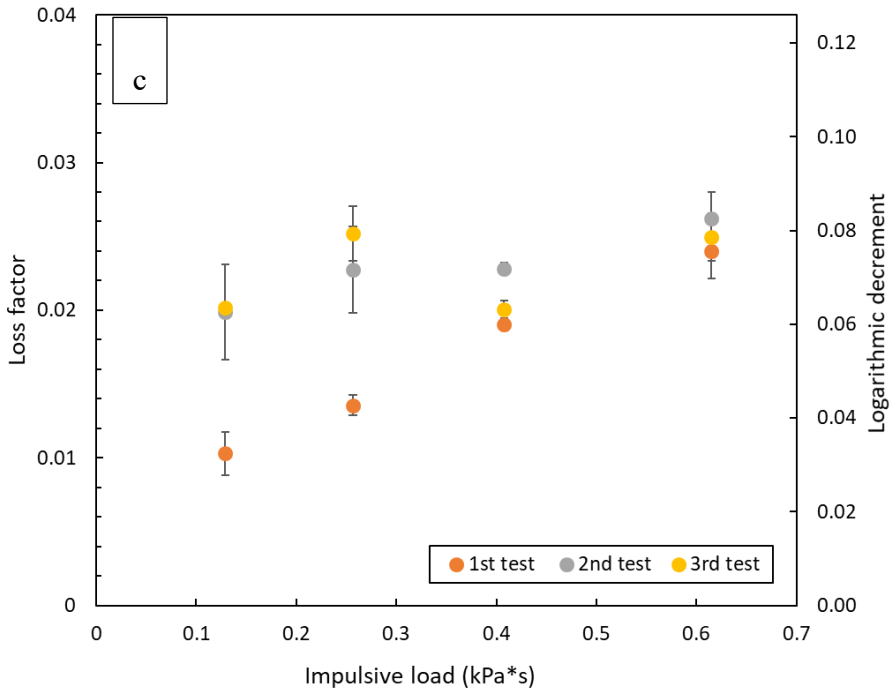

Figure 4-61 Loss factors and logarithmic decrements of syntactic foams (a) M1, (b) M2, and (c) M3 excited by the different shockwaves in three tests.

Figure 4-62 compares the loss factors and logarithmic decrements of syntactic foams M1, M2 and M3 under different impulsive loads for the three shockwave tests, respectively. In the first shockwave test (see Figure 4-62 (a)), the damping capacities of syntactic foams M1, M2 and M3 are in three different levels. Syntactic foam M1 has the highest loss factor value under any impulsive load. The loss factor of syntactic foam M2 is slightly less than that of M1, while syntactic foam M3 has the lowest loss factor. In the second and third shockwave tests, the damping capacities of syntactic foams M2 and M3 are improved at the lower impulsive loads, especially at the lowest impulsive loads, where their loss factors are comparable with that of syntactic foam M1.

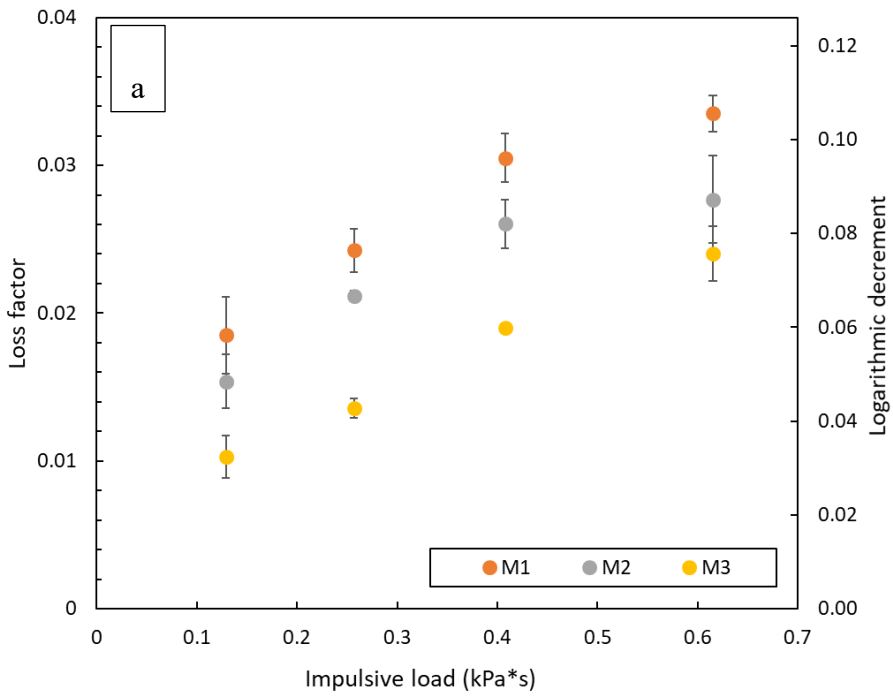

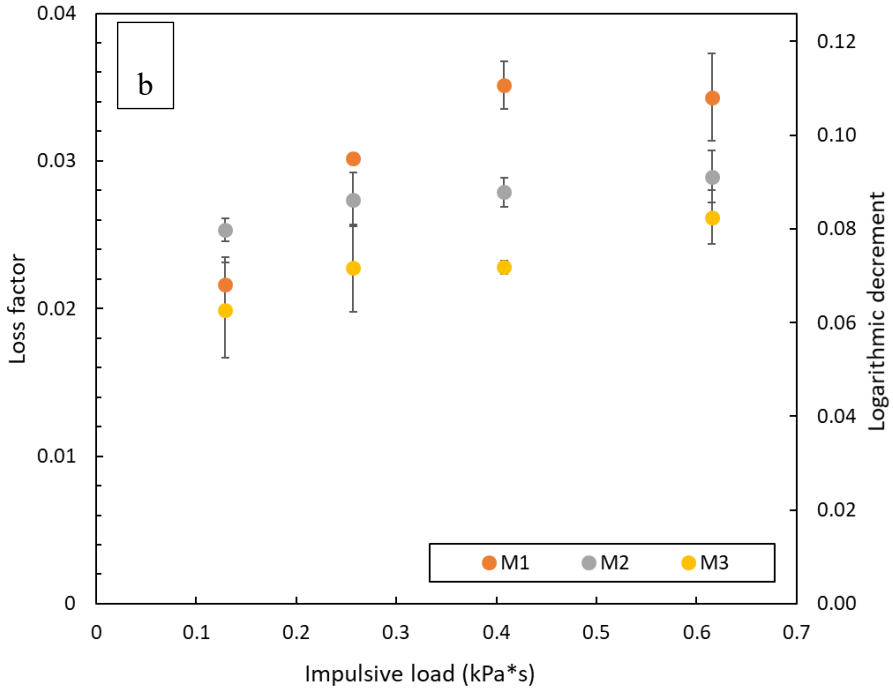

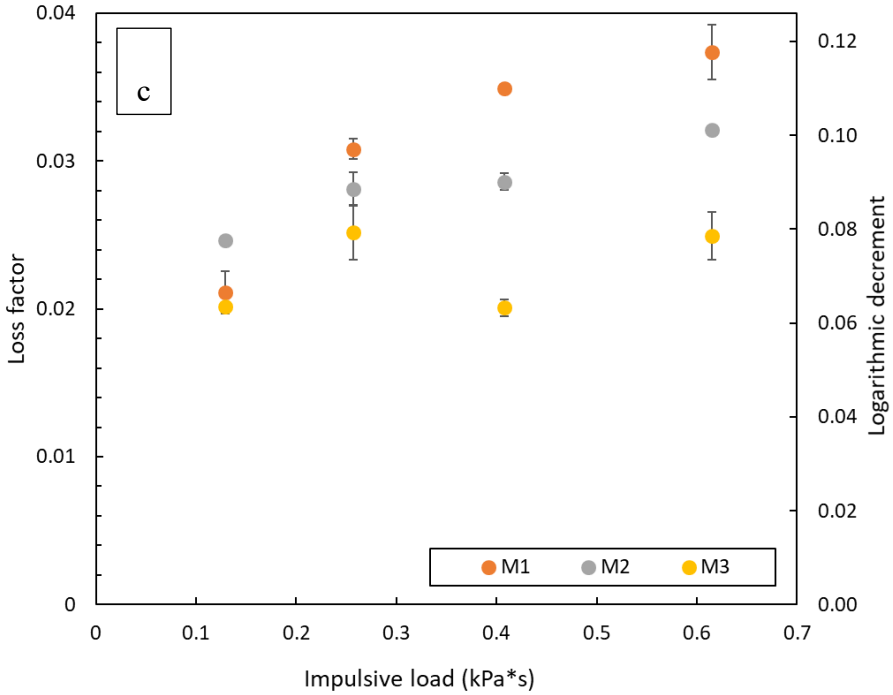

Figure 4-62 Comparison of loss factor and logarithmic decrement of syntactic foams M1, M2 and M3 in the (a) first, (b) second and (c) third shockwave tests.

4.5.2 Strain response of syntactic foams toughened with Al particles

4.5.2.1 Strain amplitude

Figure 4-63 shows the typical strain responses of the syntactic foams T1, T2, T3 and T4, excited by the impulsive load A-7mm. The strain responses confirmed that the syntactic foams with higher volume ratios of Al can also be excited by the shockwave caused by the impulsive load. The four syntactic foams have a similar initial strain of approximately 3.0×10^{-4}, which is comparable to the initial strain of syntactic foam M2 under the same impulsive load.

The strain responses of the syntactic foams toughened with Al particles also show the typical under-damped dynamic system, i.e., decaying exponentially over time. However, the syntactic foams toughened with Al need more time than the monomodal syntactic foam M2 for the damping oscillation to decay to zero. Therefore, the damping capacity of syntactic foams under a free oscillation is also related to the volume percentage of CM particles.

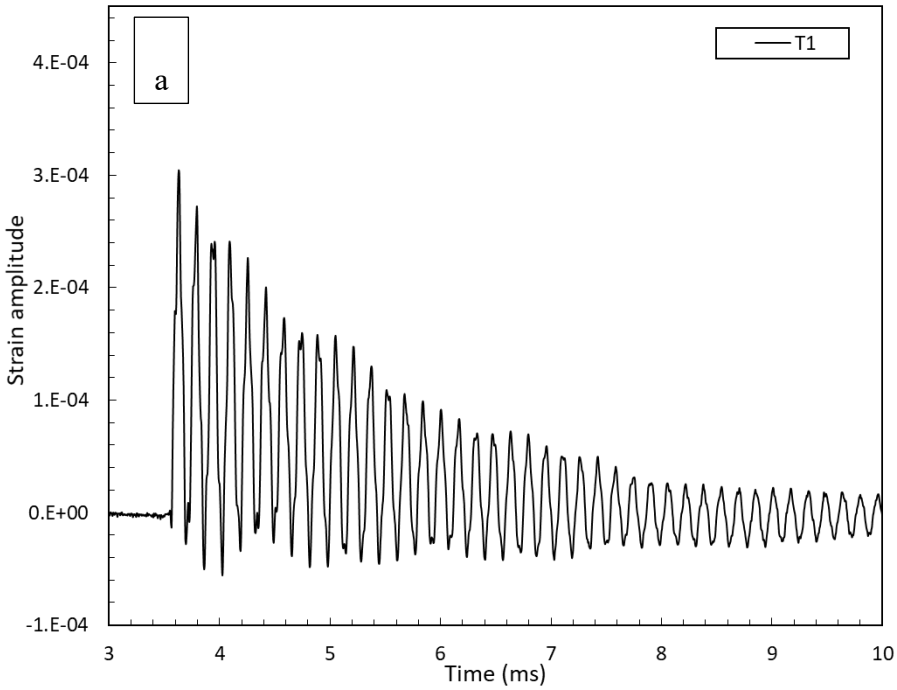
a
T1
4.E-04
3.E-04
2.E-04
1.E-04
0.E+00
-1.E-04
Strain amplitude
3
4
5
6
7
8
9
10
Time (ms)

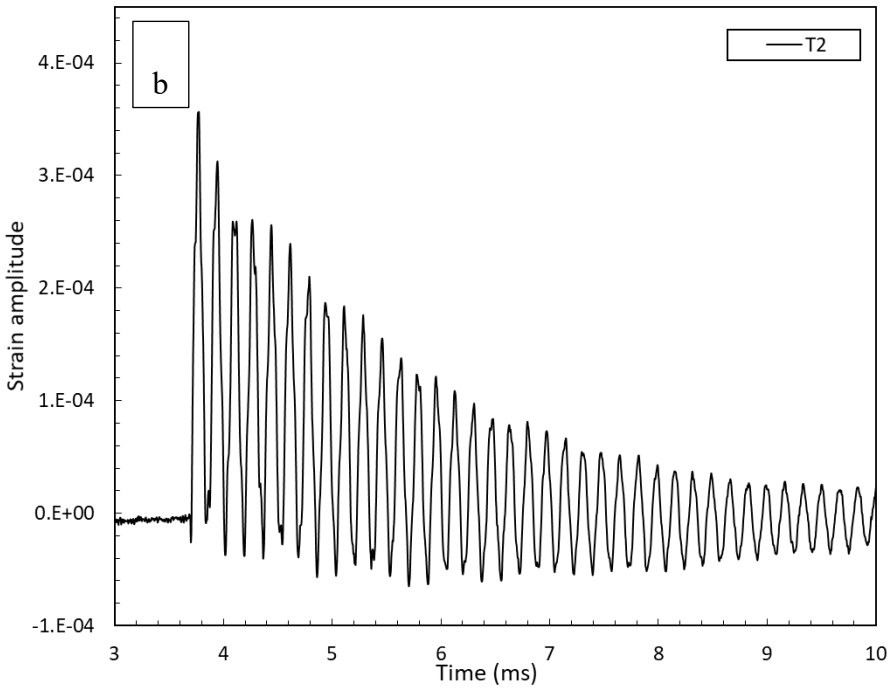
b
T2
4.E-04
3.E-04
2.E-04
1.E-04
0.E+00
-1.E-04
Strain amplitude
3
4
5
6
7
8
9
10
Time (ms)

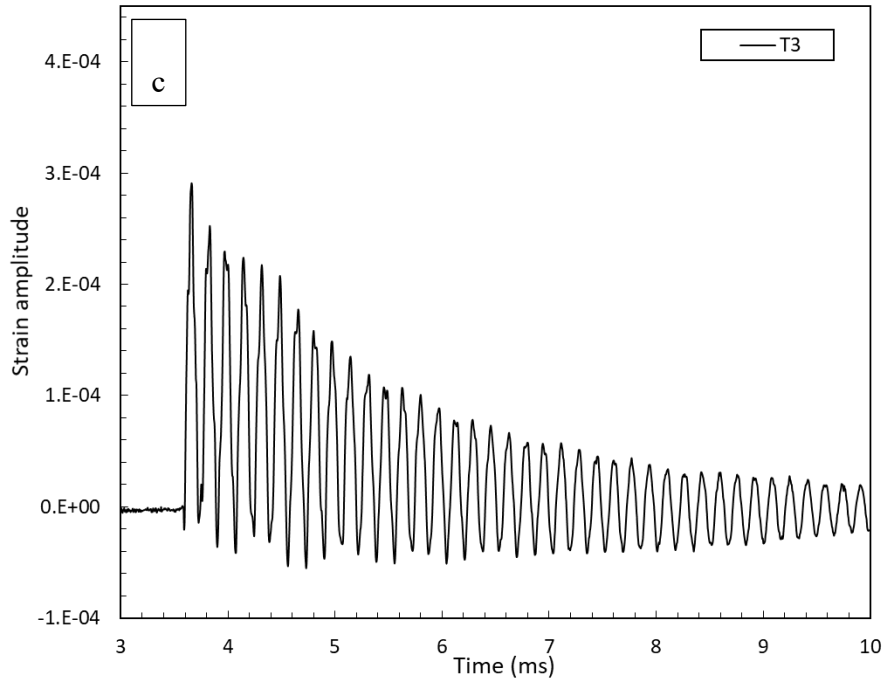

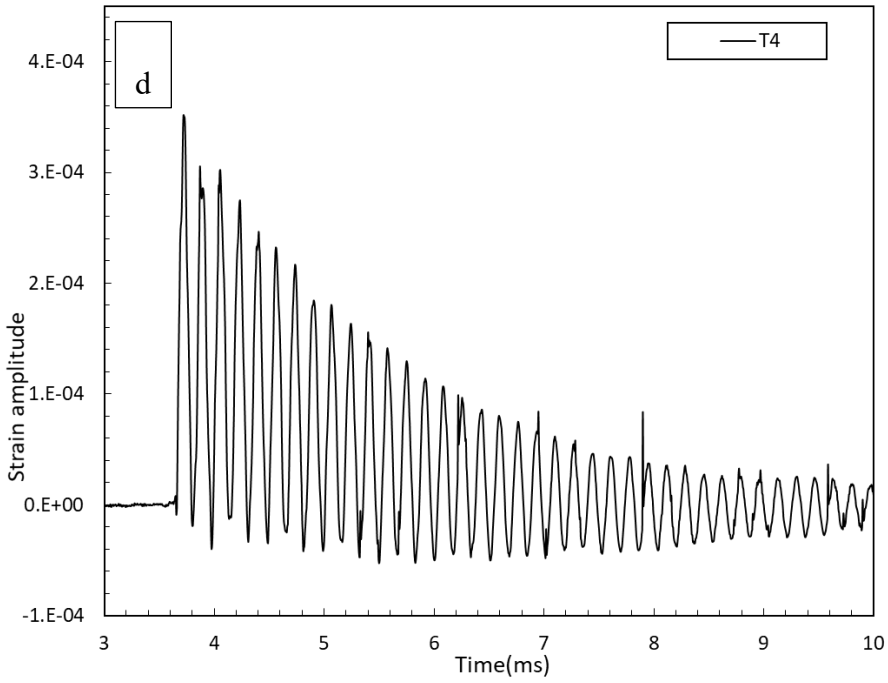

Figure 4-63 Typical strain responses of syntactic foams (a) T1, (b) T2, (c) T3, and (d) T4 excited by the shockwave A-7mm.

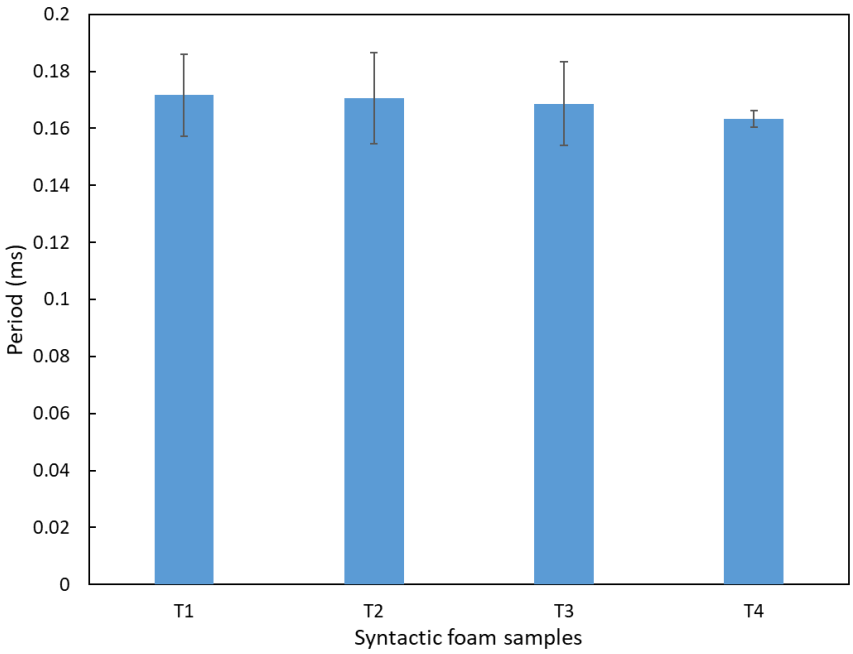

Figure 4-64 Oscillatory periods of syntactic foams T1, T2, T3 and T4 excited by the shockwave A-7mm.

The average oscillatory periods of syntactic of T1,T2,T3 and T4 are shown in Figure 4-64. The average oscillatory periods of syntactic foams toughened with Al particles are greater than those of the monomodal syntactic foams. Although the average oscillatory period seems to be proportional to the variation in the oscillatory period among syntactic foams T1, T2, T3 and T4 is insignificant.

4.5.2.2 Detrended strain amplitude

Figure 4-65 shows typical detrended strain responses of syntactic foams T1, T2, T3 and T4. It is clearly shown that the strain responses of the four syntactic foams toughened with Al particles are also free decaying oscillations.

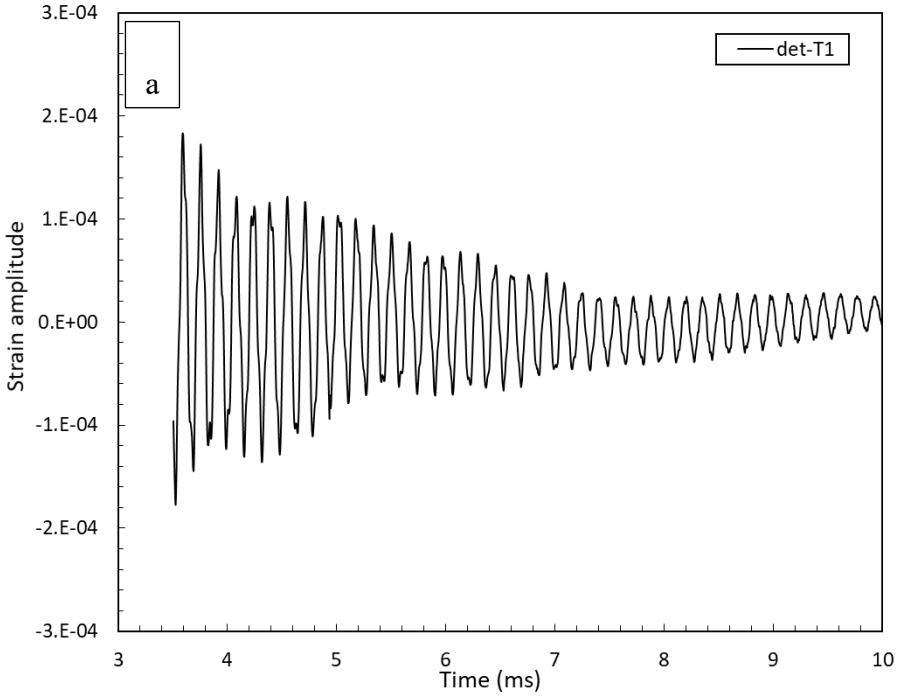

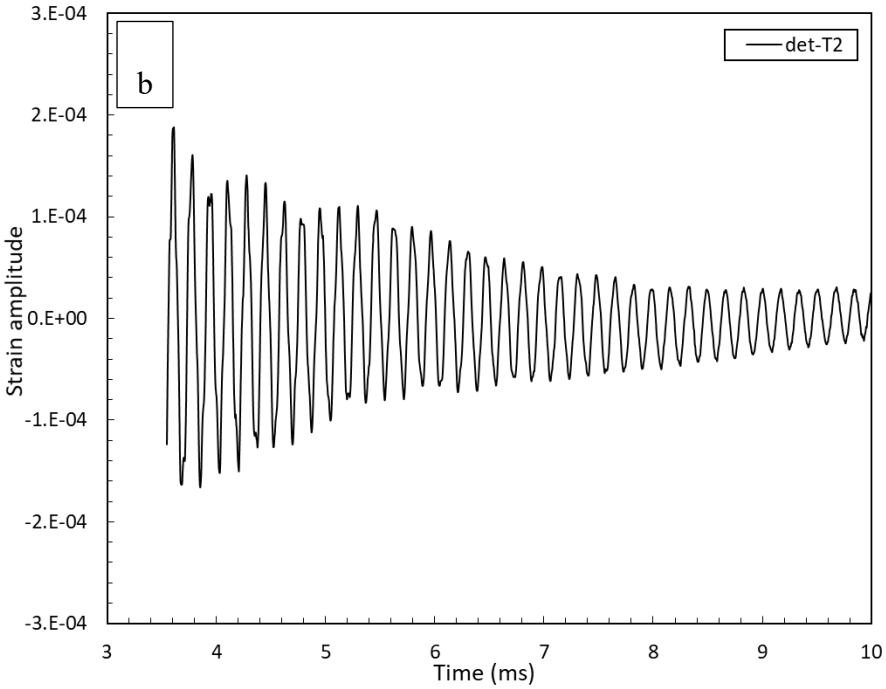
b
det-T2
3.E-04
2.E-04
1.E-04
0.E+00
-1.E-04
-2.E-04
-3.E-04
Strain amplitude
3
4
5
6
7
8
9
10
Time (ms)

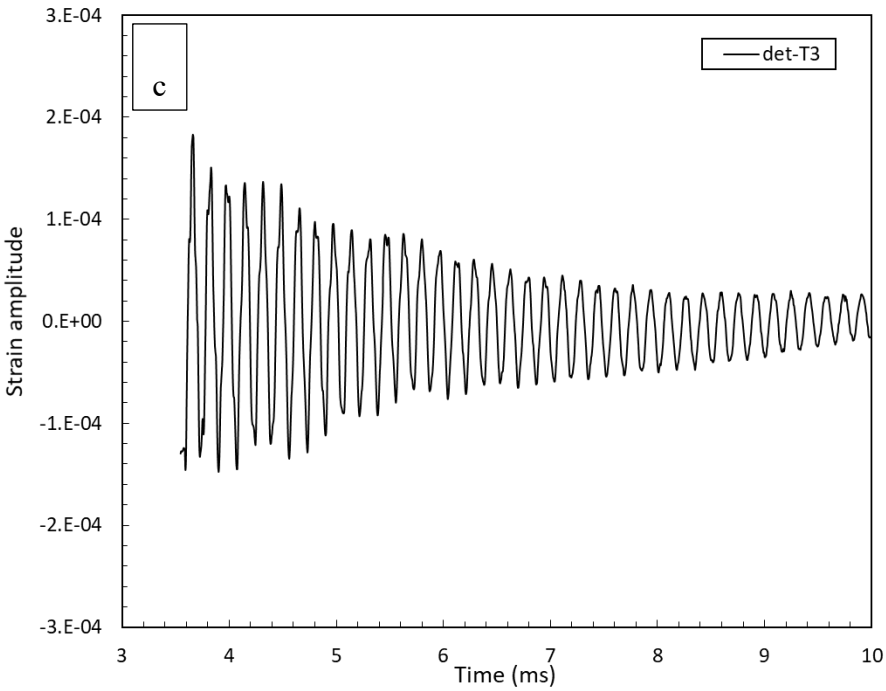
c
det-T3
3.E-04
2.E-04
1.E-04
0.E+00
-1.E-04
-2.E-04
-3.E-04
Strain amplitude
3
4
5
6
7
8
9
10
Time (ms)

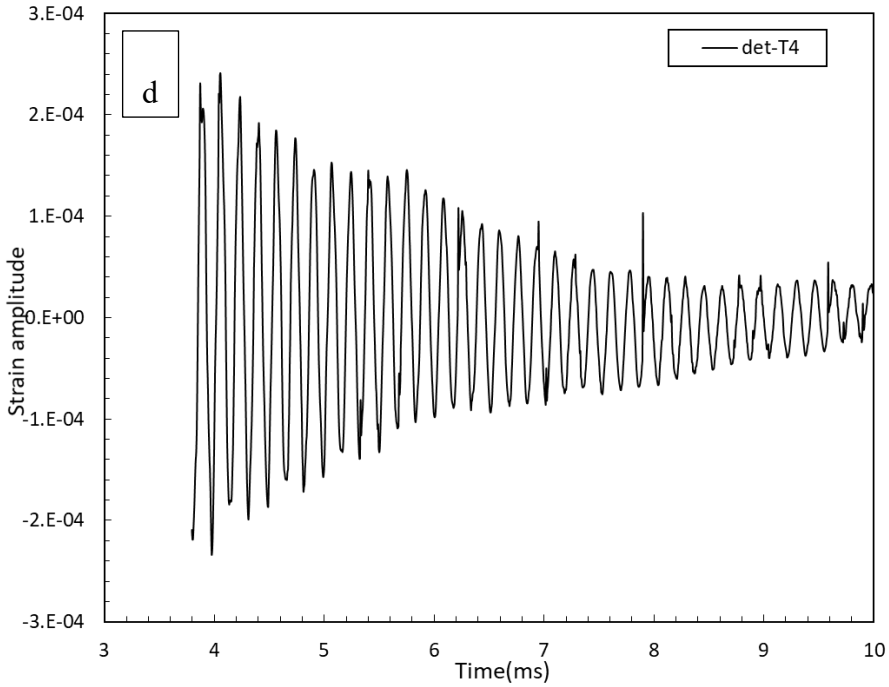

Figure 4-65 Detrended response amplitudes of syntactic foams (a) T1, (b) T2, (c) T3, and (d) T4 excited by the shockwave A-7mm.

4.5.2.3 Logarithmic decrement and loss factor

Figure 4-66 shows the natural logarithms of strain amplitude of syntactic foams T1, T2, T3 and T4. The natural logarithm of strain amplitude of each syntactic foam decreases nearly linearly with time. The logarithmic decrement was evaluated by considering the overall trend of the natural logarithm of strain amplitude i.e., the gradient of the best-fit line. Again, the shockwave does not seem to interfere with the damping measurement for syntactic foams T1, T2, T3 and T4.

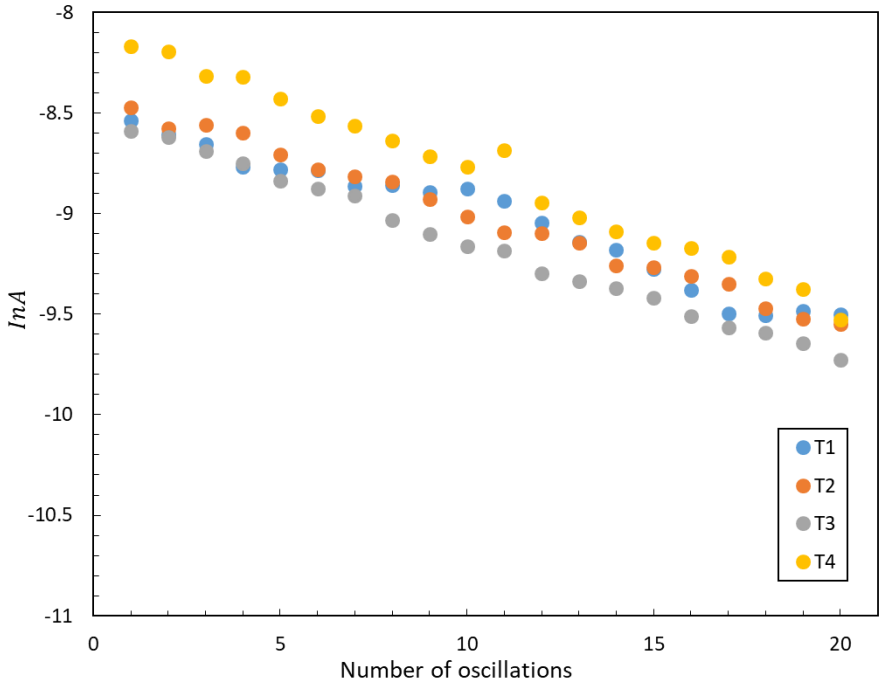

Figure 4-66 Logarithm of strain amplitudes of syntactic foams (a) T1, (b) T2, (c) T3 and (d) T4 under the shockwave A-7mm.

Figure 4-67 shows the loss factors and logarithmic decrements of the syntactic foams T1, T2, T3 and T4. The loss factors of the syntactic foams toughened with Al particles are smaller than the monomodal syntactic foam M2, which was reinforced with the same size CM particles. The loss factor increases with increasing volume percentage

of CM particles. It confirms that the damping capacity of syntactic foam in free oscillation is dependent upon the volume percentage of the CM particles.

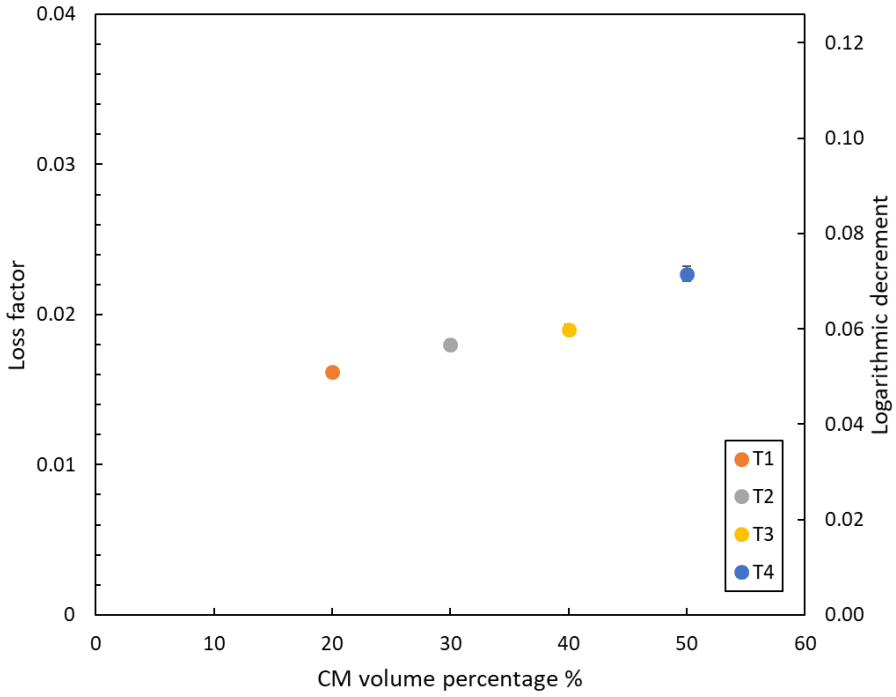

Figure 4-67 Loss factors and logarithmic decrements of syntactic foams toughened with different CM volume percentages, excited by shock wave generated by A-7mm.

4.5.3 Discussion

4.5.3.1 Damping mechanism in free oscillation

Figure 4-68 compares the loss factors of the syntactic foams measured under repetitive compression (50 cycles at 30 MPa and 60 MPa) and shockwave test (A-7mm). Although the loss factor of the syntactic foams was measured in two different testing methods, the results are very similar. It shows that the energy dissipation mechanism of the syntactic foams in free oscillation is likely the same as in the cyclic compression, i.e., caused by microcrack initiation and propagation in CM particles.

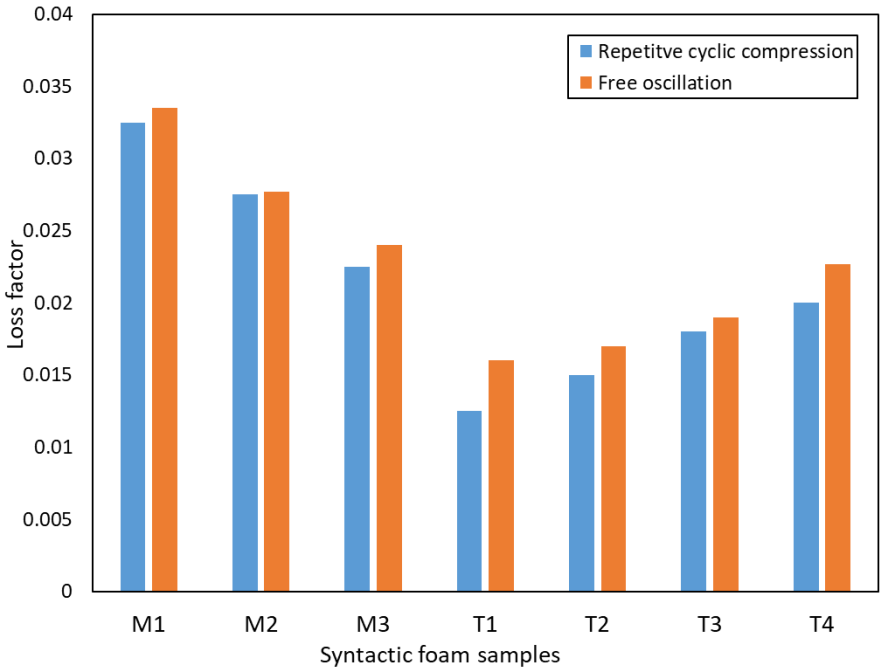

Figure 4-68 Comparison of loss factor of syntactic foam in repetitive compression and free oscillation.

The previous results of cyclic compression of the syntactic foams have demonstrated that even in the apparently elastic region, some parts of the syntactic foams have experienced localised plastic deformation due to initiation and propagation of

microcracks in the CM particles. In the syntactic foams, most CM particles are in direct contact with their neighbouring CM particles. Stress concentrations occur at these contact points and the local stress can be significantly higher than the global stress. Even if the syntactic foam is subjected to a small stress, the local stresses at some locations in the syntactic foam can reach the critical stress required for crack initiation and propagation in the CM particles.

Similarly, the shockwave energy is dissipated gradually by the initiation and propagation of microcracks in the CM particles in the syntactic foam during the free oscillation. The shockwave induced stress in the syntactic foam initially results in microcrack initiation in the CM particles and a portion of the shockwave energy is dissipated. The remaining shockwave energy is gradually dissipated by microcrack propagation in the CM particles in subsequent oscillations, until the crack develops across the whole particle. These broken particles can no longer dissipate energy. However, more un-broken CM particles will take part in the initiation and propagation of microcracks to dissipate the shockwave energy. The damping mechanism in the syntactic foams is analogous to the damping of sandwich beams in flexural vibration, where debonding of sandwich composite introduces energy dissipation (Idriss et al. 2013; Moustapha et al. 2012).

4.5.3.2 Effect of impulsive load

The results of the first shockwave test in section 4.5.1.4 show that the damping behaviour of the syntactic foam samples is affected by the magnitude of the impulsive load. This is because the impulsive load determines the number and total length of the microcracks in the CM particles in the syntactic foam. When a low impulsive load is

applied, microcracks are generated in few CM particles in the syntactic foam, because few locations can reach the critical stress enough to cause microcrack initiation and propagation. The relatively small number of microcracks lead to low damping in the syntactic foams. In contrast, a high impulsive load can cause more stress concentrations at the contact points between the CM particles in the syntactic foam and the local stress can easily reach the critical stress required for microcrack initiation and propagation in the CM particles. Therefore, higher impulsive load leads to higher damping in the syntactic foam in free oscillation. This behaviour also agrees with a previous study (Moustapha et al. 2012).

4.5.3.3 Effect of CM particle size

The results in section 4.5.1.4 show that the damping behaviour and damping capacity of the syntactic foams under free oscillation are also affected by the CM particle size. The effect of the CM particle size on the damping capacity and damping behaviour of the syntactic foam is essentially ascribed to the quantity of CM particles and the different modes of microcrack development in the CM particles.

Although the three syntactic foams have a similar CM particle volume percentage, the numbers of the CM particles in the syntactic foams are different due to different CM particle sizes. The number of CM particles in the small CM reinforced syntactic foam, M1, is much higher than that in the large CM reinforced syntactic foam, M3. Syntactic foam M1 has a better damping capacity than syntactic foams M2 and M3 in free oscillation because more CM particles can take part in energy dissipation. Particle size also affects the mode of microcrack development during free oscillation. The microcracks can move across small CM particles more easily, so microcrack initiation

or formation accounts for a large proportion of energy dissipation. Microcracks in large CM particles take longer to fully crack, so they propagate in subsequent oscillations before moving across the whole particle. Because the energy required for microcrack initiation is greater than microcrack propagation, syntactic foam M1 has the highest damping capacity.

In syntactic foam M1, the damping behaviour is similar in the three shockwave tests, i.e., the loss factor is proportional to the impulsive load. This is likely because the microcracks in the small CM particles can easily propagate across the particles. The majority of the small CM particles that participate in energy dissipation in the first shockwave test, have broken and no longer take part in energy dissipation. Hence, in the second and third shockwave tests, microcrack initiation occurs in new CM particles with nearly the same amount as in the first shockwave test. In syntactic foams M2 and M3, the loss factor at lower impulsive loads is slightly increased in the second and third shockwave tests compared with the first test. This is likely because more CM particles have microcracks at the higher impulsive load of first shockwave test. These large CM particles need more energy to become fully broken. Thus, at a lower impulsive load of the second and third shockwave tests, more CM particles participate in microcrack propagation.

4.5.3.4 Effect of CM particle volume percentage

Figure 4-67 shows that the damping capacity of syntactic foams in free oscillation is also sensitive to the volume percentage of CM particles, agreeing with the energy dissipation behaviour under the cyclic compression. With a lower volume percentage of CM particles in the syntactic foam, the syntactic foam has fewer CM particles that

can participate in microcrack initiation and propagation, resulting in lower damping capacity.

4.5.4 Summary

The monomodal syntactic foams and syntactic foams toughened with Al particles were tested in the shock tube. The four shockwaves can excite free oscillations in all the syntactic foam samples. The damping of the syntactic foams can be evaluated by considering the overall trend of the natural logarithm of strain amplitudes in the strain responses of the syntactic foams.

The damping capacities of syntactic foams M1, M2 and M3 are in three different levels. The damping behaviour of syntactic foam M1 is the same in all three shockwave tests, where the loss factor increases with the impulsive load of shockwave. The damping behaviour of syntactic foams M2 and M3 in the first shockwave test is similar to that of syntactic foam M1. The trend of loss factor of syntactic foams M2 and M3 in the second and third shockwave tests, however, changed significantly. The loss factor results of syntactic foams toughened with Al particles show that the damping capacity of syntactic foams in free oscillation is also dependent upon the volume percentage of the CM particles.

As in cyclic compression, the damping of syntactic foams in free oscillation is also caused by microcrack initiation and propagation in the particles. The effects of impulsive load, the size and volume percentage of the CM particles on the damping capacity and damping behaviour of syntactic foams can be explained by this damping mechanism.

Chapter 5 CONCLUSIONS AND FUTURE WORK

5.1 Conclusions

5.1.1 Structural properties of syntactic foams

The metal matrix syntactic foam samples fabricated by the infiltration casting process normally had two types of defects: broken CM particles filled with Al and CM particle bed not well infiltrated by Al. A modified infiltration casting process was able to minimise these defects in the syntactic foam samples. The measured densities of the syntactic foams in the present study were closer to the theoretical values than the previous studies because of reduced structural defects in the syntactic foams.

5.1.2 Static compressive and impact behaviour

The stress-strain curves of all types of syntactic foams had qualitatively a similar behaviour to cellular solids and exhibited three typical regions. The compressive strength, plateau stress, densification strain and specific energy absorption of these syntactic foams were slightly different, depending upon the Al matrix, the size and volume percentage of the CM particles. In the Charpy impact test, the absorbed energy of the syntactic foams was related to the CM particle size, because CM particle size has an influence on the fracture mechanism of the syntactic foam.

5.1.3 Cyclic compressive behaviours

Appreciable hysteresis loops were present in the stress-strain curves of all the syntactic foams under cyclic unloading-loading compression. The hysteresis loops demonstrated that there was energy dissipation or damping in the metal matrix syntactic foams during cyclic loading. The three monomodal syntactic foams had a similar specific damping capacity (SDC) of about 0.085, showing that CM particle size had no influence on the energy dissipation of the syntactic foams. The SDC of the syntactic foams increased with the volume percentage of the CM particles. The energy dissipation was due to the CM particles rather than the interfacial damping between the CM particles and the Al matrix. The dissipated energy in the syntactic foams was proportional to the square of the applied stress in the cyclic loading.

In one-stage repetitive cyclic compression, the results show that the damping behaviour of monomodal syntactic foams was sensitive to the CM particle size, and the damping capacity of the syntactic foams toughened with Al particles was determined by the volume percentage of the CM particles in the syntactic foams. In two-stage repetitive cyclic compression, both SDE and SDC at the stress amplitudes of 30 and 60 MPa decreased significantly in stage 2, while both SDE and SDC at 80 MPa in stage 2 followed the same trend as in stage 1. This confirmed that previous loading history had a strong effect on the hysteretic energy dissipation.

Microcracks in CM particles were observed in all the syntactic foams after cyclic compression. Energy dissipation of the syntactic foams during cyclic compression was caused by microcrack formation and propagation in the CM particles. The relationship between dissipated energy and applied stress agreed with Griffith theory of brittle fracture, further confirming this damping mechanism.

5.1.4 Damping behaviour of syntactic foams under shockwaves

The four shockwaves excited free oscillations in all the syntactic foam samples. The oscillation decayed exponentially over time, demonstrating a typical under-damped dynamic system. The loss factor of the syntactic foams, evaluated by considering the overall trend of the natural logarithm of the strain amplitude, was affected by the impulsive load and the size and volume percentage of the CM particles. The damping of the syntactic foams in free oscillations was also caused by microcrack initiation and propagation in the CM particles.

5.2 Future work

5.2.1 Energy dissipation under cyclic compression

The CM particle reinforced Al matrix syntactic foams exhibited excellent energy dissipation under cyclic compression in this study. The damping was found to be mainly caused by initiation and propagation of microcracks in the CM particles. Further work is needed for a more detailed study on the effect of the microspheres on energy dissipation under cyclic compression.

The microspheres used in the present study had the same wall-thickness-to-radius ratios (t/R). It would be valuable to investigate the effect of the t/R ratio on the energy dissipation of the syntactic foams. The actual dissipated energy of single CM particles in the syntactic foams during cyclic loading has not been investigated yet, and needs to be understood quantitatively in further studies. It would be interesting to compare the specific dissipated energy and specific damping capacity of Al syntactic foams made by different microspheres (e.g., SiC and glass). The fatigue cycles of energy dissipation of syntactic foams under repetitive cyclic compression which is a significant parameter in practical applications also should be studied.

The response of metal matrix syntactic foams made from other metals or alloys (e.g., Mg, Ti and Fe) under cyclic compression needs to be investigated. In addition, the present work only studied the energy dissipation of metal matrix syntactic foams fabricated by the infiltration casting process. It would be valuable to compare it with the energy dissipation of syntactic foams, fabricated by the powder metallurgy process.

5.2.2 Damping behaviour under shockwave

The damping mechanism of metal matrix syntactic foams under the shockwave was formed to be the same as in cyclic compression. In further work, different metal matrix syntactic foams need to be tested in a shock tube, in order to investigate the effects of metal matrix, microsphere and fabrication process on the damping behaviour of the syntactic foam under shockwave.

The present study investigated only four shockwaves. Further work with various impulsive shockwaves is needed to understand the damping behaviour of metals matrix syntactic foams in more depth.

The shock tube device could be modified to incorporate a high-speed 3D digital image correlation (DIC) system. The DIC measurement can help to understand the structural response and dynamic deformation of metal matrix syntactic foam samples under the shockwave and during free oscillations.

5.2.3 Numerical modelling

The current studies on the metal matrix syntactic foams are mainly based on experiments. Most studies investigated the factors that affect the mechanical properties of the syntactic foams by testing different metal matrix syntactic foams. A large amount of experimental data has been collected. These material data make numerical modelling of the mechanical behaviour of syntactic foams possible, which can significantly improve the design and application of the syntactic foams. Altenaiji et al. (2014) has developed a numerical model to simulate the dynamic behaviour of the syntactic foam. However, the model only considers the behaviour of the entire syntactic foam. Currently, there are no models taking into account the contributions of microcracking of the CMs of syntactic foam to the energy dissipation. Further development of numerical modelling of hysteretic energy dissipation is needed.

REFERENCES

Aghajanian, M.K., Langensiepen, R.A., Rocazella, M.A., Leighton, J.T. & Andersson, C.A. (1993) 'The effect of particulate loading on the mechanical behaviour of Al2O3/Al metal-matrix composites', *Journal of Materials Science*, vol. 28, no. 24, pp. 6683-6690.

Akiyama, S., Ueno, H., Imagawa, K., Kitahara, A., Nagata, S., Morimoto, K., Nishikawa, T. & Itoh, M. (1987) *Foamed metal and method of producing same*, vol. No. 4,713,277., U.S. Patent Washington, DC: U.S. Patent and Trademark Office.

Allen, B.C., Mote, M.W. & Sabroff, A.M. (1963) *Method of making foamed metal*, U.S. Patent Washington, DC: U.S. Patent and Trademark Office.

Altenaiji, M., Guan, Z.W., Cantwell, W.J., Zhao, Y. & Schleyer, G.K. (2014) 'Characterisation of aluminium matrix syntactic foams under drop weight impact', *Materials & Design*, vol. 59, pp. 296-302.

ASM (1991) *ASM Handbook*, vol. Volume 4: Heat Treating, no ASM Handbook Committee, pp. p 841-879.

ASTM (2016) *Standard Test Methods for Notched Bar Impact Testing of Metallic Materials*, ASTM International, West Conshohocken, PA,.

Babcsán, N., Beke, S. & Makk, P. (2015) *Method of producing a metal foam by oscillations and thus obtained metal foam product*, U.S. Patent, Washington, DC: U.S. Patent and Trademark Office.

Balch, D.K., O'Dwyer, J.G., Davis, G.R., Cady, C.M., Gray, G.T. & Dunand, D.C. (2005) 'Plasticity and damage in aluminum syntactic foams deformed under dynamic and quasi-static conditions', *Materials Science and Engineering: A*, vol. 391, no. 1-2, pp. 408-417.

Baumeister, J. (1990) 'Method for producing porous metal bodies', *German patent DE*, vol. 40, no. 18, p. 360.

BSI (2013) *BS EN 573-3:2013 Aluminium and aluminium alloys - chemical composition and form of wrought products. Chemical composition and form of products*, British Standards Institution.

Bunn, P. & Mottram, J. (1993) 'Manufacture and compression properties of syntactic foams', *Composites*, vol. 24, no. 7, pp. 565-571.

Castro, G. & Nutt, S.R. (2012) 'Synthesis of syntactic steel foam using mechanical pressure infiltration', *Materials Science and Engineering: A*, vol. 535, pp. 274-280.

Cavaliere, P. (2005) 'Mechanical properties of Friction Stir Processed 2618/Al2O3/20p metal matrix composite', *Composites Part A: Applied Science and Manufacturing*, vol. 36, no. 12, pp. 1657-1665.

Chavko, M., Koller, W.A., Prusaczyk, W.K. & McCarron, R.M. (2007) 'Measurement of blast wave by a miniature fiber optic pressure transducer in the rat brain', *Journal of Neuroscience Methods*, vol. 159, no. 2, pp. 277-281.

Chawla, K.K. (2012) *Composite materials: science and engineering*, Springer Science & Business Media.

Chawla, N., Andres, C., Jones, J. & Allison, J. (1999) 'The effect of reinforcement volume fraction and particle size on the fatigue behavior of an aluminum alloy/SiC composite', *Industrial heating*, vol. 66, no. 2, pp. 61-66.

Chawla, N., Andres, C., Jones, J.W. & Allison, J.E. (1998) 'Cyclic Stress-Strain Behavior of Particle Reinforced Metal Matrix Composites', *Scripta Materialia*, vol. 38, no. 10, pp. 1595-1600.

Chawla, N. & Shen, Y.L. (2001) 'Mechanical behavior of particle reinforced metal matrix composites', *Advanced engineering materials*, vol. 3, no. 6, pp. 357-370.

Chen, P.W., Liu, H., Ding, Y.S., Guo, B.Q., Chen, J.J. & Liu, H.B. (2016) 'Dynamic Deformation of Clamped Circular Plates Subjected to Confined Blast Loading', *Strain*, vol. 52, no. 6, pp. 478-491.

Clyne, T. & Withers, P. (1995) *An introduction to metal matrix composites*, Cambridge university press.

Colombo, M., Martinelli, P., Zedda, R., Albertelli, A. & Marino, N. (2015) 'Dynamic response and energy absorption of mineral–phenolic foam subjected to shock loading', *Materials & Design*, vol. 78, no. Supplement C, pp. 63-73.

Courtney, M.W. & Courtney, A.C. (2010) 'Note: A table-top blast driven shock tube', *Review of Scientific Instruments*, vol. 81, no. 12, p. 126103.

Cox, J., Luong, D., Shunmugasamy, V., Gupta, N., Strbik, O. & Cho, K. (2014) 'Dynamic and Thermal Properties of Aluminum Alloy A356/Silicon Carbide Hollow Particle Syntactic Foams', *Metals*, vol. 4, no. 4, pp. 530-548.

D'Almeida, J.R.M. (1999) 'An analysis of the effect of the diameters of glass microspheres on the mechanical behavior of glass-microsphere/epoxy-matrix composites', *Composites Science and Technology*, vol. 59, no. 14, pp. 2087-2091.

Dannemann, K.A. & Lankford, J. (2000) 'High strain rate compression of closed-cell aluminium foams', *Materials Science and Engineering: A*, vol. 293, no. 1, pp. 157-164.

Daoud, A. (2008) 'Synthesis and characterization of novel ZnAl22 syntactic foam composites via casting', *Materials Science and Engineering: A*, vol. 488, no. 1-2, pp. 281-295.

De Silva, C.W. (1999) *Vibration: fundamentals and practice*, CRC press.

Deqing, W., Weiwei, X., Xiangjun, M. & Ziyuan, S. (2005) 'Cell structure and compressive behavior of an aluminum foam', *Journal of Materials Science*, vol. 40, no. 13, pp. 3475-3480.

Deshpande, V. & Fleck, N. (2000) 'High strain rate compressive behaviour of aluminium alloy foams', *International Journal of Impact Engineering*, vol. 24, no. 3, pp. 277-298.

Dimchev, M., Caeti, R. & Gupta, N. (2010) 'Effect of carbon nanofibers on tensile and compressive characteristics of hollow particle filled composites', *Materials & Design*, vol. 31, no. 3, pp. 1332-1337.

Dou, Z.Y., Jiang, L.T., Wu, G.H., Zhang, Q., Xiu, Z.Y. & Chen, G.Q. (2007) 'High strain rate compression of cenosphere-pure aluminum syntactic foams', *Scripta Materialia*, vol. 57, no. 10, pp. 945-948.

García-Moreno, F. (2016) 'Commercial Applications of Metal Foams: Their Properties and Production', *Materials (Basel, Switzerland)*, vol. 9, no. 2, p. 85.

Gibson, L. (2000) 'Mechanical behavior of metallic foams', *Annual review of materials science*, vol. 30, no. 1, pp. 191-227.

Gibson, L.J. & Ashby, M.F. (1999) *Cellular solids: structure and properties*, Cambridge university press.

Gumus, M. (2009) *Reducing cold-start emission from internal combustion engines by means of thermal energy storage system*, vol. 29.

Guniputi, B., Mamidi, V. & Xavior, A. (2013) *A Review on Processing of Particulate Metal Matrix Composites and its Properties*, vol. 8.

Gupta, N., Luong, D.D. & Cho, K. (2012) 'Magnesium Matrix Composite Foams—Density, Mechanical Properties, and Applications', *Metals*, vol. 2, no. 4, pp. 238-252.

Gupta, N. & Nagorny, R. (2006) 'Tensile properties of glass microballoon-epoxy resin syntactic foams', *Journal of Applied Polymer Science*, vol. 102, no. 2, pp. 1254-1261.

Gupta, N., Pinisetty, D. & Shunmugasamy, V.C. (2013a) *Reinforced polymer matrix syntactic foams: effect of nano and micro-scale reinforcement*, Springer Science & Business Media.

Gupta, N. & Ricci, W. (2006) 'Comparison of compressive properties of layered syntactic foams having gradient in microballoon volume fraction and wall thickness', *Materials Science and Engineering: A*, vol. 427, no. 1–2, pp. 331-342.

Gupta, N. & Rohatgi, P.K. (2014) *Metal Matrix Syntactic Foams: Processing, Microstructure, Properties and Applications*, Destech Publications Incorporated.

Gupta, N., Woldesenbet, E. & Mensah, P. (2004) 'Compression properties of syntactic foams: effect of cenosphere radius ratio and specimen aspect ratio', *Composites Part A: Applied Science and Manufacturing*, vol. 35, no. 1, pp. 103-111.

Gupta, N., Ye, R. & Porfiri, M. (2010) 'Comparison of tensile and compressive characteristics of vinyl ester/glass microballoon syntactic foams', *Composites Part B: Engineering*, vol. 41, no. 3, pp. 236-245.

Gupta, N., Zeltmann, S.E., Shunmugasamy, V.C. & Pinisetty, D. (2013b) 'Applications of Polymer Matrix Syntactic Foams', *Jom*, vol. 66, no. 2, pp. 245-254.

Gupta, N., Zeltmann, S.E., Shunmugasamy, V.C. & Pinisetty, D. (2014) 'Applications of Polymer Matrix Syntactic Foams', *JOM*, vol. 66, no. 2, pp. 245-254.

Hartmann, M., Crössmann, I., Reindel, K. & Singer, R. (1999a) Microstructure and mechanical properties of cellular magnesium matrix composites, *Metall Foams and Porous Metal Structures, International Conference on Metal Foams and Porous Metal Structures*.

Hartmann, M., Reindel, K., Singer, R. & Crossmann, I. (1999b) Microstructure and mechanical properties of cellular magnesium matrix composites, *Metall Foams and Porous Metal Structures, International Conference on Metal Foams and Porous Metal Structures*.

Heimbs, S. (2011) 'Bird Strike Simulations on Composite Aircraft Structures', *SIMULIA Customer Conference*, pp. 73-86.

Hua, Y., Akula, P.K. & Gu, L. (2014) 'Experimental and numerical investigation of carbon fiber sandwich panels subjected to blast loading', *Composites Part B: Engineering*, vol. 56, pp. 456-463.

Ibrahim, I.A., Mohamed, F.A. & Lavernia, E.J. (1991) 'Particulate reinforced metal matrix composites — a review', *Journal of Materials Science*, vol. 26, no. 5, pp. 1137-1156.

Idris, M., Vodenitcharova, T. & Hoffman, M. (2009) 'Mechanical behaviour and energy absorption of closed-cell aluminium foam panels in uniaxial compression', *Materials Science and Engineering: A*, vol. 517, pp. 37-45.

Idriss, M., El Mahi, A., Assarar, M. & El Guerjouma, R. (2013) 'Damping analysis in cyclic fatigue loading of sandwich beams with debonding', *Composites Part B: Engineering*, vol. 44, no. 1, pp. 597-603.

ISO, I.O.f.S. (2011) *Mechanical Testing of Metals-Ductility Testing-Compression Test for Porous and Cellular Metals*, vol. Volume ISO 13314:2011, ISO,, Genva, Switzerland.

Jayatilaka, A.d.S. (1979) *Fracture of engineering brittle materials*, Applied Science publ., London.

Jin, I., Kenny, L.D. & Sang, H. (1990) *Method of producing lightweight foamed metal*, U.S. Patent Washington, DC: U.S. Patent and Trademark Office.

John, B. & Nair, C. (2010) *Update on syntactic foams*, iSmithers, Shawbury, Shropshire.

Kainer, K.U. (2006) *Basics of metal matrix composites*, Wiley-VCH GmbH & Co. KGaA, Weinheim, Germany.

Kalhapure, M.G. & Dighe, P.M. (2015) 'Impact of silicon content on mechanical properties of aluminum alloys', *Int. J. Sci. Res*, vol. 4, pp. 38-40.

Kar, K.K. (2016) *Composite materials: processing, applications, characterizations*, Springer.

Karthikeyan, C.S., Sankaran, S., Jagdish Kumar, M.N. & Kishore (2001) 'Processing and compressive strengths of syntactic foams with and without fibrous reinforcements', *Journal of Applied Polymer Science*, vol. 81, no. 2, pp. 405-411.

Katona, B., Szebényi, G. & Orbulov, I.N. (2017) 'Fatigue properties of ceramic hollow sphere filled aluminium matrix syntactic foams', *Materials Science and Engineering: A*, vol. 679, pp. 350-357.

Katona, B., Szlancsik, A., Tábi, T. & Orbulov, I.N. (2019) 'Compressive characteristics and low frequency damping of aluminium matrix syntactic foams', *Materials Science and Engineering: A*, vol. 739, pp. 140-148.

Kim, H.S. & Plubrai, P. (2004) 'Manufacturing and failure mechanisms of syntactic foam under compression☆', *Composites Part A: Applied Science and Manufacturing*, vol. 35, no. 9, pp. 1009-1015.

Kiser, M., He, M.Y. & Zok, F.W. (1999) 'The mechanical response of ceramic microballoon reinforced aluminum matrix composites under compressive loading', *Acta Materialia*, vol. 47, no. 9, pp. 2685-2694.

Klempner, D. & Frisch, K.C. (1991) *Handbook of polymeric foams and foam technology*, vol. 404, Munich etc.: Hanser.

Kulkarni, S. (2003) 'Effect of filler–fiber interactions on compressive strength of fly ash and short‐fiber epoxy composites', *Journal of Applied Polymer Science*, vol. 87, no. 5, pp. 836-841.

Kutchko, B.G. & Kim, A.G. (2006) 'Fly ash characterization by SEM–EDS', *Fuel*, vol. 85, pp. 2537-2544.

Lavernia, E., Perez, R. & Zhang, J. (1995) 'Damping behavior of discontinuously reinforced ai alloy metal-matrix composites', *Metallurgical and Materials Transactions A*, vol. 26, no. 11, pp. 2803-2818.

Lawn, B. (1993) *Fracture of Brittle Solids*, 2 edn, Cambridge University Press, Cambridge.

Lee, H.-S. & Hong, S. (2003) 'Pressure infiltration casting process and thermophysical properties of high volume fraction SiCp/Al metal matrix composites', *Materials Science and Technology (MS&T)*, vol. 19, pp. 1057-1064.

Lefebvre, L.P., Banhart, J. & Dunand, D.C. (2008) 'Porous Metals and Metallic Foams: Current Status and Recent Developments', *Advanced Engineering Materials*, vol. 10, no. 9, pp. 775-787.

Lehmhus, D., Weise, J., Baumeister, J., Peroni, L., Scapin, M., Fichera, C., Avalle, M. & Busse, M. (2014) 'Quasi-static and Dynamic Mechanical Performance of Glass

Microsphere- and Cenosphere-based 316L Syntactic Foams', *Procedia Materials Science*, vol. 4, pp. 383-387.

Li, X., Li, C., Shao, D., Chen, J., Hui, Q. & Cheng, N. (2016) 'Damping Mechanism of SiC Particle Reinforced Al Matrix Composites', *MATEC Web of Conferences*, vol. 67, p. 06006.

Licitra, L., Luong, D.D., Strbik, O.M. & Gupta, N. (2015) 'Dynamic properties of alumina hollow particle filled aluminum alloy A356 matrix syntactic foams', *Materials & Design*, vol. 66, pp. 504-515.

Ling, G., Bandak, F., Armonda, R., Grant, G. & Ecklund, J. (2009) 'Explosive Blast Neurotrauma', *Journal of Neurotrauma*, vol. 26, no. 6, pp. 815-825.

Liu, B., Huang, W., Huang, L. & Wang, H. (2012) 'Size-dependent compression deformation behaviors of high particle content B4C/Al composites', *Materials Science and Engineering: A*, vol. 534, pp. 530-535.

Liu, J., Huang, X., Zhao, K., Zhu, Z., Zhu, X. & An, L. (2019) 'Effect of reinforcement particle size on quasistatic and dynamic mechanical properties of Al-Al2O3 composites', *Journal of Alloys and Compounds*, vol. 797, pp. 1367-1371.

Llorca, J., Suresh, S. & Needleman, A. (1992) 'An experimental and numerical study of cyclic deformation in metal-matrix composites', *Metallurgical Transactions A*, vol. 23, no. 3, p. 919.

Lloyd, A., Jacques, E., Saatcioglu, M., Palermo, D., Nistor, I. & Tikka, T. (2011) 'Capabilities of a shock tube to simulate blast loading on structures', *American Concrete Institute, ACI Special Publication*, vol. 281, pp. 1-20.

Louar, M.A., Belkassem, B., Ousji, H., Spranghers, K., Kakogiannis, D., Pyl, L. & Vantomme, J. (2015) 'Explosive driven shock tube loading of aluminium plates: experimental study', *International Journal of Impact Engineering*, vol. 86, pp. 111-123.

Lu, H., Wang, X., Zhang, T., Cheng, Z. & Fang, Q. (2009) 'Design, Fabrication, and Properties of High Damping Metal Matrix Composites—A Review', *Materials*, vol. 2, no. 3, pp. 958-977.

Luong, D., Lehmhus, D., Gupta, N., Weise, J. & Bayoumi, M. (2016) 'Structure and Compressive Properties of Invar-Cenosphere Syntactic Foams', *Materials*, vol. 9, no. 2, p. 115.

Luong, D.D., Strbik, O.M., Hammond, V.H., Gupta, N. & Cho, K. (2013) 'Development of high performance lightweight aluminum alloy/SiC hollow sphere syntactic foams and compressive characterization at quasi-static and high strain rates', *Journal of Alloys and Compounds*, vol. 550, pp. 412-422.

Magalas, L. (2006) *Determination of the Logarithmic Decrement in Mechanical Spectroscopy*, vol. 115.

Mahadev, Sreenivasa, C.G. & M Shivakumar, K. (2018) *A Review on Prodution of Aluminium Metal Foams*, vol. 376.

Májlinger, K. & Orbulov, I.N. (2014) 'Characteristic compressive properties of hybrid metal matrix syntactic foams', *Materials Science and Engineering: A*, vol. 606, pp. 248-256.

Mitra, R. & Mahajan, Y. (1995) 'Interfaces in discontinuously reinforced metal matrix composites: an overview', *Bulletin of Materials Science*, vol. 18, no. 4, pp. 405-434.

Mondal, D., Majumder, J.D., Jha, N., Badkul, A., Das, S., Patel, A. & Gupta, G. (2012) 'Titanium-cenosphere syntactic foam made through powder metallurgy route', *Materials & Design*, vol. 34, pp. 82-89.

Mondal, D.P., Goel, M.D. & Das, S. (2009) 'Compressive deformation and energy absorption characteristics of closed cell aluminum-fly ash particle composite foam', *Materials Science and Engineering: A*, vol. 507, no. 1, pp. 102-109.

Moustapha, I.M., El Mahi, A., El Guerjouma, R. & Dazel, O. (2012) Damping analysis in flexural vibration of sandwich beams with debonding, *Acoustics 2012*.

Mukai, T., Kanahashi, H., Higashi, K., Miyoshi, T., Mabuchi, M. & Nieh, T. (1999) 'Experimental study of energy absorption in a close-celled aluminum foam under dynamic loading', *Scripta Materialia*, vol. 40, no. 8.

Nieh, T.G., Higashi, K. & Wadsworth, J. (2000) 'Effect of cell morphology on the compressive properties of open-cell aluminum foams', *Materials Science and Engineering: A*, vol. 283, no. 1, pp. 105-110.

Nturanabo, F., Masu, L. & Kirabira, J.B. (2019) Novel Applications of Aluminium Metal Matrix Composites, in, *Aluminum Alloys and Composites*, IntechOpen.

Orbulov, I.N. (2013) 'Metal matrix syntactic foams produced by pressure infiltration—The effect of infiltration parameters', *Materials Science and Engineering: A*, vol. 583, pp. 11-19.

Orbulov, I.N. & Dobránszky, J. (2008) 'Producing metal matrix syntactic foams by pressure infiltration', *Periodica Polytechnica Mechanical Engineering*, vol. 52, no. 1, p. 35.

Orbulov, I.N. & Ginsztler, J. (2012) 'Compressive characteristics of metal matrix syntactic foams', *Composites Part A: Applied Science and Manufacturing*, vol. 43, no. 4, pp. 553-561.

Orbulov, I.N., Németh, Á. & Dobránszky, J. (2008) Composite production by pressure infiltration, *Materials Science Forum*, vol. 589, Trans Tech Publ, pp. 137-142.

Pal, A., Verma, A., Kandpal, B.C. & Swroop saxsena, s. (2015) 'Stir Casting of Metal Matrix Composites – A Review', *International Journal of Computer & Mathematical Sciences*, vol. ISSN 2347 – 8527 Volume 4, pp. 2347-8527.

Papadopoulos, D.P., Konstantinidis, I.C., Papanastasiou, N., Skolianos, S., Lefakis, H. & Tsipas, D.N. (2004) 'Mechanical properties of Al metal foams', *Materials Letters*, vol. 58, no. 21, pp. 2574-2578.

Reglero, J.A., Rodríguez-Pérez, M.A., Solórzano, E. & de Saja, J.A. (2011) 'Aluminium foams as a filler for leading edges: Improvements in the mechanical behaviour under bird strike impact tests', *Materials & Design*, vol. 32, no. 2, pp. 907-910.

Rocha Rivero, G.A., Schultz, B.F., Ferguson, J.B., Gupta, N. & Rohatgi, P.K. (2013) 'Compressive properties of Al-A206/SiC and Mg-AZ91/SiC syntactic foams', *Journal of Materials Research*, vol. 28, no. 17, pp. 2426-2435.

Rohatgi, P.K., Gupta, N., Schultz, B.F. & Luong, D.D. (2011) 'The synthesis, compressive properties, and applications of metal matrix syntactic foams', *JOM*, vol. 63, no. 2, pp. 36-42.

Rohatgi, P.K., Kim, J.K., Gupta, N., Alaraj, S. & Daoud, A. (2006) 'Compressive characteristics of A356/fly ash cenosphere composites synthesized by pressure infiltration technique', *Composites Part A: Applied Science and Manufacturing*, vol. 37, no. 3, pp. 430-437.

Rohatgi, P.K., Matsunaga, T. & Gupta, N. (2009) 'Compressive and ultrasonic properties of polyester/fly ash composites', *Journal of Materials Science*, vol. 44, no. 6, pp. 1485-1493.

Rohatgi, P.K., Ray, S. & Liu, Y. (1992) 'Tribological properties of metal matrix-graphite particle composites', *International Materials Reviews*, vol. 37, no. 1, pp. 129-152.

Sahu, S. (2013) *ZA27-SiCp Composite Foam through Liquid Metallurgy Technique Using CaH2 as a Foaming Agent*, vol. 59.

San Marchi, C., Cao, F., Kouzeli, M. & Mortensen, A. (2002) 'Quasistatic and dynamic compression of aluminum-oxide particle reinforced pure aluminum', *Materials Science and Engineering: A*, vol. 337, no. 1, pp. 202-211.

Sankaran, S., Sekhar, K.R., Raju, G. & Kumar, M.N.J. (2006) 'Characterization of epoxy syntactic foams by dynamic mechanical analysis', *Journal of Materials Science*, vol. 41, no. 13, pp. 4041-4046.

Santa Maria, J.A., Schultz, B.F., Ferguson, J., Gupta, N. & Rohatgi, P.K. (2014) 'Effect of hollow sphere size and size distribution on the quasi-static and high strain rate compressive properties of Al-A380–Al2O3 syntactic foams', *Journal of materials science*, vol. 49, no. 3, pp. 1267-1278.

Schleyer, G., Lowak, M., Polcyn, M. & Langdon, G. (2007) 'Experimental investigation of blast wall panels under shock pressure loading', *International Journal of Impact Engineering*, vol. 34, no. 6, pp. 1095-1118.

Seshan, S., Guruprasad, A., Prabha, M. & Sudhakar, A. (2013) 'Fibre-reinforced metal matrix composites--a review', *Journal of the Indian Institute of Science*, vol. 76, no. 1, p. 1.

Simone, A.E. & Gibson, L.J. (1998) 'Effects of solid distribution on the stiffness and strength of metallic foams', *Acta Materialia*, vol. 46, no. 6, pp. 2139-2150.

Srikanth, N. & Gupta, M. (2002) 'Damping characterization of Mg–SiC composites using an integrated suspended beam method and new circle-fit approach', *Materials Research Bulletin*, vol. 37, no. 6, pp. 1149-1162.

Srivatsan, T.S. (1995) 'Cyclic strain resistance and fracture behaviour of Al2O3-particulate-reinforced 2014 aluminium alloy metal-matrix composites', *International Journal of Fatigue*, vol. 17, no. 3, pp. 183-199.

Stewart, J.B. & Pecora, C. (2015) 'Explosively driven air blast in a conical shock tube', *Review of Scientific Instruments*, vol. 86, no. 3, p. 035108.

Sugimura, Y., Meyer, J., He, M.Y., Bart-Smith, H., Grenstedt, J. & Evans, A.G. (1997) 'On the mechanical performance of closed cell Al alloy foams', *Acta Materialia*, vol. 45, no. 12, pp. 5245-5259.

Surappa, M. (2003) 'Aluminium matrix composites: Challenges and opportunities', *Sadhana*, vol. 28, no. 1-2, pp. 319-334.

Szlancsik, A., Katona, B., Bobor, K., Májlinger, K. & Orbulov, I.N. (2015) 'Compressive behaviour of aluminium matrix syntactic foams reinforced by iron hollow spheres', *Materials & Design*, vol. 83, pp. 230-237.

Tahamtan, S., Emamy, M. & Halvaee, A. (2014) 'Effects of reinforcing particle size and interface bonding strength on tensile properties and fracture behavior of Al-A206/alumina micro/nanocomposites', *Journal of Composite Materials*, vol. 48, pp. 3331-3346.

Tao, X., Zhang, L. & Zhao, Y. (2008) 'Compressive response of Al matrix syntactic foam manufactured by liquid sintering', *Proceedings of materials science and technology (MS&T).* no. Pittsburgh, Pennsylvania, pp. 2587–2594.

Tao, X., Zhang, L. & Zhao, Y. (2009) 'Al matrix syntactic foam fabricated with bimodal ceramic microspheres', *Materials & Design*, vol. 30, no. 7, pp. 2732-2736.

Tao, X. & Zhao, Y. (2009) 'Compressive behavior of Al matrix syntactic foams toughened with Al particles', *Scripta Materialia*, vol. 61, no. 5, pp. 461-464.

Tao, X.F. & Zhao, Y.Y. (2012) 'Compressive failure of Al alloy matrix syntactic foams manufactured by melt infiltration', *Materials Science and Engineering: A*, vol. 549, pp. 228-232.

Venkatanarayanan, P.S. & Stanley, A.J. (2012) 'Intermediate velocity bullet impact response of laminated glass fiber reinforced hybrid (HEP) resin carbon nano composite', *Aerospace Science and Technology*, vol. 21, no. 1, pp. 75-83.

Vogiatzis, C., Tsouknidas, A., Kountouras, D. & Skolianos, S. (2015) 'Aluminum–ceramic cenospheres syntactic foams produced by powder metallurgy route', *Materials & Design*, vol. 85, pp. 444-454.

Vyletel, G.M., Van Aken, D.C. & Allison, J.E. (1991) 'Effect of microstructure on the cyclic response and fatigue behavior of an XDTM aluminum metal matrix composite', *Scripta Metallurgica et Materialia*, vol. 25, no. 10, pp. 2405-2410.

Wei, J., Cheng, H., Zhang, Y., Han, F., Zhou, Z. & Shui, J. (2002) 'Effects of macroscopic graphite particulates on the damping behavior of commercially pure aluminum', *Materials Science and Engineering: A*, vol. 325, no. 1-2, pp. 444-453.

Wei, J.-N., Wang, D., Xie, W., Luo, J. & Han, F. (2007) 'Effects of macroscopic graphite particulates on the damping behavior of Zn–Al eutectoid alloy', *Physics Letters A*, vol. 366, no. 1-2, pp. 134-136.

Woldesenbet, E. (2005) 'Effect of Microballoon Radius Ratio on Syntactic Foam Core Sandwich Composites', *Journal of Sandwich Structures and Materials*, vol. 7, no. 2, pp. 95-111.

Woldesenbet, E., Gupta, N. & Jadhav, A. (2005) 'Effects of density and strain rate on properties of syntactic foams', *Journal of Materials Science*, vol. 40, no. 15, pp. 4009-4017.

Wu, G.H., Dou, Z.Y., Jiang, L.T. & Cao, J.H. (2006) 'Damping properties of aluminum matrix–fly ash composites', *Materials Letters*, vol. 60, no. 24, pp. 2945-2948.

Xu, D. & Schmauder, S. (1999) 'The plastic energy dissipation in metal matrix composites during cyclic loading', *Computational Materials Science*, vol. 15, no. 1, pp. 96-100.

Xue, X. & Zhao, Y. (2011) 'Ti matrix syntactic foam fabricated by powder metallurgy: Particle breakage and elastic modulus', *JOM*, vol. 63, no. 2, pp. 43-47.

Xue, X.-b., Wang, L.-q., Wang, M.-m., Lu, W.-j. & Zhang, D. (2012) 'Manufacturing, compressive behaviour and elastic modulus of Ti matrix syntactic foam fabricated by powder metallurgy', *Transactions of Nonferrous Metals Society of China*, vol. 22, pp. s188-s192.

Yan, C., Lifeng, W. & Jianyue, R. (2008) 'Multi-functional SiC/Al Composites for Aerospace Applications', *Chinese Journal of Aeronautics*, vol. 21, no. 6, pp. 578-584.

Yu, H.j., Yao, G. & Liu, Y. (2006) 'Tensile property of Al-Si closed-cell aluminum foam', *Transactions of Nonferrous Metals Society of China*, vol. 16, no. 6, pp. 1335-1340.

Yu, M. & Banhart, J. (1998) 'Mechanical properties of metal foams', *Bremen*, pp. 37-48.

Zhang, B., Lin, Y., Li, S., Zhai, D. & Wu, G. (2016) 'Quasi-static and high strain rates compressive behavior of aluminum matrix syntactic foams', *Composites Part B: Engineering*, vol. 98, no. Supplement C, pp. 288-296.

Zhang, J., Perez, R.J., Gupta, M. & Lavernia, E.J. (1993a) 'Damping behavior of particulate reinforced 2519 Al metal matrix composites', *Scripta Metallurgica et Materialia*, vol. 28, no. 1, pp. 91-96.

Zhang, J., Perez, R.J. & Lavernia, E.J. (1993b) 'Documentation of damping capacity of metallic, ceramic and metal-matrix composite materials', *Journal of Materials Science*, vol. 28, no. 9, pp. 2395-2404.

Zhang, J., Perez, R.J. & Lavernia, E.J. (1994a) 'Effect of SiC and graphite particulates on the damping behavior of metal matrix composites', *Acta Metallurgica et Materialia*, vol. 42, no. 2, pp. 395-409.

Zhang, J., Perez, R.J., Wong, C.R. & Lavernia, E.J. (1994b) 'Effects of secondary phases on the damping behaviour of metals, alloys and metal matrix composites', *Materials Science and Engineering: R: Reports*, vol. 13, no. 8, pp. 325-389.

Zhang, L. & Zhao, Y. (2007) 'Mechanical response of Al matrix syntactic foams produced by pressure infiltration casting', *Journal of Composite Materials*, vol. 41, no. 17, pp. 2105-2117.

Zhang, Q., Lin, Y., Chi, H., Chang, J. & Wu, G. (2017) 'Quasi-static and dynamic compression behavior of glass cenospheres/5A03 syntactic foam and its sandwich structure', *Composite Structures*.

Zhao, Y. & Tao, X. (2009) 'Behaviour of metal matrix syntactic foams in compression', *Mater. Sci. Technol*, pp. 1785-1794.